Faculty of Applied Earth Sciences
Department of Petroleum Engineering and Applied Geophysics

Ekofisk chalk: core measurements, stochastic reconstruction, network modeling and simulation

Saifullah Talukdar

A Dissertation
for the partial fulfillment of the requirements for the degree of Doctor Ingeniør

Trondheim, Norway
May 07, 2002

NTNU
Norwegian University of Science and Technology

URN:NBN:no-2347

To my wonderful daughters

Raida & Raisa

URN:NBN:no-2347

Abstract

This dissertation deals with (1) experimental measurements on petrophysical, reservoir engineering and morphological properties of Ekofisk chalk, (2) numerical simulation of core flood experiments to analyze and improve relative permeability data, (3) stochastic reconstruction of chalk samples from limited morphological information, (4) extraction of pore space parameters from the reconstructed samples, development of network model using pore space information, and computation of petrophysical and reservoir engineering properties from network model, and (5) development of 2D and 3D idealized fractured reservoir models and verification of the applicability of several widely used conventional upscaling techniques in fractured reservoir simulation.

Experiments have been conducted on eight Ekofisk chalk samples and porosity, absolute permeability, formation factor, and oil-water relative permeability, capillary pressure and resistivity index are measured at laboratory conditions. Mercury porosimetry data and backscatter scanning electron microscope images have also been acquired for the samples.

A numerical simulation technique involving history matching of the production profiles is employed to improve the relative permeability curves and to analyze hysteresis of the Ekofisk chalk samples. The technique was found to be a powerful tool to supplement the uncertainties in experimental measurements.

Porosity and correlation statistics obtained from backscatter scanning electron microscope images are used to reconstruct microstructures of chalk and particulate media. The reconstruction technique involves a simulated annealing algorithm, which can be constrained by an arbitrary number of morphological parameters. This flexibility of the algorithm is exploited to successfully reconstruct particulate media and chalk samples using more than one correlation functions. A technique based on conditional simulated

annealing has been introduced for exact reproduction of vuggy porosity in chalk in the form of foraminifer shells. A hybrid reconstruction technique that initializes the simulated annealing reconstruction with input generated using the Gaussian random field method has also been introduced. The technique was found to accelerate significantly the rate of convergence of the simulated annealing method. This finding is important because the main advantage of the simulated annealing method, namely its ability to impose a variety of reconstruction constraints, is usually compromised by its very slow rate of convergence.

Absolute permeability, formation factor and mercury-air capillary pressure are computed from simple network models. The input parameters for the network models were extracted from a reconstructed chalk sample. The computed permeability, formation factor and mercury-air capillary pressure correspond well with the experimental data. The predictive power of a network model for chalk is further extended through incorporating important pore-level displacement phenomena and realistic description of pore space geometry and topology. Limited results show that the model may be used to compute absolute and relative permeabilities, capillary pressure, formation factor, resistivity index and saturation exponent. The above findings suggest that the network modeling technique may be used for prediction of petrophysical and reservoir engineering properties of chalk. Further works are necessary and an outline is given with considerable details.

Two 2D, one 3D and a dual-porosity fractured reservoir models have been developed and an imbibition process involving water displacing oil is simulated at various injection rates and with different oil-to-water viscosity ratios using four widely used conventional upscaling techniques. The upscaling techniques are the Kyte & Berry, Pore Volume Weighted, Weighted Relative Permeability, and Stone. The results suggest that upscaling of fractured reservoirs may be possible using the conventional techniques. Kyte & Berry technique was found to be the most effective in all situations.

However, further investigations are necessary using realistic description of fracture length, orientation, connectivity, aperture, spacing, etc.

Acknowledgments

It has been quite a journey with moments of pleasure, pain, excitement and depression. After all, the final destination has been possible due to guidance, encouragement, care and sacrifice of several important people. I am heavily indebted to all of them. First and foremost I would like to express my sincere gratitude to Professor Ole Torsæter for engaging me in this work and for his supervision. His all-out support, kindness, and enthusiasm have been invaluable in completing this thesis in relatively short time.

During this research I spent three months at the porous media laboratory, Department of Chemical Engineering, University of Waterloo, Canada. I gratefully acknowledge the supervision of Professor Marios A. Ioannidis and the hospitality I received from his department.

I am extremely grateful to Dr. Pål-Erik Øren of STATOIL Research Center, Trondheim, Norway for sharing with me his vast experience in this subject. His suggestions and ideas were the great starting point of this work. Special thanks to Dr. James J. Howard of Phillips Petroleum Company, Bartlesville, OK, USA for his keen interest in this work, and the encouragement and support he has provided during this work.

Much credit is given to Medad T. Tweheyo, a fellow Ph.D. candidate, for helping me with the core-flood experiments, Gunnar Carlsen of SINTEF surface and colloid chemistry laboratory for mercury porosimetry measurements, Karl Isachsen of the Department of Geology for preparing thin sections and Reidar Bøe of SINTEF Petroleum Research for taking backscatter scanning electron microscope images. I would also like to thank my teachers, colleagues and staffs at the Department of Petroleum Engineering and Applied Geophysics for their cooperation and for creating a very cordial and conducive working environment.

This work has been mostly financed by a Ph.D. fellowship from Phillips Petroleum Company Norway (PPCoN). The financial support from PPCoN is

hereby gratefully acknowledged. Anne Vedvik, the contact person at PPCoN, has been very kind and helpful during the entire work.

Last but not least, I would like to thank my wife Hasin and daughters Raida and Raisa for their love and sacrifice. Hasin has been staying with me virtually giving up her medical profession and nourishing me physically and mentally and doing everything to make sure that my name get onto the list of doctoral graduates. This work has consumed much of Raida and Raisa's share on my time. Your daddy wants you to know that he loves you very much.

Contents

List of articles

Laboratory Report:

Talukdar, M.S., Tweheyo, M.T and Torsæter, O.: "Experimental Measurements of Petrophysical, Reservoir Engineering and Morphological Properties of Ekofisk Chalk," Department of Petroleum Engineering and Applied Geophysics, Norwegian University of Science and Technology, Trondheim, Norway, December 2001.

Paper 1:

Tweheyo, M.T., Talukdar, M.S. and Torsæter, O.: "Hysteresis Effects in Capillary Pressure, Relative Permeability and Resistivity Index of North Sea Chalk," SCA 2001-65, International Symposium of the Society of Core Analysts, Edinburgh, 17-19 September 2001.

Paper 2:

Tweheyo, M.T., Talukdar, M.S., Torsæter, O. and Vafaeinezhad, Y.: "Improvement of Experimental Relative Permeability of North Sea Chalk Through Simulation," Proc. 11th Oil, Gas and Petrochemical Congress & Exhibition, Tehran, Iran, 29-31 October 2001.

Paper 3:

Talukdar, M.S., Torsæter, O., Ioannidis, M.A. and Howard, J.J.: "Stochastic Reconstruction, 3D Characterization and Network Modeling of Chalk," *Journal of Petroleum Science and Engineering*, **984** (2002).

Paper 4:

Talukdar, M.S., Torsæter, O. and Ioannidis, M.A.: "Stochastic Reconstruction of Particulate Media from Two-Dimensional Images," *Journal of Colloid and Interface Science* **246** (2002).

Paper 5:

Talukdar, M.S., Torsæter, O., Ioannidis, M.A. and Howard, J.J.: "Stochastic Reconstruction of Chalk from Two-Dimensional Images," *Transport in Porous Media* **1621**, 1-23 (2002).

Paper 6:

Talukdar, M.S. and Torsæter, O.: "Reconstruction of Chalk Pore Networks from 2D Back Scatter Electron Micrographs Using A Simulated Annealing Technique," *Journal of Petroleum Science and Engineering*, **972** (2002).

Paper 7:

Talukdar, M.S., Torsæter, O. and Howard, J.J.: "Stochastic Reconstruction of Vuggy Porosity in Chalk Using A Conditional Simulated Annealing Technique," *Transport in Porous Media*, under review.

Paper 8:

Talukdar, M.S. and Torsæter, O.: "A Network Model for Two-Phase Flow in Chalk," unpublished.

Paper 9:

Talukdar, M.S., Semere, M. and Torsæter, O.: "Pore-Scale Studies of Mobilization and Recovery of Oil by Waterflooding," poster presented at the 2000 International Symposium of the Society of Core Analysts, Abu Dhabi, UAE, 18-22 October 2000.

Paper 10:

Talukdar, M.S., Banu, H.A., Torsæter, O. and Kleppe, J.: "Introducing Up-Scaling Techniques in Fractured Reservoir Simulation," *Nordic Petroleum Technology Series V* (May 2001), 189-218.

Paper 11:

Talukdar, M.S., Banu, H.A., Torsæter, O. and Kleppe, J.: "Applicability and Rate Sensitivity of Several Up Scaling Techniques in Fractured Reservoir Simulation," SPE 59048, 2000 SPE International Petroleum Conference and Exhibition in Mexico, Villahermosa, Mexico, 1-3 February 2000.

1. Introduction

This dissertation deals with experimental measurements of petrophysical, reservoir engineering and morphological properties of Ekofisk chalk, simulation of core flood experiments, stochastic reconstruction of porous microstructures, network modeling for computation of petrophysical and reservoir engineering parameters, and model development and simulation of fractured reservoirs using conventional upscaling techniques. The dissertation constitutes a collection of papers and a laboratory report describing the procedures and results from the above topics. The introductory sections briefly discuss the main results.

1.1 Background and motivation

The Ekofisk Field, located in the Norwegian Sector of the North Sea, is a high porosity, low matrix permeability naturally fractured chalk reservoir. This giant field is undergoing several improved oil recovery processes, such as, water injection, gas injection and water-alternating-gas (WAG) injection. Higher confidence in the measurement of petrophysical and reservoir engineering properties, and improved prediction of recovery processes bear significant economic value for the field. The properties of interest are the absolute and relative permeability, capillary pressure, formation factor and resistivity index. Pore-scale network models provide a powerful tool to supplement the time, cost and uncertainties involved in experimental measurements. Despite significant share of world's petroleum reside in chalk reservoirs, surprisingly, this rock type has received little attention from network modeling researchers. With the exception of Bekri *et al.* [1] and Xu *et al.* [2] network modeling techniques have been previously used in the study of sandstone reservoirs, e.g., [3-6]. While Bekri *et al.* [1] have demonstrated the feasibility of this approach for predicting absolute permeability, formation

factor and drainage air-mercury capillary pressure of homogeneous chalks, Xu *et al.* [2] have used this tool to improve the analysis of core-flood experiments in heterogeneous (vugular) chalks. Bekri *et al.* [1] extracted required parameters (pore- and throat-size distributions and average coordination number) for their regular cubic network model from stochastically reconstructed samples using conditioning and truncation of Gaussian random fields (GRF) method [1, 7-13]. This reconstruction technique can be constrained by only porosity and pore-phase autocorrelation function, which is not always successful to provide a reliable reconstruction, for example, Bekri *et al.* [1] were not successful in modeling the microstructure and transport properties of samples containing vuggy porosity in the form of hollow foraminifer shells. Imposing arbitrary morphological constraints in order to obtain a reliable reconstruction is possible by simulated annealing (SA) technique [14-20]. Clearly, there are enormous scopes to extent predictive capabilities of a network model for chalk through improved reconstruction of numerical samples.

Another way of increasing confidence in experimental measurements is by numerical simulation of the core flood experiments and analysis of relative permeability and capillary pressure data from history matching of the fluid production and other relevant data (e.g., saturation profile) [21-25]. In conventional relative permeability measurements, no points are possible before breakthrough. Also, the measured points after breakthrough are normally scattered. Relative permeability curves consisting of scattered points and no points before breakthrough are not suited for prediction of improved recovery processes. A numerical simulation approach involving history matching of the production profiles has been adopted to improve experimental relative permeability curves on a suite of Ekofisk chalk samples.

Finally, modeling of fractured reservoirs is extremely difficult due to complex geometry of fracture networks, and vast property discrepancy between matrix rock and fractures. The rock-type, and size and shape of the

matrix blocks strongly influence the matrix-fracture fluid exchange process. Due to all these complexities, many issues of the fractured reservoirs have remained unresolved, specially, the issues of upscaling. In recent years, multiple realizations of fracture networks have been generated at a very fine-scale using sophisticated tools and softwares [26-28]. However, simulation at this scale is not affordable and therefore, upscaling is essential. Upscaling is a technique to translate the fine-scale information to a more tractable scale (field-scale). Unfortunately, no reliable upscaling technique is available to date for fractured reservoir simulation. Traditional volume averaging techniques, e.g., Kyte & Berry [29], Pore Volume Weighted, Weighted Relative Permeability, Stone [30], Vertical Equilibrium [31], etc. are widely used for upscaling of conventional reservoirs. It is worthwhile to investigate the applicability of these techniques in fractured reservoir simulation.

1.2 Scope of work

The world works differently at different scales and earth sciences must therefore rely on different methods to model the diverse earth systems that range in size from atoms and molecules to the whole planet [32]. Fig. 1.1 shows the characteristic volume scales and corresponding time scales encountered in computational earth sciences, which indicate a significant overlapping among the characteristic scales and the need for the appropriate computational tools. This overlap among different length-scales provides an opportunity to compare and interpret petrophysical and reservoir engineering properties obtained at different scales using relevant computation techniques. For example, pore-network modeling technique has been used recently to simulate coreflood experiments in a heterogeneous carbonate sample [2]. Similarly, upscaling of high-resolution geological model into low-resolution field-scale simulation model is possible [33-34]. Since the transformations

reduce the amount of high-resolution information, appropriate technique must be applied so that the “fingerprints” of the fine-scale structure are retained.

The scopes of this work encompass a wide computational domain that include extraction of microstructural information from submicron size chalk pores, use of this information for pore-network reconstruction (upto few microns) and subsequent computation of petrophysical and reservoir engineering properties, and comparison with core measurements (centimeter scale), and finally, upscaling of centimeter-scale fracture-networks into meter-scale simulation gridblocks. The respective scales of interest in this work are highlighted in Fig. 1.1 and the overall workflow is portrayed in Fig. 1.2. However, the main focus in this thesis is directed towards accurate reconstruction of chalk microstructures and computation of its petrophysical and reservoir engineering properties using a network modeling approach.

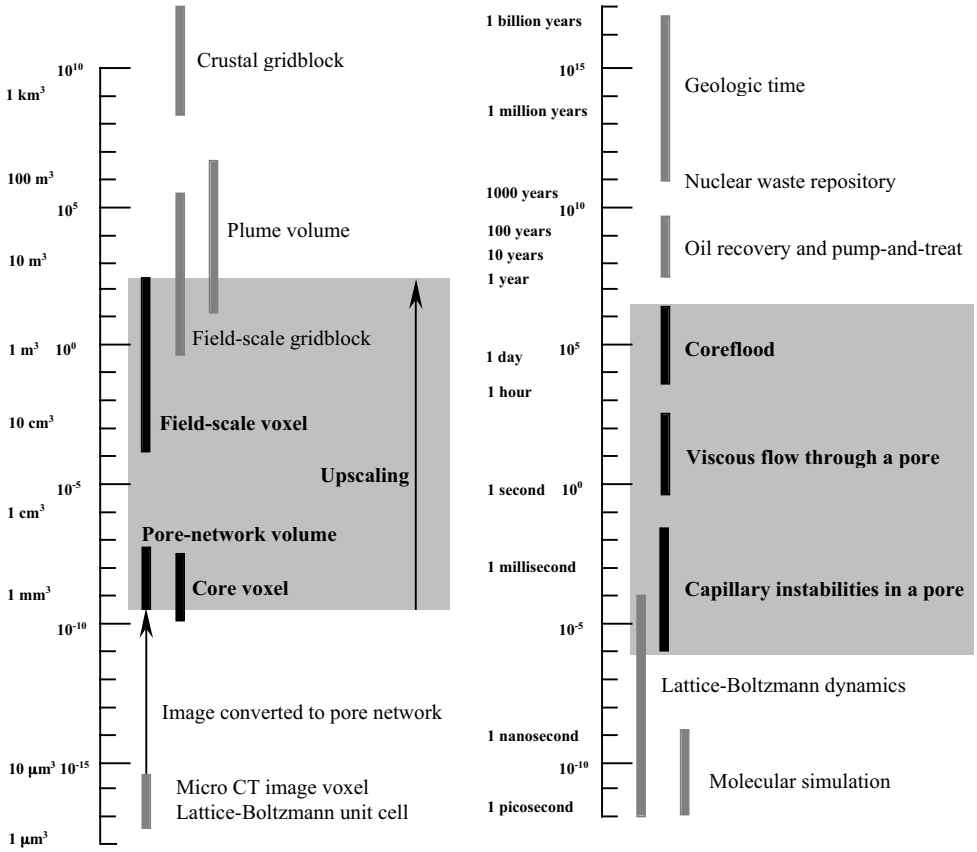

Figure 1.1—Characteristic volume scales (left) and corresponding time scales (right) encountered in computational earth sciences (after Patzek [32]).

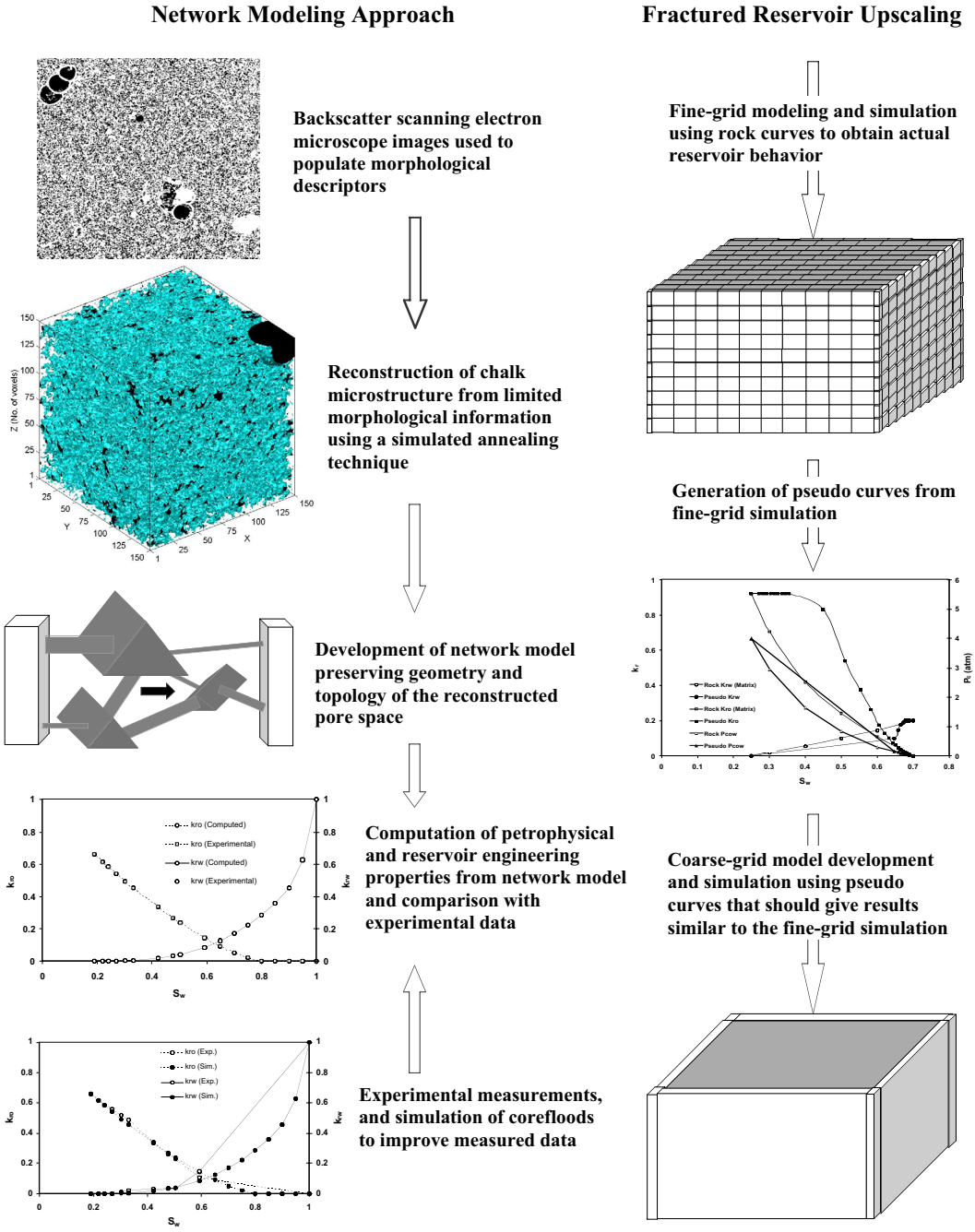

Figure 1.2—Overall work flow diagram adopted in this thesis.

1.3 Organization of the introductory sections

The introductory sections describing the main results from the laboratory report and papers are organized as follows: Section 2 summarizes results from experimental measurements. Detailed results and procedures are described in the Laboratory Report and some results have been presented in Paper 1. The core flood simulation techniques and results are discussed in Section 3 following the works presented in Papers 1-2. Section 4 presents the stochastic reconstruction of numerical chalk samples. The algorithms and detailed results are presented in Papers 3-7. Results from pore space characterization and simple network modeling have been described in Section 5. Development of a more robust network model incorporating important pore-level displacement phenomena, and realistic description of pore space geometry and topology is briefly described in Section 6. Detailed discussion on this matter is made in Paper 8 (and Paper 9). The issue of fractured reservoir upscaling is presented in Section 7 based on the results published in Papers 10-11. Section 8 summarizes the most important results. Finally, outline for future works are given in Section 9.

2. Experimental measurements

Experiments were conducted on two sets of Ekofisk chalk samples to measure petrophysical, reservoir engineering and morphological properties. The first set comprised sample 2, 3, 4 and 6 while the second set comprised sample 32, 35, 36 and 38. The measurements included porosity, absolute and relative permeabilities, capillary pressure, wettability, formation factor, resistivity index, mercury porosimetry and backscatter scanning electron microscope (SEM) imaging. The measurement techniques and analysis of data are thoroughly described in the Laboratory Report. Results from the first set of

samples have also been presented in Paper 1. The key results are briefly discussed in this section.

2.1 Preparation of samples and brine

Before the measurements, the core samples were cleaned in a Soxhlet extraction apparatus alternately by Methanol and Toluene to remove the interstitial (or filtrate) water and oil, respectively. The cores were then dried in a vacuum oven at 60^{o} C until consistent dry weights were observed for all samples. The formation brine was prepared by mixing appropriate amount of NaCl, KCl, $CaCl_2.2H_2O$ and $MgCl_2.6H_2O$ into distilled water.

2.2 Porosity and absolute permeability

Porosities of the dried core samples were measured using a standard helium porosimeter and crosschecked by a saturation method. For the first and second set of samples, the helium porosities range from 0.21 - 0.33 and 0.36 - 0.4, respectively while the brine porosities range from 0.19 - 0.31 and 0.34 - 0.38, respectively. The second set of samples therefore has a bigger storage capacity of reservoir fluids than the first one. The helium porosity is slightly higher than the brine porosity. This is due to the fact that helium has small molecules with high diffusivity that penetrate the small pores of cores easier than the brine molecules.

Air and brine permeabilities were measured using a constant head permeameter with the Hassler cell. The permeabilities of the first set of samples are lower than those of the second set of samples. For the first and second set of samples, the air permeabilities range from 0.2 - 2.6 mD and 0.84 - 3.05 mD, respectively, and the brine permeabilities range from 0.09 - 1.94 mD and 0.35 - 1.88 mD, respectively. The variations of absolute permeability

(k) with porosity (ϕ) are shown in Fig. 2.1. Permeability to air and brine are plotted against helium and brine porosities, respectively. The variation is irregular showing no correlation between k and ϕ. Bekri *et al.* [1] also observed irregular variations for similar North Sea chalk samples.

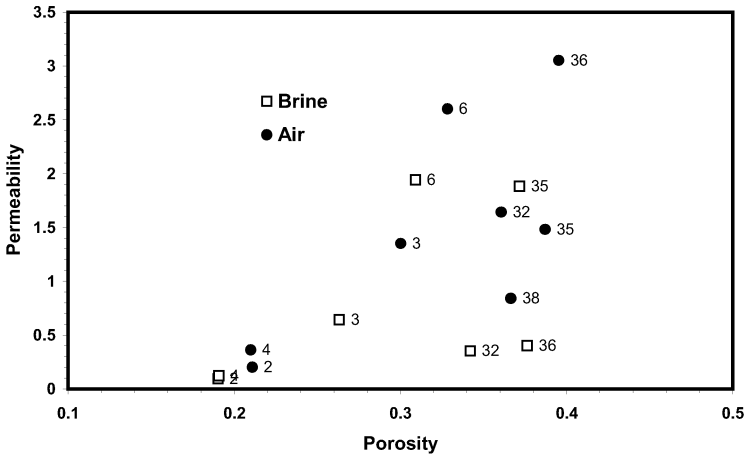

Figure 2.1—Permeability vs. porosity of Ekofisk chalk samples.

2.3 Hysteresis in relative permeability, capillary pressure and resistivity index

Accurate estimation of capillary pressure and relative permeability curves are very important for evaluating hydrocarbon recovery processes. Also, resistivity index data are important for evaluating fluid distributions in reservoirs during these processes. All these parameters are path dependent i.e. different in drainage and imbibition processes, commonly known as hysteresis, which makes them complicated to predict. A constant head permeameter with the Hassler cell was used and the unsteady state method was applied to measure relative permeability of oil and brine for both drainage and imbibition processes. The centrifuge method was used to obtain the capillary pressure curves and the resistivity of the core samples was measured

at laboratory conditions by a two-electrode method using the ratio of voltage decrease between a reference resistor and a core sample in series. Relative permeability and capillary pressure were measured on sample 2, 3, 4, 6, 32, 36 and 38. For practical reasons, sample 3 and 36 from the above seven samples were excluded from resistivity measurements.

Varying levels of hysteresis were observed in capillary pressure, relative permeability and resistivity index with the most prevalent in capillary pressure and relative permeability curves. Hysteresis was observed in both oil and water relative permeabilities, which is similar to the observations made by Eleri *et al.* [35] for intermediate-wet chalk cores. Braun and Holland [36] also observed various behaviors for different wettabilities. This result is, however, in contradiction to what is commonly observed in water-wet sandstone where little or no hysteresis is observed for the wetting phase [25, 35-39]. For the non-wetting phase, the drainage curve always lies above the imbibition curve whereas for the wetting phase, the imbibition curve lies either above or below the drainage curve. Examples of the two situations are shown in Figs. 2.2 and 2.3, respectively.

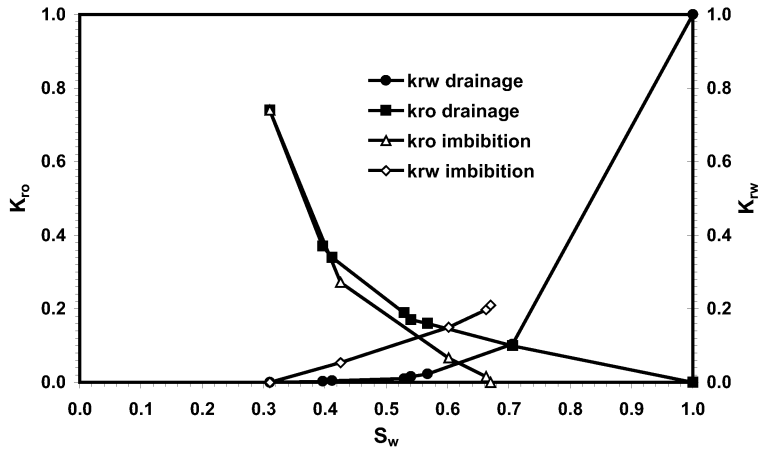

Figure 2.2—Oil and water relative permeability curves for sample 4 showing that the wetting phase imbibition curve lies above the drainage curve.

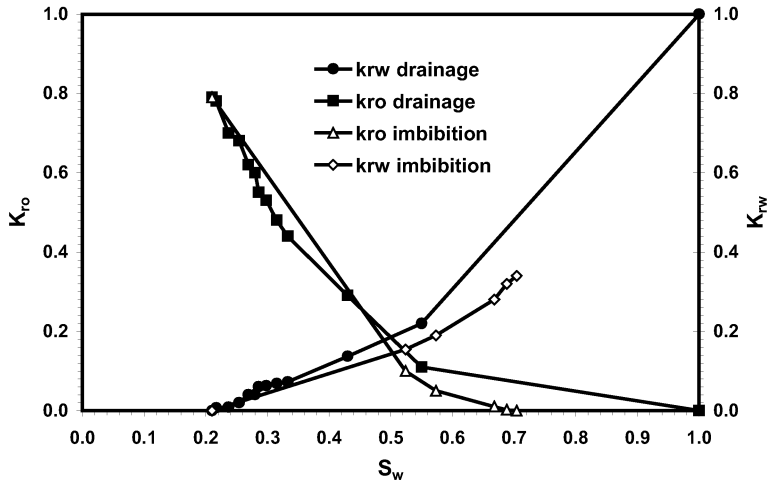

Figure 2.3—Oil and water relative permeability curves for sample 32 showing that the wetting phase imbibition curve lies below the drainage curve.

Significant resistivity hysteresis was observed in some samples (e.g., sample 2, 6 and 32), whereas others showed little or no resistivity hysteresis (e.g., sample 4 and 38). Examples of the two cases are shown in Figs. 2.4 and 2.5, respectively. A value between 1.4 and 2.52 was recorded for Archie's saturation exponent *n*. Sample 2, 6 and 32 showed significant resistivity hysteresis. The computed values of *n* for sample 2 were 1.57 and 1.41 for drainage and imbibition, respectively. The drainage and imbibition values of *n* for sample 6 and 32 were 1.71 and 1.53, and 2.07 and 1.83, respectively. Sample 4 had no resistivity hysteresis (n = 1.4) while core 38 indicated a minor hysteresis with *n*-values of 2.44 and 2.52 for drainage and imbibition, respectively. The resistivity of the rock depends on the distribution of hydrocarbons and brine in the pore space. Fluid distributions may change during drainage and imbibition resulting in resistivity hysteresis. One may expect that during imbibition, there is entrapment and snap-off of the non-wetting phase leading to long electric flow paths and consequently higher resistivity than during drainage. This behaviour has been observed in sandstone samples [40-41] but results from the chalk samples show a different

trend where the imbibition resistivity curves lie below the drainage curves (Fig. 2.4).

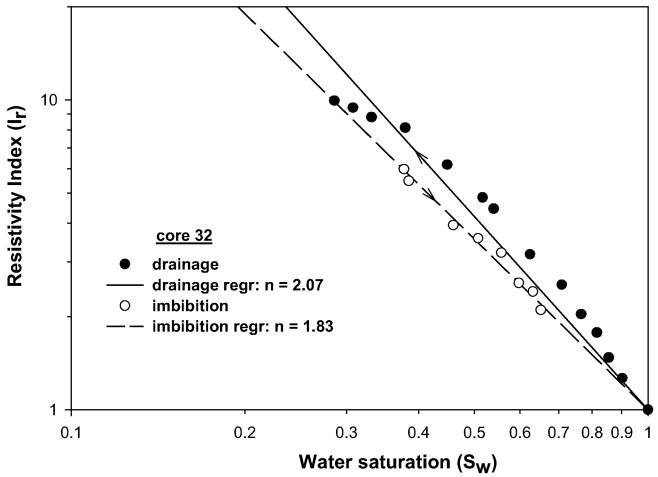

Figure 2.4—Log-log plot of I_r versus S_w (core 32) showing significant resistivity hysteresis.

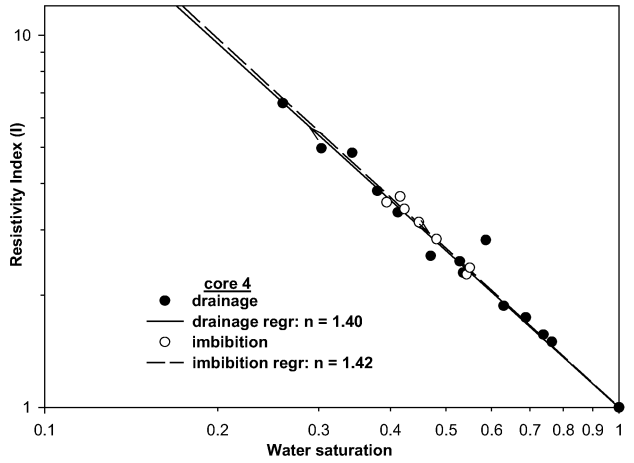

Figure 2.5—Log-log plot of I_r versus S_w (core 4) showing virtually no resistivity hysteresis.

The hysteresis behavior of the samples is discussed in details in the Laboratory Report and in Paper 1. The capillary pressure, relative permeability and resistivity index data are also provided in this report. The degree of hysteresis depends on experimental conditions (e.g., capillary end effects) as well as rock properties (e.g., wettability, pore geometry) and is usually

difficult to quantify. Therefore, there is a need to reconcile the experimental data with a reservoir simulation model that takes into account the capillary end effects by say, history-matching production profiles from the laboratory and simulation, or by pore-scale modeling that takes into account the wettability and pore geometry. These are the topics to be discussed in the next sections.

2.4 Wettability and oil recovery

The crossover saturations, and the end-point relative permeability and saturation values provide good indication about the wettability of core samples [42-43]. From these values, the Ekofisk chalk samples show typical water-wet behavior. The Amott wettability index [44-45] shows that sample 2, 3, 4 and 6 are moderately water-wet, whereas both the Amott and the USBM [46] indices indicate sample 32, 36 and 38 are strongly water-wet. This difference in wettability is reflected in the oil production characteristics. For the strongly water-wet samples, more than 80% of the recoverable oil was produced by spontaneous imbibition while the recovery by spontaneous imbibition from moderately water-wet samples was at most 53%. The negative imbibition curves indicate that the forced imbibition mechanism has less potential of being an important production mechanism for the strongly water-wet samples (see Fig. 2.6). Previous studies on Ekofisk chalk have reported similar production characteristics at various wettabilities [47-49].

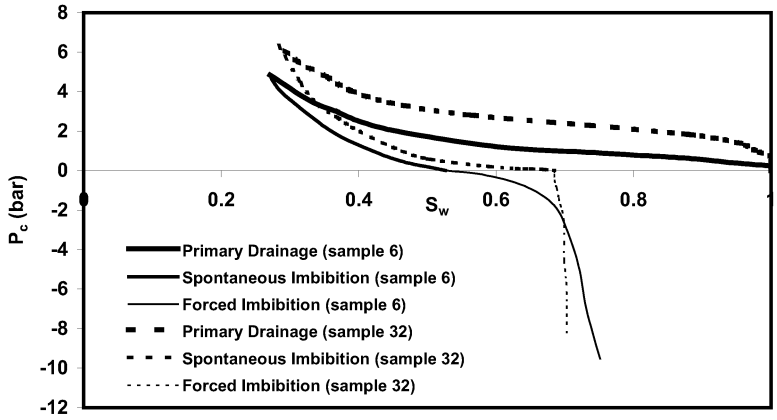

Figure 2.6—Water-oil capillary pressure curves showing that strongly water-wet samples (sample 32) has less recovery potential by forced water imbibition than moderately water-wet samples (sample 6).

2.5 Formation factor

One of the most important parameters regarding the electrical properties of rocks is the formation factor *F*. This parameter shows a relationship between water saturated rock conductivity and bulk water conductivity, and represents the factor by which the resistivity increases due to tortuosity of electric flow path in the rock sample. Archie [50] related *F* with ϕ via the cementation exponent *m* as follows:

$$F = \varphi^{-m} \qquad [2.1]$$

A plot of *F* versus ϕ is shown in Fig. 2.7. A regression analysis of the data gives *m* = 1.7 which is reasonably close to *m* = 1.78 reported for a set of 12 chalk samples from Tor Formation of the North Sea [51].

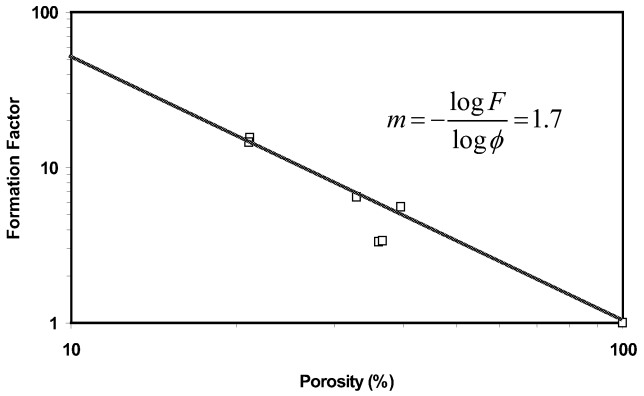

Figure 2.7—Formation factor versus porosity for Ekofisk chalk samples.

2.6 Mercury porosimetry

Mercury porosimetry measurements were conducted on sample 2, 3, 4, 32, 35, 36 and 38 to obtain mercury-air capillary pressure data. Before the measurements, the chalk samples were kept in a hot cabinet for about one day at 60^{o}C. It was then evaluated to a pressure below 10^{-4} mm Hg until a constant weight at room temperature was observed. Mercury intrusion and extrusion data provide information about the sizes of throats and pores, respectively. The cumulative distribution of pore volume by pore throat size is obtained from the intrusion data. Similarly, the retraction data provide an estimate of the cumulative distribution of pore volume by pore size.

An equivalent cylindrical capillary radius is obtained from capillary pressure. The relationship of radius of pore or throat with capillary pressure is expressed by the well-known Young-Laplace equation of capillarity,

$$P_c = \frac{2\,\sigma\,\cos\theta}{r} \qquad [2.2]$$

where r is the throat or pore radius, σ is the mercury surface tension, θ is the contact angle and P_c is the intrusion or retraction capillary pressure. The throat and pore radius distributions are calculated considering a surface tension of 480 mN/m, and a contact angle of 140° for intrusion and 120° for extrusion [52]. As an example, the cumulative mercury intrusion and extrusion volumes and the resulting throat- and pore-radius distributions for sample 3 are shown in Fig. 2.8. There is considerable overlap between the pore and throat sizes. Significant trapping of mercury is also observed. The mean radius of the throat size distribution is 0.27 μm and that for pore size distribution is 0.73 μm.

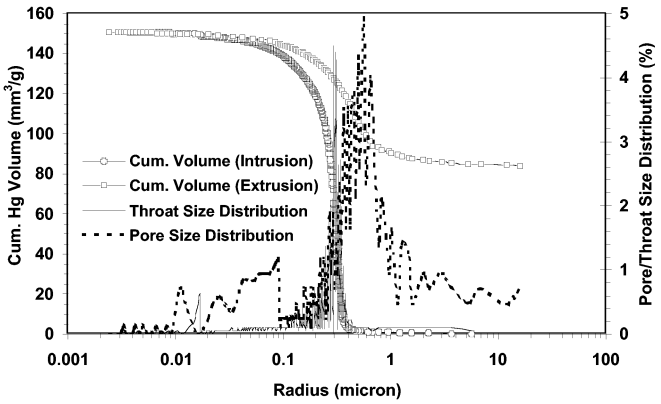

Figure 2.8—Cumulative mercury intrusion and extrusion volumes and the resulting throat- and pore-radius distributions for Ekofisk chalk sample 3.

The Ekofisk chalk samples show significant variability in mercury-air capillary pressure, specific surface area, and pore- and throat-size distributions. The mean throat and pore radii range from 0.191 - 0.544 μm and 0.727 - 4.338 μm, respectively, and the specific surface areas range from 2.99 – 4.72 μm^{-1}. These parameters do not show any particular trend with porosity or permeability. However, in general, the first set of samples has lower mean throat sizes and higher capillary pressures than those of the second set of samples. The data and plots for mercury-air capillary pressure, and pore- and throat-size distributions for all samples are presented in the Laboratory Report.

2.7 Morphological properties

The widely used stochastic reconstruction algorithms, e.g., truncation of Gaussian random fields (GRF), simulated annealing (SA), are constrained by one or more correlation functions (morphological descriptors) readily obtained from 2D backscatter scanning electron microscope (SEM) images. A set of five images was acquired at a pixel resolution of 0.136x0.136 μm^2 from each of sample 2, 3, 4, 32, 35, 36 and 38. This pixel resolution was selected in order to capture the sub-micron size pores that are abundant in chalk. The images were acquired from thin sections of the samples of approximate size 15x15x1 mm^3 impregnated with epoxy resin under vacuum. Thresholding was used to segment each image into objects of interest (void) and background (solid) on the base of gray level. The binarization sets all thresholded pixels (pore) to black and all background pixels (solid) to white. Here, thresholding was based on an analysis of the histogram of the gray values. The histograms for all images were found to be bimodal. A threshold value was selected between the peaks, such that the porosity of the thresholded image was close to the measured porosity of the sample. As an example, a gray image (together with its gray-level histogram) for sample 35 and its binary counterpart are shown in Fig. 2.9. The average porosity of the binary images was 0.381 in very good agreement with the experimental porosity of 0.38 (by helium porosimetry). The porosity was preserved within an error less than 1.2% for all other samples.

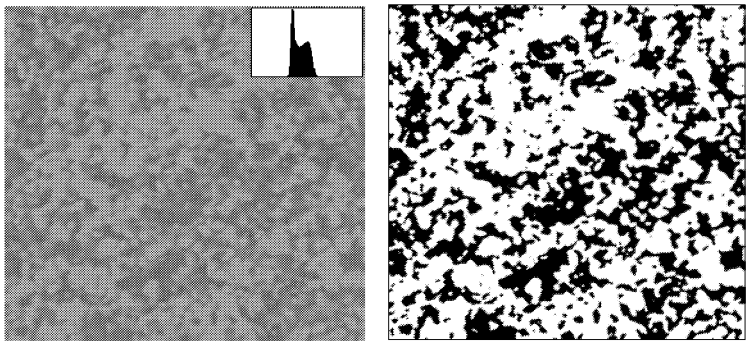

(a) **(b)**

Fig. 2.9—(a) One of the five backscatter scanning electron microscope images (gray scale) captured from Ekofisk chalk sample 35. Image size is 512x512 pixels (70x70 μm^2). Inset is a gray-value histogram of the image. (b) The image is thresholded and binarized segmenting void and solid phases shown in black and white, respectively.

The correlation functions were computed from the binary images. The functions considered were the void-phase two-point probability function (autocorrelation function) and lineal path function, and the void- and solid-phase chord distribution functions. For this purpose, the images were represented by a binary phase function $Z(\vec{r})$ defined below [8],

$$Z\left(\vec{r}\right)=\begin{cases}1 & \vec{r}\ points\ to\ pore\ space\\ 0 & otherwise\end{cases} \qquad [2.3]$$

The porosity φ and the two-point probability function of the void phase $S_2(\vec{u})$ are formally defined as the first two statistical moments of the function $Z(\vec{r})$,

$$\varphi=\left\langle Z(\vec{r})\right\rangle \qquad [2.4]$$

$$S_2(\vec{u})=\left\langle\left[Z(\vec{r})\right]\cdot\left[Z(\vec{r}+\vec{u})\right]\right\rangle \qquad [2.5]$$

where angular brackets denote statistical averages and $\vec{u}$ is a lag vector. For statistically homogeneous and isotropic porous media, φ is a constant and $S_2(\vec{u})$ is only a function of the modulus of the lag vector, *i.e.*, $S_2(\vec{u}) = S_2(u)$. The quantity $S_2(\vec{u})$ can be interpreted as the probability of finding two points at positions $\vec{r}$ and $\vec{r}+\vec{u}$ both in void phase. For all isotropic media without long-range order, $S_2(u=0)=\varphi$ and $\lim_{u\to\infty} S_2(u)=\varphi^2$. The limitation of two-point probability function is that it cannot distinguish between void and solid phases since $S_2^p(u)-\varphi^2 = S_2^g(u)-(1-\varphi)^2$, where *p* and *g* represent void and solid, respectively. This function also does not reflect information about the connectedness of the phases [15]. A normalized form of $S_2(\vec{u})$ is the so-called autocorrelation function $R_z(\vec{u})$ expressed as

$$R_Z(u) = \frac{S_2(u)-\varphi^2}{(\varphi - \varphi^2)} \qquad [2.6]$$

The slope of $S_2(u)$ or $R_z(u)$ at the origin is related to the specific surface area (the interfacial area per unit volume), *s*, which for digitized media is given by [15]

$$s = -2D\left.\frac{dS_2(u)}{du}\right|_{u=0} = -2D(\varphi-\varphi^2)\left.\frac{dR_z}{du}\right|_{u=0} \qquad [2.7]$$

where *D* is the dimensionality of the space.

The void-phase lineal path function $L(\vec{u})$ is another useful characteristic of microstructure. This quantity measures the probability that a line segment spanning from $\vec{r}$ to $\vec{r}+\vec{u}$ lies entirely within void phase. Unlike the two-point probability function, a lineal path function can distinguish between

different phases of a medium, in the sense that the lineal path function for a particular phase is not uniquely determined by simply knowing that of the complementary phase(s). Therefore, for efficient reconstructions using lineal path functions, it is important to identify which phase in the porous medium is the target phase to be reconstructed. Also unlike two-point probability function, this function contains some connectedness information, at least along a lineal path, and hence reflects certain long-range information about the system. For statistically isotropic media, the lineal-path function depends only on the distance u between the two end-points and can be expressed simply as $L(u)$. For a porous medium with porosity φ, $L(u)$ at $u = 0$ is equal to φ [15].

We adopted the procedure by Yeong and Torquato [15] to calculate $S_2(u)$ and $L(u)$. In this procedure, a sampling probe of u pixels in length is successively translated along a row of pixels, a distance of one pixel at a time, until the whole image is spanned. $S_2(u)$ and $L(u)$ are then computed from the number of occurrences that the two end-points of the probe fall in void spaces or the probe entirely fall in void spaces, respectively, and finally, dividing the number of occurrences by the total number of trials.

Two other important morphological descriptors are the chord distribution functions $C_i(u)$ where the subscript i refers to either void or solid [52]. A chord is the length u between intersections of a line with the two-phase interface. These quantities can be directly interpreted in terms of microstructural features, as it contains phase connectedness and correlation information along a lineal path. That is, if $C_i(u) \neq 0$ for large values of u, there exist connected regions of phase i at scale u. Importantly, the value of u at which $C_i(u)$ is maximum provides an estimate of the length scale associated with phase i [53].

The correlation functions [$S_2(u)$, $L(u)$, $C_v(u)$ and $C_s(u)$] were calculated along the two principal directions for each of the five images of a

sample. The average functions for sample 35 are shown in Fig. 2.10. The data and plots for all other samples are presented in the Laboratory Report. As can be observed in Fig. 2.10, $S_2(u)$ gets its long-range value of $\varphi^2 = 0.145$ at a lag of 6 μm (44 pixels). This function [$R_z(u)$ instead, shown in the Laboratory Report] corresponds well with that reported for similar North Sea chalks [1]. $L(u)$ is negligible after a lag of approximately 10 μm (74 pixels). The shape of the curve is consistent with that for sandstone samples [16]. The peaks of $C_v(u)$ and $C_s(u)$ indicate the most abundant pore and particle sizes, respectively. Similarly, the maximum lags at which they vanish represent the maximum pore and particle sizes. The most abundant pore and particle sizes in sample 35 are 0.68 and 1.09 μm while their maximum sizes are approximately 10 and 15 μm, respectively. Unfortunately no published data are available for chalk to confirm the consistency of $L(u)$, $C_v(u)$ and $C_s(u)$.

The specific surface area s of sample 35 calculated from Eq. 2.7 was 1.24 μm^{-1} (see the Laboratory Report for all other samples). This value differs significantly from the value obtained by mercury intrusion porosimetry (MIP), which was 3.14 μm^{-1}. This discrepancy is expected, considering the limited resolution (0.136 μm/pixel) of the image data. The magnitude of specific surface area is dependent on the size of the "probe" used to measure it. Since MIP detects pore volume invaded at capillary pressures corresponding to equivalent cylindrical pore radii smaller than 0.136 μm, it is expected that MIP will yield a higher specific surface area.

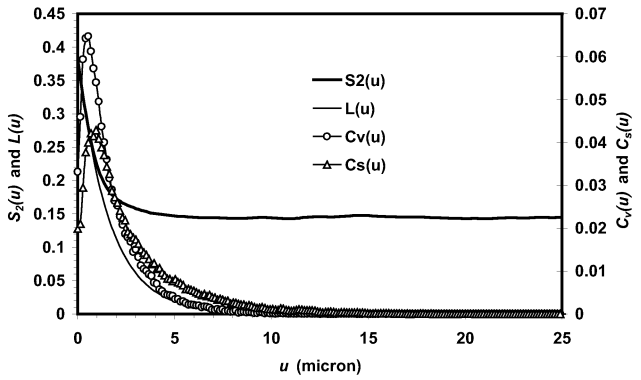

Fig. 2.10—Average $S_2(u)$, $L(u)$, $C_v(u)$ and $C_s(u)$ for Ekofisk chalk sample 35.

3. Simulation of core flood experiments

Reservoir simulation studies are routinely carried out to design a first development plan, to support ongoing reservoir management, to assess the potential and progress of any improved recovery scheme or to enable the screening of options reviving mature fields. To perform such a simulation, the relative permeability and capillary pressure functions are to be specified at all locations throughout the reservoir. Consequently, accurate determination of these functions is an issue of great concern to the oil industry. As there is typically insufficient information to determine reliable estimates of these functions from data gathered from field tests or production history, they are generally determined through laboratory core-flood experiments, which are thought to mimic what could happen during formation and subsequent recovery processes of a hydrocarbon reservoir. Unfortunately, laboratory experiments have pitfalls/artefacts, for example, the interference of capillary pressure on the measurement of relative permeability, the so-called capillary end effect, is a long-standing issue. Therefore, quality control of the experimental data is a matter of great practical significance. Further, direct measurement of three-phase relative permeability and capillary pressure is

extremely difficult and expensive and even impractical to measure for the full range of possible saturation paths that may occur in three-phase flow. Three-phase behavior is therefore almost always estimated from two-phase data on the basis of empirical models, such as, that by Stone [54]. Numerical simulations of the experiments have proved to be an excellent tool to interpret the experimental data and to produce reliable and fit-for-purpose results [21-24]. In this technique, the core flood experiments are simulated consecutively by changing input relative permeability and capillary pressure data until a reasonable match is obtained between the experimental production profiles (and/or other profiles, e.g., saturation) and the simulated ones. Usually, the input data are generated using empirical correlations honoring the key parameters, such as, the end-point values. We adopted this technique to improve the quality of two-phase (oil-water) relative permeability curves (Paper 2) and to interpret hysteresis (Paper 1) of the Ekofisk chalk samples. The oil and water production profiles were used as the history matching parameters. The procedures have been discussed thoroughly in Paper 2 and elsewhere [23-24]. Only a brief description will be given here.

3.1 Simulation model

For simulation of core flood experiments, a one-dimensional black-oil simulation model was developed through dividing the core sample into 100 equal grid blocks. The circular cross-section of the cylindrical core was converted into equivalent square cross-section. The inlet and outlet blocks were further refined to account for the capillary end-effects [22] (see Fig. 3.1). The inlet and outlet pipes of the core holder were simulated as the injection and production wells, respectively. The pipes were connected to the core sample via two dummy blocks added at the two ends. The length of the dummy block was equal to the adjacent refined core block. The dummy blocks can be considered as fluid banks having porosity 1.0, zero capillary pressure

and very high permeability. Therefore, they are treated as separate region in the simulation model.

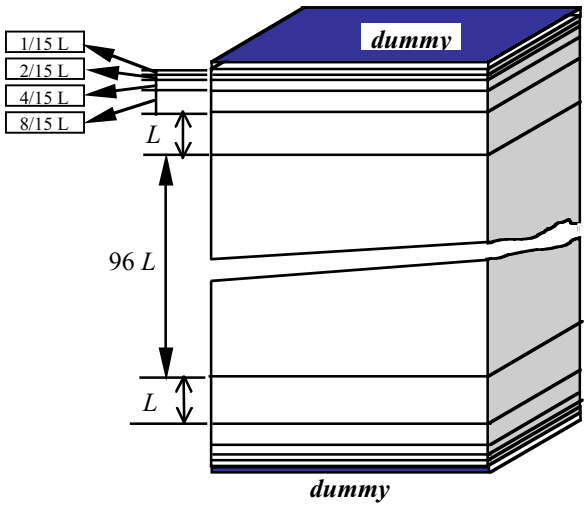

Figure 3.1—Core flood simulation model.

3.2 Model equations

In excess of core dimensions and equilibration data, relative permeability and capillary pressure functions are important input parameters for reservoir simulation. The initial functions of relative permeability were generated using the modified Corey exponent representation incorporating oil and water end-point relative permeability values [22, 24]:

$$k_{rwo}(S_w) = k_{rwe}\left[\frac{S_w - S_{wi}}{1 - S_{wi} - S_{orw}}\right]^{N_w} \quad [3.1]$$

$$k_{row}(S_o) = k_{rowe}\left[\frac{S_o - S_{orw}}{1 - S_{wi} - S_{orw}}\right]^{N_{ow}} \quad [3.2]$$

where, $N_w = \frac{2+3\lambda}{\lambda}$ and $N_{ow} = \frac{2+\lambda}{\lambda}$ for water-wet cases. While end-point relative permeability values define the extent of the relative permeability curves, N_w and N_{ow} define their curvatures. The end-point values obtained from the laboratory experiments were used in the expressions while the exponents were calculated using pore size distribution index λ. λ characterizes the range of the pore sizes in a rock. The larger the value of λ the more uniform is the pore size distribution. For natural sandstones and some limestones, λ lie between 0.5 and 4. λ can be obtained from drainage capillary pressure curves or from a Leverett J-function curve. Brooks and Corey [55] proposed the following relationship for determining λ based on experimental capillary pressure and saturation data:

$$\left(\frac{P_c}{P_{cew}}\right)^{-\lambda} = S_w^* \qquad [3.3]$$

where, S_w^* is the effective water saturation defined by,

$$S_w^* = \left(\frac{S_w - S_{wi}}{1 - S_{wi}}\right) \qquad [3.4]$$

Equation 3.4 shows that the reciprocal of the slope of a straight line on a log-log plot of P_c versus S_w^* defines λ.

As shown in Fig. 2.6, the oil-water capillary pressure curves for the Ekofisk chalk samples have three separate parts. Primary drainage and forced imbibition parts were obtained from centrifuge measurements. In the centrifuge, many measurement points are possible by stepping up the speed at small increments and hence smooth curves. Spontaneous imbibition is obtained in one step by decreasing the capillary pressure from the maximum

positive value to zero immediately after primary drainage. The spontaneous imbibition curve was modelled from initial water saturation (S_{wi}) and water saturation after spontaneous imbibition (S_{wsp}) using Eq. 3.5 [56].

$$P_{cowi}(S_w) = P_{cew}\left[\frac{S_w - S_{wi}}{S_{wsp} - S_{wi}}\right]^{-\frac{1}{\lambda}} - P_{cew} \qquad [3.5]$$

3.3 Simulation results

History matching of the oil and water production profiles was successful for drainage and imbibition processes within error bars of ±4% for oil and ±6% for water at all measurement points (see Fig. 3.2 for an example).

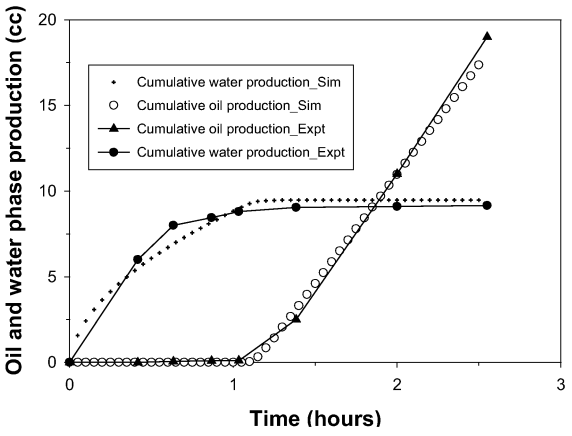

Figure 3.2—Experimental and simulated production profiles for Ekofisk chalk sample 38 (imbibition process).

The pore size distribution index at history match corresponds well with the experimental value. It suggests that Brooks and Corey relationship [55] is well suited for this type of chalk samples at least for oil-water system. The history-matched relative permeability curves also compare very favourable with the experimental curves at measurement points. As an example, Fig. 3.3 shows the

experimental and simulated relative permeability curves for sample 38. The simulated curves demonstrate how successful this simulation approach is to obtain smooth relatively permeability curves consisting of points before breakthrough. Another advantage of this approach is that in case of water-wet samples, where there is little or no oil production after breakthrough during the imbibition process, useful data can be obtained. While the experimental curves consist of only few points, the simulated curves may consist of as many data points as needed. This procedure is also useful in analyzing hysteresis effects. This is because few experimental data points are not adequate to show complete trend of the drainage and imbibition relative permeability curves (see Paper 1 for further details). In this work, only production profiles have been used as history matching parameters. This prediction technique may be made even more accurate by using more history matching parameters, such as, saturation profile along the length of the core [22-24].

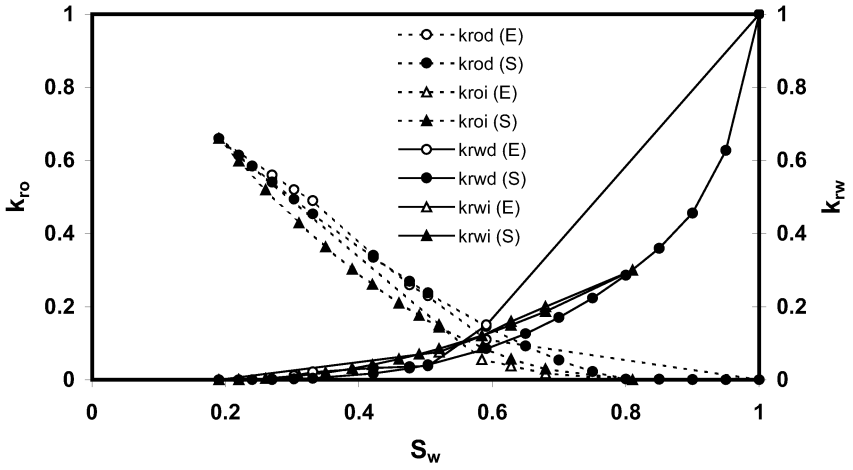

Figure 3.3—Experimental and simulated relative permeability curves for Ekofisk chalk sample 38 (E for experiment and S for simulation).

4. Stochastic reconstruction of porous samples

Pore-scale network modeling techniques have been used in the recent years as a tool to predict a variety of petrophysical and reservoir engineering properties from pore structure information. The important properties include absolute permeability and formation factor [1, 3-5, 57], relative permeability [3-6, 58-69], capillary pressure [3-5, 58-61, 64, 66-67, 69], resistivity index [70-71], and wettability characteristics [60-61, 63-65, 71-75]. By comparison to methods based on direct solution of the relevant transport equations in complex 3D pore geometries (e.g., Stokes' equation for single phase flow), network models provide a computationally efficient way to predict these properties. The requisite information (pore and throat shape and size distributions, pore-to-pore connectivity and spatial correlation) is, however, quite difficult to determine. A description of the pore space of the medium under consideration in the form of 3D volume data is required for both direct computation of transport properties and for extracting key geometric and topological parameters needed by network models. X-ray computed microtomography [76-79] and scanning laser confocal microscopy [80] can provide good quality volume images of the pore space. Unfortunately, these techniques are not suited for routine application. Most importantly, its resolution is not sufficient to image the sub-micron size pores that are abundant in chalk. In the absence of experimental 3D volume data, 3D stochastic reconstruction from limited statistical information obtainable from 2D microscopic images is a viable alternative. For the case of chalk, whose microstructure is too complex to reproduce by explicit modeling of the grain depositional and diagenetic processes [3], stochastic reconstruction is also the only alternative.

The conditioning and truncation of Gaussian random fields (GRF) is a widely used stochastic reconstruction technique [1, 7-13]. The approach is mathematically elegant and computationally efficient, but unfortunately

limited to imposing the porosity and pore-pore autocorrelation function of the reference (real) medium as the only reconstruction constraints. Much greater flexibility is offered by the simulated annealing (SA) method. SA is a global optimization technique, which can be constrained by an arbitrary number of morphological constraints [14-20]. Despite its flexibility, the SA method is limited by slow convergence. This makes the reconstruction of reasonably large samples (e.g., 256^3 voxels) impractical at the present time. It is therefore, very important to find a way to accelerate the rate of convergence of SA method while reconstructing large samples with more than one constraints. A *hybrid GRF/SA* technique in which the SA reconstruction is initialized with input generated using the GRF method has been introduced in this study to accelerate the rate of convergence in the SA process. Extensive studies have been conducted on reconstruction of porous samples using the SA technique and applying various combinations of the morphological descriptors. The morphological descriptors considered in this study are the void-phase autocorrelation and lineal path functions, and solid-phase chord distribution function. The quality of reconstructions has been evaluated qualitatively and quantitatively in terms of morphological parameters. The procedures and results have been discussed in details in Papers 3-6.

North Sea chalk samples contain significant amount of vuggy porosity in the form of hollow foraminifer shells. The vuggy porosity has been found to affect fluid and electric transport properties [9, 81]. An attempt was made by Bekri *et al.* [1] to reconstruct chalk samples containing significant amount of hollow shells using a GRF method. The reconstruction technique was not successful to reproduce them. A technique based on *conditional simulated annealing* (CSA) has been introduced in this study to reconstruct foraminifer shells of any size and shape. This issue has been addressed in Paper 7. A brief review of the algorithms and results will be given in this section.

4.1 Reconstruction algorithms

For a stochastic reconstruction using the GRF method, only φ and $R_z(u)$ are used while in the SA method, any combination of $R_z(u)$, $L(u)$ and $C_i(u)$ or other constraints can be used. The basic idea behind the GRF method is to generate values of the phase function $Z(\vec{r})$ on a cubic grid of fixed size (e.g., 256^3 voxels) in a manner that satisfies the target φ and $R_z(u)$. The reconstruction starts from a realization of a continuous 3D uncorrelated Gaussian field. This uncorrelated field is subsequently passed through a linear filter that introduces spatial correlation. The linear filter is constructed from the target φ and $R_z(u)$ so that the requisite binary field $Z(\vec{r})$ is obtained by a final thresholding operation.

The main idea behind the SA technique is to gradually transform an unstructured ("high-energy") configuration of solid and void voxels (pixels in 2D) into a "minimum-energy" configuration, where "energy" is measured in terms of deviations from a set of target, experimentally determined, functions conveying morphological information, *e.g.*, $R_z(u)$. This is a stochastic optimization problem with an objective function generally defined in terms of *n* reference functions as:

$$E = \sum_n \sum_{u=0}^{u_n^{max}} \left[f_n(u) - \widetilde{f}_n(u) \right]^2 \qquad [4.1]$$

where, f_n and $\widetilde{f}_n$ are the simulated and reference functions, respectively. Each reference function $\widetilde{f}_n$ is matched to a maximum lag u_n^{max}. The simulation begins by randomly designating fractions ϕ and (1-ϕ) of void and solid phase voxels, respectively, on a grid of size $L \times M \times N$ voxels ($L \times M$ pixels in 2D). At each iteration step *k*, a void and a solid voxel are chosen at

random and their phase function values are interchanged. This interchange slightly modifies the functions f_n and therefore changes the energy of the system while preserving the porosity. A voxel interchange is accepted with a probability p_a given by the Metropolis rule [82],

$$p_a^{(k)} = \begin{cases} 1 & if\ \Delta E^{(k)} \le 0 \\ e^{-\Delta E^{(k)}/T^{(k)}} & if\ \Delta E^{(k)} > 0 \end{cases} \qquad [4.2]$$

where $\Delta E^{(k)} = E^{(k+1)} - E^{(k)}$ and $T^{(k)}$ is a control parameter representing the "*temperature*" of the system. The starting value and the rate of reduction of *T* are governed by an *annealing schedule*. This schedule should be such that a global optimum is achieved as quickly as possible without getting trapped at any local minima (see Papers 3-7 for further details).

For reconstruction of vuggy porosity (in the form of hollow foraminifer shells) using a conditional simulated annealing, a slight modification of the binary phase function $Z(\vec{r})$ has been proposed:

$$Z(\vec{r}) = \begin{cases} 1 & \vec{r}\ points\ to\ pore\ space\ not\ belonging\ to\ foraminifer\ shells \\ 0 & \vec{r}\ points\ to\ solid\ space\ not\ belonging\ to\ foraminifer\ shells \\ 2 & \vec{r}\ points\ to\ solid\ space\ belonging\ to\ foraminifer\ shells \\ 3 & \vec{r}\ points\ to\ pore\ space\ belonging\ to\ foraminifer\ shells \end{cases} \qquad [4.3]$$

In the proposed conditional simulated annealing method, the simulation begins by placing required number of foraminifer shells of size, shape and porosity similar to that observed in the microscopic images at random or specified locations. The solid and void voxels belonging to the foraminifer shells are designated with phase function values 2 and 3, respectively (cf. Eq. [4.3]). The porosity of the sample is then adjusted by designating fraction φ_{nv}

($\varphi_{nv} = \varphi - \varphi_v$, where, φ_v and φ_{nv} are the vuggy and non-vuggy porosities, respectively) from the remaining voxels to a phase function value 1. The rest of the voxels are designated with a phase function value 0. During subsequent iteration steps, a void and a solid voxel not belonging to the foraminifer shells (i.e., phase function values 1 and 0, respectively) are chosen at random and their phase function values are interchanged leaving the foraminifer shells unchanged. However, the voxels belonging to the foraminifer shells are considered during computation of the correlation functions in order to maintain consistency in the global correlation statistics.

4.2 Reconstruction results

The potential of *hybrid GRF/SA* reconstruction was tested on a sample (ϕ = 0.3) containing 100^3 voxels. Three cases were studied: In Case 1, the SA method was used with an initial configuration that corresponds to a cube of size 100^3 voxels extracted from a GRF-generated realization of size 256^3 voxels. In this case annealing was started at high initial temperature allowing the system to "melt". Case 2 differs from Case 1 in that annealing was started at low initial temperature preventing "melting" of the system. In Case 3, the conventional SA method was applied, with the annealing process starting at high initial temperature from a random, uncorrelated configuration.

As a result of further reduction of energy in the system by SA method, improved match of the autocorrelation functions in all directions was observed for Cases 1 and 2 by comparison to the initial, GRF-generated configuration. Visual observations revealed that the quality of the reconstructed images was also better in terms of the shape of the rock-pore interface and the number of isolated void and solid clusters. From the point of view of computational efficiency, initialization of SA with a GRF-generated, instead of an uncorrelated random configuration was encouraging. The simulations performed on an IBM RS6000 SP Model 9076-260 computer showed that the

conventional SA reconstruction required 5.89 CPU hours (22.7 million iterations), but only 3.88 hours (15.7 million iterations) when the annealing process was started from GRF reconstruction at low initial temperature. For a larger model (e.g., 256^3 voxels), the savings in CPU time would be considerably more significant. However, there was no gain when the annealing process was started at high initial temperature allowing the system to melt first and then cool again.

The technique was applied further to reconstruct a sample of size 256^3 voxels. The starting energy (after GRF reconstruction) calculated from Eq. 4.1 was 0.0283. This energy was reduced by an order of magnitude (0.0026) in about 9 hours on an IBM RS6000 SP Model 9076-260 computer. The annealing was started at low initial temperature, therefore, the energy decreased gradually and no "melting" took place. An improved match of the autocorrelation function and a "smoother" image was observed for this modest reduction of energy. Interestingly an improved match of the other correlation functions not imposed as constraints was also observed. Fig. 4.1 shows the match between target and simulated $R_z(u)$ and $C_s(u)$ in x-direction where only $R_z(u)$ was optimized along the three orthogonal directions. Similar or better match was obtained in other directions and hence are not shown (see Paper 3 for further details).

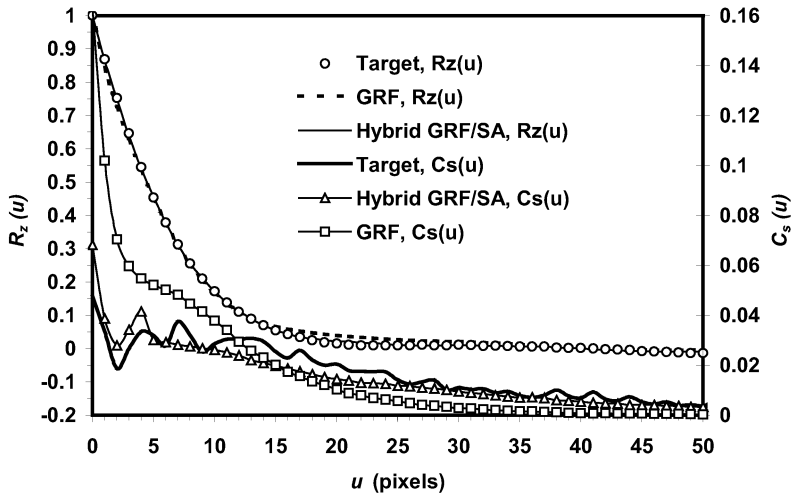

Figure 4.1—Target and simulated *Rz(u)* and *Cs(u)* in *x*-direction showing that the Hybrid GRF/SA technique produced better match in both optimized and unoptimized correlation functions. *Rz(u)* was optimized. Similar or better match was obtained in other directions and hence are not shown.

There are evidences that use of void-phase autocorrelation function is not always sufficient to provide faithful replica of the microstructure under study. As pointed out previously Bekri *et al.* [1] was not successful in reconstructing North Sea chalk samples containing significant amout of vuggy porosity in the form of hollow foraminifer shells. Levitz [10] observed that this constraint was insufficient to reproduce the granular appearance of a pack of clay-coated silica particles. He further showed that although the reconstructed image matched the void-phase autocorrelation function and chord distribution function, it did not match the solid-phase chord distribution of the reference microstructure. This was also the case for Kainourgiakis *et al.* [12] who attempted to reconstruct the microstructure of a random pack of spherical particles. The later two works motivated us to examine the hypothesis that the solid-phase chord distribution function contains sufficient additional information to reconstruct the microstructure of particulate porous media by stochastic optimization methods. Using SA technique, we demonstrated that this function indeed contains additional information that is critical for the reconstruction of the morphology of lightly consolidated pack of glass spheres

and the microstructure of the pack of clay-coated silica particles exhibiting short-range order. The work has been published in Paper 4. The main results are discussed briefly below.

The use of solid-phase chord distribution function together with void-phase autocorrelation function (Case 1) rendered better appearance of a sphere pack over what was achieved by either solid-phase chord distribution function (Case 2) or void-phase autocorrelation function alone (Case 3). The reconstructed samples from the three cases are compared with one of the sixty-five target images in Fig. 4.2. The differences are quite visible. In general, the morphology of the sphere aggregate is evident in Case 1 and 2. However, a distinct difference can also be observed, namely Case 2 reconstruction produces somewhat smaller particle features than the target microstructure. Contrary to this, Case 1 produces relatively larger particle features, which is more consistent with the target microstructure. Both reconstruction cases essentially reproduce the distinct appearance of a sphere pack. The roundness of the solid-void interface is clearly visible, as are the shapes of pore space features seen in the real medium. It is noted that the extreme regularity of the solid-void interface in the real aggregate of spheres is not perfectly reproduced. This is in part due to the fact that the reference functions were optimized only along the two orthogonal directions. While this is a standard approach aimed at reducing computational costs, some artificial anisotropy along the non-optimized directions is introduced for the case of media exhibiting short-range order. This anisotropy can be removed by optimizing in more directions [83]. The result is quite different in Case 3 where the solid phase in the reconstructed medium appears completely amorphous. In addition, numerous small void-phase features appear in the reconstructed image. This indicates that the void-phase autocorrelation function is inadequate to reproduce the morphology of the sphere aggregate.

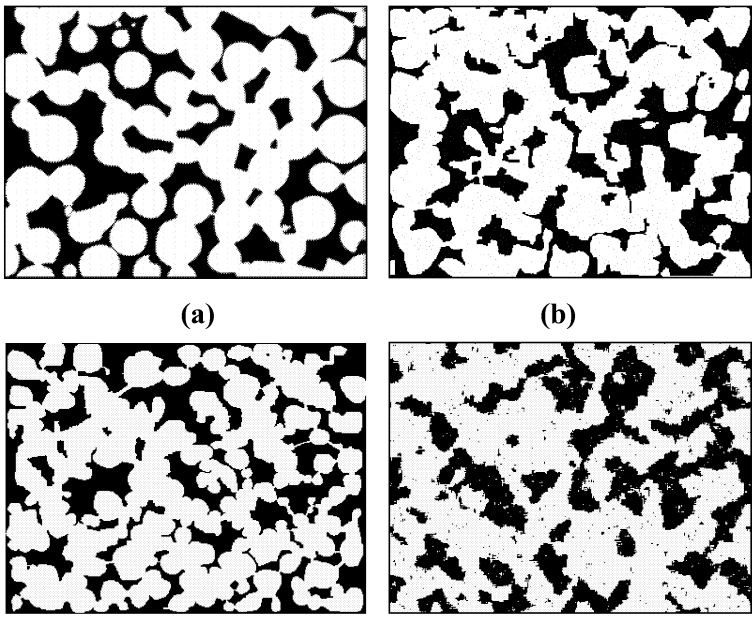

Figure 4.2—Target and reconstructed pack of glass spheres: (a) A representative image of real aggregate of glass spheres. Image size is 768x576 pixels. Pixel size is 2.1x2.1 μm^2. (b) Reconstruction from the void-phase autocorrelation function and the solid-phase chord distribution function (Case 1). (c) Reconstruction from the solid-phase chord distribution function only (Case 2). (d) Reconstruction from the void-phase autocorrelation function only (Case 3). Pore space is shown in black.

As shown in Fig. 4.3, for Case 1 the void-phase autocorrelation functions and the solid-phase chord distribution functions (along the orthogonal directions) of the reconstructed medium match the respective reference functions remarkably well. For Case 2 excellent agreement of the solid-phase chord distribution functions is observed, but deviation from the reference void-phase autocorrelation functions is also evident, mainly at large lags. This can be understood by considering that significant correlation information is, in fact, contained in the chord distribution function. For Case 3 the simulated autocorrelation functions match perfectly the reference functions, but considerable disagreement is observed between the simulated and reference chord distribution functions.

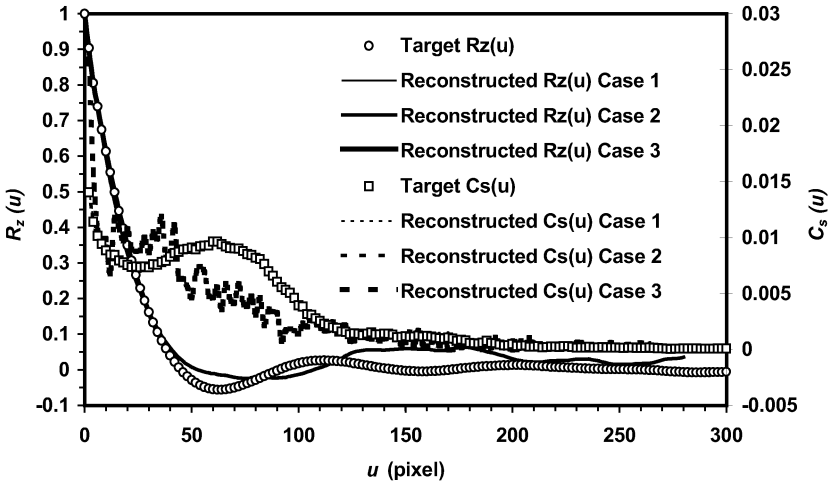

Figure 4.3—Void-phase autocorrelation function and solid-phase chord distribution function of the target (reference) images and the reconstructed samples shown in Fig. 4.2. Functions along *x*-direction are shown. Agreement along the *y*-direction is similar and hence is not shown.

The necessity of the solid-phase chord distribution function for the stochastic reconstruction of particulate media was further verified by reconstructing the microstructure of a pack of irregular silica particles, peviously considered by Levitz [10]. This microstructure would be extremely difficult, if not impossible, to simulate using any of the currently known particle deposition algorithms. Two cases were considered. In the first case the void-phase autocorrelation function and the solid-phase chord distribution function were optimized while in the second case the chord distribution functions of the solid and void phases were used. A significant improvement in the visual appearance of the reconstructed microstructure was easily recognizable when compared with the one reconstructed by Leviz using the void-phase autocorrelation function only. Reconstruction using exclusively chord length information (second case) produced a microstructure remarkably similar to the first case. This finding supports the conclusion that imposing the pore-phase chord distribution function (or its surrogate lineal path function) as an additional constraint is largely redundant if the void-phase autocorrelation

function is also imposed as a constraint. For further details of the results, see Paper 4.

Results from reconstruction of chalk samples (ϕ = 0.3) with interparticle porosity only (with no appreciable amount of vuggy porosity) using different combinations of the correlation functions ($R_z(u)$ and $C_v(u)$ in orthogonal directions, and $C_s(v)$ in orthogonal and diagonal directions) seem to suggest that the use of void-phase autocorrelation function alone is sufficient to produce a reasonable replica of the microstructure. Quantitative analysis (s, $\bar{\lambda}$, average cluster size, fraction of isolated pore clusters, local porosity and percolation probability distributions, etc.) of 2D reconstructions using different morphological constraints revealed that imposing chord distribution functions results only in minor improvement over what is achieved by using the void-phase autocorrelation function as the only constraint. This is in sharp contrast with what was observed for particulate media exhibiting short-range order. This result was further verified by geometric and topological characterization of a 3D replica of the sample generated using only autocorrelation function constraints. Pore and throat size distributions determined by 3D pore space characterization matched reasonably with mercury porosimetry results. The predicted permeability and formation factor were shown to be in very good agreement with experimentally determined values. The results have been published in Paper 5.

In a separate study, also involving reconstruction of chalk samples (ϕ = 0.38) containing no appreciable amount of vuggy porosity, we demonstrated that simulated annealing technique may be used to reconstruct chalk microstructure with reasonable accuracy using the void-phase two-point probability function (a surrogate of the autocorrelation function) and/or the void-phase lineal path function (a surrogate of the chord distribution function). The void-phase two-point probability function produced slightly better reconstruction than the void-phase lineal path function. Imposing void-phase lineal path function resulted in slight improvement (specially in local

percolation probabilities), over what was achieved by using the void-phase two-point probability function as the only constraint. The use of periodic boundary conditions, which is applied to approximate a finite volume of the simulation model as an infinite volume of the periodic medium, was studied for two different sample sizes and was found not critically important when reasonably large samples are reconstructed. For further details of the results, see Paper 6.

The sharp contrast in the behavior of chalk and particulate media with respect to the solid-phase chord distribution function may be explained as follows: (1) the solid-phase chord distribution function of the particulate media has a wide distribution bearing unique signature of the microstructure. On contrary, chalk samples display much narrower distribution (see Fig. 4.4). Even in chalk, the void-phase chord distribution function is very similar to the solid-phase chord distribution function. Therefore, this function bears no unique signature of the microstructure and hence poses virtually no impact on the reconstruction; and (2) particulate media display appreciable short-range order in the void-phase autocorrelation function which is not the case for chalk (see Fig. 4.4). It has been observed that sampling this function along only orthogonal directions for samples displaying appreciable short-range order may induce significant artificial anisotropy along the non-optimized directions [84]. For the opposite reason, sampling void-phase autocorrelation function along only orthogonal directions may be sufficient for chalk.

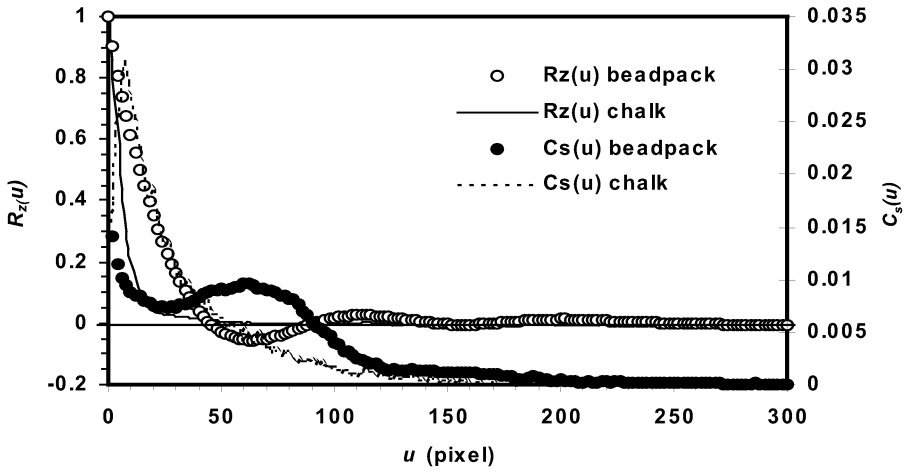

Figure 4.4—$R_z(u)$ and $C_s(u)$ of the pack of glass spheres and Ekofisk chalk showing that the pack of glass spheres displays appreciable short-range order in $R_z(u)$ and a wide distribution in $C_s(u)$.

North Sea chalk samples contain significant amount of vuggy porosity associated with large cavities found in foraminifer shell fragments or other dissolution features. Lucia [81] suggested that the chalk permeability is controlled by the amount of interparticle pore space, presence of separate vugs (vugs are interconnected through the interparticle pore network) contribute little, if any, to the permeability. However, the presence of touching vugs (vugs are interconnected by direct contact with each other) may contribute to the permeability significantly and the capillary pressure may be significantly different. Ioannidis *et al.* [9] observed a quite variable resistivity and formation factor values depending on the fraction of vuggy porosity present in the sample. These results suggest that the vuggy porosity has an effect on fluid and electric transport properties. Considering the economic significance of chalk reservoirs and the variability of their transport properties depending on the amount of vuggy porosity, it is worthwhile to investigate whether chalk reconstruction including reliable representation of vuggy porosity is possible. A technique based on *conditional simulated annealing* (CSA) has been introduced for this purpose. The technique and the 2D and 3D reconstruction results have been presented in Paper 7. A 2D example is given below.

The 2D example is the sample *p13* from Ekofisk field previously considered by Bekri *et al*. [1], a BSE image of which is shown in Fig. 4.5(a). Total and vuggy porosities (in the form of hollow foraminifer shells) for the sample are 0.39 and 0.09, respectively. It must be mentioned here that the GRF method was not successful to reproduce the microstructure of this sample, resulting in computed values of permeability that were very different from the experimental one [1]. Also, reproduction of the hollow shells was not possible with any combination of the correlation functions using the conventional simulated annealing method. An example is shown in Fig. 4.5(b) where $R_z(u)$ in two orthogonal directions, and $C_v(u)$ and $C_s(v)$ in two orthogonal and diagonal directions were used. The reconstructed sample using the CSA technique is shown in Fig. 4.5(c). It is readily observed that the complex morphology of this sample is well reproduced while maintaining the global correlation statistics (shown in Paper 7).

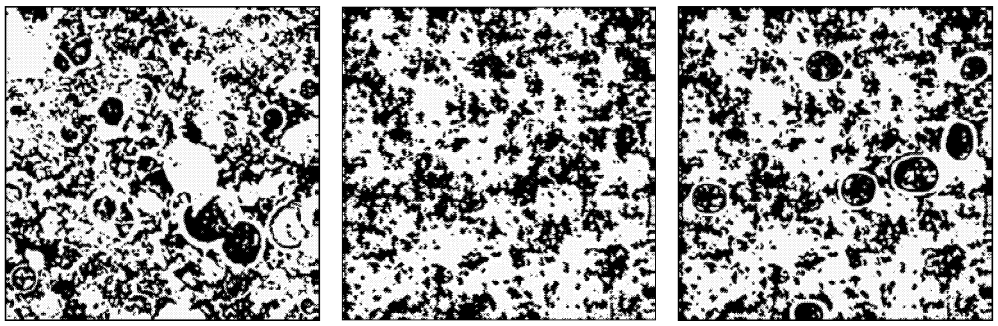

(a) **(b)** **(c)**

Fig. 4.5—2D reconstruction of sample *p13* [1]; (a) one of the five target images (400x400 pixels), (b) reconstructed sample (400x400 pixels) using conventional simulated annealing, (c) reconstructed sample (400x400 pixels) using conditional simulated annealing. Pore space is shown in black.

5. Pore space characterization and network modeling

For simulation of fluid and electric transport through pore networks, the reconstructed pore spaces are characterized to obtain geometric and topological information. The information are used directly or converted into equivalent network model for flow simulation. The characterization technique and network modeling are described briefly in this section.

5.1 Pore space characterization

Two reconstructed 3D samples of size 256^3 voxels using the GRF and hybrid GRF/SA techniques, respectively (described in Section 4.2) were characterized using the pore space partitioning algorithms developed by Liang *et al.* [85]. The method is based on partitioning of pore space into nodal pores by identifying local minima in the cross-sectional area of the pore space channels using a skeleton link scanning procedure. The methodology takes advantage of a 3D, connectivity preserving, fully parallel thinning algorithm developed by Ma and Sonka [86]. The thinning algorithm is used to extract the skeleton (medial axis) of the pore space. The skeleton serves as the basis for characterization of the reconstructed media. The characterization provides the distributions of pore volume V_p, throat area A_t, throat hydraulic radius R_H and coordination number, as well as the distributions of hydraulic and electrical conductance of distinct pore space channels. The thinning and characterization algorithms are well documented in the above references and will not be detailed here. The reconstructed sample (GRF) and an example skeleton (not from this sample) are shown in Fig. 5.1.

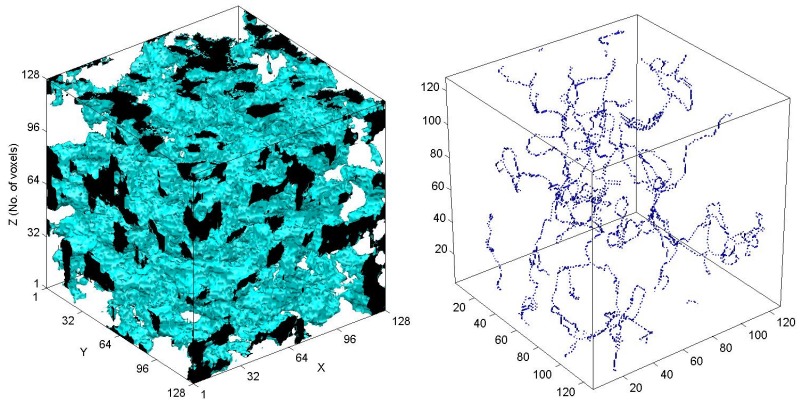

(a) **(b)**

Fig. 5.1—(a) Microstructure of a 3D chalk sample reconstructed using the hybrid GRF/SA technique. A subvolume of 128^3 voxels is shown. The pore space is shown opaque with ends in black. The solid is transparent. (b) An example skeleton of the pore space.

Assuming that the pores are cubic and that the throats have a square cross-section, the pore volume and throat area distributions were converted to equivalent pore and throat sizes using the following relationships,

$$R_p = \left(\frac{V_p}{8} \right)^{1/3} \qquad [5.1]$$

$$R_t = \left(\frac{A_t}{4} \right)^{1/2} \qquad [5.2]$$

The pore- and throat-size distributions of the two reconstructed samples obtained from 3D characterization are compared with the respective distributions from mercury porosimetry in Fig. 5.2. The range of pore and throat sizes found in the reconstructed chalk samples agrees well with the range of pore and throat sizes estimated from mercury porosimetry. However, the overall match is poor. Also, the mean throat and pore radii of the reconstructed samples (0.18 and 0.31 μm, respectively) differ considerably with those estimated from mercury porosimetry (0.27 and 0.73 μm,

respectively). Some differences are expected because mercury porosimetry in reality does not provide accurate pore or throat size distributions, rather provides mercury volume distributions as a function of applied pressure. The cumulative distribution of pore volume by pore throat size is obtained from the intrusion data. Similarly, the retraction data provide an estimate of the cumulative distribution of pore volume by pore size. As such, they are volume weighted. It is also understood that these estimates are compromised by pore space accessibility limitations - large pores are not invaded at the pressure corresponding to their size if they are shielded by smaller pores and, for the case of retraction data, permanent trapping of mercury [87].

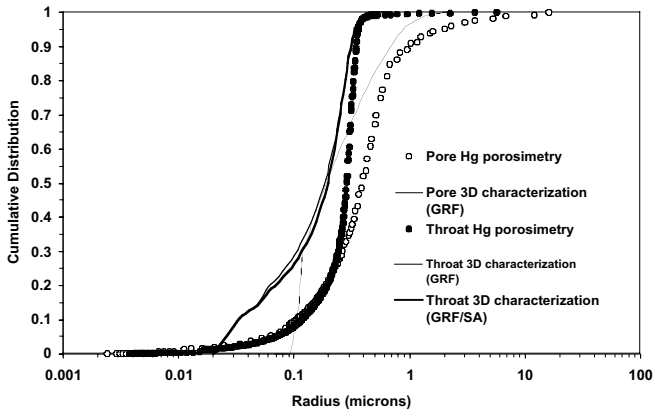

Fig. 5.2—Comparison of the pore and throat size distributions between mercury porosimetry and 3D characterization.

The coordination number distributions of the two reconstructed samples are shown in Fig. 5.3. The samples have slightly different coordination number distributions and average values of the distributions (4.8 for GRF while 5.1 for hybrid GRF/SA). The average coordination numbers are much higher than that obtained by Bekri *et al.* [1] for similar chalk (approximately 3.2). This discrepancy is probably due to limitations of the characterization methodology employed in the previous study. There are few pores having coordination number as high as 28. The 3D characterization of the reconstructed chalk (GRF case) estimated 2264 pores and 7916 throats in a

sample of 35x35x35 μm^3. As expected, the pore/throat size distributions and coordination number distributions of the two samples differ only slightly.

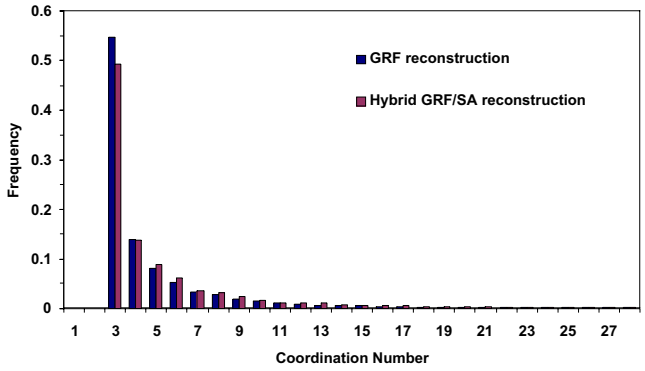

Fig. 5.3—Comparison of the coordination number distributions between the two reconstructed samples.

5.2 Network modeling

Permeability, formation factor and mercury-air capillary pressure of the reconstructed 3D sample [Fig. 5.1(a)] were computed using an equivalent network model. Permeability and formation factor were also predicted using the reconstructed microstructure itself. The computed properties were compared with the experimental values. The computation techniques and results are described briefly in this section.

5.2.1 Equivalent network modeling approach

The equivalent network model of chalk pore structure was constructed based on bond-correlated site percolation concept detailed by Ioannidis and Chatzis [57, 87]. Construction of an equivalent model has been described in details in Paper 3. Briefly, a regular cubic lattice model is constructed as follows: (1) select number of lattice nodes (cubic pores). Each node is connected to six neighboring nodes through volumeless throats; (2) use site percolation to

remove nodes and associated throats until the desired average coordination number is achieved; (3) assign pore sizes randomly from the known pore volume distribution. A bias is introduced on the assignment so that larger pores preferentially occupy sites of greater coordination number; (4) assign throat sizes following a bond-correlated site percolation scheme, whereby larger throats are assigned to bonds connecting larger pores; (5) adjust node-to-node distance (lattice constant l_c) to obtain the required porosity; and finally (6) adjust specific surface area by a fractal "decoration" of the pores. The transformation of an irregular porous medium into a fractal-decorated cubic network model is sketched in Fig. 5.4.

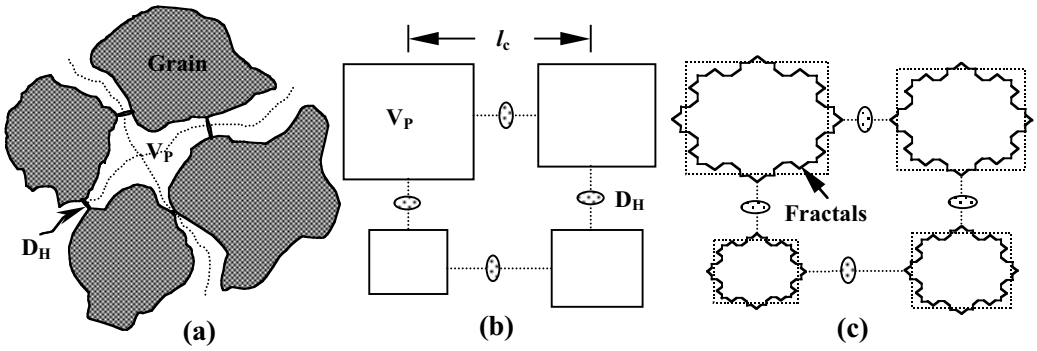

Fig. 5.4—Construction of a network model; (a) real porous medium; (b) equivalent network model; (c) fractal decoration to match specific surface area.

Computation of absolute permeability (k) and formation factor (F) is based on an electric analogue-linear network concept detailed by Ioannidis and Chatzis [57, 87]. Absolute permeability is calculated from Darcy's equation,

$$k = \frac{\mu L Q}{A \Delta P} \qquad [5.3]$$

where, L and A are the model length and flow area, respectively, and Q is the volumetric flow rate at an applied pressure differential ΔP. μ is the viscosity of the fluid flowing through the model. Electric conductivity (and hence F)

can be calculated from similar equation by replacing pressure difference with voltage difference ΔV and fluid flow rate with current flow rate (I).

The flow rate Q (or I) is calculated from known pressures (voltages) at the nodes. The nodal pressures (voltages) are obtained by solving mass (or electric current) balance equations at all nodes coupled with appropriate initial and boundary conditions,

$$\sum_j q_{ij} = g_{ij}\left(P_j - P_i\right) = 0 \qquad [5.4]$$

where q_{ij} is the flow rate through link between nodes i and j, and j runs over all links connected to node i, P_i and P_j are the nodal pressures and g_{ij} is the equivalent hydraulic (electric) conductance for the link between nodes i and j. The equivalent hydraulic or electrical conductance of each link (resistor) in the network model is calculated from the following equations:

$$g_h = \frac{\xi R_t^4}{8 l_e} f(\xi) \qquad [5.5]$$

$$g_e = \frac{4 \xi R_t^2}{l_e} \qquad [5.6]$$

where, l_e is an equivalent length estimated as,

$$l_{eij} = l_c - (R_{pi} + R_{pj}) \qquad [5.7]$$

In these equations, $f(\xi)$ is a function of the throat aspect ratio ($\xi = 1$ here) and R_{pi}, R_{pj} are the sizes of adjacent pores.

Predictions of permeability and formation factor from the network model are 0.643 mD and 13.5, respectively, which are reasonably close to the experimental values (1.35 mD and 10.4, respectively).

The mercury-air capillary pressure curve was computed following the well-documented bond-correlated site percolation process of non-wetting phase invasion [57, 87]. The computed capillary pressure curve is compared to the experimental one in Fig. 5.5. The network model predicts a breakthrough capillary pressure and radius of 24.5×10^5 Pa and 0.29 μm respectively. The agreement is reasonably good considering the approximate nature of the network model and the fact that no adjustable parameters were used. The discrepancy in the range 30×10^5 - 100×10^5 Pa is most likely due to the fact that the fraction of the volume of each pore that is contributed by fractal decoration (and therefore contributes to late filling) is small.

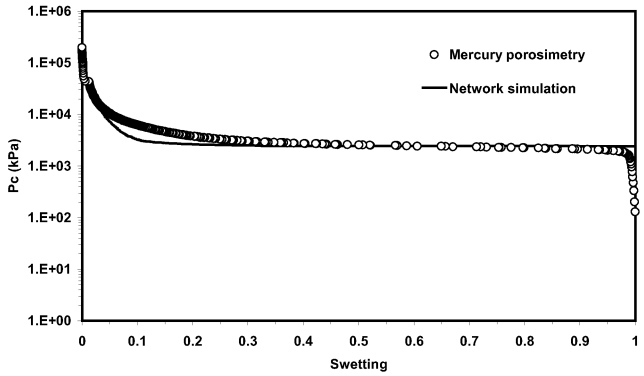

Fig. 5.5—Experimental and simulated mercury-air drainage capillary pressure curves.

5.2.2 Prediction from reconstructed microstructure

It must be emphasized that the network model is only an approximation of the pore space in chalk. The quality of this approximation must be judged not by comparing the predicted petrophysical properties with experimental data, but also by comparing them with predictions obtained using the reconstructed

microstructure itself. For this reason, the permeability of the reconstructed chalk was also calculated by solving the equivalent resistor network problem as described by Liang *et al.* [11] and the formation factor by random-walk simulation [9]. Only a brief description of the techniques will be given here (see Paper 5 for further details).

The so-called equivalent resistor network method [11] is basically the same as the electric analogue-linear network concept of Ioannidis and Chatzis [57, 87] described in Section 5.2.1. The main difference is the use of exact geometric and topological description of the reconstructed microstructure in the calculation of pore sizes and hydraulic/electrical conductance of the individual flow paths. Using the skeleton or medial axis of the pore space [Fig. 5.1(b)] as the basis, the technique identifies local minima surrounding a pore body, which enables to calculate the volume of individual pores. Each of the skeleton branches is then followed and the area and perimeter at every voxel location are calculated by scanning the pore space wall perpendicular to the flow path. Hydraulic/electric conductance is calculated at each location using area and perimeter values. The elemental conductances along a pore channel are binned to obtain the effective conductance between two nodal points. Absolute permeability is computed by solving mass balance equations at all nodes and applying Darcy's equation as described previously. The computed absolute permeability was 1.73 mD, in good agreement with the experimentally measured value of 1.35 mD.

The reconstructed microstructure was further used to predict F by a random-walk simulation [9]. Briefly, the simulation involves calculation of the mean-squared displacement versus time for a number of Brownian particles taking discrete steps inside the reconstructed pore space. A random walker is placed at the center of a randomly selected void voxel with coordinates (i_o, j_o, k_o) and is allowed to take random steps from its current location to the center of any of its nearest-neighboring pore voxels with coordinates (i, j, k) with

equal probability. At any point in time, the displacement R_E of the random walker is measured as,

$$R_E = \sqrt{(i-i_o)^2 + (j-j_o)^2 + (k-k_o)^2} \qquad [5.8]$$

For sufficiently long travel time, the mean-squared displacement $\langle R_E^2 \rangle$, averaged over all random walks, is a linear function of the travel time t,

$$\langle R_E^2 \rangle = \left(\frac{\sigma}{\phi} \right) t \qquad [5.9]$$

where σ is the effective electrical conductivity. σ is related to the formation factor F through the well-known Archie's equation, $F = \frac{\sigma_o}{\sigma} = \varphi^{-m}$ where, σ_o is the conductivity of the pore fluid and m is known as the cementation exponent. The formation factor is computed from the slope of the straight line, Eq. 5.9. A random-walk simulation involving 5000 random walkers computed a formation factor of 12.3 for the reconstructed 3D sample, in good agreement with the experimentally determined value of 10.4.

Permeability and formation factor predicted from simulation directly on the reconstructed microstructure should be considered more reliable, because the convergent-divergent geometry and exact spatial arrangement of all flow paths is taken into account. On the other hand, the network model considers flow paths as channels of uniform cross-section and slightly underestimates the hydraulic and electrical conductivity.

6. Adding predictive power to a network model for chalk

The network modeling approaches adopted previously (Section 5.2) have limitations, for example, the equivalent network model neither represents the exact topology and connectivity of the real porous media nor includes all important pore level flow processes (e.g., corner flow, wettability alteration, trapping, etc.). Further, the predictions from reconstructed microstructure are limited to absolute permeability (equivalent resistor network model) and formation factor (random-walk simulation).

The pores of real porous media consist of angular corners, which retain wetting fluid and allow two or more fluids to flow simultaneously through the same pore. Further, experimental measurements have demonstrated that most mineral surfaces become oil-wet after prolonged contact with crude oil [88-90]. The wettability alteration and flow of wetting fluid through pore corners have tremendous impact on fluid and electric transport behavior and therefore, must be duly accounted for in a network model. Since the pioneering work by Fatt [91-93], our physical understanding of two- and three-phase pore-scale displacement mechanisms has increased significantly, e.g., [94-104]. Consequently, more sophisticated network models incorporating realistic flow physics have immerged with different predictive capabilities, such as relative permeability and capillary pressure hysteresis [58, 65], the effects of wettability [60-61, 63-64, 71-75, 105-106], three-phase flow [6, 59, 62-63, 66, 107-112], modeling multiphase flow in fractures and matrix/fracture transfer [113], and prediction of relative permeability for an internal gas drive process (gas liberation during depressurization) [114]. With an exception to handful of studies, e.g., [3-6], most of the network models use idealized pore networks, which do not adequately represent the complex pore space morphology and thus greatly limit their application in the petroleum industry. Furthermore, chalk has received very little attention from the network modeling researchers

(only exceptions are Bekri *et al.* [1] and Xu *et al.* [2]). While Bekri *et al.* [1] have demonstrated the feasibility of this approach for predicting absolute permeability, formation factor and drainage air-mercury capillary pressure of homogeneous chalks, Xu *et al.* [2] have used this tool to improve the analysis of core-flood experiments in vugular chalks. These authors neither used realistic description of the pore space geometry and topology, nor all aspects of pore-level displacement phenomena e.g., corner flow, wettability alteration, trapping, etc. Clearly, there is a need to add predictive power to a network model for chalk through incorporating important pore-level displacement processes and realistic description of pore space geometry and topology. Development of such a model has been pursued in this study in light of recent advances in this area [5, 32, 61, 115]. Drainage part of the model is briefly described in this section. Detailed description of drainage and imbibition processes can be found in Paper 8. Imbibition displacement mechanisms have not been implemented fully in this study and require further work. Outline for future works is given in Paper 8 with considerable details.

6.1 Pore model

The complex and chaotic pore space of chalk as obtained from a stochastic reconstruction, e.g., the one shown Fig. 5.1(a), is converted into an equivalent pore network that captures essential features of the pore space and yet simple to deal with mathematically and numerically. Before transformation, the essential task is the topological and geometrical characterization of the reconstructed sample. The characterization technique must calculate the following: (1) location, length, average cross-sectional area and corresponding perimeter length of each pore-body within the sample; (2) number of connected pore-bodies and their locations to each pore-body; (3) length, average cross-sectional area and corresponding perimeter length of all pore-throats connected to each of the pore-bodies; and (4) list of boundary pore-

bodies and pore-throats. Characterization of the reconstructed sample is not within the scope of this study and will not be discussed further. For future work on this topic, the readers are referred to Liang *et al.* [85], Bakke and Øren [3], and the public domain software and literature by Lindquist [116].

From the known geometric and topological data, irregular pore space (pore-body and pore-throat) is converted to translationally symmetric pore channels of triangular shapes [3, 32] where the triangular pore geometry is variable and is dictated by the so-called shape factor G and the inscribed circle radius r of the pore space under consideration. The shape factor is defined by [117],

$$G = \frac{A}{P^2} = \frac{r}{2P} = \frac{1}{4\sum_{i=1}^{3} \cot \beta_i} = \frac{1}{4} \tan \beta_1 \tan \beta_2 \cot(\beta_1 + \beta_2) \qquad [6.1]$$

where A is the pore cross-sectional area, P is the corresponding perimeter length and β_i (i=1, 2, 3) are the corner half-angles ($0 \le \beta_1 \le \beta_2 \le \beta_3 \le \pi/2$). The shape factor ranges from zero for a slit-shaped pore to 0.048 for an equilateral triangular pore. Therefore, depending on its value, the triangular pore geometry may take different shapes, two of which are shown in Fig. 6.1 (see Paper 8 for selection of the non-unique corner half-angles).

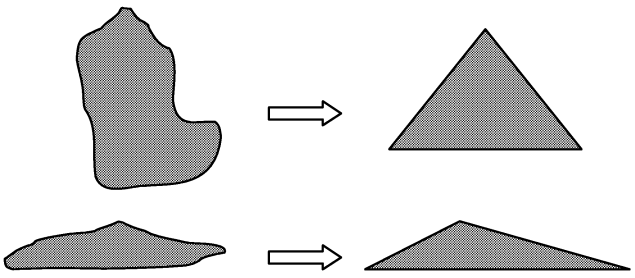

Fig. 6.1—Shape of triangular pore geometry depending on the shape factor of the pore space.

The descriptors of the network model are: (1) pore-body locations and their cross-sectional area, perimeter and length; (2) number of pore-bodies and their exact locations connected to each of the pore-bodies, and the cross-sectional area, perimeter and length of the connecting pore-throats; and (3) the pore-throats connected to the inlet and outlet faces of the sample. The displacing fluid is injected from an external reservoir through the throats connected to the inlet face while the displaced fluid escapes through the outlet face on the opposite side. The pore-body locations may be expressed by their *i*-, *j*- and *k*-indices or simply by designating them with numbers. In this study, the inlet fluid reservoir is designated with zero, a single number for each of the internal pore-bodies (ascending order from inlet to the outlet) and a number '*n+1*' for the outlet fluid reservoir where *n* is the total number of internal pore-bodies (see Fig. 6.2 for a 2D example). This numbering allows to use a *do loop* in Fortran to run over the pore-bodies. A second *do loop* is used to run over all pore-throats (1 to *z* where *z* is the coordination number) attached to each of the pore-bodies.

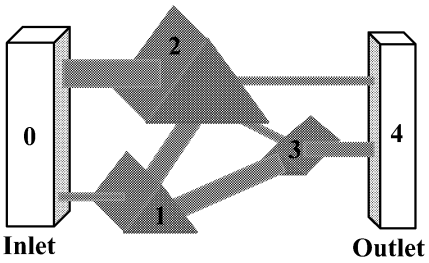

Fig. 6.2—A simple 2D network model showing the numbering convention.

6.2 Drainage displacement

The rock is assumed to be water-wet. Therefore, water displacement by oil is a drainage process. The main assumption regarding displacement is that the capillary force dominates at the pore-scale, which is reasonable for low

capillary number (10^{-6} or less, see Paper 9 for a definition of the capillary number).

Primary drainage process represents the migration of oil into water-filled reservoir. Initially the model is 100% saturated with water. Primary drainage is a pure bond invasion-percolation process [117]. The calculations are performed in order of increasing threshold capillary entry-pressures; only the accessible pore-throats (adjacent to an oil-filled pore-body) and associated pore-bodies are invaded at each step. Primary drainage continues until some maximum capillary pressure $P_{c,max}$ is reached. We use Øren *et al.*'s [5] generalization of Mason and Morrow's [118] expression for the threshold capillary entry-pressure where the Mayer and Stowe [119], and Prinsen [120-122] (MS-P) method is utilized. The MS-P method relies on equating the curvature of the corner arc-menisci (AM's) to the curvature of the invading interface. The threshold capillary entry-pressure in primary drainage $P^e_{c,pd}$ in a triangular pore is expressed as

$$P^e_{c,pd} = \frac{\sigma}{r_{pd}} = \frac{\sigma}{r} cos\,\theta_r \left(1 + 2\sqrt{\pi G}\right) F_d\left(\theta_r, G, C\right) \qquad [6.2]$$

where, θ_r is the receding contact angle, r_{pd} is the radius of curvature in primary drainage, and F_d is a function of corner half-angles through C where F_d and C are expressed as follows:

$$F_d\left(\theta_r, G, C\right) = \frac{1 + \sqrt{1 - 4GC / cos^2\,\theta_r}}{\left(1 + 2\sqrt{\pi G}\right)} \qquad [6.3]$$

$$C = \sum_{i=1}^{3} \left[cos\,\theta_r \frac{cos\left(\theta_r + \beta_i\right)}{sin\,\beta_i} - \left(\frac{\pi}{2} - \theta_r - \beta_i\right) \right] \qquad [6.4]$$

C is not universal for a given G if the AM's are not present in all pore corners. However, for strongly water-wet system (i.e., θ_r = 0), F_d = 1, regardless of how many pore corners have the water AM.

When a pore is filled with a single fluid, the area occupied by that fluid is calculated from $A = \frac{r^2}{4G}$. If water is present as AM's in the corners, the area occupied by water is given by

$$A_w = \left(\frac{\sigma}{P_c}\right)^2 \sum_{i=1}^{3}\left[\frac{\cos\theta_r \cos(\theta_r + \beta_i)}{\sin\beta_i} - \frac{\pi}{2}\left(1 - \frac{\theta_r + \beta_i}{\pi/2}\right)\right] \qquad [6.5]$$

and the area occupied by oil is given by $A_o = A - A_w$. The volume of each phase in a pore-body or pore-throat is obtained by multiplying the corresponding area with the pore length. The overall saturation of each phase is found by adding the volume of each phase in every pore-body and pore-throat and dividing by the total volume of the network.

For a pore-body or pore-throat containing a single fluid, the hydraulic conductance g is approximated from Poiseuille's law [5]

$$g = \frac{3r^2 A}{20\mu} \qquad [6.6]$$

If oil occupies the center of a pore with water present as AM's in the corners, the oil conductance is found from Eq. 6.6 with A replaced by A_o. When water is present as AM's in a corner i with a contact angle less than $\frac{\pi}{2} - \beta_i$, the water conductance for the corner is

$$g_{w,i} = \frac{\left(\frac{\sigma}{P_c}\right)^2 A_{w,i}}{C_{w,i}\mu_w} \qquad [6.7]$$

The total conductance is the sum of all the corner conductances. In the equation, C_w is a dimensionless flow resistance factor that accounts for the reduction in water conductance close to the pore wall and is a function of corner geometry, contact angle and boundary condition at the oil-water interface. C_w is calculated from an approximate expression due to Zhou *et al.* [115].

$$C_{w,i} = \frac{12\sin^2\beta_i(1-\varphi_3)^2(\varphi_2+\varphi_1)^2}{(1-\sin\beta_i)^2(\varphi_2\cos\theta_r-\varphi_1)\varphi_3^2} \qquad [6.8]$$

where $\phi_1 = \frac{\pi}{2} - \beta_i - \theta_r$, $\phi_2 = \cot\beta_i\cos\theta_r - \sin\theta_r$ and $\varphi_3 = \left(\frac{\pi}{2} - \beta_i\right)tan\,\beta_i$.

If the contact angle is greater than $\frac{\pi}{2} - \beta_i$, the curvature of the AM is negative and the water conductance for the corner may be calculated from an approximate equation [5],

$$g_{w,i} = \frac{A_{w,i}^2}{C_{w,i}\kappa_i\mu_w} \qquad [6.9]$$

where C_w is evaluated from Eq. 6.8 at $\theta_r = 0$, i.e.,

$$C_{w,i} = \frac{12\sin^2\beta_i(1-\varphi_3)(1+\varphi_3)^2}{tan\,\beta_i(1-\sin\beta_i)^2\varphi_3^2} \qquad [6.10]$$

and

$$\kappa_i = \frac{\cos\beta_i}{\sin\beta_i} - \frac{\pi}{2} + \beta_i \qquad [6.11]$$

6.3 Macroscopic properties

In laminar flow of two immiscible fluids, the flow rate of fluid *i* (*i* = oil, water) between two connecting pore-bodies *j* and *k* is given by (see Fig. 6.3)

$$q_{i,jk} = \frac{g_{i,jk}}{l_{jk}}\left(p_{i,j} - p_{i,k}\right), \quad i = o, w \qquad [6.12]$$

where l_{jk} is the spacing between the pore-body centers and $g_{i,jk}$ [$m^4/Pa.s$] is the effective hydraulic conductance of phase *i* between the two pore-bodies.

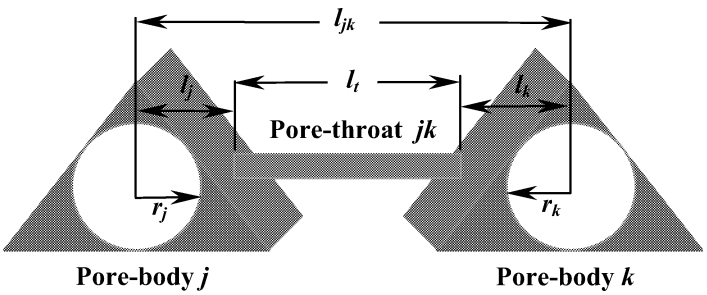

Fig. 6.3—Geometry of a unit-flow channel. The inscribed circles are the cross-sections of the largest spheres that can pass through each pore-body.

The overall flow conductance is the harmonic mean of the conductances of the connecting pore-throats and its two pore-bodies (one-half of each pore-body)

$$\frac{l_{jk}}{g_{i,jk}} = \frac{l_t}{g_{i,t}} + \frac{1}{2}\left(\frac{l_j}{g_{i,j}} + \frac{l_k}{g_{i,k}}\right), \quad i = o, w \qquad [6.13]$$

In steady-state flow of incompressible immiscible fluids, mass conservation in each pore-body is imposed:

$$\sum_k q_{i,jk} = \frac{g_{i,jk}}{l_{jk}}\left(p_{i,j} - p_{i,k}\right) = 0, \quad i = o, w \qquad [6.14]$$

where k runs over all the pore-throats that are connected to pore-body j. The index j runs over all pore-bodies that do not belong to the inlet and outlet faces of the model, i.e., internal pore-bodies. Eqs. 6.13 and 6.14 together with appropriate initial and boundary conditions constitute a complete set of linear equations, which can be solved by a linear solver for the unknown pore-body pressures. We applied a Conjugate Gradient (CG) method of Hestenes and Stiefel as outlined by Batrouni and Hansen [123] (see Paper 8 for a brief description).

To calculate the absolute permeability, the network is filled with a single fluid and a constant pressure differential is imposed across the network ΔP. The system is then let to relax by the CG method. From the pressure distribution, the total flow rate Q (through the inlet pore-throats) is calculated and, thus, the absolute permeability from Darcy's equation [Eq. 5.3].

The relative permeabilities k_r are computed by performing two separate calculations at several level of capillary pressure (average wetting phase saturation). The first calculation is done for water, which spans the entire network, and the second one is restricted to the pore-bodies and pore-throats invaded by oil. Darcy's law is applied for each of the phases

$$k_{r,i}\left(S_w\right) = \frac{\mu_i \, L \, Q_i}{kA \, \Delta P_i} \qquad [6.15]$$

Because of the analogy between Poiseuille's law and Ohm's law, the flow of electric current can also be described by Eqs. 6.13 and 6.14 but with pressure replaced by voltage, Q by current I, ΔP by voltage difference ΔV and g by electric conductance g_e. The electrical conductance g_e is assumed to be dependant only on the pore geometry i.e., pore walls are non-conductors and is given by

$$g_e = \sigma_w A \qquad [6.16]$$

where σ_w is the electrical conductivity of water which is known. The electrical conductivity σ of the pore network is computed by applying a constant voltage drop across the model and then applying Eqs. 6.13 and 6.14 to find the current flow between each of the connecting pore-bodies and hence the total current flow through the model. The formation factor is then calculated simply from

$$F = \frac{\sigma_w}{\sigma} \qquad [6.17]$$

Resistivity index I_r is also calculated at various stages of the displacement but, unlike for relative permeabilities, the calculation is performed only on water because oil is a non-conductor. Contrary to the calculation of F, we only consider pore cross-sectional A_w which is occupied by water and, thus, $g_e = \sigma_w A_w$.

6.4 Drainage results

The drainage part of the flow model is implemented in Fortran 90 (see Paper 8, Appendix A for the codes) and tested on a regular cubic-lattice model of 3x3x3 pore-bodies (see Paper 8, Appendix B for input data). The pore cross-sectional areas and corresponding perimeter lengths are selected randomly which correspond to an equivalent cylindrical pore-body and pore-throat radii range from 0.5 - 1.0 μm and 0.2 - 0.4 μm, respectively and the geometric shape factor G ranges from 0.03 – 0.048. For L = 13.6 μm, A = 13.62 μm^2 and ΔP = 2 μPa, we calculated absolute permeability k = 0.055 mD and formation factor F = 72.34. The capillary pressure, relative permeability and resistivity index curves are shown in Figs. 6.4 through 6.6. A value of 0.93 is calculated for the Archie's saturation exponent n from the I_r vs. S_w plot.

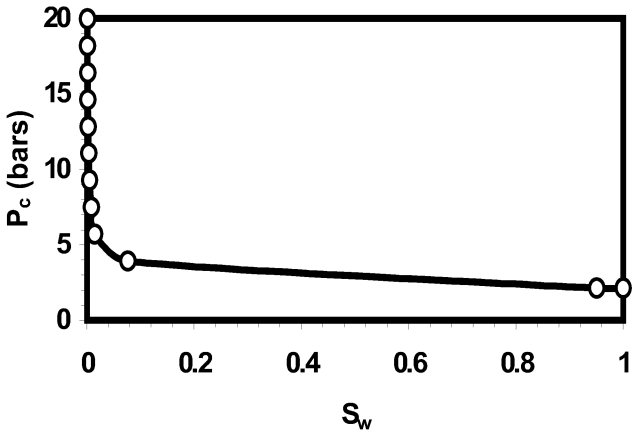

Fig. 6.4—Computed capillary pressure curve for a regular cubic-lattice model of 3x3x3 pore-bodies.

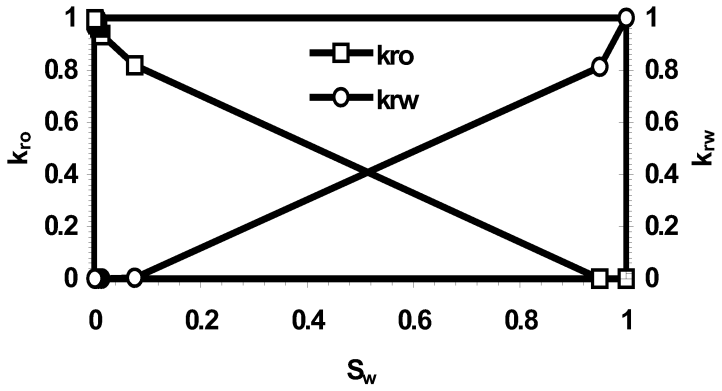

Fig. 6.5—Computed relative permeability curves for a regular cubic-lattice model of 3x3x3 pore-bodies.

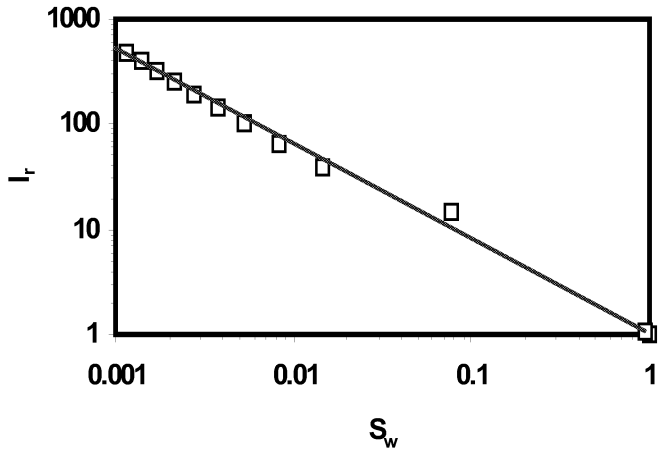

Fig. 6.6—Computed resistivity index curve for a regular cubic-lattice model of 3x3x3 pore-bodies.

As can be observed, the usual shapes of the capillary pressure, relative permeability and resistivity index curves are conceived even for this simple network model. Clearly, for the model to be predictive, the realistic variations of the chalk pores are to be included. It is important to note that the network modeling technique may be used to compute the above curves for the whole range of water saturations, specially, at very low water saturations. This is important in evaluating improved oil recovery processes but is usually not measurable by standard laboratory experiments.

7. Upscaling of fractured reservoirs

The Ekofisk reservoir is a high porosity (25-48%), low matrix permeability (1-5 mD) naturally fractured chalk. The fractures increase the effective permeability significantly and influence the recovery behavior greatly [124]. Therefore, the effects of the fine-scale fractures must be accounted for in a field-scale simulation. Recent improvements in tools and softwares enable to characterize fracture system at a very fine-scale comprising of millions of cells for a field [26-28]. A full-field simulation at this scale is not viable due to limitations in available computer technology. Therefore, there is a need to bride this gap where a field-scale simulation should be possible entailing no loss of fluid flow behavior due to small-scale heterogeneity. Upscaling is frequently applied to capture the fine-scale accuracy in a field-scale simulation [33-34, 125]. The technique is essentially an averaging of the fine-grid properties which, when applied on a coarser-grid model, produces results similar to the fine-grid model. There are several upscaling techniques (e.g., Kyte & Berry (K&B) [29], Pore Volume Weighted (PVW), Weighted Relative Permeability (WRP), Stone [30], Vertical Equilibrium (VE) [31]) widely used for conventional reservoirs to (a) represent three-dimensional models in two dimensions [126]; (b) represent fine layering in a few layer model [127]; (c) control numerical dispersion [29]; and (d) model the well effects such as coning, partial penetration, position of a well within a grid block, etc. [128]. Insofar as the fractured reservoir is concerned, the upscaling techniques are limited in their ability to parameterize the conceptual model of Warren and Root [129], i.e. to obtain effective permeability of matrix blocks [130], and equivalent matrix block dimensions and effective permeability [131]. This study is intended to develop idealized models representative of the Ekofisk field matrix block size and to verify the applicability of conventional upscaling techniques in fractured reservoir simulation. Detailed description of

the models, theories and results are presented in Papers 10 and 11. Only a brief review will be given in this section.

7.1 Models

Two 2D, one 3D and a dual-porosity model have been developed to simulate an imbibition process (water displacing oil) at various injection rates and oil-water viscosity ratios. Four widely used conventional up-scaling techniques (Kyte & Berry, Pore Volume Weighted, Weighted Relative Permeability, and Stone) have been used to calculate average properties (pseudos) from fractured fine-grid simulation, which are then applied to the coarse-grid model.

The first 2D model (Model-1) consists of 12x12x1 fine-grid and 3x1x1 equivalent coarse-grid (Fig. 7.1). The fine-grid model has fractures (no shading) surrounding the matrix blocks (shaded gray) but the coarse-grid model has no fracture. The matrix blocks of the fine-grid model have dimensions of 10cmx10cm each, whereas the fractures have a width of 0.1cm, making the total model size 100.2cmx100.2cmx10cm. The main matrix block of the coarse-grid model (middle) has dimension 100cmx100.2cmx10cm. The two narrow matrix blocks at the two opposite sides having dimensions 0.1cmx100.2cmx10cm each are just to put the wells at the respective locations. This matrix block size represents one of the most prevalent sizes in the Ekofisk field, which ranges from 0.3 m to 1.0 m [132-133]. The objective for developing this model is to convert a fractured fine-grid system into an equivalent coarse-grid system containing no fracture, which, in turn, may be simulated as a conventional reservoir.

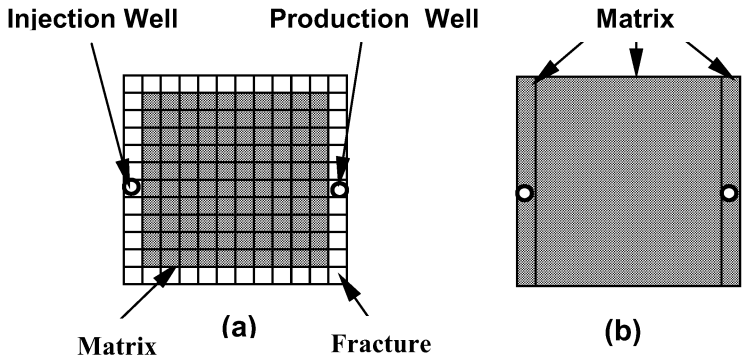

Fig. 7.1—Model-1; (a) 12x12x1 fine-grid model, (b) 3x1x1 equivalent coarse-grid model. The width of the fractures is exaggerated.

The second 2D model (Model-2) is exactly the same as Model-1, but unlike Model-1, the only one matrix block in the coarse-grid model is surrounded by fractures. The equivalent coarse-grid system has 3x3x1 grid blocks (Fig. 7.2). The objective for this model is to convert fractured fine-grid system into equivalent coarse-grid dual-porosity system.

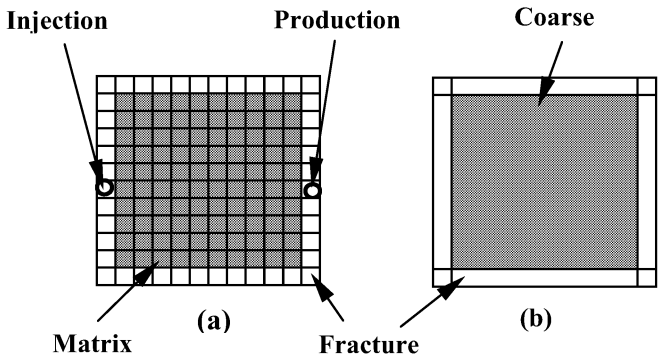

Fig. 7.2—Model-2; (a) 12x12x1 fine-grid model, (b) 3x3x1 equivalent coarse-grid model. The width of the fractures is not shown to scale relative to the matrix.

The 3D model is illustrated in Fig. 7.3. The fine-grid model consists of 10 layers each of which is similar to the fine-grid system in Model-1 or 2. Therefore, the model size is 12x12X10 grids. The equivalent coarse-grid

system consists of 3x3x1 grids. In both fine- and coarse-grid models, the matrix blocks are surrounded by fractures. The model converts fractured fine-grid 3D system into equivalent 2D coarse-grid dual-porosity system.

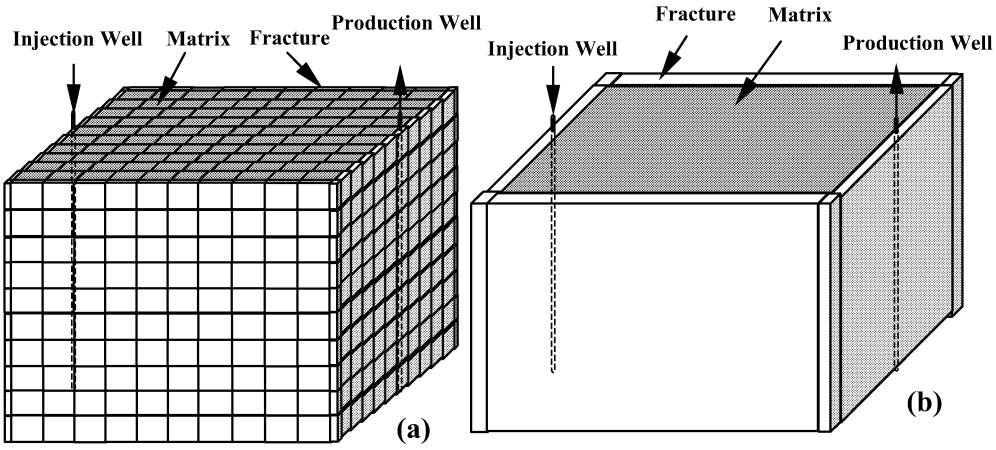

Fig. 7.3—3D-model; (a) 12x12x10 fine-grid model, (b) 3x3x1 equivalent coarse-grid model.

To investigate the validity of the conventional upscaling techniques in dual-porosity models, a dual-porosity model was developed according to the requirements of Eclipse 100. The requirement for dual porosity models in Eclipse is that the number of layers must be even and at least two. This is because the matrix layer has to be underlain by a fracture layer. The fine-grid dual-porosity model consists of 10x10x1 fine-grid matrix blocks surrounded by 140 fine-grid fracture blocks: 10 to the left, 10 to the right and 120 at the bottom. The coarse-grid model consists of a coarse matrix block and 5 course fracture blocks (model size 3x1x2) as shown in Fig. 7.4. The model dimension is 100.2cmx100cmx10.1cm.

Fig. 7.4—Equivalent dual-porosity model of 3x1x2 coarse-grid. Fine-grid model is not shown. Also, fracture width is not shown to scale.

7.2 Simulation aspects

The basic rock and fluid properties are given in Papers 10 and 11. The fracture blocks were defined as separate region and were assigned with different relative permeability and capillary pressure curves. For simplicity linear relative permeability and zero capillary pressure were assumed for the fracture. The injection well was controlled by surface injection rate whereas the production well was set at bottom hole pressure control. The minimum bottom hole pressure was 288 atm. The models were initialized with a pressure of 300 atm referenced at the top of the reservoir.

Model-1 and 2 were simulated at 20, 40, 80 and 120 cc/hr injection rates. At each injection rate, three different oil to water viscosity ratios (i.e., 1, 4 and 8) were used. The 3D-model has a volume 10 times higher than the 2D-models. Three injection rates, i.e., 200, 600 and 1200 cc/hr were considered for this model, each of them again with viscosity ratios of 1, 4 and 8. The dual-porosity model was simulated at a single injection rate (40 cc/hr) with a viscosity ratio of 4. The Kyte & Berry, Pore Volume Weighted, Weighted Relative Permeability, and Stone techniques were studied at all cases specified above. Oil recovery and water-cut from the coarse-grid simulations are compared with those from the respective fine-grid models to evaluate the effectiveness of the cases.

7.3 Results

Pseudos were generated from fine-grid simulations and were found to be different from rock curves. As an example, the Kyte and Berry pseudo-relative permeability and capillary pressure curves for 3D-model at 200cc/hr injection rate and viscosity ratio of 8.0 are compared with the respective rock functions in Fig. 7.5. The pseudo curves exhibit typical double slope behavior of fractured reservoir.

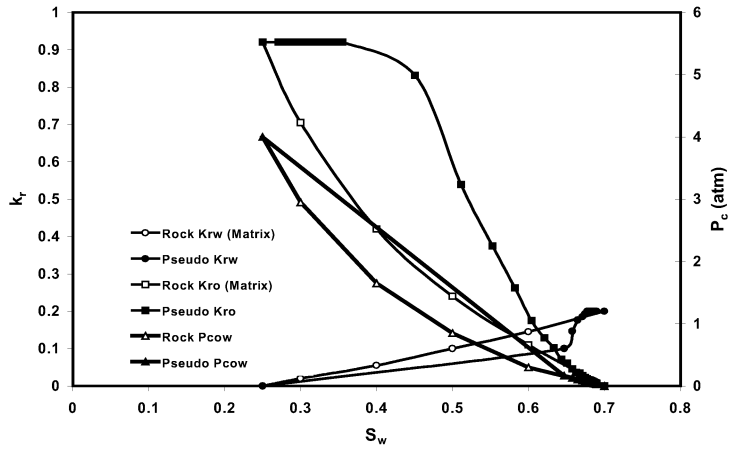

Fig. 7.5—Rock and pseudo relative permeability and capillary pressure curves (Kyte and Berry pseudo curves are generated for 3D-model at 200 cc/hr injection rate and viscosity ratio of 8.0).

The main observation from Model-1, where fractured fine-grid system was converted into equivalent coarse-grid system containing no fracture and was simulated as conventional reservoir, is that the pseudo techniques have negligible rate sensitivity at low oil-to-water viscosity ratio but they are slightly rate sensitive at high viscosity ratio. This observation is illustrated in Figs. 7.6-7.9. Each of the figures contains six graphs. The solid line is the actual prediction from fine-grid simulation using rock curves, and the broken line represents coarse-grid behavior also from rock curves while the other four graphs represent coarse-grid predictions from four different pseudo techniques. For viscosity ratio 1, the field oil recovery predictions from

coarse-grid simulations using different pseudo techniques are very close to that obtained from fine-grid simulation using rock curves. These results are quite different from coarse-grid prediction using rock curve. Similar behavior was observed for field water cut and hence are not discussed here. The pseudo techniques have limited rate sensitivity as they predict almost similar behavior in oil recovery and water cut at low and high rates. The pseudo techniques appear to be sensitive to viscosity ratio. At both low and high rates, recoveries predicted from pseudos have bigger deviation from fine-grid prediction for high viscosity ratio compared to those for low viscosity ratio. At high viscosity ratio, pseodo techniques are rate sensitive to some extent as they produce different trends at different rates.

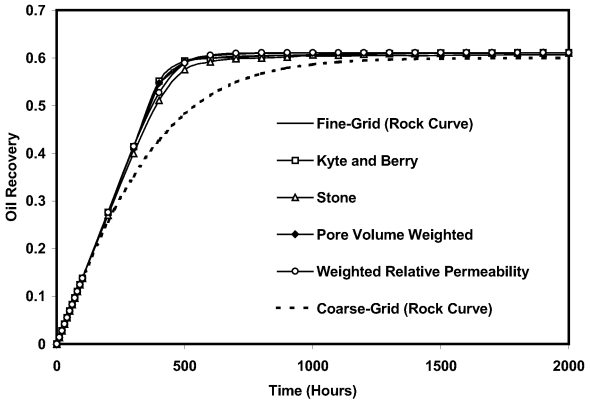

Fig. 7.6—Field oil recovery from Model-1 with oil-to-water viscosity ratio 1 at injection rate 20 cc/hr.

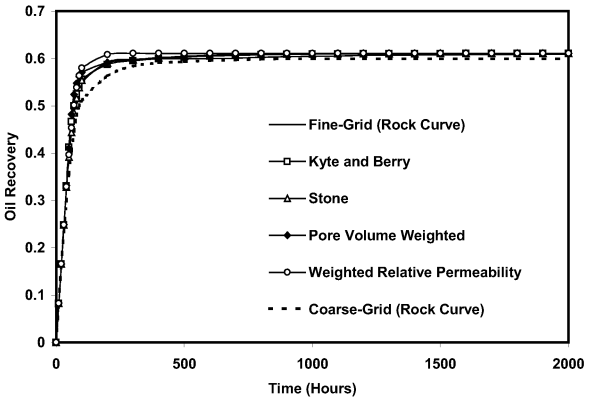

Fig. 7.7—Field oil recovery from Model-1 with oil-to-water viscosity ratio 1 at injection rate 120 cc/hr.

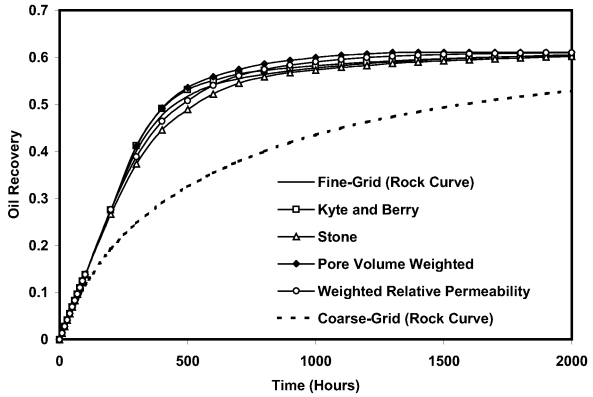

Fig. 7.8—Field oil recovery from Model-1 with oil-to-water viscosity ratio 8 at injection rate 20 cc/hr.

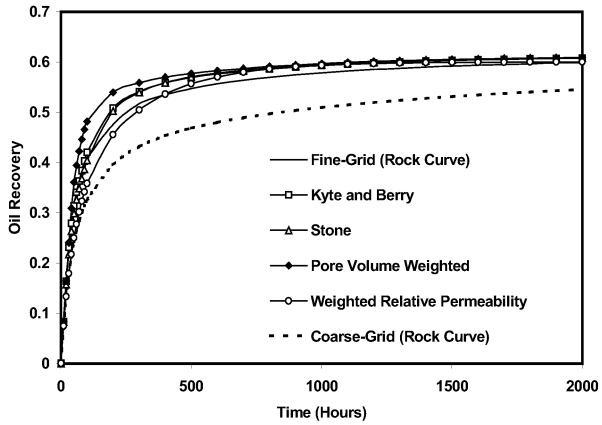

Fig. 7.9—Field oil recovery from Model-1 with oil-to-water viscosity ratio 8 at injection rate 120 cc/hr.

Results from Model-2, where fractured fine-grid system was converted into an equivalent coarse-grid dual-porosity system, predict that the Kyte and Berry, and the Pore Volume Weighted techniques are insensitive to viscosity ratio or injection rate while the Stone and the Weighted Relative Permeability techniques are sensitive to both injection rate and viscosity ratio. The Stone technique predicts slightly higher whereas the Weighted Relative Permeability technique predicts slightly lower recovery. The recovery results are shown in Figs. 7.10-7.13.

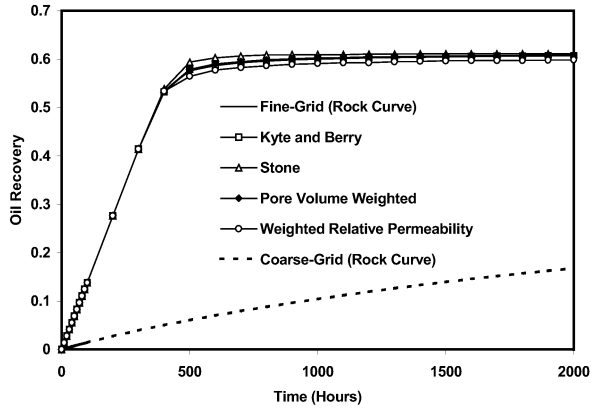

Fig. 7.10—Field oil recovery from Model-2 with oil-to-water viscosity ratio 1 at injection rate 20 cc/hr.

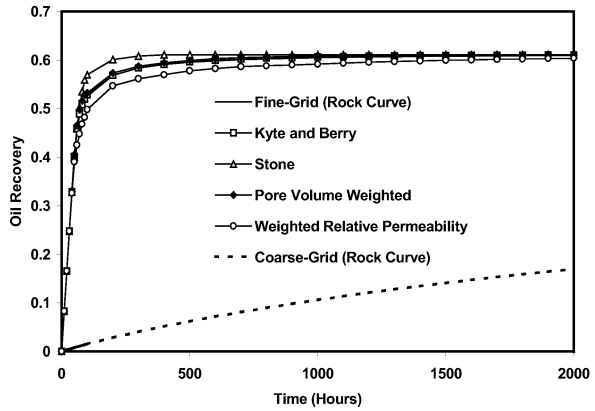

Fig. 7.11—Field oil recovery from Model-2 with oil-to-water viscosity ratio 1 at injection rate 120 cc/hr.

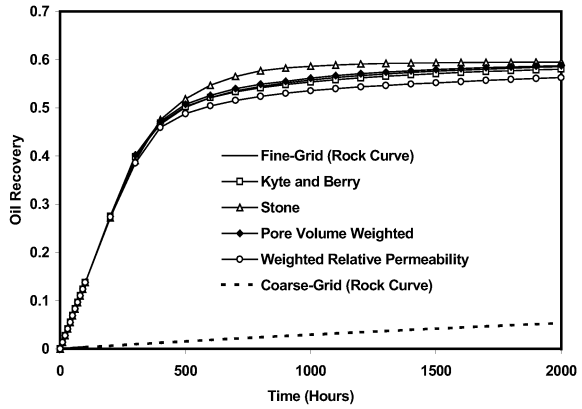

Fig. 7.12—Field oil recovery from Model-2 with oil-to-water viscosity ratio 8 at injection rate 20 cc/hr.

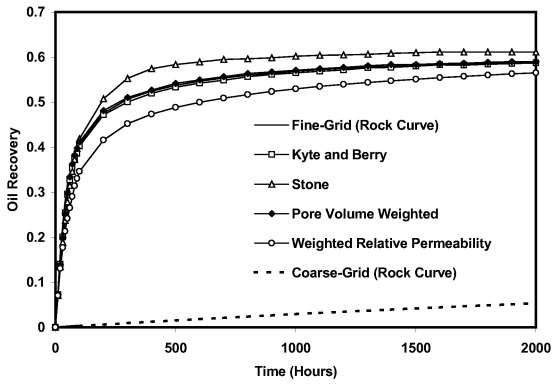

Fig. 7.13—Field oil recovery from Model-2 with oil-to-water viscosity ratio 8 at injection rate 120 cc/hr.

For the 3D-model, where fractured fine-grid 3D system was converted into equivalent 2D coarse-grid dual-porosity system, the pseudo techniques appear to be sensitive to both injection rate and viscosity ratio. Similar to Model-2, the viscosity ratio has more dominant effect than the injection rate. Unlike Model-2, however, the Kyte and Berry and the Pore Volume Weighted techniques are sensitive to viscosity ratio and injection rate. For this model, the Stone and the Pore Volume Weighted techniques give higher recovery, whereas Kyte and Berry and the Weighted Relative Permeability techniques give lower recovery than the fine-grid prediction. See Paper 11 for further details.

The fine-grid dual-porosity model was simulated with rock curves and the equivalent coarse-grid model with both rock- and the four pseudo-curves. Simulations were performed at an injection rate of 40 cc/hr with a viscosity ratio of 4. The shape factor (σ), which controls the flow between the matrix and the fracture was assigned on a cell-by-cell basis and was calculated as outlined by Kazemi *et al.* [134]. The oil recovery is shown in Fig. 7.14. With exception in the early stages, the oil recoveries obtained from coarse-grid simulations using either rock or pseudo curves are different from fine-grid results. The coarse-grid model with rock curves gives almost identical result to those with pseudo curves. This means that the pseudo techniques under

consideration are not adequate to produce fine-grid results in a dual-porosity simulation in Eclipse 100.

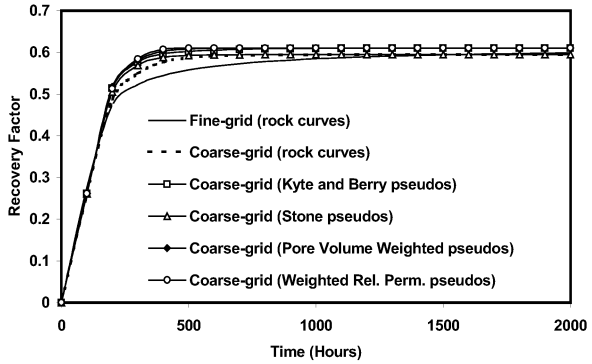

Fig. 7.14—Field oil recovery from dual-porosity model with oil-to-water viscosity ratio 4 at injection rate 40 cc/hr.

Based on results from the 2D and 3D models, a rough guideline may be established to select the most effective pseudo technique for a particular situation. The recommended technique/techniques are listed in Table 7.1 with respect to the model type, injection rate and viscosity ratio.

Table 7.1—The most effective pseudo technique/techniques for the fractured reservoir upscaling cases studied.

Model Type	Low Viscosity Ratio		High Viscosity Ratio	
	Low Rate	High Rate	Low Rate	High Rate
Model-1	WRP	K&B	K&B	K&B
Model-2	PVW, K&B	PVW, K&B	PVW, K&B	PVW, K&B
3D Model	PVW	PVW	K&B	K&B

For Model-1 at low injection rate with low viscosity ratio, though the WRP technique is the most effective one, the K&B technique is very close to it. For 3D-model with low viscosity ratio, K&B technique is also very close to the PVW technique. Therefore, the K&B technique appears to the most effective one irrespective of injection rate and viscosity ratio.

8. Summary

Contributions have been made in the area of experimental measurements on petrophysical, reservoir engineering and morphological properties of Ekofisk chalk, numerical simulation of core flood experiments to improve relative permeability curves and to analyze hysteresis, stochastic reconstruction of porous microstructure from limited morphological parameters, network modeling for computation of petrophysical and reservoir engineering properties, and upscaling of fractured reservoirs. The important findings are described below:

Experimental measurements on eight Ekofisk chalk samples provide a comprehensive data set on porosity, absolute and relative permeabilities, capillary pressure, resisitvity index, formation factor, mercury-air capillary pressure, and correlation statistics. Some of the data correspond well with published data for similar North Sea chalks while the others cannot be verified due to lack of published data.

Numerical simulation of core flood experiments is a powerful tool that can be used to obtain fit-for-purpose relative permeability curves. The technique is useful in analyzing hysteresis of the Ekofisk chalk samples.

Stochastic reconstruction of simple and complex porous microstructure is possible from limited morphological information readily obtained from 2D microscopic images using a simulated annealing (SA) technique. Selection of appropriate morphological descriptor(s) is important for the medium under consideration. For example, use of void-phase autocorrelation function alone is not sufficient to produce faithful replica of particulate media. A combination of void-phase autocorrelation function and solid-phase chord distribution function is necessary to render granular appearance of a particulate medium. Use of void-phase autocorrelation function alone seems to work well for reconstruction of chalk sample containing no appreciable amount of vuggy porosity. Reproduction of vuggy porosity in the form of foraminifer shells of

representative shape and size is possible by the use a conditional simulated annealing. Initialization of the SA reconstruction with input generated using the Gaussian random field method accelerates significantly the rate of convergence of SA reconstruction. This finding is important because the main advantage of SA method, namely its ability to impose a variety of reconstruction constraints, is usually compromised by its very slow rate of convergence.

Limited application of simple network models seems to suggest that this technique may be used to compute petrophysical and reservoir engineering properties of chalk. Computed permeability, formation factor and mercury-air capillary pressure curve correspond well with the experimental data. The predictive power of a network model for chalk may be further extended through incorporating important pore-level displacement processes (e.g., corner flow, wettability alteration, trapping, etc.) and realistic description of pore space geometry and topology. Limited results from a regular cubic-lattice model of 3x3x3 pore-bodies show that the model may be used to compute absolute and relative permeabilities, capillary pressure, formation factor, resistivity index and saturation exponent. However, further works are necessary and an outline is given with considerable details.

Numerous simulations performed on idealized 2D and 3D models at various recovery rates and with different oil-to-water viscosity ratios suggest that upscaling of fractured reservoirs may be possible using the widely used conventional upscaling techniques, such as, the Kyte & Berry, Pore Volume Weighted, Weighted Relative Permeability, and Stone techniques. Kyte & Berry technique is found to be the most effective in all situations. However, further investigations are necessary using realistic description of the fracture-system (e.g., length, orientation, connectivity, aperture, spacing). Outline for a further work is given.

9. Further works

Outlines for two further works have been given in this section. The first study is related to extension of the predictive capability of a network model for chalk and the second one is related to development of a more realistic model for fractured reservoir upscaling.

9.1 Extension of a network model

1. A realistic description of the chalk pore geometry and topology is to be given as input to the drainage network model described in Section 6. The requisite pore space descriptors are detailed in Paper 8 and are accessible by characterization of the stochastically reconstructed pore spaces.
2. The imbibition part of the model is described in details in Paper 8 but is not implemented. The imbibition displacement processes are to be implemented and simulated using the characterized pore space descriptors.

9.2 Fractured reservoir upscaling

The models developed in this study for upscaling of fractured reservoirs (Section 7) are idealized and not representative of actual field situation. In reality, fracture networks are very irregular, and the length, orientation, connectivity, aperture and spacing (density) of the fractures affect the effective properties significantly. In addition, the rock-type, and size and shape of the matrix blocks strongly influence the matrix-fracture fluid exchange process. Clearly, these aspects have not been addressed in our study.

Traditionally, we use the conventional single-porosity reservoir models to obtain accurate flow behavior at fine scale. However, an important question remains unresolved whether the conventional models can avoid numerical

problems associated with modeling vast property contrast between matrix rock and fractures of a real fracture system. This issue needs to be resolved. The objectives of the further work would be two folded:

1. Verify the applicability of conventional simulation models in modeling real matrix/fracture contrasts. If current simulators fail to avoid numerical problems, develop an improved model.
2. Investigate the applicability of available upscaling techniques in simulating realistic fracture system. Develop (if necessary) a reliable technique that would use double-porosity or single-porosity simulators and provides results as accurate as the fine scale simulation.

The steps to be followed for the study are as follows:

- Review of different fracture patterns and properties of fracture systems for the field concerned. The properties include distributions of length, orientation, connectivity, aperture, spacing (density) and permeability of the fractures, and size and permeability of the matrix blocks.
- Develop a realistic fine-grid simulation model incorporating the above data.
- Simulate single-phase (oil, gas) and two-phase (oil-water, oil-gas, gas-water) flows in the fine-grid model using available simulator(s). Verify whether the current models are adequate to avoid numerical problems associated with modeling sharp contrast between matrix and fracture properties of the fine-grid model. If not, develop an improved model.
- Investigate the available upscaling techniques (single-porosity and double-porosity) in great details and verify as to what extent they can be applied to the fracture system under consideration. Some upscaling techniques try to convert a naturally fractured reservoir into an equivalent single-porosity system. In some fractured systems, the oil-water fronts in fractures flow much faster than those in the matrix. In such a system, single-porosity upscaling is not adequate and an equivalent double-porosity model would be necessary.

Nomenclature

A	*Model/pore cross-sectional area*
A_o	*Cross-sectional area of a pore occupied by oil*
A_w	*Cross-sectional area of a pore occupied by water*
A_t	*Area of a throat*
$C_i(\vec{u})$	*Chord distribution function at a lag vector* $\vec{u}$ *(i = void, solid)*
C_w	*Dimensionless resistance factor*
E	*Energy in the simulated annealing (SA) algorithm*
F	*Formation factor*
f_n	*Simulated correlation function in the SA algorithm*
$\tilde{f}_n$	*Reference correlation function in the SA algorithm*
I_r	*Resistivity index*
G	*Geometric shape factor*
g_e	*Electric conductance*
g, g_h	*Hydraulic conductance*
g_{ij}	*Conductance between nodes i and j*
k	*Absolute permeability*
k_{ro}	*Oil relative permeability*
k_{rod}	*Drainage oil relative permeability*
k_{roi}	*Imbibition oil relative permeability*
k_{row}	*Oil relative permeability in water-oil two phase system*
k_{rowe}	*End-point oil relative permeability in water-oil two phase system*
k_{rw}	*Water relative permeability*
k_{rwd}	*Drainage water relative permeability*
k_{rwe}	*End-point water relative permeability in water-oil two phase system*

k_{rwi}	*Imbibition water relative permeability*
k_{rwo}	*Water relative permeability in water-oil two phase system*
L	*Length to be used in Darcy's equation*
l_c	*Lattice constant of the equivalent network model*
l_e	*Equivalent length of a link*
l_{jk}	*Length between nodes j and k*
$L(\vec{u})$	*Lineal path function at a lag vector* $\vec{u}$
m	*Cementation exponent*
N_{ow}	*Corey representation exponent, oil to water* ($N_{ow} \approx$ *2-4 for water-wet, 6-8 for oil-wet and 3-6 for intermediate-wet)*
N_w	*Corey representation exponent, water to oil* ($N_w \approx$ *5-8 for water-wet, 2-3 for oil-wet and 3-5 for intermediate-wet)*
P	*Pressure at a node, perimeter length of a pore*
ΔP	*Pressure differential to be used in Darcy's equation*
p_a	*Acceptance probability in the SA algorithm*
p_c	*Capillary pressure*
P_{cew}	*Entry capillary pressure in water-oil system*
$P^e_{c,pd}$	*Capillary entry-pressure for primary drainage*
$P_{c,max}$	*Maximum capillary pressure in primary drainage*
P_{cog}	*Gas-oil capillary pressure*
Q	*Total flow rate to be used in Darcy's equation*
q_{ij}	*Flow rate between nodes i and j*
r	*Pore/throat radius, inscribe circle radius of a pore*
R_E	*Displacement of a random walker*
R_H	*Hydraulic radius*
R_p	*Pore radius*
r_{pd}	*Radius of curvature in primary drainage*
R_t	*Throat radius*
$R_z(\vec{u})$	*Autocorrelation function at a lag vector* $\vec{u}$

s	*Specific surface area*
S_o	*Oil saturation*
S_{orw}	*Residual oil saturation after water injection*
S_w	*Water saturation*
S_{wi}	*Initial water saturation*
S_{wsp}	*Water saturation after spontaneous imbibition*
$S_2(\vec{u})$	*Two-point correlation function at a lag vector* $\vec{u}$
t	*Travel time in random-walk simulation*
T	*Temperature in the SA algorithm*
V_p	*Volume of a pore*
$Z(\vec{r})$	*Binary phase function at a point vector* $\vec{r}$
β_i	*Corner half-angles (i=1, 2, 3)*
$\overline{\lambda}$	*Correlation length*
λ	*Pore size distribution index ($\lambda \approx 0.5$-4, λ is greater for more uniform pore size distribution)*
ζ	*Aspect ratio*
σ	*Electric conductivity, shape factor, interfacial/surface tension*
ϕ	*Porosity*
ϕ_{nv}	*Non-vuggy porosity*
ϕ_v	*Vuggy porosity*
θ	*Contact angle*
θ_r	*Receding contact angle*
μ	*Fluid viscosity*
BSE	*Backscatter scanning electron*
CSA	*Conditional simulated annealing*
GRF	*Gaussian random fields*
K&B	*Kyte and Berry*
PVW	*Pore volume weighted*
SA	*Simulated annealing*

SEM *Scanning electron microscope*

WRP *Weighted relative permeability*

References

1. Bekri, S., Xu, K., Yousefian, F., Adler, P.M., Thovert, J.-F., Muller, J., Iden, K., Psyllos, A., Stubos, A.K., and Ioannidis, M.A.: "Pore Geometry and Transport Properties in North Sea Chalk," *J. Pet. Sci. and Eng.* **25**, 107-134 (2000).
2. Xu, B., Kamath, J., Yortsos, Y.C. and Lee, S.H.: "Use of Pore Network Models to Simulate Laboratory Corefloods in a Heterogeneous Carbonate Sample," *SPEJ* **4**(3), 179-186 (Sep. 1999).
3. Bakke, S. and Øren, P.E.: "3-D Pore-Scale Modeling of Sandstones and Flow Simulations in the Pore Networks," *SPEJ* **2** (June 1997), 136-149.
4. Nilsen, L.S., Øren, P.E., Bakke, S. and Henriquez, A.: "Prediction of Relative Permeability and Capillary Pressure From a Pore Model," SPE 35531, European 3-D Reservoir Modeling Conf., Stavanger, Norway, 16-17 April (1996).
5. Øren, P.E., Bakke, S. and Arntzen, O.J.: "Extending Predictive Capabilities to Network Models," *SPEJ* (Dec. 1998), 324-336.
6. Lerdahl, T.R. and Øren, P.E.: "A predictive network model for three-phase flow in porous media," SPE 59311, SPE/DOE Improved Oil Recovery Symposium, Tulsa, OK, 3-5 April (2000).
7. Quiblier, J.A.: "A New Three-Dimensional Modeling Technique for Studying Porous Media," *J. of Coll. and Interface Sci.* **98**, 84-102 (1984).
8. Adler, P.M., Jacquin, C.G. and Quiblier, J.A.: "Flow in Simulated Porous Media," *Int. J. of Multiphase Flow* **16** (4), 691-712 (1990).

9. Ioannidis, M.A., Kwiecien, M.J., and Chatzis, I.: "Electrical Conductivity and Percolation Aspects of Statistically Homogeneous Porous Media," *Trans. in Por. Media* **29**, 61 (1997).
10. Levitz, P.: "Off-Lattice Reconstruction of Porous Media: Critical Evaluation, Geometrical Confinement and Molecular Transport," *Advances in Coll. and Interface Sci.* **76/77**, 71-106 (1998).
11. Liang, Z., Ioannidis, M.A., and Chatzis, I.: "Permeability and Electrical Conductivity of Porous Media from 3D Stochastic Replicas of the Microstructure," *Chem. Eng. Sci.* **55**, 5247 (2000).
12. Kainourgiakis, M.E., Kikkinides, E.S., Steriotis, Th.A., Stubos, A.K., Tzevelekos, K.P., and Kanellopoulos, N.K.: "Structural and Transport Properties of Alumina Porous Membranes from Process-Based and Statistical Reconstruction Techniques," *J. Coll. Interface Sci.* **231**, 158 (2000).
13. Biswal, B., Manwart, C., Hilfer, R., Bakke, S. and Øren, P.E.: "Quantitative Analysis of Experimental and Synthetic Microstructures for Sedimentary Rock," *Physica A* **273**, 452-475 (1999).
14. Hazlett, R.D.: "Statistical Characterization and Stochastic Modeling of Pore Networks in Relation to Fluid Flow, *Math. Geol.* **29**, 801-822 (1997).
15. Yeong, C.L.Y., and Torquato, S.: "Reconstructing Random Media," *Phys. Rev. E* **57**, 495-506 (1998).
16. Yeong, C.L.Y. and Torquato, S.: "Reconstructing Random Media. II. Three-Dimensional Media from Two-Dimensional Cuts," *Phys. Rev. E* **58**, 224-233 (1998).
17. Manwart, C., Torquato, S., and Hilfer, R.: "Stochastic Reconstruction of Sandstones," *Phys. Rev. E* **62**, 893 (2000).
18. Liang, Z., Ioannidis, M.A. and Chatzis, I.: "Reconstruction of 3D Porous Media Using Simulated Annealing," *Proc.* of the XIII Intl.

Conf. on Computational Methods in Water Resources, Alberta, Canada, 25-29 (2000).

19. Talukdar, M.S., Torsaeter, O. and Ioannidis, M.A.: "Stochastic Reconstruction of Particulate Media from 2D Images," *J. of Coll. and Interface Sci.* **246** (2002).
20. Talukdar, M.S., Torsaeter, O., Ioannidis, M.A. and Howard, J.J.: "Stochastic Reconstruction of Chalk from Two-Dimensional Images," *Trans. in Por. Media* **1621**, 1-23 (2002).
21. Kokkedee, J.A., Boom, W., Frens, A.M. and Maas, J.C.: "Improved Special Core Analysis: Scope for a Reduced Residual Oil Saturation," SCA 9601, Intl. Symp. of the Society of Core Analyts, Montpellier, France, 8-10 Sept. (1996).
22. Yu, S.Y., Akervoll, I., Torsaeter, O., Stensen, J.A., Kleppe, J. and Midtlyng, S.H.: "History Matching Gas Injection Processes with In-Situ Saturation Measurements and Process Hysteresis," SPE 48842, SPE Intl. Conf., Beijing, China, 2-6 Nov. (1998).
23. Akervoll, I. Talukdar, M.S., Midtlyng, S.H., Torsæter, O. and Stensen, J.A.: "History Matching WAG Injection Experiments Performed Under CT Surveillance to Obtain Relative Permeability and Capillary Pressure," Paper 17, 20th Annual Intl. Energy Agency Workshop and Symp., Paris, France, 21-24 Sep. (1999).
24. Akervoll, I., Talukdar, M.S., Midtlyng, S.H., Stensen, J.A. and Torsaeter, O.: "WAG Injection Experiments With In-Situ Saturation Measurements at Reservoir Conditions and Simulations," SPE 59323, SPE/DOE Enhanced Oil Recovery Symp., Tulsa, OK, 3-5 April (2000).
25. Poulsen, S., Skauge.T, Dyrhol, S.O., Stenby, E. and Skauge, A.: "Including Capillary Pressure in Simulations of Steady-State Relative Permeability Experiments," SCA 2014, Intl. Symp. of the Society of Core Analysts, Abu Dhabi, UAE, 18-22 Oct. (2000).

26. Yang, Y.K. and Deo, M.D.: "Full-Tensor Multiphase Flow Simulations With Applications to Upscaling and Discrete-Fracture Models," SPE 66348, Reservoir Simulation Symp. Houston, TX, 11-14 Feb. (2001).
27. Ouenes, A.: "Practical Application of Fuzzy Logic and Neural Networks to Fractured Reservoir Characterization," *Computers and Geosciences* **26** (7), ed. Shahab Mohagegh (2000).
28. Ouenes, A. and Hartley, L.J.: "Integrated Fractured Reservoir Modeling Using Both Discrete and Continuum Approaches," SPE 62939, Annual Tech. Conf., Dallas, TX, 1-4 Oct. (2000).
29. Kyte, J.R. and Berry, D.W.: "New Pseudo Functions to Control Numerical Dispersion," *SPEJ* (Aug. 1975), 269-276.
30. Stone, H.L.: "Rigorous Black Oil Pseudofunctions," SPE 21207, 11th SPE Symp. on Reservoir Simulation, Anaheim, California, 17-20 Feb. (1991).
31. Coats, K.H., Dempsey, J.R. and Henderson, J.H.: "The Use of Vertical Equilibrium in Two Dimensional Simulation of Three-Dimensional Reservoir Performance," *SPEJ* (March 1971), 63.
32. Patzek, T.W.: "Verification of a Complete Pore Network Simulator of Drainage and Imbibition," *SPEJ* (June 2001), 144-156.
33. Agarwal, B., Thomas, L.K., Sylte, J.E. and O'Meara, D.J.: "Reservoir Characterization of Ekofisk Field: A Giant, Fractured Chalk Reservoir in the Norwegian North Sea - Upscaling," SPE 38875, SPE Annual Tech. Conf. and Exh., San Antonio, TX, 5-8 Oct. (1997).
34. Chambers, K. T., DeBaun, D. R., Durlofsky, L. J., Taggart, I. J., Bernath, A., Shen, A.Y., Legarre, H. A. and Goggin, D. J.: "Geologic Modeling, Upscaling and Simulation of Faulted Reservoirs Using Faulted Stratigraphic Grids," SPE 51889, SPE Reservoir Simulation Symp. Houston, TX, 14-17 Feb. (1999).

35. Eleri, O.O., Graue, A. and Skauge, A.: “Steady-State and Unsteady-State Two-Phase Relative Permeability Hysteresis and Measurements of Three-Phase Relative Permeabilities Using Imaging Techniques,” SPE 30764, SPE Annual Tech. Conf. and Exh., Dallas, TX, 22-25 Oct. (1995).
36. Braun, E.M., and Holland, R.: "Relative Permeability Hysteresis: Laboratory Measurements and a Conceptual Model," *SPERE* (August 1995), 222.
37. Honarpour, M., Koederitz, L. and Harvey, A.H.: *Relative Permeabilities of Petroleum Reservoirs*, CRC Press, Boca Raton, FL, 1-5 (1986).
38. Skauge, A. and Larsen, J.A.: “Three-Phase Relative Permeabilities and trapped Gas Measurements Related to WAG Processes,” SCA 9421, 1994 Intl. Symp. of the Society of Core Analysts, Stavanger, 12-14 Sept. (1994).
39. Eleri, O.O., Graue, A., Larsen, J.A. and Skauge, A.: “Calculation of Three-Phase Relative Permeabilities from Displacement Experiments with Measurements of In-Situ Saturation,” SCA 9507, 1995 Intl. Symp. of the Society of Core Analysts, San Francisco, CA, 12-14 Sep. (1995).
40. Moss, A.K., Jing, X.D., and Archer, J.S.: "Laboratory Investigation of Wettability and Hysteresis Effects on Resistivity Index and Capillary Pressure Characteristics," *Proc.* 5th Intl. Symp. on Evaluation of Reservoir Wettability and Its Effect on Oil Recovery, Trondheim, Norway, 338-349 (1999).
41. Mitchell, P., and Brown, G.: "The Effect of Imbibition on the Value of the Saturation Exponent and the Implications for Depleting Reservoirs," *Proc.* European *SPWLA* Meeting, Aberdeen (1994).

42. Anderson, W.G.: “Wettability Literature Survey-Part 5: The Effect of Wettability on Relative Permeability,” *JPT* (November 1987), 1453-1468.

43. Craig, F.F.: “The Reservoir Engineering Aspects of Waterflooding,” *SPE Monograph Series* **3**, Richardson, TX, 12-44 (1971).

44. Amott, E.: "Observations Relating the Wettability of Porous Rocks," *Trans. AIME* **216**,156-162 (1959).

45. Cuiec, L.E.: “Wettability and Oil Reservoirs,” *In* North Sea Oil and Gas Reservoirs (ed. Kleppe *et al.*), Graham & Trotman, 193-207 (1987).

46. Donaldson, E.C., Thomas, R.D. and Lorenz, P.B.: “Wettability Determination and its Effect on Recovery Efficiency,” *SPEJ* **13**(3) (1969).

47. Torsæter, O.: "An Experimental Study of Water Imbibition in North Sea Chalk," SPE 12688, SPE/DOE Enhanced Oil Recovery Symp., Tulsa, OK, 15-18 April (1984).

48. Tobola, D.P.: "The Contribution of Oil Production Mechanisms as Determined by a Novel Centrifuge Technique," SCA 9617, Intl. Sym. of the Society of Core Analysts, Montpellier, 8-10 Sept. (1996).

49. Graue, A., Bognø, T., Moe, R.W., Baldwin, B.A., Spinler, E.A., Maloney, D., Tobola, D.P.: "Impacts of Wettability on Capillary Pressure and Relative Permeability," SCA 9515, Intl. Symp. of Core Analysts, Colorado, 1-4 August (1999).

50. Archie, G.E.: "The Electrical Resistivity Log as an Aid in Determining some Reservoir Characteristics," *Trans. AIME* **146**, 54 (1942).

51. Torsæter, O.: "An Experimental Study of Water Imbibition in North Sea Chalk," Ph.D. thesis, The Norwegian Institute of Technology, The University of Trondheim, Norway, (July 1983).

52. Salmas, C. and Androutsopoulos, G.: “Mercury Porosimetry: Contact Angle Hysteresis of Materials with Controlled Pore Structure,” *J. Coll. and Interface Sci.* **239**, 178-189 (2001) (and references therein).
53. Roberts, A.P. and Torquato, S.: “Chord-Distribution Functions of Three-Dimensional Random Media: Approximate First-Passage Times of Gaussian Process,” *Phys. Rev. E* **59**, 4953-4963 (1999).
54. Stone, H.L.: “Probability Model for Estimating Three-Phase Relative Permeability,” *JPT*, 214 (1970).
55. Standing, M.B.: "Notes on Relative Permeability Relationship," The Norwegian Institute of Technology, Trondheim (1975).
56. Hegre, M. and Kristiansen, S.: “Evaluation of Tertiary Flooding in Fractured Chalk Using Numerical Simulation Models,” *In:* RUTH - A Norwegian Research Program on Improved Oil Recovery, Program Summary, eds. S.M. Skjæveland, A. Skauge, L. Hinderaker, and C.D. Sisk, Norwegian Petroleum Directorate, Stavanger (1996).
57. Ioannidis, M.A. and Chatzis, I.: “Network Modeling of Pore Structure and Transport Properties of Porous Media,” *Chem. Eng. Sci.* **48**, 951 (1993).
58. Jerauld, G.R. and Salter, S.J.: “The Effect of Pore Structure on Hysteresis in Relative Permeability and Capillary Pressure: Pore Level Modeling,” *Trans. in Por. Media* **5**, 103-151 (1990).
59. Mani, V. and Mohanty, K.K.: “pore-Level Network Modeling of Three-Phase Capillary Pressure and Relative Permeability Curves,” *SPEJ* (Sep. 1998), 238-248.
60. Blunt, M.J.: “Effect of Heterogeneity and Wetting on Relative Permeability Using Pore Level Modeling,” *SPEJ* **2** (March 1997), 70-87.
61. Blunt, M.J.: “Pore Level Modeling of the Effects of Wettability,” *SPEJ* **2** (Dec. 1997), 494-510.

62. Fenwick, D.H. and Blunt, M.J.: "Network Modeling of Three-Phase Flow in Porous Media," *SPEJ* **3**, 86-97 (1998).

63. Hui, M.H. and Blunt, M.J.: "Pore-Scale Modeling of Three-Phase Flow and the Effects of Wettability," SPE 59309, SPE/DOE Improved Oil Recovery Symp., Tulsa, OK, 3-5 April (2000).

64. McDougall, S.R. and Sorbie, K.S.: "The Impact of Wettability on Waterflooding: Pore-Scale Simulation," *SPERE* **10** (Aug. 1995), 208-213.

65. Dixit, A.B., McDougall, S.R. and Sorbie, K.S.: "A Pore-Level Investigation of Relative Permeability Hysteresis in Water-Wet Systems," *SPEJ* (June 1998), 115-123.

66. Van Dijke, M.I.J., McDougall, S.R. and Sorbie, K.S.: "Three-Phase Capillary Pressure and Relative Permeability Relationships in Mixed-Wet Systems," *Trans. in Por. Media* **44**, 1-32 (2001).

67. McDougall, S.R., Cruickshank, J. and Sorbie, K.S.: "Anchoring Methodologies for Pore-Scale Network Models: Application to Relative Permeability and Capillary Pressure Prediction," SCA 2001-15, *Proc.* Intl. Symp. of the Society of Core Analysts, Edinburgh, Scotland, 17-19 Sep. (2001).

68. Laroche, C., Vizika, O., Hamon, G. and Courtial, R.: "Two-Phase Flow Properties Prediction from Small-Scale Data Using Pore-Network Modeling," SCA 2001-16, *Proc.* Intl. Symp. of the Society of Core Analysts, Edinburgh, Scotland, 17-19 Sep. (2001).

69. Laroche, C.: "Capillary Pressure and Relative Permeability Curves in Mixed-Wet Media Using Network Modeling," *Prod.* 6th Intl. Symp. on Reservoir Wettability and its Effects on Oil Recovery, Socorro, NM, 27-28 Sep. (2000).

70. Tsakiroglou, C.D. and Fleury, M.: "Pore Network Analysis of Resistivity Index for Water-Wet Porous Media," *Trans. in Por. Media* **35**, 89-128 (1999).

71. Man, H.N. and Jing, X.D.: "Pore Network Modeling of Electrical Resistivity and Capillary Pressure Characteristics," *Trans. in Por. Media* **41**, 263-286 (2000).
72. Blunt, M.J.: "Physically-Based Network Modeling of Multiphase Flow in Intermediate-Wet Porous Media," *J. Pet. Sci. and Eng.* **20**, 117-125 (1998).
73. Dixit, A.B., McDougall, S.R., Sorbie, K.S. and Buckley, J.S.: "Pore-Scale Modeling of Wettability Effects and Their Influence on Oil Recovery," *SPEREE* **2**(1) (Feb. 1999), 25-36.
74. Dixit, A.B., Buckley, J.S., McDougall, S.R. and Sorbie, K.S.: "Empirical Measures of Wettability in Porous Media and the Relationship between Them Derived From Pore-Scale Modeling," *Trans. in Por. Media* **40**, 27-54 (2000).
75. Laroche, C., Vizika, O., and Kalaydjian, F.: "Network Modeling to Predict the Effect of Wettability Heterogeneities on Multiphase Flow," SPE 56674, SPE Annual Tech. Conf. and Exh., Houston, TX, 3-6 Oct. (1999).
76. Spanne, P., Thovert, J., Jacquin, C., Lindquist, W., Jones, K. and Adler, P.: "Synchrotron Computed Microtomography of Porous Media: Topology and Transports," *Phys. Rev. Lett.*, **73**, 2001-2004 (1994).
77. Coles, M.E., Spanne, P., Muegge, E.L., and Jones, K.W.: "Computed Microtomography of Reservoir Core Samples," *Proc.* 1994 Intl. Symp. of the Society of Core Analysts, Stavanger, Norway (1994).
78. Hazlett, R.D.: "Simulation of Capillary-Dominated Displacements in Microtomographic Images of Reservoir Rocks," *Trans. in Por. Media*, **20**, 21-35 (1995).
79. Coles, M.E., Hazlett, R.D., Muegge, E.L., Jones, K.W., Andrews, B., Dowd, B., Siddons, P., Peskin, A., Spanne, P. and Soll, W.E.: "Developments in Synchrotron X-Ray Microtomography with

Applications to Flow in Porous Media," SPE 36531, Annual Tech. Conf. and Exh., Denver, Colorado, 6-9 Oct. (1996).

80. Fredrich, J., Menendez, B., and Wong, T.-F.: "Imaging the Pore Structure of Geomaterials," *Science* **268**, 276-279 (1995).
81. Lucia, F.J.: "Petrophysical Parameters Estimated from Visual Descriptions of Carbonate Rocks: A Field Classification of Carbonate Pore Space," *JPT* **35**(3), 629 (1983).
82. Metropolis, N., Rosenbluth, A., Rosenbluth, M., Teller, A. and Teller, E.: "Equation of State Calculations by Fast Computing Machines," *J. Chem. Phys.* **21**, 1087-1092 (1953).
83. Sheehan, N., and Torquato, S.: "Generating Microstructures with Specified Correlation Functions," *J. Appl. Phys.* **89**(1), 53-60 (2001).
84. Cule, D. and Torquato, S.: "Generating Random Media from Limited Microstructural Information via Stochastic Optimization," *J. Appl. Phys.* **86**(6), 3428-3437 (1999).
85. Liang, Z., Ioannidis, M.A. and Chatzis, I.: "Geometric and Topological Analysis of Three-Dimensional Porous Media: Pore Space Partitioning Based on Morphological Skeletonization," *J. of Coll. and Interface Sci.* **221**, 13-24 (2000).
86. Ma, C.M. and Sonka, M.: "A Fully Parallel 3D Thinning Algorithm and its Applications," *Comput. Vision Image Understanding* **64**, 420 (1996).
87. Ioannidis, M.A. and Chatzis, I.: "A mixed-percolation model of capillary hysteresis and entrapment in mercury porosimetry," *J. of Coll. and Interface Sci.* **161**, 278 (1993).
88. Dullien, F.A.L: "Porous Media, Fluid Transport and Pore Structure," *Academic Press*, San Diego, California (1992).
89. Craig, F.R.: "The Reservoir Engineering Aspects of Waterflooding," *Society of Petroleum Engineers*, New York (1993).

90. Legens, C., Toulhoat, H., Cuiec, L., Villieras, F. and Palermo, T.: "Wettability Change Related to Adsorption of Organic Acids on Calcite: Experimental and *Ab Initio* Computational Studies," *SPEJ* **4**(4), 328-333 (Dec. 1999).
91. Fatt, I.: "The Network Model of Porous Media I. Capillary Pressure Characteristics," *Trans. AIME* **207**, 144-159 (1956).
92. Fatt, I.: "The Network Model of Porous Media II. Dynamic Properties of a Single Size Tube Network," *Trans. AIME* **207**, 160-163 (1956).
93. Fatt, I.: "The Network Model of Porous Media III. Dynamic Properties of Networks with Tube Radius Distribution," *Trans. AIME* **207**, 164-181 (1956).
94. Salathiel, R.A.: "Oil Recovery by Surface Film Drainage in Mixed-Wettability Rocks," *JPT* **25**, 1216 (1973).
95. Lenormand, R., Zarcone, C. and Sarr, A.: "Mechanisms of the Displacement of One Fluid by Another in a Network of Capillary Ducts," *J. Fluid. Mech.* **135**, 337-353 (1983).
96. Lenormand, R. and Zarcone, C.: "Role of Roughness and Edges During Imbibition in Square Capillaries," SPE 13264, 59th Annual Tech. Conf. and Exh., Houston, Texas, 16-19 Sep. (1984).
97. Li, Y. and Wardlaw, N.C.: "The Influence of Wettability and Critical Pore-Throat Size Ratio on Snap-Off," *J. Coll. Interface Sci.* **109**(2), 461-472 (1986).
98. Chatzis, I., Kantzas, A. and Dullien, F.A.L.: "On the Investigation of Gravity-Assisted Inert Gas Injection Using Micromodels, Long Berea Sandstone Cores, and Computer-Assisted Tomography," SPE 18284, 63rd Annual Tech. Conf. and Exh., Houston, TX, 2-5 Oct. (1988).

99. Øren, P.E., Billiotte, J. and Pinczewski, W.V.: "Mobilization of Waterflood Residual Oil by Gas Injection for Water-Wet Conditions," *SPEFE* **7**, 70-78 (March 1992).

100. Soll, W.E., Celia, M.A. and Wilson, J.L.: "Micromodel Studies of Three-Fluid Porous Media Systems: Pore-Scale Processes Relating to Capillary Pressure-Saturation Relationships," *Water Resources Research* **29**(9), 2963-2974 (1993).

101. Øren, P.E. and Pinczewski, W.V.: "Effect of Wettability and Spreading on Recovery of Waterflood Residual Oil by Immiscible Gasflooding," *SPEFE* **9**, 149-156 (June 1994).

102. Øren, P.E. and Pinczewski, W.V.: "Fluid Distribution and Pore-Scale Displacement Mechanisms in Drainage Dominated Three-Phase Flow," *Trans. in Por. Media* **20**, 105-133 (1995).

103. Dong, M. Dullien, F.A.L. and Chatzis, I.: "Imbibition of Oil in Film Form Over Water Present in Edges of Capillaries with an Angular Cross-Section," *J. Coll. Interface Sci.* **172**, 278-288 (1995).

104. Keller, A.A., Blunt, M. J. and Roberts, P.V.: "Micromodel Observation of the Role of Oil Layers in Three-Phase Flow," *Trans. in Por. Media* **26**(3), 277-297 (1997).

105. Heiba, A.A., Davis, H.T. and Scriven, L.E.: "Effect of Wettability on Two-Phase Relative Permeabilities and Capillary Pressures," SPE 12172, 58th Annual Tech. Conf. and Exh., San Francisco, CA, 5-8 Oct. (1983).

106. Mohanty, K.K. and Salter, S.J.: "Multiphase Flow in Porous Media: III. Oil Mobilization, Transverse Dispersion, and Wettability," SPE 12127, 58th Annual Tech. Conf. and Exh., San Francisco, CA, 5-8 Oct. (1983).

107. Soll, W.E. and Celia, M.A.: "A Modified Percolation Approach to Simulating Three-Fluid Capillary Pressure-Saturation Relationships," *Advances in Water Resources* **16** (2), 107-126 (1993).

108. Øren, P.E., Billiotte, J. and Pinczewski, W.V.: "Pore-Scale Network Modeling of Waterflood Residual Oil Recovery by Immiscible Gas Flooding," SPE 27814, SPE/DOE 9th Symposium on Improved Oil Recovery, Tulsa, Oklahoma, 17-20 April (1994).
109. Fenwick, D.H. and Blunt, M.J.: "Three-Dimensional Modeling of Three-Phase Imbibition and Drainage," *Advances in Water Resources* **25**(2), 121-143 (1998).
110. Pereira, G.G., Pinczewski, W.V., Chan, D.Y.C., Paterson, L. and Øren, P.E.: "Pore-Scale Network Model for Drainage-Dominated Three-Phase Flow in Porous Media," *Trans. in Por. Media* **24**, 167-201 (1996).
111. Mani, V. and Mohanty, K.K.: "Effect of the Spreading Coefficient on Three-Phase Flow in Porous Media," *J. Coll. Interface Sci.* **187**, 45 (1997).
112. Heiba, A.A., Davis, H.T. and Scriven, L.E.: "Statistical Network Theory of Three-Phase Relative Permeabilities," SPE 12690, SPE/DOE 4th Symposium on Enhanced Oil Recovery, Tulsa, Oklahoma, 15-18 April (1984).
113. Hughes, R.G. and Blunt, M.J.: "pore-Scale Modeling of Multiphase Flow in Fractures and Matrix/Fracture Transfer," SPE 56411, SPE Annual Tech. Conf. and Exh., Houston, TX, 3-6 Oct., (1999).
114. Poulsen, S., McDougall, S.R., Sorbie, K.S., and Skauge, A.: "Network Modeling of Internal and External Gas Drive," SCA 2001-17, *Proc.* Intl. Symp. of the Society of Core Analysts, Edinburgh, Scotland, 17-19 Sep. (2001).
115. Zhou, D., Blunt, M. and Orr Jr., F.M.: "Hydrocarbon Drainage along Corners of Noncircular Capillaries," *J. Coll. and Interface Sci.* **187**, 11-21 (1997).
116. Lindquist, W.B.: "3DMA: A Package for Geometric Analysis of 2- and 3D Biphase Images," http://www.ams.sunysb.edu/

~lindquis/3dma/3dma.html for literature and ftp://ams.sunysb.edu/pub/lindquis/ for public domain software.

117. Wilkinson, D. and Willemsen, J.F.: "Invasion Percolation: A New Form of Percolation Theory," *J. Physics A* **16**, 3365 (1983).
118. Mason, G. and Morrow, N.R.: "Capillary Behavior of a Perfectly Wetting Liquid in Irregular Triangular Tubes," *J. Coll. and Interface Sci.* **141**, 262 (1991).
119. Mayer, R.P. and Stowe, R.A.: "Mercury Porosimetry-Breakthrough Pressure for Penetration Between Packed Spheres," *J. Coll. and Interface Sci.* **20**, 893 (1965).
120. Princen, H.M.: "Capillary Phenomena in Assemblies of Parallel Cylinders. I. Capillary Rise Between Two Cylinders," *J. Coll. and Interface Sci.* **30**, 60 (1969).
121. Princen, H.M.: "Capillary Phenomena in Assemblies of Parallel Cylinders. II. Capillary Rise in Systems With More Than Two Cylinders," *J. Coll. and Interface Sci.* **30**, 359 (1969).
122. Princen, H.M.: "Capillary Phenomena in Assemblies of Parallel Cylinders. III. Liquid Columns Between Horizontal Parallel Cylinders," *J. Coll. and Interface Sci.* **34**, 171 (1970).
123. Batrouni, G.G. and Hansen, A.: "Fourier Acceleration of Iterative Processes in Disordered Systems," *J. Statistical Physics* **52** (3/4), 747 (1988).
124. Sulak, R.M.: "Ekofisk Field: The First 20 Years," *JPT* (Oct. 1991), 1265.
125. Ballin, P.R., Clifford, P.J. and Christie, M.A.: "Cupiagua: A Complex Full-Field Fractured Reservoir Study Using Compositional Upscaling," SPE 66376, SPE Reservoir Simulation Symp., Houston, TX, 11-14 Feb. (2001).
126. Jacks, H.H., Smith, O.J.E., and Mattax, C.C.: "The modeling of a Three-Dimensional Reservoir with a Two-Dimensional Reservoir

Simulator-The Use of Dynamic Pseudo Functions," *SPEJ* (June 1973), 175.

127. Darman, N.H., Durlofsky, L.J., Sorbie, K.S. and Pickup, G.E.: "Upscaling Immiscible Gas Displacements: Quantitative Use of Fine Grid Flow Data in Grid Coarsening Schemes," *SPEJ* (March 2001), 47.
128. Emanuel, A.S., and Cook, G.W.: "Pseudorelative Permeability for Well Modeling," *SPEJ* (Feb. 1974), 7.
129. Warren, J.E. and Root, P.J.: "The Behavior of Naturally Fractured Reservoir," *SPEJ* (Sep. 1963), 245.
130. Lough, M.F., Lee, S.H. and Kamath, J.: "A New Method to Calculate the Effective Permeability of Grid Blocks Used in the Simulation of Naturally Fractured Reservoirs," SPE 36730, 1996 Annual Tech. Conf. and Exh., Colorado, 6-9 Oct. (1996).
131. Bourbiaux, B.J., Cacas, M.C., Sarda, S. and Sabathier, J.C.: "A Fast and Efficient Methodology to Convert Fractured Reservoir Images into a Dual-Porosity Model," SPE 38907, 1997 Annual Tech. Conf. and Exh., San Antonio, TX, 5-8 Oct. (1997).
132. Agarwal, B., Allen, L.R. and Farrel, H.E.: "Ekofisk Field Reservoir Characterization: Mapping Permeability Through Facies and Fracture Intensity," *SPEFE* (Dec. 1997), 227.
133. Thomas, L.K., Dixon, T.N., Pierson, R.G. and Hermansen, H.: "Ekofisk Nitrogen Injection," *SPEFE* (June 1991), 151.
134. Kazemi, H., Merrill Jr., L.S., Porterfield, K.L. and Zeman, P.R.: "Numerical Simulation of Water-Oil Flow in Naturally Fractured Reservoirs," *SPEJ* (Dec. 1976), 317.

Faculty of Applied Earth Sciences
Department of Petroleum Engineering and Applied Geophysics

Experimental Measurements of Petrophysical, Reservoir Engineering and Morphological Properties of Ekofisk Chalk

Laboratory Report

Talukdar, M.S., Tweheyo, M.T and Torsæter, O.

Trondheim, Norway
December 2001

NTNU
Norwegian University of
Science and Technology

URN:NBN:no-2347

Table of Contents

1. Introduction

Experimental measurements have been conducted on two sets of Ekofisk chalk samples to acquire comprehensive data set on petrophysical, reservoir engineering and morphological properties. Both sets comprise four samples each labeled as 2, 3, 4 and 6 for the first set and 32, 35, 36 and 38 for the second set. The selected samples constitute a wide range of porosities varying from 0.21 to 0.4. The measurements include porosity, absolute and relative permeabilities, capillary pressure, wettability index, formation factor, resistivity index, mercury porosimetry and backscatter scanning electron microscope images. The usages of the experimental data are as follows: 1) absolute and relative permeabilities, capillary pressure, formation factor and resistivity index are to be compared with respective values computed from pore-scale network modeling; 2) porosity and correlation statistics obtained from backscatter scanning electron microscope images are the necessary input parameters to the algorithm for stochastic reconstruction of numerical chalk samples; and 3) capillary pressures from mercury porosimetry measurements are to be compared with those from network simulation. Also, the pore and throat size distributions extracted from mercury porosimetry data are useful to evaluate the quality of stochastic reconstructions. This report describes the experimental procedures and analysis of the data.

2. Preparation of samples and brine

The core samples were cleaned in a Soxhlet extraction apparatus alternately by Methanol and Toluene to remove the interstitial (or filtrate) water and oil, respectively. They were cleaned first by Methanol for 24 hours and then by Toluene for another 24 hours. The cycle was repeated three times for proper cleaning. The cleaned cores were dried in a vacuum oven at 60^{o} C until consistent dry weights were observed for all samples. The dimensions, dry weight and grain density of the samples are summarized in Table 1. The grain volume was measured using a helium porosimeter.

Table 1—Dimensions, dry weight and grain density of the core samples.

Core	L (cm)	D (cm)	V_b (cm^3)	A (cm^2)	W_{dry} (g)	V_g (cm^3)	ρ_g (g/cm^3)
2	4.27	3.74	46.886	10.980	99.84	37.0	2.70
3	4.22	3.75	46.585	11.039	87.72	32.6	2.69
4	4.15	3.74	45.568	10.980	96.91	36.0	2.69
6	3.79	3.71	40.950	10.805	74.80	27.5	2.72
32	4.56	3.75	50.364	11.045	87.41	32.20	2.71
35	4.56	3.77	50.902	11.163	83.99	31.20	2.69
36	2.63	3.77	29.358	11.163	47.95	17.75	2.70
38	4.27	3.77	47.665	11.163	82.12	30.20	2.72

URN:NBN:no-2347

The formation brine compatible to the reservoir was prepared by mixing 35.736g NaCl, 0.298g KCl, 32.281g $CaCl_2.2H_2O$, 4.350g $MgCl_2.6H_2O$ and 927.335g H_2O to make 1000g of brine. The solution was saturated with calcite in order to avoid chalk dissolution. The density of the brine was found to be 1.0472 g/cm^3.

3. Measurement of porosity

Porosities of the dried core samples were measured using a standard helium porosimeter. The helium porosimeter uses the principle of gas expansion as described by Boyle's law. A known volume (reference cell volume) of helium gas, at a predetermined pressure, is isothermally expanded into a sample chamber. After expansion, the resultant equilibrium pressure is measured. This pressure depends on the volume of the sample chamber minus the rock grain volume. The effective porosity then can be calculated from the following equation:

$$\varphi_e(fraction) = \frac{(V_b - V_g)}{V_b} \quad [1]$$

where, V_b is the bulk volume of the core and V_g is the volume of grain and non-connected pores. Again, $V_g=V_1-V_2$, where V_1 is the volume of the matrix cup without core and V_2 is the volume of the matrix cup with core.

The liquid (brine) porosity was calculated using a saturation method. In this method, the dry core is saturated with a fluid of known density and the weight increase is recorded. The effective porosity is determined from,

$$\varphi_e(fraction) = \frac{V_p}{V_b} \quad [2]$$

where, V_p is the pore volume determined from, $V_p=W_f/\rho_f$. W_f is the weight of the fluid determined from, $W_f=W_{sat}-W_{dry}$. W_{sat} and W_{dry} are the saturated and dry weights of the sample, respectively. The effective porosity values are presented in Table 2.

Table 2—Effective porosities of the core samples.

Core	ϕ_{He} (fraction)	ϕ_{brine} (fraction)
2	0.21	0.19
3	0.30	0.26
4	0.21	0.19
6	0.33	0.31
32	0.36	0.34
35	0.39	0.37
36	0.40	0.38
38	0.37	0.35

4. Measurement of absolute permeability

Air and brine permeabilities were measured using a constant head permeameter with the Hassler cell. The Darcy's equation [1] is normally used to estimate permeability of a porous medium. The equation is,

$$\frac{q}{A} = v = \frac{k}{\mu}\frac{\Delta P}{L} \qquad [3]$$

where, q is the fluid flow rate, A is the cross-sectional area, v is the flow velocity, k is the permeability, μ is the fluid viscosity, ΔP is the differential pressure and L is the length of the core sample. The equation is valid for *laminar flow* in porous media. To measure brine permeability, the sample is first saturated with brine and then displaced by the same brine at constant ΔP. Three different ΔP are applied and at each ΔP the volume of brine production V_w in 6 hours (ΔT) is recorded. The slope m of the line ΔP *vs.* V_w can be defined by Darcy's equation as follows,

$$m = \frac{\mu_w L}{k A \Delta T} \qquad [4]$$

The absolute brine permeability, k_{brine} and the absolute brine injectivity, I_{brine} are calculated using the following equations:

$$k_{brine} = \frac{\mu_w L V_w}{A \Delta T \Delta P} = \frac{\mu_w L}{m A \Delta T} \qquad [5]$$

$$I_{brine} = \frac{V_w}{A \Delta T \Delta P} = \frac{1}{m A \Delta T} \qquad [6]$$

The viscosity of brine was measured to be 1.05 cp. The calculated k_{brine} and I_{brine} values are shown in Table 3.

To measure air permeability, the dry core sample is put in the Hassler cell and then air is injected at constant ΔP. Several ΔP are applied and at each ΔP the flow rate q is recorded. For gas flows, the laminar flow assumption is not always valid. For ideal gas the following form of the Darcy's equation is used:

$$q_{atm} = \frac{A k_a}{\mu L}\frac{\left(P_1^2 - P_2^2\right)}{2 P_{atm}} \qquad [7]$$

where, P_1 and P_2 are the pressures at the inlet and outlet sides of the Hassler cell. The measured (apparent) air permeability k_a is influenced by the mean

pressure P_{av} of the sample. The mean pressure is regulated through changing P_1 and P_2. The gas flow is measured at atmospheric conditions, thus $P_{atm} = 1$ atm. Air viscosity at room conditions was found to be 0.0179 cp. The plot of k_a *vs.* $1/P_{av}$ is a straight line. The intercept of this line when extrapolated to infinite average pressure ($1/P_{av} = 0$) represents the absolute or the equivalent liquid permeability k_L of the core sample. Klinkenberg [2] reported variations in gas permeabilities compared to non-reactive liquid permeabilities. These variations were considered to be due to slippage, a phenomenon well-known with respect to gas flow in capillary tubes. Klinkenberg related k_a to k_L as follows:

$$k_a = k_L\left(1 + \frac{b}{P_{av}}\right) \qquad [8]$$

where, b is a constant known as Klinkenberg constant depends on the mean free path of the molecules of the flowing gas at P_{av}. The values of k_L and b for the core samples are also shown in Table 3.

Table 3—Air and brine permeabilities of the core samples.

Core	k_{brine} (mD)	I_{brine} (cm/s.bar)	k_L (mD)	b (abs atm)
2	0.09	$2.0\text{x}10^{-05}$	0.20	1.729
3	0.64	$1.4\text{x}10^{-04}$	1.35	1.567
4	0.12	$2.7\text{x}10^{-05}$	0.36	1.668
6	1.94	$4.9\text{x}10^{-04}$	2.60	1.678
32	0.35	$7.3\text{x}10^{-05}$	1.64	2.573
35	-	-	1.48	3.865
36	1.88	$1.1\text{x}10^{-04}$	3.05	1.848
38	0.40	$8.7\text{x}10^{-05}$	0.84	3.766

Note: Core 35 broke down.

5. Measurement of relative permeability

The absolute permeabilities (air or brine) described previously are related to the core sample 100% saturation with a single fluid. Relative permeability is related to the core sample saturated with two or more fluids, such as water, oil and gas. If more than one fluid is present in the core, the movement of one fluid is influenced by other fluid(s) and therefore, it is important to measure relative permeability of each of the fluids present in the core. A constant head permeameter with the Hassler cell was used for the flooding processes. The relative permeabilities of oil and brine for both drainage and imbibition processes were measured using unsteady-state method as it is relatively simple and fast. The unsteady state method is also called Welge's [3] method because

the calculation is based on the theory of the improved Buckley and Leverett's [4] mechanism of fluid displacement in porous media.

To measure two-phase (oil-water) relative permeabilities, the core is first saturated with 100% water and then water is displaced by oil under a constant differential pressure until no more water production is observed, defining the initial water saturation S_{wi}. The process is then reversed and oil is displaced by brine until no more oil is produced, defining the residual oil saturation S_{or}. With the recording of pressure drop, and produced volumes of oil and water, it is possible to calculate relative permeabilities using Welge's method briefly described below (oil displacing water):

Welge's extension of the Buckley-Leverett concept states that

$$S_{o,av} - S_{o2} = f_{w2} Q_o \qquad [9]$$

where, subscript *2* denotes the outlet end of the core and $S_{o,av}$ is the average oil saturation in the core, Q_o is the cumulative oil injected (in pore volumes), and f_{w2} is the fraction of water in the outlet stream. Again,

$$S_{o,av} = \frac{N_p}{V_p} \qquad [10]$$

where, N_p is the cumulative water produced and V_p is the pore volume. Since Q_o and $S_{o,av}$ can be measured experimentally, f_{w2} can be determined from the plot of Q_o *vs.* $S_{o,av}$ as follows:

$$f_{w2} = \frac{dS_{o,av}}{dQ_o} \qquad [11]$$

Hence, oil saturation at the outlet (S_{o2}) can be calculated using Eq. [9]. By definition f_{w2} and f_{o2} may be expressed as:

$$f_{w2} = \frac{q_w}{q_w + q_o} \qquad [12]$$

$$f_{o2} = 1 - f_{w2} \qquad [13]$$

where, q_w and q_o are the instantaneous water and oil flow rates, respectively. Combining Eq. [12] with Darcy's law, it can be shown that:

$$f_{w2} = \frac{1}{1 + \frac{k_{ro}}{k_{rw}} \frac{\mu_w}{\mu_o}} \quad [14]$$

Since the viscosities are known, the relative permeability ratio k_{ro}/k_{rw} can be determined from Eq. [14]. Relative permeability of water at $S_{w2}=1-S_{o2}$ can be determined from the following equation:

$$k_{rw}(S_{w2}) = f_{w2} \frac{d(\frac{1}{Q_o})}{d(\frac{1}{Q_o I_r})} \quad [15]$$

where, I_r is the relative injectivity defined by $I_r=\Delta V_t/\Delta V_w$ in which ΔV_t and ΔV_w are the produced volumes of water and oil (total), and water, respectively in each time step. Relative permeability of oil at S_{o2} can be determined from the ratio, k_{ro}/k_{rw}.

The drainage and imbibition relative permeabilities of oil and water for seven samples are shown in Fig. 1 through 7. Sample 35 broke down before this measurement and hence is not shown. The data for the plots are presented in Table A.1 through A.4 while the oil and water recoveries are shown in Table A.5 through A.11 of Appendix A.

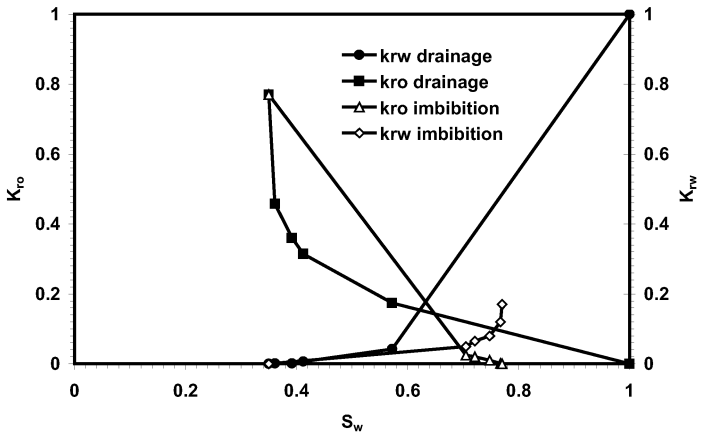

Figure 1—Oil and water relative permeabilities of core 2.

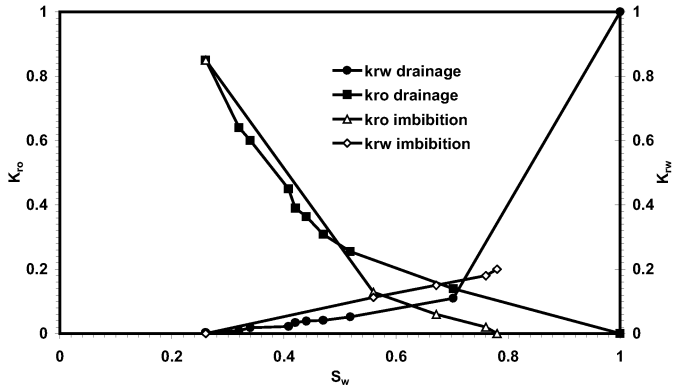

Figure 2—Oil and water relative permeabilities of core 3.

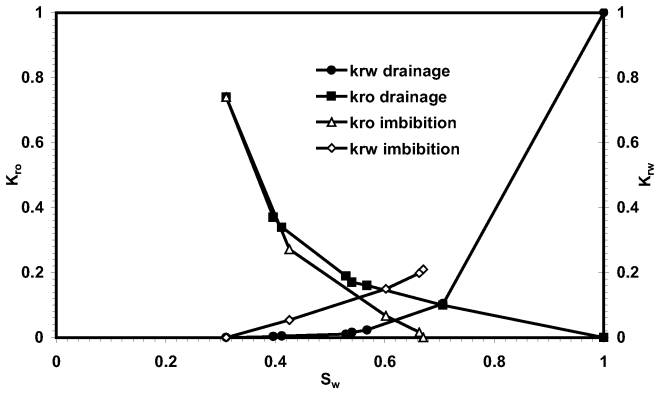

Figure 3—Oil and water relative permeabilities of core 4.

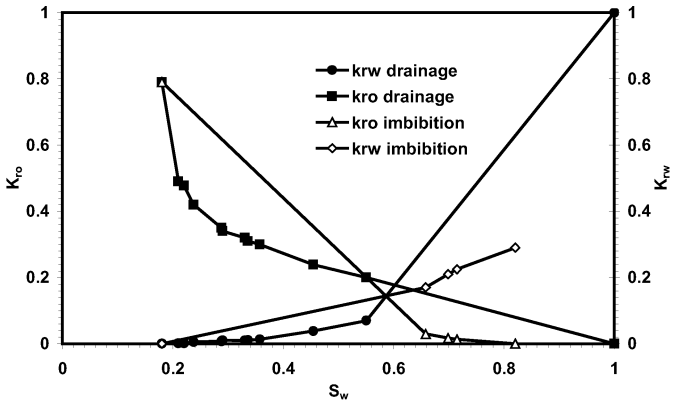

Figure 4—Oil and water relative permeabilities of core 6.

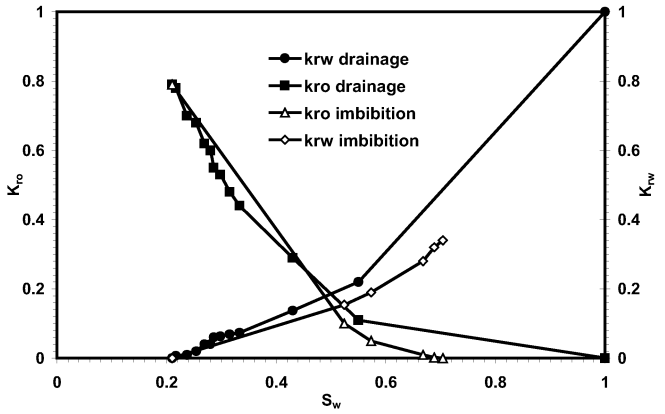

Figure 5—Oil and water relative permeabilities of core 32.

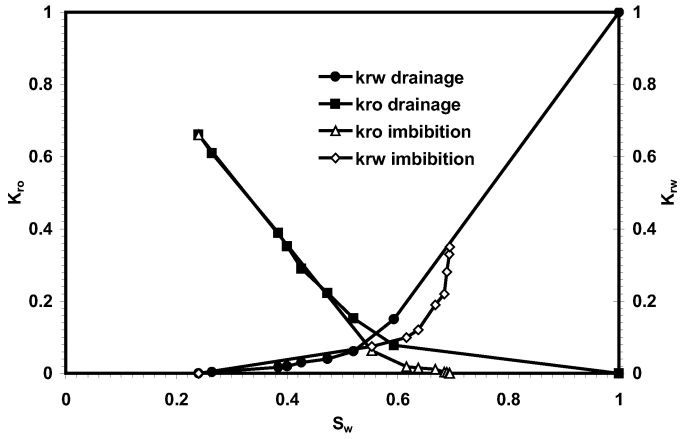

Figure 6—Oil and water relative permeabilities of core 36.

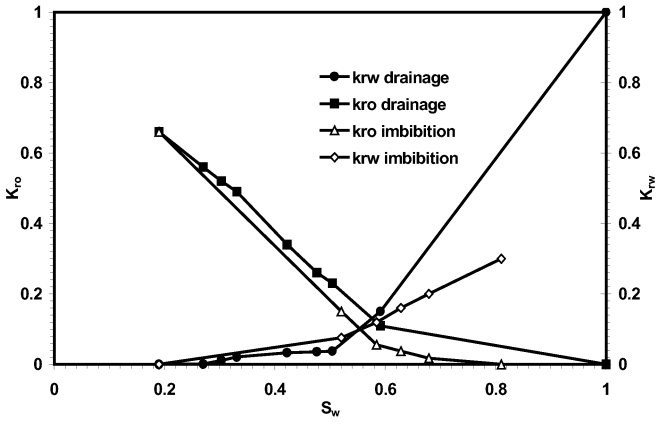

Figure 7—Oil and water relative permeabilities of core 38.

The key parameters for drainage and imbibition relative permeability curves are summarized in Table 4.

Table 4—Key parameters for drainage and imbibition relative permeability curves.

Core	S_{wi}	S_w at $k_{ro}=k_{rw}$		k_{roe} (k_{ro} at S_{wi})	S_{or}	k_{rwe} (k_{rw} at S_{or})
		Drainage	Imbibition			
2	0.35	0.63	0.69	0.77	0.23	0.17
3	0.26	0.73	0.57	0.85	0.22	0.20
4	0.31	0.70	0.55	0.74	0.33	0.21
6	0.18	0.63	0.55	0.79	0.18	0.29
32	0.21	0.52	0.50	0.79	0.30	0.34
36	0.24	0.57	0.55	0.66	0.31	0.35
38	0.19	0.58	0.55	0.66	0.19	0.30

6. Measurement of capillary pressure

When two immiscible fluids are in contact in the interstices of a porous medium, a discontinuity in pressure exists across the interface separating them. The difference in pressure is called the capillary pressure P_c which is the pressure in the non-wetting phase minus the pressure in the wetting phase,

$$P_c = P_{nw} - P_w \qquad [16]$$

For an oil-water system, the capillary pressure becomes,

$$\frac{dP_c}{dz} = (\rho_w - \rho_o)g \qquad [17]$$

In this study the centrifuge method was used to obtain the capillary pressure curves. By this method a complete capillary pressure curve may be obtained in a few hours and several samples can be run simultaneously. The method is claimed to be accurate, to reach equilibrium rapidly, give good reproducibility, and is able to produce high-pressure differences between phases. The Beckman Model LH-M Ultracentrifuge was used in this study. A schematic diagram of a core in a centrifuge is shown in Fig. 8.

URN:NBN:no-2347

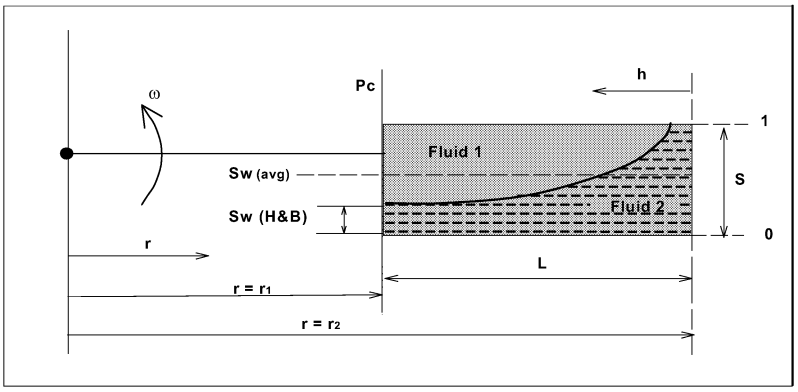

Figure 8—Schematic diagram of a core in a centrifuge with its boundary conditions.

The core samples were saturated with the wetting phase (brine) and rotated in the non-wetting phase (*n*-decane, ρ_o = 0.7274 g/cc, μ_o = 0.9 cp, σ_{ow} = 24.03 mN/m) at increasing speeds up to some maximum value. The average water saturations at each speed were calculated from observations of the brine produced (the liquid volume is read with a stroboscope while the centrifuge is in motion). The samples were then removed and submerged in brine for minimum 300 hours and spontaneously produced oil was recorded. This step was followed by centrifuging in brine where negative capillary pressure data were obtained. The samples were then submerged in oil for minimum 300 hours to determine spontaneous uptake of oil. Lastly, they were centrifuged in brine and secondary drainage data were obtained.

Hassler and Brunner [5] presented the basic concepts involved in the use of the centrifuge by relating the performance of a small core in a field of high acceleration. If the cylindrical core of length L is subjected to an acceleration $a_c = -\omega^2 r$ where ω is angular velocity of the centrifuge and r is the distance from the axis of rotation, then from Eq. [17] we have,

$$\frac{\partial P_c}{\partial r} = \Delta \rho a_c \qquad [18]$$

Given the boundary conditions shown in Fig. 8, the differential equation can be solved by simple integration,

$$P_c = \int_{r_2}^{r} \Delta \rho a_c dr \qquad [19]$$

$$P_c(r) = -\int_{r_2}^{r} \Delta\rho\omega^2 r dr \qquad [20]$$

The capillary pressure at the outer face of the core is zero, $P_c(r_2) = 0$, therefore,

$$P_c(r) = \tfrac{1}{2}\Delta\rho\omega^2\left(r_2^2 - r^2\right) \qquad [21]$$

and for a continuous phase, the capillary pressure at the inner face is,

$$P_{cL} = P_c(L) = \tfrac{1}{2}\Delta\rho\omega^2\left(r_2^2 - r_1^2\right) \qquad [22]$$

Now, the main purpose is to relate the capillary pressure and saturation S for a given core which gives the saturation in the core at equilibrium with the capillary pressure, $S=S(P_c)$. The saturation at a distance h above the outer face of the core can not be measured directly. However, the average saturation, which is the ratio of remaining liquid volume after production to pore volume can be written as,

$$\overline{S} = \frac{1}{r_2 - r_1}\int_{r_2}^{r_1} S(r)dr \qquad [23]$$

We will have a relationship of saturation as a function of capillary pressure, $S=S(P_c)$, therefore, Eq. [23] can be expressed as follows by changing integration variable,

$$P_c(r_2) = 0 \text{ and } P_c(r_1) = P_{cL}$$

$$\overline{S} = \frac{1}{r_2 - r_1}\int_{P_{cL}}^{0} \frac{S(P_c)dP_c}{-\Delta\rho\omega^2 r} \qquad [24]$$

An expression for r is obtained from Eq. [21],

$$r = r_2\sqrt{1 - \frac{P_c}{\tfrac{1}{2}\Delta\rho\omega^2 r_2^2}} \qquad [25]$$

and we obtain,

$$\overline{S} = \frac{1}{(r_2 - r_1)\Delta\rho\omega^2 r_2} \int_0^{P_{cL}} \frac{S(P_c)dP_c}{\sqrt{1 - \frac{P_c}{\frac{1}{2}\Delta\rho\omega^2 r_2^2}}} \qquad [26]$$

and with mathematical manipulation it becomes,

$$\overline{S}P_{cL} = \cos^2(\alpha/2) \int_0^{P_{cL}} \frac{S(p_c)dP_c}{\sqrt{1 - \frac{P_c}{P_{cL}}\sin^2\alpha}} \qquad [27]$$

where, $\cos\alpha = \frac{r_1}{r_2}$, $\cos^2(\alpha/2) = \frac{1}{2}(1 + \cos\alpha) = \frac{r_1 + r_2}{2r_2}$ and $\sin^2\alpha = 1 - \cos^2\alpha = 1 - \frac{r_1^2}{r_2^2}$

Eq. [27] can not be solved easily to obtain unknown function *S*. For small values of α (small core sample), the acceleration gradient along the core can be neglected. Assuming $r_1/r_2 \approx 1$, we get $\cos^2(\alpha/2)=1$ and $\sin^2(\alpha)=0$. Eq. [27] reduces to,

$$\overline{S}P_{cL} = \int_0^{P_{cL}} S(P_c)dP_c \qquad [28]$$

or in differentiation form,

$$S_L = \frac{d}{dP_{cL}}\left(\overline{S}P_{cL}\right) \qquad [29]$$

The value of saturation that goes with each value at P_{cL}, which now represents the capillary pressure, was obtained from a plot of $\overline{S}P_{cL}$ versus P_{cL} by graphical differentiation. Spontaneous imbibition is obtained in one step by decreasing the capillary pressure from the maximum positive value to zero immediately after primary drainage. The spontaneous imbibition curve was modelled from initial water saturation (S_{wi}) and water saturation after spontaneous imbibition (S_{wsp}) using Eq. 30 [6].

$$P_{csp}(S_w) = P_{ce}\left[\frac{S_w - S_{wi}}{1 - S_{wsp} - S_{wi}}\right]^{-\frac{1}{\lambda}} - P_{ce} \qquad [30]$$

Results for capillary pressure/saturation relationships from centrifuge experiments are shown in Fig. 9 through 15. The data are presented in Appendix A [Table A.12 through A.18].

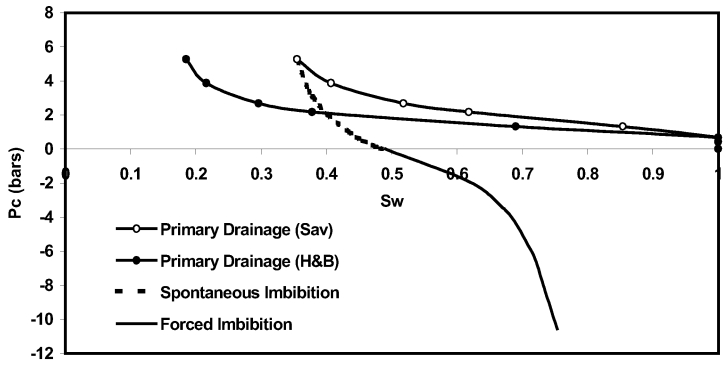

Figure 9—Water-oil capillary pressure (core 2).

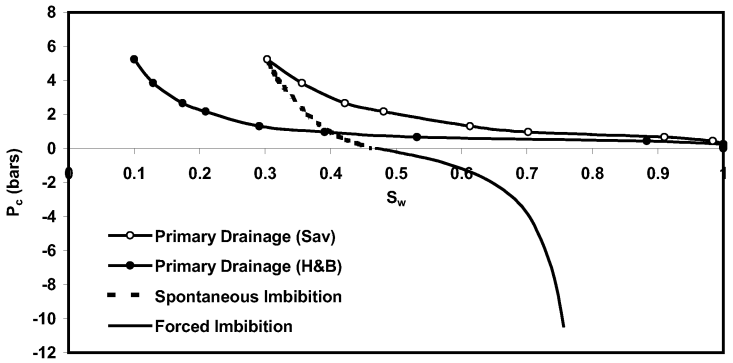

Figure 10—Water-oil capillary pressure (core 3).

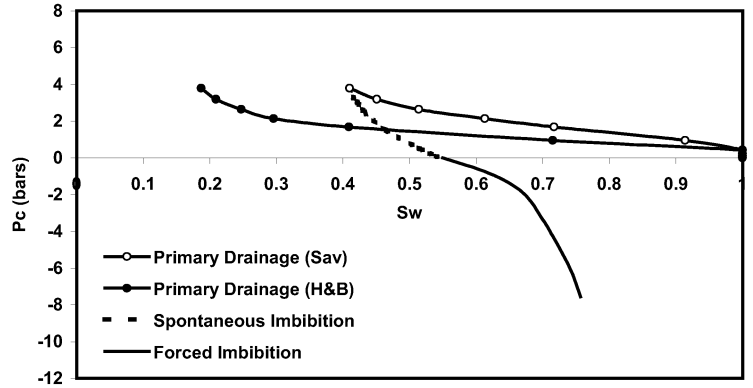

Figure 11—Water-oil capillary pressure (core 4).

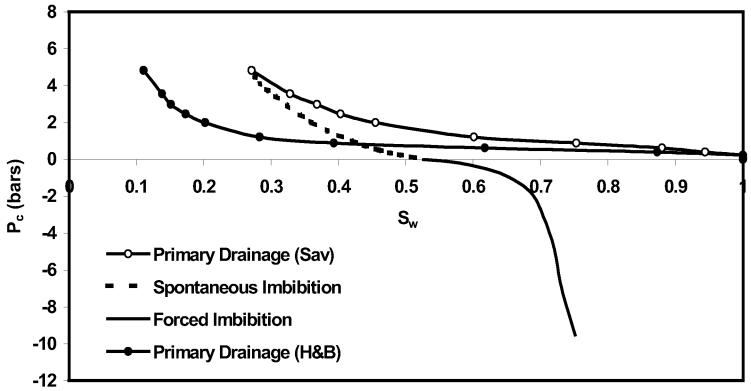

Figure 12—Water-oil capillary pressure (core 6).

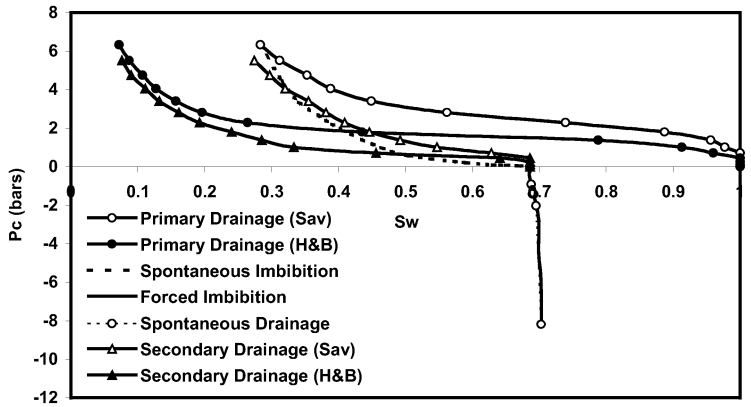

Figure 13—Water-oil capillary pressure (core 32).

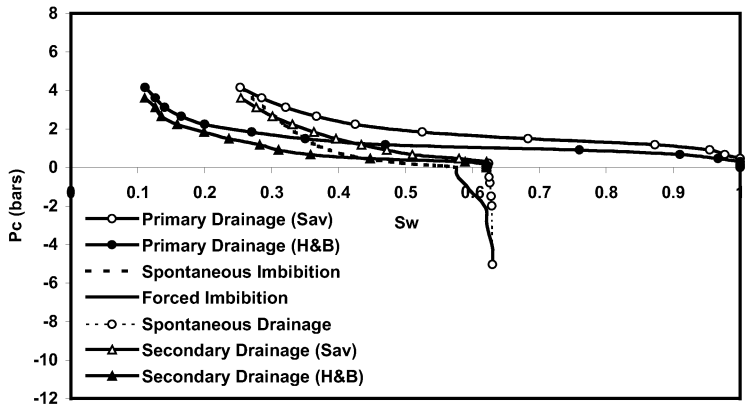

Figure 14—Water-oil capillary pressure (core 36).

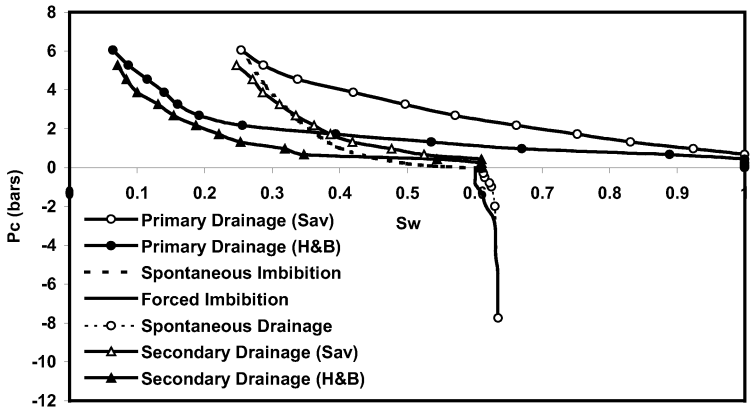

Figure 15—Water-oil capillary pressure (core 38).

The key parameters from capillary pressure measurements are summarized in Table 5.

Table 5—Summary of key parameters from capillary pressure/ saturation data.

Core	S_{wi} (avg)	S_{wi} (H&B)	Entry pressure P_{ce} (bar)	P_c at S_{wi} (bar)	S_w after spontaneous imbibition, S_{wsp}	S_{or}	P_c at S_{or} (bar)
2	0.36	0.19	0.67	5.27	0.49	0.25	-10.54
3	0.30	0.10	0.24	5.23	0.47	0.24	-10.44
4	0.41	0.19	0.42	3.79	0.55	0.23	-10.29
6	0.27	0.11	0.22	4.83	0.53	0.25	-9.51
32	0.283	0.072	1.013	6.331	0.685	0.30	-8.19
36	0.253	0.111	0.664	4.148	0.576	0.37	-5.04
38	0.254	0.064	0.968	6.049	0.601	0.37	-7.77

7. Measurement of wettability

Amott [7] proposed a wettability index which can be estimated from spontaneous and forced oil and water productions,

$$WI_{Amott} = r_w - r_o \qquad [31]$$

where, $r_w = \dfrac{V_{osp}}{V_{osp} + V_{od}}$ and $r_o = \dfrac{V_{wsp}}{V_{wsp} + V_{wd}}$ are kwon as the Amott indices for water and oil, respectively. V_{osp} and V_{wsp} are the spontaneous oil and water production, respectively, and V_{od} and V_{wd} are their displaced counterparts. The index may also be expressed in terms of saturations (see Fig. 17),

$$WI_{Amott} = \frac{S_{wsp} - S_{wi}}{1 - S_{wi} - S_{or}} - \frac{S_{osp} - S_{or}}{1 - S_{wi} - S_{or}} \quad [32]$$

where, S_{wsp} and S_{osp} are the water saturation after spontaneous water imbibition and oil saturation after spontaneous oil uptake, respectively, and S_{wi} and S_{or} are the initial water and residual oil saturations, respectively. For an extremely water-wet system r_w is positive and r_o is zero. Similarly, for an oil-wet system r_o is positive and r_w is zero. For a uniformly neutral wettability both r_w and r_o are zero. Cuiec [8] proposed the following wettability scale for water-wet, intermediate-wet and oil-wet cores:

WI	-1.0	-0.3	-0.1	+0.1	+0.3	+1.0
		Slightly oil-wet	Neutral	Slightly water-wet		
	Oil-wet	Intermediate			Water-wet	

Figure 16—Wettability scale adopted by Cuiec [8].

The shape of the capillary pressure curve is not taken into account in the Amott index. A more complete wettability number is represented by the USBM index, which is defined as the logarithm of the ratio of the areas A_w and A_o (see Fig. 17),

$$WI_{USBM} = log_{10} \frac{A_w}{A_o} \quad [33]$$

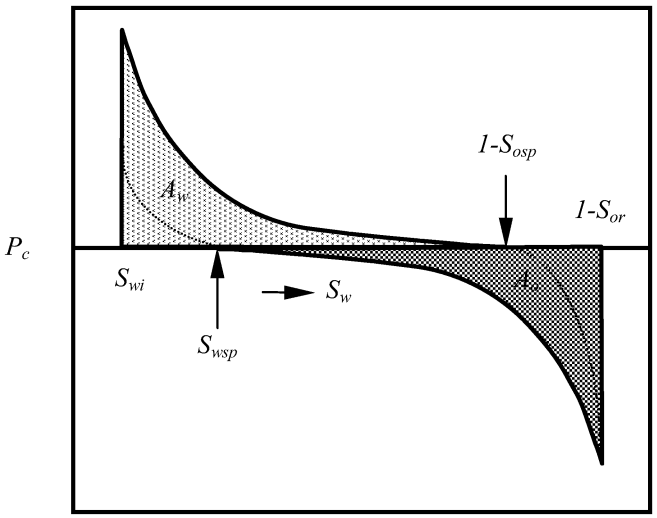

Figure 17—Imbibition and drainage capillary pressure curves, required to determine the Amott and USBM wettability indices.

For an extremely water-wet system USBM index is very large and positive, for an intermediate-wet it lies around zero and for an extremely oil-wet system it will be very large and negative.

Results from wettability tests are shown in Table 6. A FORTRAN program was used to calculate A_w and A_o. The Amott index reveals that sample 2, 3, 4 and 6 are moderately water-wet while both the Amott and the USBM indices indicate sample 32, 36 and 38 to be strongly water-wet.

Table 6—Evaluation of wettability by Amott and USBM methods.

Core number	**2**	**3**	**4**	**6**	**32**	**36**	**38**
V_{osp} (cc)	1.2	2.05	1.22	3.22	6.92	3.56	5.75
V_{od} (cc)	2.35	3.88	1.90	2.85	0.32	0.60	0.55
V_{wsp} (cc)	0	0	0	0	0.30	0.10	0.41
V_{wd} (cc)	-	-	-	-	7.10	4.05	6.00
Water index, r_w	0.34	0.35	0.39	0.53	0.96	0.86	0.91
Oil index, r_o	-	-	-	-	0.04	0.02	0.06
$WI_{Amott} = r_w - r_o$	0.34	0.35	0.39	0.53	0.92	0.84	0.85
Area A_w (cm^2)	-	-	-	-	82.00	51.21	65.56
Area A_o (cm^2)	-	-	-	-	2.25	5.60	5.64
$WI_{USBM} = log_{10}(A_w/A_o)$	-	-	-	-	1.56	0.96	1.07

8. Measurement of resistivity

The porous rocks without conductive pore fluid are nonconductors. The electrical properties of a rock depend on the geometry of the void spaces and the fluid with which those void spaces are filled. Oil and gas are nonconductors while water is a conductor when it contains dissolved salts. Due to conductive nature of formation water, the electrical well-log technique is an important tool in the determination of water saturation and thereby a reliable resource for *in-situ* hydrocarbon evaluation. Resistivity is a parameter used to measure the conductivity of the rock partially or fully filled with conductive brine,

$$R = \frac{rA}{L} \qquad [34]$$

where, R is the resistivity [Ω.m], and r, A and L are the resistance [Ω], cross-sectional area [m^2] and length [m], respectively. The most fundamental concept considering electrical properties of rocks is the formation factor F, as defined by Archie [9],

$$F = \frac{R_o}{R_w} = \varphi^{-m} \quad [35]$$

where, R_o is the resistivity of the rock when saturated 100% with formation water, R_w is the resistivity of the formation water and m is called the cementation exponent. F shows a relationship between water saturated rock conductivity and bulk water conductivity. Obviously, the factor depends on the pore structure of the rock. The second fundamental notion of electrical properties of porous rocks containing both water and hydrocarbons is the resistivity index I_r,

$$I_r = \frac{R_t}{R_o} \quad [36]$$

where, R_t and R_o are the resistivity of the rock when partially and fully saturated with formation brine, respectively. This parameter can be readily correlated with *in-situ* water and hydrocarbon saturations via available saturation models. One of the widely used models is the so-called Archie's empirical equation [9],

$$I_r = S_w^{-n} \quad [37]$$

The exponent n is known as the Archie's saturation exponent. A log-log plot of I_r versus S_w is normally used to calculate n.

The resistivity of the core samples was measured at laboratory conditions by a two-electrode method using the ratio of voltage decrease between a reference resistor and a core sample in series. The experimental setup is shown in Fig. 18. The cleaned and dried core samples were fully saturated with formation brine and placed in the resistivity cell to measure R_o. The cores were then placed in a core holder and the brine was displaced by *n*-decane using a pump. Saturation changes were measured by weighing and double-checked by the amount of brine produced. At each reduction in saturation, the sample was transferred to the resistivity cell and the drainage resistivity indices were determined. Saturation and resistivity indices for the imbibition cycle were achieved similarly. In this case, the cores were saturated with *n*-decane at initial water saturation and the oil was displaced by brine in steps until S_{or} was reached.

The results from resistivity measurements are shown in Figs. 19 through 23. Core 3 and 35 broke down before resistivity measurements while core 36 was too short for the resistivity apparatus in the laboratory and hence are not shown. The data are presented in Appendix A [Table A.19 and A.20].

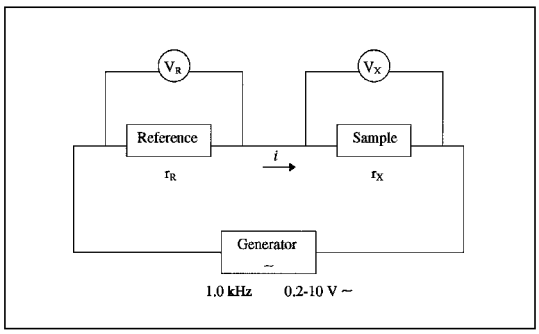

Figure 18—Experimental setup for resistivity measurement using two-electrode method.

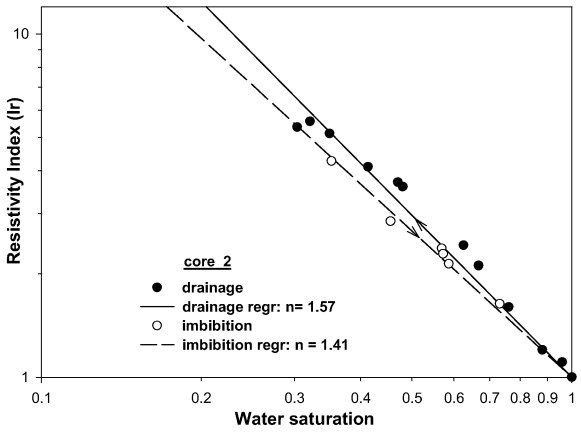

Figure 19— Log-log plot of I_r versus S_w (core 2).

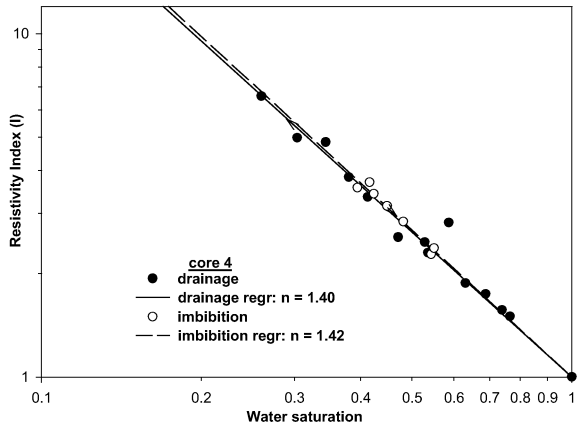

Figure 20— Log-log plot of I_r versus S_w (core 4).

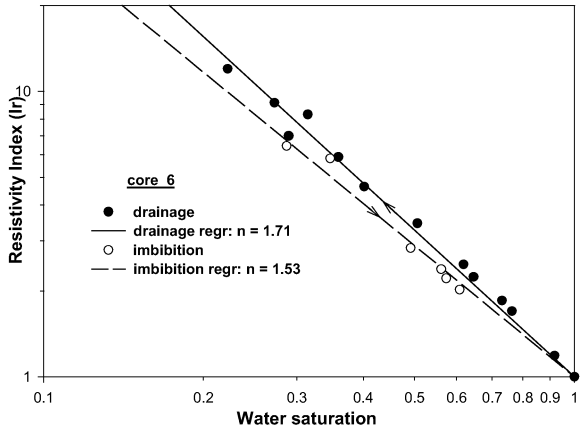

Figure 21— Log-log plot of I_r versus S_w (core 6).

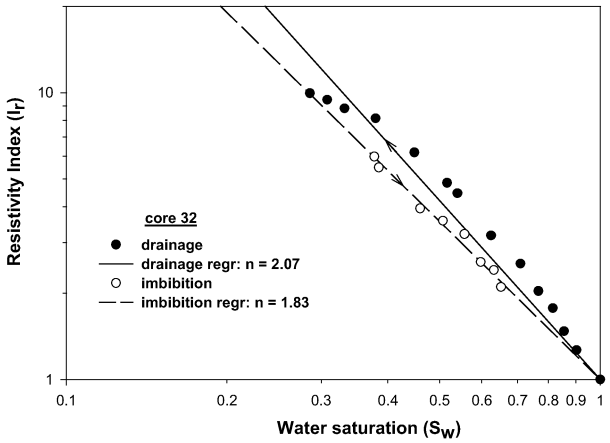

Figure 22— Log-log plot of I_r versus S_w (core 32).

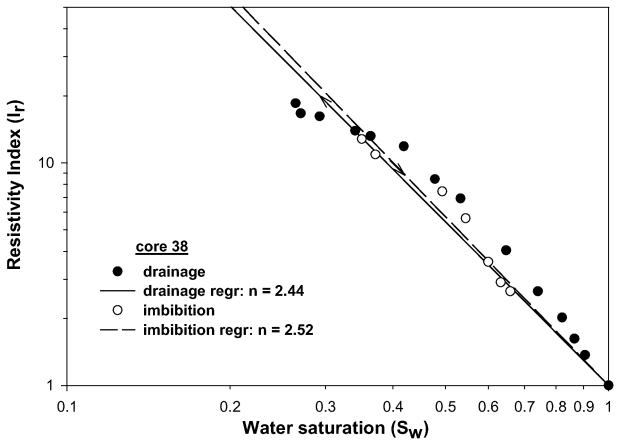

Figure 23— Log-log plot of I_r versus S_w (core 38).

The formation factor F is calculated when the core is saturated 100% with the formation brine. A value of F greater than one represents the factor by which the resistivity increases due to tortuosity of electric flow path in the rock sample. The calculated formation factors for samples 2, 3, 4, 6, 32, 36 and 38 are 15.53, 10.4, 14.58, 6.41, 3.34, 5.56 and 3.37, respectively. The values are consistent with those reported previously for a set of 12 chalk samples from Tor Formation of the North Sea [10].

9. Mercury porosimetry measurements

Mercury porosimetry measurements were conducted on sample 2, 3, 4, 32, 35, 36 and 38. Experiments were performed using Carlo Erba Macropores Unit 120, Carlo Erba Porosimeter 2000 and Micrometrics AccuPyc 1330 Helium-Pycnometer. Before the measurements, the chalk samples were kept in a hot cabinet for about one day at 60°C. It was then evacuated to a pressure below 10^{-4} mm Hg until a constant weight at room temperature was observed. Several rock parameters were measured together with mercury intrusion and extrusion porosimetry data. A list of the parameters and their values are shown in Table 7. The mercury-air capillary pressure curves for the samples are shown in Fig. 24 as a function of wetting-phase (air) saturation.

Table 7—Rock parameters from mercury porosimetry measurements.

	Sample						
Parameter	**2**	**3**	**4**	**32**	**35**	**36**	**38**
S_g (m^2/g)	1.52	1.76	1.50	1.17	1.17	1.11	1.38
ρ_b (g/cm^3)	2.141	1.914	2.201	1.794	1.664	1.728	1.752
ρ_s (g/cm^3)	2.702	2.696	2.698	2.691	2.685	2.690	2.688
V_p (cm^3/g)	0.097	0.151	0.083	0.185	0.229	0.205	0.197
V_b (cm^3/g)	0.467	0.522	0.454	0.557	0.601	0.579	0.571
$\phi_{Hg} = V_p/V_b$	0.208	0.288	0.183	0.332	0.381	0.354	0.346
$\varphi_{He} = 1 - \frac{\rho_b}{\rho_s}$	0.208	0.29	0.184	0.333	0.380	0.357	0.348
W_b (g)	1.89	1.27	1.78	1.62	1.23	1.15	1.35

The pore size distribution of a porous material is obtained from mercury intrusion data. The technique is based on the mercury property to behave as non-wetting liquid with solid material. Due to this property, mercury penetrates through the open pores of a solid sample under the effect of an increasing pressure. By measuring the volume of mercury penetrated in the sample pores and the equilibrium pressure at which intrusion occurs, experimental data are obtained to calculate pore volume distribution as a function of their radius. The determination of the pore size (radius) following the technique of mercury penetration is based on the behavior of non-wetting

liquids in capillaries. A liquid coming in contact with a solid porous material and behaving as a non-wetting agent (namely, if the contact angle of the liquid with that solid material exceeds 90^o) cannot be spontaneously absorbed by the pores of the solid itself because of the surface tension. However, this resistance to penetration can be won by applying an external pressure. Required pressure depends on the pore size. The relation between the pore size and the applied pressure, assuming the pore is cylindrical, is expressed by the well known Young-Laplace equation of capillarity,

$$P = \frac{2\,\sigma\,\cos\theta}{r} \qquad [38]$$

where, r is the pore radius, σ is the mercury surface tension, θ is the contact angle and P is the absolute applied pressure. For intrusion, if the applied pressure is larger than the capillary pressure for a throat, penetration of a throat by mercury occurs and the pore behind the throat will be filled with mercury. For extrusion, interface will vacate a pore if the applied pressure is less than the capillary pressure of the interface in the pore. Thus, whereas throats are the deciding barriers during intrusion, pores are the deciding barriers for extrusion [11].

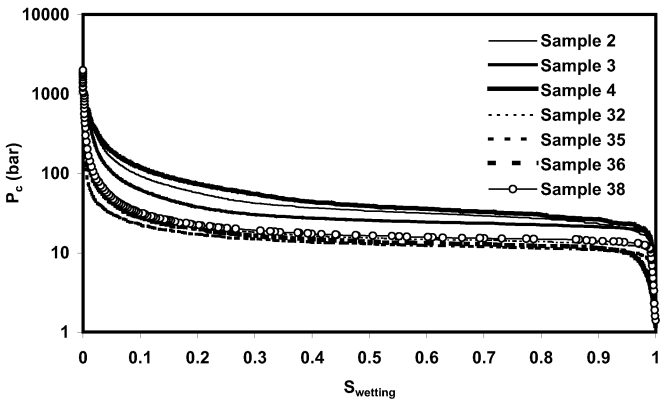

Figure 24—Mercury-air capillary pressure for the Ekofisk chalk samples.

Contact angle hysteresis is a well-known phenomenon in mercury porosimetry measurements. The hysteresis arises due to different contact angles that prevail during mercury intrusion and extrusion. Considering a surface tension of 480 mN/m and a receding contact angle (θ_r) of 140^o, the throat radius can be expressed as,

$$r_t = \frac{7.354}{P} \qquad [39]$$

where, r_t and P are expressed in micrometers and bars, respectively. Similarly, considering an advancing contact angle (θ_a) of 120° [12], the pore radius can be expressed as,

$$r_p = \frac{4.8}{P} \qquad [40]$$

The calculated throat and pore size distributions are shown in Figs. 25 and 26, respectively. The mean throat and pore radii of the samples obtained from the distributions are presented in Table 8. The mercury intrusion and extrusion volume data as a function of pressure are given in Appendix A (Table A.21 through A.24).

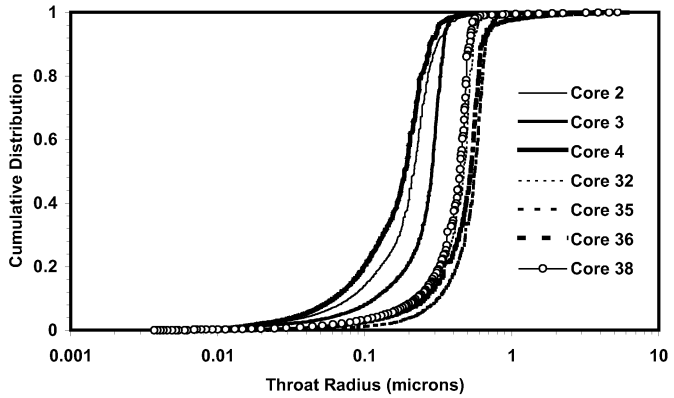

Figure 25—Throat size distribution of the chalk samples obtained from mercury porosimetry data.

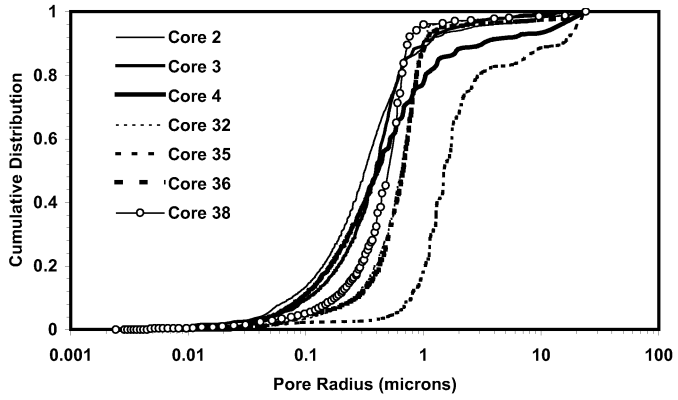

Figure 26—Pore size distribution of the chalk samples obtained from mercury porosimetry data.

Table 8—Mean throat- and pore-radii of the chalk samples obtained from mercury porosimetry data.

Parameter	Sample						
	2	3	4	32	35	36	38
Mean throat radius (μm)	0.230	0.271	0.191	0.447	0.544	0.522	0.421
Mean pore radius (μm)	0.955	0.727	1.969	0.873	4.338	1.286	0.906

10. Backscatter SEM images and morphological properties

The widely used stochastic reconstruction algorithms, e.g., truncation of Gaussian Random Fields (GRF), Simulated Annealing (SA), are constrained by one or more morphological descriptors readily obtained from 2D backscatter Scanning Electron Microscope (SEM) images. A set of five images was acquired at a pixel resolution of 0.136x0.136 μm^2 (512x512 pixels, 1500x magnification) from each of sample 2, 3, 4, 32, 35, 36 and 38. This pixel resolution was selected in order to capture the sub-micron size pores that are abundant in chalk. Image acquisition, processing and computation of the most commonly used morphological parameters are briefly described in this section.

For backscatter SEM imaging, thin sections are prepared by cutting approximately 15x15x1 mm^3 plates from the cleaned and dried core samples and polishing them to obtain flat surfaces. The thin sections are then impregnated with epoxy resin under vacuum. In backscatter SEM, a narrow beam of monochromatic electrons is focused on a tiny area (dwell point) of the polished surface. Elastic collisions take place between the incident electrons and the atoms of the specimen and the incident electrons scatter "backward" 180 degrees with no appreciable loss of energy. The backscattered electrons are then counted using a semiconductor device mounted on the bottom of the objective lens. This quantity is translated into gray intensity (0 to 255) and a pixel is displayed on a cathode ray tube (CRT) with the appropriate gray level. The beam is then moved to its next dwell point and the process is repeated for the required number of pixels. The intensity of the pixel varies directly with the atomic number of the specimen at the dwell point. Higher atomic number elements (more collisions) appear brighter than lower atomic number elements.

Thresholding was used to segment each image into objects of interest (void) and background (solid) on the base of gray level. The binarization sets all thresholded pixels (pore) to black and all background pixels (solid) to white. Here, thresholding was based on an analysis of the histogram of the gray values. The histograms for all images were found to be bimodal. A

threshold value was selected between the peaks, such that the porosity of the thresholded image was close to the measured porosity of the chalk sample. The image porosities of the chalk samples (average over 5 images for each sample) are compared with their experimental counterparts in Table 9. The absolute error is less than 1.2% in all cases.

Table 9—Experimental and image porosities of the chalk samples.

	Sample						
ϕ **from,**	**2**	**3**	**4**	**32**	**35**	**36**	**38**
Experiment	0.208	0.3	0.184	0.333	0.380	0.357	0.348
Image	0.207	0.3	0.183	0.335	0.381	0.354	0.352

The binarized images were used to compute several correlation functions to be used for stochastic reconstruction of numerical chalk samples. The computed correlation functions are void-phase autocorrelation function (two-point correlation function) and lineal path function, and void- and solid-phase chord distribution functions. The definition of the correlation functions and measurement techniques are briefly described below:

The binarized image is represented by a binary phase function $Z(\vec{r})$ [13] defined as,

$$Z(\vec{r}) = \begin{cases} 1 & \vec{r}\ points\ to\ pore\ space \\ 0 & otherwise \end{cases} \qquad [41]$$

For a statistically homogeneous medium, the porosity φ, and the autocorrelation function of the void phase $R_z(\vec{u})$, are defined as the first two statistical moments of the function $Z(\vec{r})$,

$$\varphi = \langle Z(\vec{r}) \rangle \qquad [42]$$

$$R_z(\vec{u}) = \frac{\langle [Z(\vec{r}) - \varphi] \cdot [Z(\vec{r} + \vec{u}) - \varphi] \rangle}{\varphi - \varphi^2} \qquad [43]$$

where, angular brackets denote statistical averages and $\vec{u}$ is a lag vector. A surrogate of $R_z(\vec{u})$ is the so-called two-point probability function $S_2(\vec{u})$. The quantity $S_2(\vec{u})$ can be interpreted as the probability of finding two points at positions $\vec{r}$ and $\vec{r} + \vec{u}$ both in void phase. For statistically homogeneous and isotropic porous media, $S_2(\vec{u})$ is only a function of the modulus of the lag vector, i.e., $S_2(\vec{u}) = S_2(u)$. For all isotropic media without long-range

order, $S_2(u=0)=\varphi$ and $\lim_{u\to\infty} S_2(u)=\varphi^2$. Once $S_2(u)$ is known, $R_z(u)$ can be calculated from,

$$R_Z(u)=\frac{S_2(u)-\varphi^2}{(\varphi-\varphi^2)} \qquad [44]$$

For a digitized medium, $S_2(u)$ can be calculated by successively translating a sampling rod of u pixels in length a distance of one pixel at a time, spanning the whole image, counting the number of occurrences that the two end-points of the rod fall in pores and finally, dividing the number of occurrences by the total number of trials. Periodic boundary conditions were implemented in order to approximate an infinite medium with a finite grid. $R_z(u)$ was calculated using Eq. [44] along the two orthogonal directions for all five images of each sample and then averaged. The average functions for the seven samples are shown in Fig. 27 [see Appendix A (Table A.25) for data].

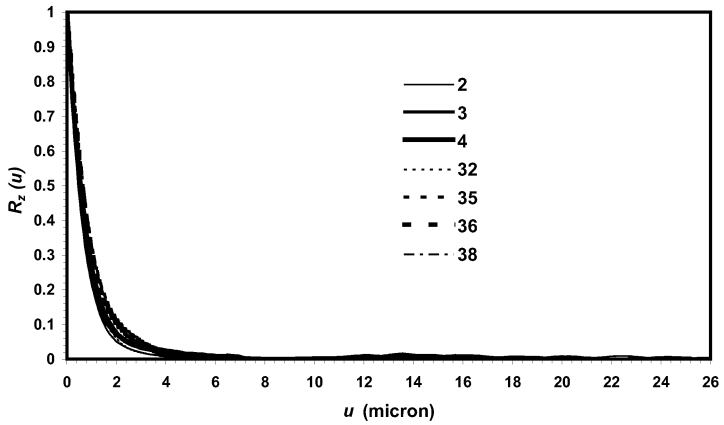

Figure 27—Void-phase autocorrelation functions of the Ekofisk chalk samples.

The slope of $R_z(\vec{u})$ at the origin is related to the specific surface area (the interfacial area per unit volume), s, which for digitized media is given by [14],

$$s=-2D(\varphi-\varphi^2)\left.\frac{dR_z}{du}\right|_{u=0} \qquad [45]$$

where D is the dimensionality of the space. The specific surface areas for the samples calculated from Eq. [45] (assuming D = 3) are compared with those obtained from mercury intrusion porosimetry (MIP) in Table 10. The s values computed from $R_z(\vec{u})$ differ significantly from the values obtained from MIP.

Table 10—Comparison of specific surface areas obtained from mercury porosimetry and autocorrelation function.

s (μm^{-1}) from,	Sample						
	2	**3**	**4**	**32**	**35**	**36**	**38**
Mercury porosimetry	4.11	4.72	4.05	3.15	3.14	2.99	3.71
$R_z(\vec{u})$	1.06	1.32	0.99	1.31	1.24	1.26	1.34

While autocorrelation function does not reflect information about the connectedness of the phases, the void-phase lineal path function $L(\vec{u})$ contains some connectedness information, at least along a lineal path, and hence reflects certain long-range information about the system. This quantity measures the probability that a line segment spanning from $\vec{r}$ to $\vec{r}+\vec{u}$ lies entirely within void phase. For statistically isotropic media, $L(\vec{u})$ depends only on the distance u between the two end-points and can be expressed simply as $L(u)$. For a porous medium with porosity φ, $L(u)$ at $u=0$ is equal to φ. For a digitized medium, $L(u)$ can be calculated by successively translating a sampling rod of u pixels in length a distance of one pixel at a time, spanning the whole image, counting the number of occurrences that the rod entirely fall in pores and finally, dividing the number of occurrences by the total number of trials. The measurement of $L(u)$ can be made much more efficient by simply identifying the lengths of the pore chords present in the system [14]. The average $L(u)$ functions are shown in Fig. 28 and the data are presented in Appendix A (Table A.26).

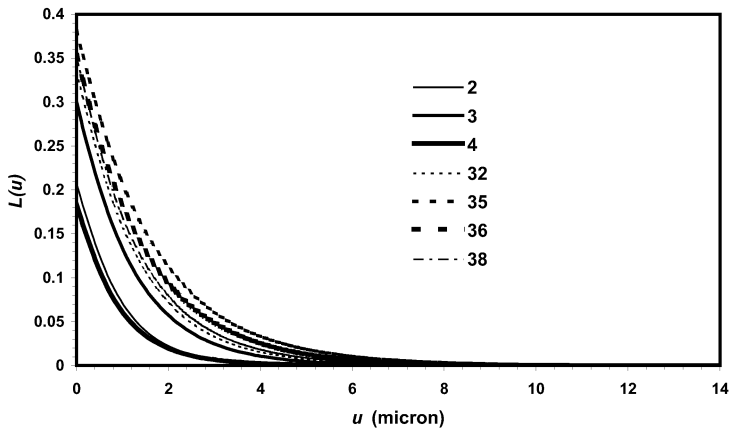

Figure 28—Void-phase lineal path functions of the Ekofisk chalk samples.

Another useful characteristic of porous microstructure is the chord distribution function $C_i(u)$, where i represents either void or solid. A chord is the length u between intersections of a line with the two-phase interface. The

chord distribution function can be directly interpreted in terms of microstructural features, as it contains phase connectedness and correlation information along a lineal path [15]. That is, if $C_i(u) \neq 0$ for large values of u, there exist connected regions of phase i at scale u. Importantly, the value of u at which $C_i(u)$ is maximum provides an estimate of the length scale associated with phase i. $C_s(u)$ and $C_v(u)$ was also calculated along the two orthogonal directions and averaged over five images of each sample. The functions are shown in Fig. 29 and Fig. 30 for solid and void phase, respectively while the data are presented in Appendix A (Table A.27 and A.28). The mean size and peak of the $C_s(u)$ and $C_v(u)$ distributions are shown in Table 11.

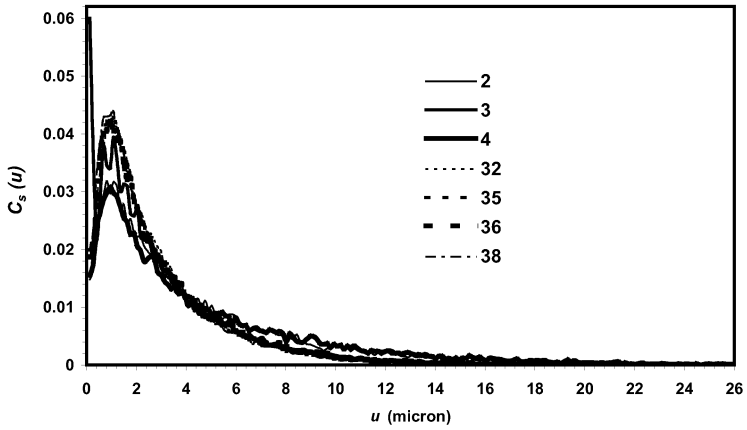

Figure 29—Solid-phase chord distribution functions of the Ekofisk chalk samples.

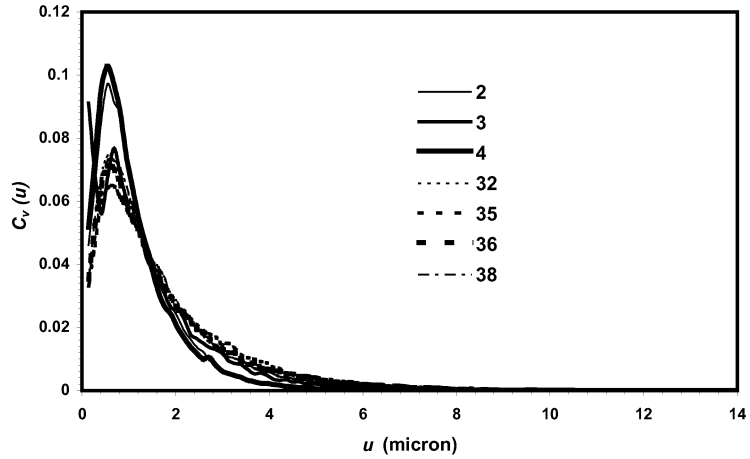

Figure 30—Void-phase chord distribution functions of the Ekofisk chalk samples.

Table 11—The mean size and peak of $C_s(u)$ and $C_v(u)$ distributions .

Parameter	Sample						
	2	3	4	32	35	36	38
Mean $C_s(u)$, μm	4.24	2.96	4.62	2.97	2.89	2.99	2.83
Mean $C_v(u)$, μm	1.17	1.37	1.12	1.53	1.81	1.68	1.57
Peak $C_s(u)$, μm	0.82	1.09	0.95	0.95	1.09	0.95	1.09
Peak $C_v(u)$, μm	0.54	0.68	0.54	0.54	0.68	0.54	0.68

One may expect that the mean pore size obtained from the $C_v(u)$ distribution should correspond well with the mean pore diameter obtained from mercury retraction data. A cross-plot of the two is shown in Fig. 31**.** The mean pore size is heavily weighted towards mercury retraction data meaning that the pore size obtained from mercury porosimetry is much higher than that obtained from $C_s(u)$ distribution.

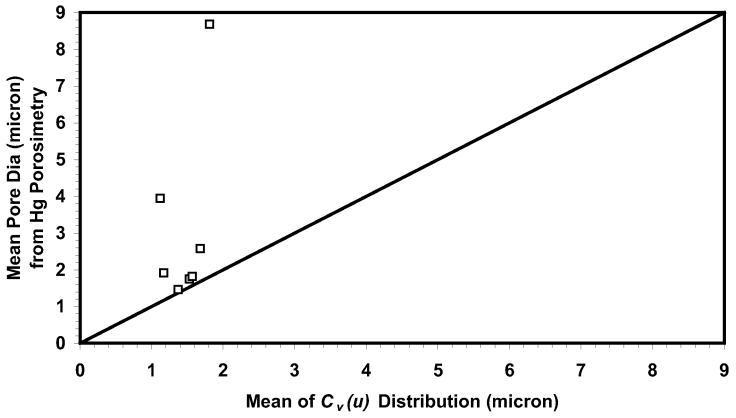

Figure 31—Cross-plot of mean pore size from $C_v(u)$ distribution against mean pore diameter from mercury retraction data.

11. Discussions

The porosities of the first set of samples are relatively lower than those of the second set of samples. The porosities measured with helium (helium porosimetry) range from 0.21 - 0.33 and 0.36 - 0.4 for the first and second set, respectively and those measured with brine (saturation method) range from 0.19 - 0.31 and 0.34 - 0.38 for the two sets, respectively. The second set of samples therefore has a bigger storage capacity of reservoir fluids than the first one. The helium porosity is slightly higher than the brine porosity. This is due to the fact that helium has small molecules with high diffusivity that penetrate

the small pores of cores easier than the brine molecules. The permeabilities of the first set of samples are also lower than those of the second set of samples. The air permeabilities of the first and second set of samples range from 0.2 - 2.6 mD and 0.84 - 3.05 mD, respectively while the brine permeabilities range from 0.09 - 1.94 mD and 0.35 - 1.88 mD for the two sets, respectively.

Hysteresis is observed in both oil- and water-phase relative permeabilities (Figs. 1-7), and oil-water capillary pressure (Figs. 9-15). This suggests that different fluid distributions exist at a given saturation during drainage and imbibition processes. The change in fluid distributions is mainly attributed to the trapping of non-wetting phase and difference in advancing and receding contact angles. Even though hysteresis is more pronounced and consistent in oil relative permeability, it is also present in the water relative permeability. This is in contradiction to what is commonly observed in water-wet sandstone where little or no hysteresis is observed for the wetting phase. A common assumption when modeling hysteresis is that no hysteresis is observed for the wetting phase. However, various behaviors are observed for different wettabilities [16]. For chalk, which range from moderately water-wet (e.g., samples 2, 3, 4 and 6) to strongly water-wet (e.g., samples 32, 36 and 38), hysteresis is observed for both oil and water relative permeabilities.

The hysteresis in the non-wetting phase relative permeability is consistent with the drainage curve having greater value than the imbibition curve at a given saturation. However, no unique behavior is observed in the wetting-phase, and imbibition relative permeability can go either above or below the drainage relative permeability. The behavior seems to be controlled by a variety of parameters among which wettability and pore geometry are the most important. The possible explanation for the non-wetting phase relative permeability is that under drainage, both capillary forces and viscous forces operate in a direction that promote desaturation of the largest pores. Under imbibition operations, however, capillary forces and viscous forces operate, in effect, in opposite directions. Capillary forces favor resaturation of the smallest pores first while viscous forces favor the largest pores first. The net effect is that pore sizes are not resaturated in the same sequence during imbibition as they are desaturated during drainage. During the imbibition process, a portion of the non-wetting phase becomes trapped by the wetting phase and consequently does not contribute to relative permeability. This leads to a lower relative permeability value on the imbibition curve than on the drainage curve for same saturation. Standing [17] gives a detailed description on relative permeability hysteresis in two-phase flow. For the wetting-phase relative permeability, the amount of wetting phase above the irreducible value is mobile and contributes to relative permeability. During imbibition, as the wetting phase increases from its initial value, some non-wetting phase is trapped. As a result of this entrapment, the wetting phase occupies pores of larger sizes at a given saturation than it would have occupied had entrapment not occurred. As fluids flow easier in larger pores than in smaller pores, the effect of the entrapment is to yield a large value of relative permeability [17].

Thus, directionally, the imbibition relative permeability curve would lie above the drainage curve as shown in Fig. 3. On the other hand, the entrapment of the non-wetting phase could result in slightly longer flow paths for the wetting phase - which would act towards decreasing the imbibition relative permeability as shown in Fig. 5. The degree of hysteresis experienced is usually difficult to quantify. Therefore, there is a need to reconcile the experimental data with a simulation model that takes into account the capillary end effects by say, history-matching production profiles from the laboratory and simulation [18-21], which is also a topic of this dissertation.

Considering the key end-point saturation and relative permeability values, and the crossover saturations, the chalk samples show typical water-wet behavior [22-23]. The Amott wettability index shows that sample 2, 3, 4 and 6 are moderately water-wet whereas both the Amott and the USBM indices indicate sample 32, 36 and 38 to be strongly water-wet. This difference in wettability is reflected in the oil production characteristics. For the strongly water-wet samples, more than 80% of the recoverable oil was produced by spontaneous imbibition while the recovery by spontaneous imbibition from moderately water-wet samples was at most 53%. The negative imbibition curves indicate that the forced imbibition mechanism has less potential of being an important production mechanism for the strongly water-wet samples (see Figs. 13-15). Previous studies on Ekofisk chalk [24-26] have reported similar production characteristics at various wettabilities.

A value between 1.4 and 2.52 was recorded for Archie's saturation exponent n. Significant resistivity hysteresis was observed for sample 2, 6 and 32 (Figs. 19, 21 and 22). The computed vaules of n for core 2 were 1.57 and 1.41 for drainage and imbibition, respectively. Values of n for core 6 were 1.71 and 1.53 while for core 32 the values were 2.07 and 1.83. Core 4 (Fig. 20) had no resistivity hysteresis (n = 1.4) while core 38 (Fig. 23) indicated a minor hysteresis with n-values of 2.44 and 2.52 for drainage and imbibition, respectively. The resistivity of the rock depends on the distribution of hydrocarbons and brine in the pore space and the formation of continuous and non-continuous films around the rock surface. The distribution of fluids may change during drainage and imbibition processes resulting in resistivity hysteresis.

Archie's empirical equation (Eq. [37]) was derived for clean water-wet sandstones over a reasonable range of water saturations and porosities. In practice, however, extraction of cores, and geological features including wettability, fractures, vugs, electrical conductive minerals, microporosity, rugged grain surfaces, salinity of formation brine, temperature, pore geometry, mineralogy and formation stress have been found to cause deviation from the linearity scale [27]. This results in either an increased n with decreasing S_w (positive curvature), or a decreasing n with decreasing S_w (negative curvature). The presence of fractures have been found to cause negative curvatures as water saturation decreases [28]. This behaviour is clearly observed in Fig. 22 and 23. Although there was no attempt to correlate this variation, fractures

could visibly be observed in some of the cores used in this study. In water-wet formations and cleaned cores, n has a typical value of 2. The relatively low values of n in some of the samples may be due to the effects of cleaning. Cleaning may reduce oil-wet surface areas within the pore space and maintain the lengths and conducting paths of brine in the sample for a wider range of saturations [29-30].

The negligible hysteresis observed in some of the samples could be expected because for samples with a water-wet tendency, the brine will occupy the small pores during both drainage and imbibition. This fluid distribution maintains more or less the same lengths and cross-sectional areas of the conducting paths and hence little changes in resistivity [31-32]. This behaviour has been indicated in water-wet sandstone but might not generally apply. However, one would expect that during imbibition, there is entrapment and snap-off of the non-wetting phase leading to long flow paths and higher resistivity than during drainage. This behaviour has been observed in sandstone [32-33] but results from the chalk samples show a different trend where the imbibition resistivity curves lie below the drainage curves (see Figs. 19, 21 and 22). This trend may be explained as follows: 1) with increase in brine saturation during imbibition, some oil is trapped causing longer electric flow paths whereas brine occupies pores of larger sizes yielding larger cross-sectional area for electricity to flow. The net result is a decrease in resistivity [34-35]; 2) due to tight nature of chalk samples, the fluids may not have reached equilibrium state at each measurement step causing lower resistivity; 3) presence of conductive fractures may have contributed to higher electric conductivity during imbibition; and 4) accuracy of measurements using two-electrode method is also a matter of concern.

The chalk samples show significant variability in mercury-air capillary pressure (Fig. 24), and pore- and throat-size distributions (Figs. 25-26). The mean throat and pore sizes range from 0.191 - 0.544 μm and 0.727 - 4.338 μm, respectively. These parameters show no particular trend with porosity or permeability. However, in general, the first set of samples has lower mean throat sizes and higher capillary pressures than those of the second set of samples. The selection of a receding contact angle of 140^{o} is fairly accurate [12] and applicable for chalk. However, advancing contact angle is highly dependent on pore structure, for example, θ_a = 100.5 – 107.5^{o} for anodic alumina and controlled pore glasses, and θ_a = 118 – 121^{o} for nuclepore polymer membranes was observed [12]. The size of pore [Eq. 40] is very sensitive to the advancing contact angle. Therefore, a reliable value for θ_a is necessary for chalk.

The void-phase autocorrelation functions for the samples show no appreciable correlation beyond a lag of approximately 60 pixels (Fig. 27). The autocorrelation functions correspond well with those reported for similar North Sea chalks [36]. The specific surface area s computed from the autocorrelation function differs significantly from the value obtained from mercury intrusion porosimetry (MIP) (see Table 11). This discrepancy is due

to the limited resolution (0.136 μm/pixel) of the image data. The magnitude of *s* is dependent on the size of the "probe" used to measure it. Since MIP detects pore volume invaded at capillary pressures corresponding to equivalent cylindrical pore radii smaller than 0.136 μm, it is expected that MIP will yield a higher specific surface area.

The void-phase lineal path functions for the samples vanish at a lag of about 70 pixels (Fig. 28). The shape of the curves is consistent with that for sandstone samples [14], unfortunately, no published data is available for chalk. The peaks of $C_s(u)$ and $C_v(u)$ distributions indicate that the most abundant particle and pore sizes in the Ekofisk chalk samples range from 0.82 - 1.09 μm and 0.54 - 0.68 μm, respectively. No published data is available to confirm this.

12. Conclusions

1. The chalk samples can be classified into two groups of low porosity (sample 2, 3, 4 and 6) and high porosity (sample 32, 36 and 38). The latter group indicated strongly water-wet chalk while the former group indicated moderately water-wet chalk.
2. The samples indicated considerable hysteresis in capillary pressure and relative permeability. This observation can be attributed to the changes in fluid distribution during drainage and imbibition.
3. A great number of rock and laboratory parameters seem to influence the electrical conductivity of chalk. Resistivity hysteresis was not highly pronounced for all samples and where it occurred, the imbibition resistivity was found to be lower than the drainage resistivity.
4. The production characteristics show that forced imbibition has more potential of being an oil production mechanism in moderately water-wet chalk than in strongly water-wet chalk.
5. Significant variability was observed among the samples in specific surface area, mercury-air capillary pressure, and pore- and throat-size distributions. In general, the first set of samples has lower mean throat radii and higher capillary pressures than those of the second set of samples.
6. The most abundant particle and pore sizes in the Ekofisk chalk samples range from 0.82 - 1.09 μm and 0.54 - 0.68 μm, respectively.

Nomenclature

A *Cross-sectional area of core, cm²*
A_o *Area under forced imbibition P_c curve, cm²*
A_w *Area under secondary drainage P_c curve, cm²*

b	*Klinkenberg constant, abs atm*
$C_s(\vec{u})$	*Solid-phase chord distribution function at lag vector* $\vec{u}$
D	*Core diameter, cm*
f_o	*Fraction flow of oil*
f_w	*Fraction flow of water*
I_{brine}	*Brine injectivity, cm/s.atm*
I_r	*Resistivity index*
k	*Absolute permeability, mD*
k_a	*Air permeability, mD*
k_{brine}	*Absolute brine permeability, mD*
k_L	*Equivalent liquid permeability*
k_{ro}	*Relative permeability of oil*
k_{roe}	k_{ro} *at* S_{wi}
k_{rw}	*Relative permeability of water*
k_{rwe}	k_{rw} *at* S_{or}
L	*Core length, cm*
$L(\vec{u})$	*Lineal path function function at a lag vector* $\vec{u}$
m	*Cementation exponent*
n	*Archie's saturation exponent*
P	*Mercury injection/retraction pressure, bar*
P_1	*Inlet pressure, atm*
P_2	*Outlet pressure, atm*
P_{atm}	*Atmospheric pressure, atm*
P_{av}	*Mean pressure, atm*
P_c	*Capillary pressure, bar*
P_{ce}	*Entry capillary pressure, bar*
P_{csp}	*Capillary pressure during spontaneous imbibition, bar*
P_{nw}	*Non-wetting phase pressure, bar*
P_w	*Wetting phase pressure, bar*
ΔP	*Differential pressure, bar*
q	*Flow rate,* cm^3/s
q_{atm}	*Flow rate at atmospheric pressure,* cm^3/s
Q_o	*Cumulative oil injected, PV*
q_o	*Oil flow rate,* cm^3/s
q_w	*Water flow rate,* cm^3/s
r_t	*Throat radius,* μm
r_p	*Pore radius,* μm
R	*Resistivity,* $\Omega.m$
r_1	*Distance from axis of rotation to inner face of the core*
r_2	*Distance from axis of rotation to outer face of the core*
r_o	*Oil index*
R_o	*Resistivity of core saturated with 100% brine,* $\Omega.m$
R_t	*Resistivity of core partially saturated with brine,* $\Omega.m$
r_w	*Water index*

R_w	*Resistivity of brine, Ω.m*
$R_z(\vec{u})$	*Autocorrelation function at a lag vector $\vec{u}$*
$S_2(\vec{u})$	*Two-point probability function at a lag vector $\vec{u}$*
$\overline{S}$	*Average saturation in the core*
S_g	*Specific surface area, m^2/g*
s	*Specific surface area, μm^{-1}*
S_o	*Oil saturation*
S_{or}	*Residual oil saturation*
S_{osp}	*Oil saturation after spontaneous oil uptake*
S_w	*Water saturation*
S_{wi}	*Initial water saturation*
S_{wsp}	*Water saturation after spontaneous water imbibition*
ΔT	*Differential time, s*
v	*Flow velocity, cm/s*
V_b	*Bulk volume of core, cm^3*
V_g	*Grain volume of core, cm^3*
V_{od}	*Volume of oil displaced by forced water imbibition, cm^3*
V_{osp}	*Volume of oil displaced by spont. water imbibition, cm^3*
V_p	*Pore volume of core, cm^3*
V_w	*Volume of brine production, cm^3*
V_{wd}	*Volume of water displaced by forced uptake of oil, cm^3*
V_{wsp}	*Volume of water displaced by spont. oil uptake, cm^3*
W_{dry}	*Dry weight of core, g*
W_f	*Weight of fluid, g*
W_{sat}	*Saturated weight of core, g*
$Z(\vec{r})$	*Binary phase function*
θ_r	*Receding contact angle*
θ_a	*Advancing contact angle*
μ	*Fluid viscosity, cp*
σ	*Interfacial tension, mN/m*
λ	*Pore size distribution index*
ϕ_{brine}	*Porosity measured with brine*
ϕ_e	*Effective porosity*
ρ_f	*Density of fluid, g/cm^3*
ρ_g	*Grain density of core, g/cm^3*
ϕ_{He}	*Porosity measured with helium*
ϕ_{Hg}	*Porosity measured with mercury*
ρ_o	*Density of oil, g/cm^3*
μ_o	*Oil viscosity, cp*
ω	*Angular velocity of the centrifuge*
ρ_w	*Density of water, g/cm^3*
μ_w	*Water viscosity, cp*
SEM	*Scanning electron microscope*

WI_{Amott} Amott wettability index
WI_{USBM} USBM wettability index
FWPT Field (core) water production total
FOPT Field (core) oil production total
MIP Mercury intrusion porosimetry

Acknowledgments

We gratefully acknowledge the financial support from Phillips Petroleum Company Norway for this study.

References

1. Darcy, H.: “Les Fontaines Publiques de la Ville de Dijo,” Victor Dalmont, Paris (1856).
2. Klinkenberg, L.J.: “The Permeability of Porous to Liquids and Gases,” *API Drill. and Prod. Prac.*, 200 (1941).
3. Welge, H.J.: “A Simplified Method for Computing Oil Recovery by Gas or Water Drive,” *Trans. AIME* **195**, 91-98 (1952).
4. Buckley, S.E. and Leverett, M.C.: “Mechanism of Fluid Displacement in Sands,” *Trans. AIME* **146**, 107-116 (1942).
5. Hassler, G.L., and Brunner, E.: "Measurement of Capillary Pressure in Small Core Samples," *Trans. AIME* **160**, 114-123 (1945).
6. da Silva, F.V.: "Primary and Enhanced Recovery of Ekofisk Field: A Single- and Double-Porosity Numerical Simulation Study," paper SPE 19840 presented at the SPE Annual Technical Conference and Exhibition, San Antonio, TX, USA, 8-11 October (1989).
7. Amott, E.: "Observations Relating the Wettability of Porous Rocks," *Trans. AIME* **216**,156-162 (1959).
8. Cuiec, L.E.: “Wettability and Oil Reservoirs,” *In* North Sea Oil and Gas Reservoirs (ed. Kleppe *et al.*), Graham & Trotman, 193-207 (1987).
9. Archie, G.E.: "The Electrical Resistivity Log as an Aid in Determining some Reservoir Characteristics," *Trans. AIME* **146**, 54 (1942).
10. Torsæter, O.: "An Experimental Study of Water Imbibition in North Sea Chalk," Ph.D. thesis, The Norwegian Institute of Technology, The University of Trondheim, Norway, (July 1983).
11. Yu, L. and Wardlaw, N.C.: “Quantitative Determination of Pore Structure from Mercury Capillary Pressure Curves,” *In*: Interfacial Phenomena in Petroleum Recovery, ed. N.R. Morrow, *Surfactant Science Series* **36**, 101-156.

12. Salmas, C. and Androutsopoulos, G.: "Mercury Porosimetry: Contact Angle Hysteresis of Materials with Controlled Pore Structure," *J. Colloid Interface Sci.* **239**, 178-189 (2001) (and references therein).
13. Adler, P.M., Jacquin, C.G. and Quiblier, J.A.: "Flow in Simulated Porous Media," *Int. J. Multiphase Flow* **16** (4), 691-712 (1990).
14. Yeong, C.L.Y., and Torquato, S.: "Reconstructing Random Media," *Physical Review E* **57**, 495-506 (1998).
15. Roberts, A.P. and Torquato, S.: "Chord-Distribution Functions of Three-Dimensional Random Media: Approximate First-Passage Times of Gaussian Process," *Phys. Rev. E* **59**, 4953-4963 (1999).
16. Braun, E.M., and Holland, R.: "Relative Permeability Hysteresis: Laboratory Measurements and a Conceptual Model," *SPERE* (August 1995), 222-28.
17. Standing, M.B.: "Notes on Relative Permeability Relationship," The Norwegian Institute of Technology, Trondheim (1975).
18. Yu, S.Y., Akervoll, I., Torsæter, O., Stensen, J.A., Kleppe, J., and Midtlyng, S.H.: "History Matching Gas Injection Processes with In-Situ Saturation Measurements and Process Hysteresis," SPE 48842, Int Conference and Exhibition, Beijing, 2-6 Nov. (1998).
19. Akervoll, I., Talukdar, M.S., Midtlyng, S.H., Torsæter, O. and Stensen, J.Å.: "History Matching WAG Injection Experiments Performed Under CT Surveillance to Obtain Relative Permeability and Capillary Pressure," 20th Annual International Energy Agency Workshop and Symposium (paper no. 17), Paris, France, 21-24 Sept. (1999).
20. Akervoll, I., Talukdar, M.S., Midtlyng, S.H., Stensen, J.Å and Torsæter, O.: "WAG Injection Experiments With In-Situ Saturation Measurements at Reservoir Conditions and Simulations," SPE 59323, SPE/DOE Improved Oil Recovery Symposium, Tulsa, Oklahoma, 3-5 April (2000).
21. Tweheyo, M.T., Talukdar, M.S., Torsæter, O. and Vafaeinezhad, Y.: "Improvement of Experimental Relative Permeability of North Sea Chalk Through Simulation," 11th Oil, Gas and Petrochemical Congress & Exhibition, Tehran, Iran, 29-31 Oct. (2001).
22. Anderson, W.G.: "Wettability Literature Survey-Part 5: The Effect of Wettability on Relative Permeability," *JPT*, November 1987, 1453-1468.
23. Craig, F.F.: "The Reservoir Engineering Aspects of Waterflooding," *SPE Monograph Series*, Richardson, TX, **3**, 12-44 (1971).
24. Torsæter, O.: "An Experimental Study of Water Imbibition in North Sea Chalk," SPE 12688, SPE/DOE Enhanced Oil Recovery Symposium, Tulsa, OK, 15-18 April (1984).
25. Tobola, D.P.: "The Contribution of Oil Production Mechanisms as Determined by a Novel Centrifuge Technique," SCA 9617, International Symposium of Core Analysts, Montpellier, 8-10 Sept. (1996).
26. Graue, A., Bognø, T., Moe, R.W., Baldwin, B.A., Spinler, E.A., Maloney, D., Tobola, D.P.: "Impacts of Wettability on Capillary Pressure and

Relative Permeability," SCA 9515, International Symposium of Core Analysts, Colorado, 1-4 August (1999).
27. Stalheim, S.O. and Eidesmo, T.: "Is the Saturation Exponent *n* a Constant?" *In*: *SPWLA* 36th Annual Logging Symposium, New Orleans, 26-29 June (1995).
28. Rasmus, J.C.: "A Summary of the Effect of Various Pore Geometries and their Wettabilities on Measurement of in situ Values of Cementation and Saturation Exponent," *SPWLA Trans.* **II**, 9-13 June (1986).
29. Moore, J.: "Laboratory Determined Electrical Logging Parameters of the Bradford Third Sand," *Producers Monthly* **5**, 30-39 (March 22, 1958).
30. Sweeney, S.A., Jennings, Jr.: "Effect of Wettability on the Electrical Resistivity of Carbonate Rock from a Petroleum Reservoir," *J. of Phys. Chem.* **64**, 551-53 (May 1960).
31. Wei, J., and Lile, O.: "Resistivity Index Hysteresis and Its Significance in Electrical Well Log Interpretation," Proc. European *SPWLA* Formation Evaluation Symposium, Stavanger, May 5-7 (1993).
32. Moss, A.K., Jing, X.D., and Archer, J.S.: "Laboratory Investigation of Wettability and Hysteresis Effects on Resistivity Index and Capillary Pressure Characteristics," Proc. 5th Int. Symp. on Evaluation of Reservoir Wettability and Its Effect on Oil Recovery, Trondheim, Norway, 338-349 (1999).
33. Mitchell, P., and Brown, G.: "The Effect of Imbibition on the Value of the Saturation Exponent and the Implications for Depleting Reservoirs," Proc. European *SPWLA* Meeting, Aberdeen (1994).
34. Swanson, B.F.: "Rationalising the Influence of Crude Wetting on Reservoir Fluid Flow With Electrical Resistivity Behaviour," *JPT* (Aug. 1980), 1459-64.
35. Longeron, D.G., Argaud, M.G., and Feraud, J.P.: "Effect of Overburden Pressure and the Nature of Microscopic Distribution of Fluids on Electrical Properties of Rock Samples," *SPE Formation Evaluation*, (June 1989), 194-202.
36. Bekri, S., Xu, K., Yousefian, F., Adler, P.M., Thovert, J.-F., Muller, J., Iden, K., Psyllos, A., Stubos, A.K., and Ioannidis, M.A.: “Pore Geometry and Transport Properties in North Sea Chalk,” *J. Petrol. Sci. Eng.* **25**, 107 (2000).

Appendix A

The data for most of figures in the laboratory report are presented in this Appendix.

Table A.1—Drainage relative permeability for core 2, 3, 4 and 6 (Figs. 1-4).

Core 2			Core 3			Core 4			Core 6		
S_w	k_{rw}	k_{ro}	S_w	k_{rw}	k_{ro}	S_w	k_{rw}	k_{ro}	S_w	k_{rw}	k_{ro}
1	1	0	1	1	0	1	1	0	1	1	0
0.572	0.042	0.174	0.702	0.110	0.140	0.706	0.104	0.100	0.551	0.070	0.200
0.412	0.006	0.314	0.518	0.052	0.255	0.567	0.023	0.160	0.454	0.038	0.239
0.392	0.001	0.360	0.470	0.041	0.309	0.540	0.016	0.170	0.358	0.014	0.300
0.361	0.001	0.457	0.440	0.039	0.363	0.529	0.010	0.189	0.336	0.011	0.310
0.350	0	0.770	0.420	0.034	0.390	0.412	0.005	0.339	0.331	0.010	0.320
			0.408	0.022	0.450	0.396	0.003	0.370	0.290	0.010	0.340
			0.340	0.0180	0.600	0.310	0	0.740	0.288	7.0×10^{-3}	0.350
			0.320	0.009	0.640				0.238	5.0×10^{-3}	0.420
			0.260	0	0.850				0.220	1.0×10^{-3}	0.478
									0.210	1.0×10^{-3}	0.490
									0.180	0	0.790

Table A.2—Imbibition relative permeability for core 2, 3, 4 and 6 (Figs. 1-4).

Core 2			Core 3			Core 4			Core 6		
S_w	k_{rw}	k_{ro}	S_w	k_{rw}	k_{ro}	S_w	k_{rw}	k_{ro}	S_w	k_{rw}	k_{ro}
0.350	0	0.770	0.260	0	0.850	0.310	0	0.740	0.180	0	0.790
0.705	0.050	0.025	0.560	0.113	0.129	0.426	0.054	0.272	0.658	0.170	0.030
0.721	0.065	0.020	0.672	0.150	0.060	0.602	0.150	0.067	0.699	0.210	0.017
0.748	0.080	0.010	0.760	0.180	0.020	0.663	0.198	0.016	0.715	0.225	0.013
0.767	0.120	0.001	0.780	0.200	0	0.670	0.210	0	0.820	0.290	0
0.770	0.170	0									

Table A.3—Drainage relative permeability for core 32, 36 and 38 (Figs. 5-7).

Core 32			Core 36			Core 38		
S_w	k_{rw}	k_{ro}	S_w	k_{rw}	k_{ro}	S_w	k_{rw}	k_{ro}
1	1	0	1	1	0	1	1	0
0.550	0.220	0.110	0.593	0.150	0.078	0.591	0.150	0.110
0.430	0.137	0.290	0.520	0.061	0.153	0.504	0.038	0.230
0.333	0.073	0.440	0.473	0.040	0.222	0.476	0.036	0.260
0.315	0.069	0.480	0.426	0.030	0.290	0.422	0.033	0.340
0.298	0.063	0.530	0.400	0.020	0.352	0.331	0.021	0.490
0.286	0.060	0.550	0.384	0.017	0.389	0.303	0.011	0.520
0.280	0.040	0.600	0.264	0.0041	0.610	0.270	0.001	0.560
0.269	0.040	0.620	0.264	0.0041	0.610	0.190	0	0.660
0.254	0.020	0.680	0.240	0	0.661			
0.237	0.0091	0.700						
0.217	0.007	0.780						
0.210	0	0.790						

Table A.4—Imbibition relative permeability for core 32, 36 and 38 (Figs. 5-7).

Core 32			Core 36			Core 38		
S_w	k_{rw}	k_{ro}	S_w	k_{rw}	k_{ro}	S_w	k_{rw}	k_{ro}
0.210	0	0.790	0.240	0	0.660	0.190	0	0.660
0.524	0.154	0.100	0.553	0.074	0.063	0.520	0.076	0.150
0.573	0.190	0.050	0.616	0.099	0.019	0.584	0.120	0.056
0.668	0.280	0.010	0.637	0.120	0.015	0.628	0.160	0.038
0.688	0.320	2.046×10^{-3}	0.668	0.190	0.012	0.679	0.200	0.018
0.704	0.340	0	0.684	0.220	3.424×10^{-3}	0.810	0.300	0
			0.689	0.281	3.060×10^{-3}			
			0.693	0.330	8.216×10^{-4}			
			0.694	0.350	0			

Table A.5—Experimental oil and water recoveries for core 2 (ΔP = 5.0 bars).

Drainage			Imbibition		
Time (hours)	FWPT (cm^3)	FOPT (cm^3)	Time (hours)	FWPT (cm^3)	FOPT (cm^3)
0	0	0	0	0	0
4	4.6	0	5.333	0	2.1
7.25	5.38	3.8	9.133	1.1	3.4
21.25	5.65	27.65	24.4	11.39	3.65
26.75	5.75	37.85	27.9	14.35	3.75
43.25	5.8	72.85	30.9	16.2	3.8
50	5.82	84	48.4	34.2	3.9

Table A.6—Experimental oil and water recoveries for core 3 (ΔP = 2.5 bars).

			Imbibition		
Time (hours)	FWPT (cm^3)	FOPT (cm^3)	Time (hours)	FWPT (cm^3)	FOPT (cm^3)
0	0	0	0	0	0
0.367	2.35	0	0.3	0	1.45
0.783	4.15	0.5	0.967	0.5	3.55
1.2	5.6	1.25	1.967	1.52	5.4
1.617	6.8	2.25	2.967	4.9	5.65
2.033	7.6	3.75	4.467	12.3	5.8
2.45	7.95	5.75	5.357	16.7	5.95
2.8667	8.15	7.9			
3.2833	8.35	10			
3.7	8.55	12.1			
4.11667	8.7	14.35			
6.117	9.25	24.35			
7.42222	9.55	31.3			
22.92222	10.5	122.29			

Table A.7—Experimental oil and water recoveries for core 4 (ΔP = 4.2 bars).

			Imbibition		
Time (hours)	FWPT (cm^3)	FOPT (cm^3)	Time (hours)	FWPT (cm^3)	FOPT (cm^3)
0	0	0	0	0	0
1.833	2.7	0	0.217	0	0.65
3.833	4.95	0.2	2.217	0.25	2.55
5.833	5.75	1	4.217	1.65	3.03
8.083	6	3.55	6.3	3.95	3.1
10.25	6.36	6.65	23.3	37.75	3.2
23.3	6.45	37.75			
27.3	6.59	46.65			
43.367	6.65	86.55			
50.2	6.7	104			

Table A.8—Experimental oil and water recoveries for core 6 (ΔP = 2.5 bars).

			Imbibition		
Time (hours)	FWPT (cm^3)	FOPT (cm^3)	Time (hours)	FWPT (cm^3)	FOPT (cm^3)
0	0	0	0	0	0
0.5	6	0	0.225	0	4.2
0.75	7.7	0.6	0.558	0.72	6.5
1	8.35	3.7	0.892	5.22	6.85
1.333	8.95	8.1	1.225	12.22	6.9
1.667	9.2	13.05	2.225	33.42	7.17
2	9.4	18.45			
2.5	9.7	27.15			
3.333	10.1	41.75			
4.333	10.5	60.35			
6.333	10.95	97.35			
8.333	11.1	137.1			
23.4667	11.9	460.25			

Table A.9—Experimental oil and water recoveries for core 32 (ΔP = 3.0 bars).

			Imbibition		
Time (hours)	FWPT (cm^3)	FOPT (cm^3)	Time (hours)	FWPT (cm^3)	FOPT (cm^3)
0	0	0	0	0	0
0.55	8.6	0	0.41666667	0	6.9
0.75	10.4	0.5	0.5	0.5	7.7
0.86111111	11.2	2.1	0.58333333	1.4	8.5
1.02777778	11.5	4.4	0.83333333	5.2	8.75
1.19444444	11.8	7	1.08333333	10.4	8.95
1.36111111	12.1	9.6	1.2	13.4	9.02
1.52777778	12.3	12.2			
1.69444444	12.4	15.1			
2.19444444	12.6	23.9			
2.77777778	12.85	33.85			
3.77777778	13.15	53.55			
4.36111111	13.5	73.3			

Table A.10—Experimental oil and water recoveries for core 36 (ΔP = 2.5 bars).

			Imbibition		
Time (hours)	FWPT (cm^3)	FOPT (cm^3)	Time (hours)	FWPT (cm^3)	FOPT (cm^3)
0	0	0	0	0	0
0.583333333	3	0	0.116666667	0	3
0.916666667	3.9	0.15	0.183333333	0.2	3.6
1.25	4.6	1.5	0.216666667	0.7	3.8
1.583333333	5.05	3.45	0.283333333	2.2	4.1
2.083333333	5.5	6.2	0.35	4.2	4.25
2.583333333	5.75	10.75	0.483333333	7.5	4.3
3.083333333	5.9	16.55	0.65	11.78	4.34
3.716666667	6.05	23.85	1.133333333	25.86	4.36
4.183333333	6.06	39.85			

Table A.11—Experimental oil and water recoveries for core 38 (ΔP = 2.5 bars).

			Imbibition		
Time (hours)	FWPT (cm^3)	FOPT (cm^3)	Time (hours)	FWPT (cm^3)	FOPT (cm^3)
0	0	0	0	0	0
0.75	9.2	0	0.416666667	0	6
0.833333333	9.9	0.15	0.633333333	0.05	8
0.916666667	10.2	0.3	0.866666667	0.09	8.45
1	10.6	0.5	1.033333333	0.1	8.8
1.083333333	10.8	1	1.383333333	2.5	9.05
1.333333333	11.1	2	2	11	9.1
1.7	11.5	4.2	2.55	19	9.15
2.316666667	11.85	8.15			
3.066666667	12.1	14.2			
3.566666667	12.2	18.7			
4.94	12.65	35.2			

Table A.12—Water-oil capillary pressure data for core 2 (Fig. 9).

Primary Drainage					Forced Imbibition			
RPM	P_c (bar)	V_{brine}(cc) produced	S_w (avg)	S_w (H&B)	RPM	P_c (bar)	V_{oil} (cc) Produced	S_w (avg)
0	0	0	1	1	0	0	0	0.49
2000	0.43	0	1	1	3000	-1.94	0.50	0.62
2500	0.67	0	1	1	4000	-3.44	0.80	0.67
3500	1.32	0.50	0.85	0.69	4500	-4.36	1.00	0.69
4500	2.18	3.85	0.62	0.38	5000	-5.38	1.25	0.71
5000	2.69	4.30	0.52	0.30	5500	-6.51	1.70	0.72
6000	3.87	5.20	0.41	0.22	6000	-7.75	2.05	0.73
7000	5.27	5.75	0.36	0.19	7000	-10.5	2.35	0.75

Table A.13—Water-oil capillary pressure data for core 3 (Fig. 10).

Primary Drainage					Forced Imbibition			
RPM	P_c (bar)	V_{brine}(cc) produced	S_w (avg)	S_w (H&B)	RPM	P_c (bar)	V_{oil} (cc) produced	S_w (avg)
0	0	0	1	1	0	0	0	0.47
1000	0.11	0	1	1	1000	-0.21	0	0.50
1500	0.24	0	1	1	2000	-0.85	1.15	0.57
2000	0.43	0.20	0.98	0.88	3000	-1.92	1.75	0.64
2500	0.67	2.35	0.91	0.53	4000	-3.41	2.85	0.69
3000	0.96	3.55	0.70	0.39	5000	-5.33	3.45	0.72
3500	1.31	4.75	0.61	0.29	6000	-7.67	3.67	0.74
4500	2.16	5.51	0.48	0.21	7000	-10.4	3.88	0.76
5000	2.67	6.35	0.42	0.17				
6000	3.84	7.65	0.36	0.13				
7000	5.23	8.55	0.30	0.10				

Table A.14—Water-oil capillary pressure data for core 4 (Fig. 11).

Primary Drainage					Forced Imbibition			
RPM	P_c (bar)	V_{brine}(cc) produced	S_w (avg)	S_w (H&B)	RPM	P_c (bar)	V_{oil} (cc) produced	S_w (avg)
0	0	0	1	1	0	0	0	0.55
1000	0.11	0	1	1	2000	-0.84	0.25	0.62
1500	0.24	0	1	1	3000	-1.89	0.50	0.67
2000	0.42	0	1	1	4000	-3.36	1.00	0.70
3000	0.95	0.75	0.91	0.72	4500	-4.25	1.20	0.72
4000	1.69	2.20	0.72	0.41	5000	-5.25	1.40	0.73
4500	2.13	3.10	0.61	0.30	5500	-6.35	1.65	0.75
5000	2.63	3.70	0.51	0.25	6000	-7.56	1.80	0.76
5500	3.19	4.25	0.45	0.21	7000	-10.3	1.90	0.77
6000	3.79	4.70	0.41	0.19				

Table A.15—Water-oil capillary pressure data for core 6 (Fig. 12).

Primary Drainage					Forced Imbibition			
RPM	P_c (bar)	V_{brine}(cc) produced	S_w (avg)	S_w (H&B)	RPM	P_c (bar)	V_{oil} (cc) produced	S_w (avg)
0	0	0	1	1	0	0	0	0.53
1000	0.10	0	1	1	1000	-0.19	0.55	0.58
1500	0.22	0	1	1	2000	-0.78	1.20	0.64
2000	0.39	0.05	0.94	0.87	3000	-1.75	1.75	0.68
2500	0.62	1.25	0.88	0.62	4000	-3.11	2.25	0.70
3000	0.89	3.50	0.75	0.39	5000	-4.85	2.45	0.72
3500	1.21	5.05	0.60	0.28	6000	-6.99	2.60	0.73
4500	2.00	6.90	0.46	0.20	7000	-9.51	2.85	0.75
5000	2.47	7.55	0.40	0.17				
5500	2.98	8.00	0.37	0.15				
6000	3.55	8.50	0.33	0.14				
7000	4.83	9.23	0.27	0.11				

Table A.16—Water-oil capillary pressure data for core 32 (Fig. 13).

RPM	Primary Drainage				Forced Imbibition			Secondary Drainage			
	P_c (bar)	V_{brine} (cc) Produced	S_w (avg)	S_w (H&B)	P_c (bar)	V_{oil} (cc) produced	S_w (avg)	Pc (bar)	V_{brine}(cc) produced	S_w (avg)	S_w (H&B)
0	0	0	1	1	0	0	0.685	0	0	0.686	0.686
1000	0.113	0	1	1	-0.227	0	0.685	0.113	0	0.686	0.686
1500	0.253	0	1	1	-0.512	0	0.685	0.253	0	0.686	0.686
2000	0.45	0	1	1	-0.91	0.05	0.688	0.45	0	0.686	0.641
2500	0.703	0	1	0.96	-1.422	0.1	0.691	0.703	1	0.628	0.456
3000	1.013	0.4	0.977	0.913	-2.047	0.2	0.696	1.013	2.4	0.547	0.333
3500	1.379	0.75	0.956	0.788	-2.787	0.25	0.699	1.379	3.35	0.492	0.285
4000	1.801	1.95	0.887	0.435	-3.64	0.25	0.699	1.801	4.14	0.446	0.24
4500	2.279	4.5	0.739	0.264	-4.606	0.25	0.699	2.279	4.77	0.409	0.192
5000	2.814	7.55	0.562	0.196	-5.687	0.3	0.702	2.814	5.25	0.381	0.161
5500	3.405	9.5	0.449	0.157	-6.881	0.32	0.703	3.405	5.7	0.355	0.132
6000	4.052	10.55	0.388	0.127	-8.189	0.32	0.703	4.052	6.3	0.32	0.111
6500	4.755	11.15	0.353	0.107				4.755	6.7	0.297	0.09
7000	5.515	11.85	0.312	0.087				5.515	7.1	0.274	0.076
7500	6.331	12.35	0.283	0.072							

Table A.17—Water-oil capillary pressure data for core 36 (Fig. 14).

RPM	Primary Drainage				Forced Imbibition			Secondary Drainage			
	P_c (bar)	V_{brine} (cc) produced	S_w (avg)	S_w (H&B)	P_c (bar)	V_{oil} (cc) produced	S_w (avg)	Pc (bar)	V_{brine}(cc) produced	S_w (avg)	S_w (H&B)
0	0	0	1	1	0	0	0.576	0	0	0.621	0.621
1000	0.074	0	1	1	-0.14	0	0.576	0.074	0	0.621	0.621
1500	0.166	0	1	1	-0.315	0	0.576	0.166	0	0.621	0.621
2000	0.295	0	1	1	-0.56	0.05	0.58	0.295	0	0.621	0.589
2500	0.461	0	1	0.967	-0.875	0.15	0.589	0.461	0.45	0.58	0.447
3000	0.664	0.25	0.977	0.91	-1.26	0.25	0.598	0.664	1.22	0.51	0.358
3500	0.903	0.5	0.955	0.76	-1.715	0.4	0.612	0.903	1.65	0.472	0.31
4000	1.18	1.4	0.873	0.47	-2.24	0.5	0.621	1.18	2.07	0.434	0.282
4500	1.493	3.5	0.683	0.35	-2.835	0.5	0.621	1.493	2.48	0.396	0.236
5000	1.843	5.25	0.525	0.27	-3.5	0.55	0.625	1.843	2.85	0.363	0.199
5500	2.23	6.35	0.425	0.2	-4.236	0.6	0.63	2.23	3.2	0.331	0.159
6000	2.654	7	0.367	0.165	-5.041	0.6	0.63	2.654	3.54	0.301	0.135
6500	3.115	7.5	0.321	0.14				3.115	3.8	0.277	0.126
7000	3.613	7.9	0.285	0.126				3.613	4.05	0.254	0.11
7500	4.148	8.25	0.253	0.111							

Table A.18—Water-oil capillary pressure data for core 38 (Fig. 15).

RPM	Primary Drainage				Forced Imbibition			Secondary Drainage			
	P_c (bar)	V_{brine} (cc) Produced	S_w (avg)	S_w (H&B)	P_c (bar)	V_{oil} (cc) produced	S_w (avg)	Pc (bar)	V_{brine} (cc) Produced	S_w (avg)	S_w (H&B)
0	0	0	1	1	0	0	0.601	0	0	0.61	0.61
1000	0.108	0	1	1	-0.215	0	0.601	0.108	0	0.61	0.61
1500	0.242	0	1	1	-0.484	0	0.601	0.242	0	0.61	0.61
2000	0.43	0	1	1	-0.861	0	0.601	0.43	0	0.61	0.544
2500	0.672	0	1	0.889	-1.345	0.16	0.611	0.672	1.4	0.525	0.347
3000	0.968	1.25	0.924	0.67	-1.936	0.25	0.616	0.968	2.2	0.477	0.319
3500	1.317	2.8	0.831	0.536	-2.636	0.45	0.628	1.317	3.15	0.419	0.253
4000	1.721	4.1	0.752	0.394	-3.443	0.5	0.631	1.721	3.7	0.386	0.221
4500	2.178	5.6	0.662	0.256	-4.357	0.5	0.631	2.178	4.1	0.362	0.187
5000	2.689	7.1	0.571	0.192	-5.379	0.55	0.634	2.689	4.55	0.335	0.154
5500	3.253	8.33	0.497	0.16	-6.509	0.55	0.634	3.253	4.95	0.311	0.131
6000	3.872	9.6	0.42	0.14	-7.746	0.55	0.634	3.872	5.35	0.286	0.1
6500	4.544	10.95	0.338	0.115				4.544	5.6	0.271	0.084
7000	5.27	11.8	0.287	0.087				5.27	6	0.247	0.071
7500	6.049	12.35	0.254	0.064							

Table A.19— Results from resistivity tests on core 2, 4 and 6 (Figs. 19-21).

Core 2				Core 4				Core 6			
Drainage		Imbibition		Drainage		Imbibition		Drainage		Imbibition	
S_w	I_r	S_w	I_r	S_w	I_r	S_w	I_r	S_w	I_r	S_w	I_r
1.000	1.000	0.352	4.264	1.000	1.000	0.394	3.558	1.000	1.000	0.287	6.440
0.960	1.107	0.455	2.849	0.764	1.500	0.416	3.688	0.918	1.185	0.347	5.815
0.900	0.900	0.569	2.371	0.739	1.568	0.423	3.414	0.763	1.700	0.492	2.826
0.880	1.200	0.572	2.286	0.688	1.744	0.449	3.146	0.731	1.850	0.561	2.381
0.760	1.600	0.586	2.140	0.630	1.875	0.481	2.833	0.646	2.240	0.574	2.211
0.668	2.114	0.731	1.635	0.586	2.816	0.543	2.276	0.618	2.476	0.609	2.020
0.625	2.424			0.543	2.294	0.550	2.374	0.507	3.450		
0.480	3.587			0.536	2.303			0.402	4.635		
0.470	3.680			0.528	2.468			0.359	5.887		
0.413	4.100			0.470	2.554			0.315	8.300		
0.349	5.126			0.412	3.345			0.290	6.985		
0.321	5.561			0.380	3.818			0.272	9.122		
0.303	5.351			0.343	4.832			0.222	12.00		
				0.303	4.969						
				0.260	6.571						

Table A.20— Results from resistivity tests on core 32 and 38 (Figs. 22-23).

Core 32				Core 38			
Drainage		Imbibition		Drainage		Imbibition	
S_w	I_r	S_w	I_r	S_w	I_r	S_w	I_r
1	1	0.3775	5.9792	1	1	0.3501	12.760
0.9030	1.2648	0.3849	5.4811	0.9047	1.3685	0.3711	10.892
0.8554	1.4748	0.4599	3.9439	0.8647	1.6223	0.4931	7.4399
0.8151	1.7738	0.5075	3.5751	0.8209	2.0149	0.5445	5.6249
0.7657	2.0343	0.5570	3.2114	0.7408	2.6439	0.5998	3.5862
0.7089	2.5331	0.5972	2.5653	0.6474	4.0366	0.6322	2.8987
0.6247	3.1729	0.6320	2.4064	0.5331	6.9097	0.6589	2.6424
0.5405	4.4557	0.6522	2.0987	0.4778	8.4392		
0.5167	4.8438			0.4187	11.841		
0.4489	6.1847			0.3635	13.177		
0.3794	8.1374			0.3406	13.909		
0.3318	8.8016			0.2929	16.152		
0.3080	9.4429			0.2701	16.677		
0.2860	9.9524			0.2643	18.507		

Table A.21—Mercury intrusion data for core 2, 3, 4 and 32 (related to Fig. 25, data volume has been reduced slightly).

Intrusion							
Sample 2		Sample 3		Sample 4		Sample 32	
P [bar]	V [mm^3/g]	P [bar]	V [mm^3/g]	P [bar]	V [mm^3/g]	P [bar]	V [mm^3/g]
1.3	0.05	1.3	0.08	1.7	0.06	1.2	0.06
1.5	0.16	2	0.24	2.5	0.17	1.9	0.19
2.1	0.37	4.7	0.55	5.9	0.39	2.3	0.31
7	0.79	10.8	1.1	15.5	0.79	2.8	0.43
14.2	1.16	15.8	1.73	17.8	1.24	3.5	0.56
15	1.37	16.4	1.88	18.5	1.46	3.9	0.68
16.6	1.8	17.9	2.67	20.1	1.8	4.3	0.8
17.9	2.75	18.8	3.3	21.8	2.93	4.8	0.93
19.5	4.12	19.9	5.97	23.1	3.83	5.4	1.05
20.7	5.49	20.5	8.32	24	6.53	6	1.18
21	5.7	20.7	9.74	24.4	6.64	7.2	1.42
22.4	7.82	21.4	16.49	26.4	8.44	7.8	1.55
23.8	10.14	21.9	24.34	27.2	11.37	8.5	1.67
24.7	12.25	22.3	26.38	27.9	13.28	8.9	1.92
24.9	12.57	22.4	30.31	28	13.51	9.8	2.17
26.9	18.27	23.4	42.09	31.3	20.48	10.6	2.48
27.2	20.91	23.5	43.19	31.5	20.82	10.8	2.6
27.7	21.44	24	51.67	32.2	23.41	11.1	2.97
28.8	27.67	24.9	64.86	33.2	26.22	11.6	4.33
30.1	32.11	25.5	74.13	34.4	31.06	11.8	5.32
30.7	35.07	25.7	75.23	34.8	31.4	12.4	8.54
31.4	38.66	26.1	81.35	36.3	34.89	12.6	11.02
31.8	39.5	26.3	84.02	37.4	38.04	12.7	11.26
32.6	42.78	26.9	86.69	38.1	40.8	12.9	15.97
33.7	49.22	27.8	94.7	40.6	46.09	13.3	17.7
34.5	50.17	28.3	96.27	42.1	47.21	13.4	19.31
35.2	53.34	28.4	96.58	42.3	47.44	13.5	24.63
36.6	57.25	29.2	100.82	43.9	50.03	13.5	30.2
37.9	60.84	30	105.06	45	51.83	13.7	33.17
38.9	61.52	30.3	105.22	46.1	52.22	13.8	33.79
41.1	66.17	31.6	109.31	47.7	54.02	14.2	48.39
42.6	68.39	32.5	111.66	50	55.37	14.3	49.76
43.6	69.23	32.7	112.45	50.4	55.6	14.4	51.86
45	70.5	33.7	114.17	51.8	56.84	14.5	60.89
46.3	71.61	34.3	114.8	53.6	57.46	14.6	69.93
47.7	72.45	34.8	115.9	54.5	57.91	14.7	70.43
48.4	73.3	35.7	117.63	56	59.26	14.8	80.82
49.7	73.93	36.4	118.57	57.9	59.93	14.9	83.67
51.1	74.78	38	121.08	60.4	61.51	15.1	85.4
52.4	75.31	38.8	121.95	62	61.9	15.2	87.51
53.6	75.89	39.7	122.73	63.8	62.92	15.5	95.92
54.1	76.42	40.4	123.05	64.5	63.14	15.6	97.28
56.7	77.37	41.6	124.3	66.7	64.49	15.8	102.85
58	78.11	42.5	125.09	68.3	64.94	15.9	105.7
58.6	78.53	43.5	125.72	69	65.17	16	106.07
63.3	80.38	45.9	127.84	75	67.02	16.1	106.32
64.5	80.59	46.9	128.31	75.8	67.36	16.3	111.02
64.9	80.69	47.7	128.62	76.1	67.47	16.4	111.52
67	81.43	49.3	129.88	78.9	68.2	16.5	111.64
67.5	81.75	50.4	130.51	80.5	68.54	16.7	115.85
69.1	82.01	51.9	131.13	80.9	68.77	17.7	124.88
71.4	82.65	52.3	131.45	82.9	69.33	17.8	127.98
72.5	83.28	52.9	131.61	84.9	69.78	17.9	128.6
75	83.7	53.6	132	87.2	70.17	18.3	130.45
76.2	84.23	55.4	132.63	89.1	70.74	18.4	131.07
77.3	84.5	57.5	133.73	90.5	71.07	18.5	132.93
78.7	84.6	58.1	133.88	91.4	71.19	18.8	135.4
81	85.34	59.2	134.35	94.1	71.69	19	137.26
84	85.76	59.4	134.67	96.4	72.03	19.3	137.88

85.8	86.13	61.5	135.06	98.5	72.59	19.6	139.74
86.3	86.34	61.8	135.37	101.2	72.99	20.1	142.21
89.4	86.66	63.2	135.85	103.7	73.21	20.4	143.45
91.2	87.08	65	136.32	105.6	73.44	20.5	145.92
93.8	87.45	65.4	136.47	107.5	73.89	21.2	148.4
96.1	87.66	66.6	136.95	110.1	74.06	21.8	149.64
96.6	87.77	67.6	137.26	110.5	74.17	22.1	150.26
97.5	87.98	69.2	137.5	117.5	74.9	22.3	152.11
98.1	88.09	70.2	137.81	117.6	75.01	22.7	153.35
103.1	88.56	70.6	137.97	122.7	75.35	23	153.97
106	88.88	71.5	138.28	126.4	75.63	23.6	155.21
106.3	88.98	73	138.44	129.2	75.97	24	156.45
111.1	89.35	74.7	138.91	129.9	76.08	24.2	157.06
113.3	89.56	76.2	139.38	136.3	76.59	24.8	158.3
114.6	89.67	77.9	139.46	139.7	76.65	25.2	159.54
117	89.93	79.9	139.93	141.6	76.87	25.8	160.16
119.3	90.04	81.3	140.24	149.6	77.38	26.3	161.4
123.7	90.3	83.3	140.4	152.5	77.6	26.6	162.63
127.2	90.62	85.5	140.79	155.4	77.66	27.8	163.87
129.5	90.73	86.5	140.95	158.4	77.88	28.1	164.49
132.4	90.89	88.1	141.26	160.8	78	28.9	165.11
136.4	91.1	91.6	141.74	169.1	78.39	30.3	166.97
141.4	91.36	93	141.81	173.3	78.56	30.7	167.58
144.5	91.57	95.7	142.13	176	78.67	31.3	168.2
146.1	91.68	98.4	142.44	181	78.84	32.3	168.82
150	91.84	103.3	142.83	183	78.95	33.5	169.44
152.8	91.94	106.5	143.15	195	79.29	34.1	170.06
159.9	92.31	107.6	143.31	201	79.52	34.5	170.68
165.4	92.47	110.8	143.54	205	79.57	35.7	171.3
168.2	92.57	112.9	143.7	211	79.74	36.6	171.92
173.4	92.73	120.8	144.25	223	80.02	38.2	172.47
176	92.84	125	144.48	231	80.19	40	173.71
189	93.16	127.9	144.64	240	80.36	41.6	174.33
196	93.31	132.6	144.88	244	80.42	43.4	174.95
200	93.42	135.6	145.03	254	80.59	45.6	175.51
207	93.58	146.7	145.58	259	80.64	47.4	176.12
222	93.79	153.4	145.82	276	80.87	49	176.74
230	93.95	157.5	145.9	295	81.04	52.2	177.36
242	94.05	164.8	146.13	302	81.15	55.9	177.92
246	94.16	177.7	146.53	323	81.32	60.1	178.54
257	94.26	187	146.68	338	81.43	63.8	179.1
263	94.37	198	146.92	346	81.49	74.1	180.27
284	94.53	205	147	368	81.65	80.8	180.83
306	94.69	217	147.15	373	81.71	90.3	181.38
314	94.74	223	147.31	391	81.82	101.5	181.88
339	94.9	243	147.55	400	81.88	117.4	182.38
354	95	266	147.78	424	82.05	135.8	182.87
364	95.06	273	147.86	442	82.16	157.6	183.3
414	95.22	301	148.1	479	82.33	186	183.67
424	95.27	319	148.25	490	82.39	223	184.05
456	95.37	339	148.33	522	82.44	268	184.29
477	95.43	379	148.57	530	82.5	387	184.6
519	95.59	417	148.65	583	82.72	452	184.66
564	95.69	440	149.67	607	82.72	519	184.79
635	95.85	484	149.98	668	82.89	683	184.79
662	95.9	847	150.29	692	82.95	825	184.85
701	96.75	1221	150.45	753	83.06	972	184.91
751	96.96	1539	150.45	996	83.34	1030	185.04
1932	96.96	1601	150.53	1999	83.34	1966	185.04

Table A.22—Mercury intrusion data for core 35, 36 and 38 (related to Fig. 25, data volume has been reduced slightly).

Intrusion					
Sample 35		Sample 36		Sample 38	
P [bar]	V [mm^3/g]	P [bar]	V [mm^3/g]	P [bar]	V [mm^3/g]
1.2	0.08	1.2	0.09	1.4	0.07
1.7	0.24	1.4	0.26	1.6	0.22
2	0.41	1.6	0.43	1.9	0.37
2.4	0.57	1.8	0.61	2.3	0.52
2.9	0.73	2.1	0.78	3.3	0.67
3.3	0.9	2.2	0.96	3.9	0.82
3.9	1.06	2.6	1.13	4.8	0.97
4.4	1.22	2.9	1.3	5.7	1.11
5	1.39	3.2	1.48	6.9	1.26
5.2	1.55	3.3	1.65	8.1	1.41
6.6	2.04	4	2	8.5	1.56
6.8	2.2	4.1	2.17	10	1.71
7.7	2.53	4.3	2.35	11.1	1.78
8	2.69	4.5	2.52	11.4	2.08
8.5	3.5	4.7	2.7	12.1	3.27
8.8	3.67	5.1	2.87	12.5	3.71
9.3	5.46	5.3	3.22	13.1	5.94
9.5	5.95	5.7	3.39	13.2	6.09
9.8	6.93	5.8	3.57	13.6	10.85
9.9	7.09	5.9	3.74	13.8	12.63
10	9.86	6.6	4.44	13.9	14.56
10.1	10.27	7	4.78	14	18.28
10.3	11.08	7.3	4.96	14.1	21.84
10.4	15.48	7.5	5.31	14.4	23.92
10.6	16.29	8	6	14.6	26.45
10.7	19.88	8.3	6.18	14.7	27.49
11	22.32	8.6	7.22	14.9	42.05
11.2	30.8	9.1	7.39	15	44.58
11.3	38.29	9.3	8.44	15.1	53.05
11.5	47.25	9.9	9.31	15.2	59.14
11.6	50.19	10.3	11.31	15.3	60.63
11.7	57.85	10.6	11.48	15.4	66.72
11.8	60.45	10.9	15.14	15.5	73.41
11.9	62.41	11	15.83	15.6	76.97
12	70.07	11.4	19.14	15.8	78.46
12.1	76.75	11.5	20.88	15.9	85.74
12.3	85.38	11.7	22.62	16.1	88.42
12.4	91.74	12	29.23	16.3	90.94
12.5	94.35	12.1	33.06	16.4	97.48
12.6	101.03	12.2	40.71	16.5	103.13
12.7	102.66	12.4	45.24	16.6	103.43
12.8	111.62	12.5	52.72	16.7	109.96
13	113.9	12.6	56.72	16.9	110.26
13.1	116.67	12.8	59.33	17.2	115.16
13.2	117.65	12.9	60.9	17.3	118.58
13.3	124.98	13	70.81	17.6	119.92
13.4	130.52	13.1	72.9	17.8	122.89
13.5	131.99	13.2	80.73	17.9	123.34
13.6	137.53	13.4	88.04	18.2	129.43
13.7	137.85	13.5	96.56	18.4	131.21
13.8	138.99	13.9	101.96	18.6	132.7
14	144.86	14	107.7	18.7	132.85
14.1	146.16	14.2	109.26	19	136.27
14.2	148.61	14.3	115.18	20.1	144.74
14.3	152.03	14.5	116.05	20.4	147.71
14.5	152.35	14.6	119.7	20.6	149.94
15	161.15	14.9	122.49	20.8	150.68
15.2	163.6	15	123.71	21.3	152.91
15.3	166.86	15.1	126.84	21.6	153.65

15.4	170.12	15.2	129.62	22	156.62
15.9	172.56	15.6	133.8	22.3	157.37
16.2	174.19	15.7	134.15	22.6	159.6
16.4	176.63	15.8	136.58	23.2	160.34
16.6	179.89	15.9	139.89	23.6	161.82
17	181.52	16.3	140.41	23.8	164.05
17.2	183.15	16.4	143.02	24.7	165.54
17.4	185.6	16.7	145.98	25.5	167.03
17.8	188.04	16.8	146.67	25.8	167.77
18	188.85	17.2	149.63	26	168.51
18.5	190.48	17.6	152.07	26.3	169.25
18.7	192.93	17.9	152.41	27	170.74
19.2	193.74	18	155.2	27.3	172.23
19.5	196.19	18.4	157.29	28.4	172.97
19.8	197.82	18.6	159.9	28.7	173.71
20.4	200.26	19.1	160.42	29	175.2
21.1	201.89	19.3	160.59	30.5	175.94
21.6	202.7	19.4	160.77	31.2	176.68
21.9	205.15	19.8	162.51	31.7	178.17
22.7	205.96	21.3	169.46	33.2	178.91
23.3	206.78	21.7	172.94	34.1	179.66
23.7	207.59	22.6	173.81	34.8	180.4
24	209.22	22.8	174.68	35.3	181.14
24.7	210.85	23.1	176.42	37	181.89
26	211.67	24.2	178.16	38.1	182.55
27.5	214.11	24.6	179.9	39.1	183.3
28.5	214.93	25.6	180.77	40.7	184.04
29.4	215.74	26.7	182.51	42.1	184.78
29.8	216.56	27.2	183.38	43.7	185.53
30.9	217.37	27.7	184.25	45.9	186.2
32	218.18	29.1	185.99	47.4	186.94
32.7	219	29.6	186.86	51	187.68
34.3	219.81	30.6	187.73	53.6	188.35
36.1	220.63	31	188.6	56.7	189.09
38.4	221.36	32.8	189.47	60.7	189.84
40.1	222.18	33.2	190.34	65.6	190.5
41.4	222.99	35.6	191.21	70.2	191.17
44.5	223.81	36.5	192.08	78.1	191.84
48.4	224.54	38.2	192.87	83.9	192.58
53.9	225.27	40.6	193.74	92.5	193.18
61.1	226.01	44.7	195.48	105.5	193.85
70.7	226.74	47.9	196.26	121	194.44
87.3	227.39	50.8	197.13	143	194.96
124.7	227.8	55.5	197.91	166.9	195.48
185	228.04	59.3	198.78	202	195.85
271	228.04	65.5	199.57	251	196.15
344	228.04	73.2	200.35	302	196.45
410	228.12	80.6	201.13	373	196.45
489	228.12	95	201.83	432	196.67
562	228.12	109.5	202.52	498	196.75
622	228.37	128.8	203.22	563	196.89
691	228.45	160.5	203.74	651	196.89
764	228.45	200	204.18	735	196.89
816	228.78	252	204.44	801	196.89
885	228.86	315	204.61	881	196.89
964	228.86	381	204.78	950	196.89
1040	228.86	450	204.87	1019	197.04
1112	228.94	520	204.96	1066	197.34
1949	228.94	1942	204.96	1989	197.34

Table A.23—Mercury extrusion data core 2, 3, 4 and 32 (related to Fig. 26, data volume has been reduced slightly).

Extrusion							
Sample 2		Sample 3		Sample 4		Sample 32	
P [bar]	V [mm^3/g]	P [bar]	V [mm^3/g]	P [bar]	V [mm^3/g]	P [bar]	V [mm^3/g]
1932	96.96	1989	150.53	1999	83.34	1966	185.04
698	96.75	1458	150.45	209	83.29	1625	185.04
549	96.69	1129	150.37	200	83.23	1526	185.04
324	96.59	955	150.29	191	83.17	1435	185.04
261	96.53	718	150.22	185	83.12	1356	185.04
167.3	96.11	433	149.67	158.6	83.01	1269	185.04
130.9	95.8	371	149.43	151	82.95	1185	185.04
106.5	95.43	237	149.27	145.4	82.84	1108	185.04
86.5	94.63	192	148.88	140.4	82.78	1033	185.04
84.5	94.53	142	148.65	134.2	82.72	947	184.91
78.7	94.37	91.7	147.55	120.5	82.61	878	184.85
76.1	94.26	76.7	146.92	115.9	82.5	795	184.85
73.8	94.21	63.6	146.29	110.5	82.44	729	184.79
70.9	94.11	57.1	145.58	106.5	82.33	625	184.79
69.5	94	53.3	144.8	101.9	82.27	558	184.79
65.6	93.84	50.9	144.56	94.3	82.11	504	184.79
63	93.74	49.9	144.41	91	81.99	445	184.66
62	93.63	48.5	144.25	86.7	81.94	378	184.6
59.9	93.52	47.6	144.09	83.8	81.82	301	184.48
58.6	93.42	46.3	143.93	80.6	81.77	240	184.29
56.1	93.26	44.7	143.62	75.9	81.54	191	184.05
54.5	93.16	44	143.46	73.5	81.49	147.4	183.3
53.1	93.05	43.1	143.31	71.2	81.37	106.7	182.99
52.1	92.94	42.3	143.23	68.9	81.26	85.3	182.56
50.9	92.89	41.4	143.07	66.7	81.15	69.3	182.07
48.8	92.68	40.1	142.76	62.7	80.98	58.7	181.51
47.6	92.57	39.7	142.6	60.7	80.87	50.1	181.01
46.9	92.47	38.9	142.44	59.1	80.75	43.8	180.39
46.1	92.36	37.9	142.29	57.3	80.7	39.3	179.84
45.1	92.26	37.7	142.13	55.8	80.59	35.7	179.22
43.4	92.05	36.3	141.81	53.4	80.36	32.5	178.66
42.7	91.99	35.9	141.5	51.4	80.25	29.7	178.04
42.1	91.89	34.5	141.26	50.6	80.19	28	177.42
41.4	91.78	33.8	141.11	49.4	80.08	26.4	176.87
40.5	91.68	33.4	140.95	48.2	79.97	25	176.25
38.8	91.36	32.6	140.64	45.5	79.74	23.5	175.63
38.3	91.25	32	140.48	45.1	79.63	22.3	175.01
37.5	91.15	31.8	140.32	43.7	79.52	21.2	174.39
37.1	91.04	31.1	140.17	42.8	79.46	20.7	173.77
36.4	90.94	30.7	139.69	41.9	79.35	19.4	173.15
35.5	90.73	29	139.07	40	79.12	18.8	172.6
34.9	90.67	28.3	138.75	39.1	79.01	18	171.98
34.2	90.46	28.1	138.59	38.7	78.9	17.6	171.36
33.7	90.36	27.5	138.44	37.7	78.78	17.2	170.74
32.8	90.14	27.3	138.12	36.7	78.67	16.4	170.12
31.2	89.72	26.3	137.57	35.8	78.45	16	168.88
30.8	89.62	25.5	137.26	35.1	78.22	15.2	168.27
30.2	89.51	25.1	136.79	33.7	78.05	14.8	167.03
29.9	89.41	24.3	136.47	32.5	77.94	14	165.79
29.4	89.19	24	136.16	31.7	77.83	13.7	164.55
28.6	88.88	23.2	135.53	31.1	77.6	13	163.31
27.6	88.67	22.6	135.06	30.5	77.49	12.6	160.84
27.2	88.35	22.3	134.9	30.3	77.38	11.8	159.6
26.4	88.3	21.5	134.12	29.6	77.27	11.4	156.51
26	88.09	21.1	133.65	29.1	77.04	11.1	155.27
24.9	87.56	19.9	132.23	27.7	76.82	10.5	152.18
24.2	87.45	19.4	132.08	27.3	76.59	10.1	150.32
23.8	87.03	19.1	131.45	26.5	76.53	9.6	148.52
22.9	86.82	18.6	131.21	26.3	76.31	9.3	143.57

22.4	86.4	18.3	130.43	25.4	76.08	8.7	141.1
21.3	85.76	17.2	128.54	24.4	75.75	8.4	135.53
21	85.66	16.3	127.29	23.9	75.52	8.2	132.43
20.4	85.44	16	126.82	23	75.41	7.6	126.25
20.1	85.02	15.4	125.87	22.5	75.07	7.4	123.15
19.4	84.81	15.1	125.25	21.8	74.96	7.1	116.96
18.1	83.91	14.3	122.58	21.2	74.51	5.9	93.08
17.6	83.17	13.6	121.63	20.6	74.28	5.7	89.86
17.2	82.96	13.2	119.28	20.3	74.17	5.4	83.54
16.6	82.43	12.5	118.18	19.6	73.72	5.2	80.45
16.4	82.12	12.1	115.82	19.2	73.5	4.8	74.76
15.5	81.17	11.2	112.37	17.8	72.88	4.5	72.16
15.1	80.85	10.5	109.86	17.4	72.65	4.3	68.2
14.2	79.79	10.2	108.44	16.8	72.31	3.4	67.21
13.8	79.27	9.6	105.54	16.5	72.09	2.8	66.59
13	78.42	9.3	103.81	15.9	71.75	1.8	65.72
12.1	77.26	8.2	98.94	14.8	70.96	1.5	65.47
11.8	76.84	7.5	96.27	14.4	70.63	1.1	64.98
10.7	75.36	7.1	93.91	13.9	69.95	0.8	64.73
10.1	74.72	6.2	92.97	13.1	69.61	0.7	64.36
9.3	73.72	5.8	91.56	12.8	69.27	0.6	64.24
8.3	72.35	4.7	89.83	11.9	68.49	0.5	63.87
8.1	71.82	4.1	89.52	11.3	67.81	0.4	63.12
7.8	71.08	3.8	88.58	10.9	67.47	0.3	62.63
7.1	70.55	3.2	87.79	10.5	66.57		
6.6	69.71	3	87.48	9.6	66.18		
5.3	68.97	2.1	86.38	8.5	64.83		
4.5	68.33	1.6	85.75	8.3	64.49		
4.2	68.02	1.3	85.28	8	63.7		
4	67.6	0.9	84.96	7.3	63.25		
3.4	67.38	0.7	84.49	7	62.24		
2.4	66.86	0.3	83.71	5.7	60.66		
2	66.64			4.9	60.21		
1.7	66.43			4.6	59.31		
1.2	66.22			4.3	58.98		
0.9	66.12			3.8	58.53		
0.6	65.8			2.7	57.4		
0.5	65.59			2.4	56.84		
0.4	65.48			1.7	56.61		
0.3	65.27			1.4	56.16		
0.2	64.96			1.2	55.94		
				0.7	55.49		
				0.5	55.37		
				0.4	55.04		
				0.3	54.36		
				0.2	53.35		

Table A.24—Mercury extrusion data for core 35, 36 and 38 (related to Fig. 26).

Extrusion					
Sample 35		Sample 36		Sample 38	
P [bar]	V [mm^3/g]	P [bar]	V [mm^3/g]	P [bar]	V [mm^3/g]
1949	228.94	1942	204.96	1989	197.34
1647	228.94	1666	204.96	1679	197.34
1552	228.94	1577	204.96	1579	197.34
1477	228.94	1486	204.96	1482	197.34
1396	228.94	1398	204.96	1398	197.34
1304	228.94	1336	204.96	1318	197.34
1228	228.94	1254	204.96	1235	197.34
1156	228.94	1179	204.96	1159	197.34
1078	228.94	1118	204.96	1078	197.34
998	228.86	1057	204.96	998	197.04
933	228.86	997	204.96	924	196.89
859	228.86	939	204.96	856	196.89
787	228.78	879	204.96	790	196.89

714	228.45	817	204.96	715	196.89
638	228.45	757	204.96	642	196.89
577	228.37	678	204.96	579	196.89
504	228.12	613	204.96	498	196.89
437	228.12	547	204.96	437	196.75
370	228.12	472	204.96	369	196.45
298	228.04	398	204.87	297	196.45
235	228.04	336	204.78	247	196.15
172	228.04	269	204.61	197	195.85
106.7	227.8	202	204.44	156.5	195.48
52.5	226.82	158.9	203.74	117.2	194.44
16.9	226.41	116.4	203.22	93.2	193.85
10.8	225.6	83.3	201.83	77.2	193.25
9.3	224.87	63.6	199.56	63.9	192.66
8.2	224.05	50.4	197.91	56.2	191.99
7.5	223.24	40.1	197.13	49.2	191.32
7.1	222.42	35.9	196.26	43.9	190.58
6.8	220.79	31.5	195.48	40.1	189.91
6.2	219.98	28.1	194.61	37.5	189.17
5.9	217.53	24.8	193.82	35.1	188.42
5.3	215.9	24	192.95	32.7	187.76
5.1	214.27	21.8	192.08	31.3	187.01
4.6	209.39	20.4	191.21	29	186.27
4.3	206.94	19.3	190.34	27.6	185.53
4.2	201.24	18.4	189.56	26.4	184.86
3.8	197.98	17.2	188.69	25.3	184.12
3.7	191.46	16.9	187.82	23.9	183.37
3.3	188.2	16	186.95	23.5	182.63
3.2	180.87	15.8	186.08	22.6	181.89
2.9	177.61	14.6	183.47	21.7	181.14
2.8	174.35	14.1	182.6	20.6	179.66
2.7	167.83	13.3	180.86	20.1	178.91
2.4	164.58	13	179.99	19.3	178.17
2.2	159.69	12.4	177.38	18.9	177.5
1.9	157.24	12.1	176.51	17.9	176.76
1.7	153.98	11.6	175.64	17.7	176.02
1.5	152.35	11.3	172.16	17.1	174.53
1.2	150.73	10.9	170.42	16.7	173.79
0.8	149.91	10.2	165.2	15.9	171.56
0.5	145.35	8.1	140.93	15.4	170.82
0.4	144.7	7.8	137.1	15	168.59
0.3	143.23	7.3	128.58	14.3	167.1
0.2	134.43	7.1	124.23	14	165.61
		6.8	115.35	13.4	164.13
		6.6	110.83	13.1	163.39
		6.3	101.43	12.5	160.41
		6.1	96.91	12.1	158.18
		5.9	87.52	11.8	152.98
		5.6	82.82	11.1	150.75
		5.5	78.29	10.8	145.55
		5.1	69.6	10.1	142.58
		4.8	65.59	8.2	118.73
		4.3	58.98	8	111.15
		3.8	56.89	7.6	107.44
		3.3	54.81	7.3	99.71
		2.3	54.28	7.1	96
		1.9	53.41	6.6	89.01
		1.3	53.07	6.3	85.89
		1.1	52.72	5.5	83.51
		0.9	52.54	4.8	81.28
		0.8	52.37	3.3	80.84
		0.7	52.02	2.6	79.95
		0.6	51.85	1.9	79.65
		0.5	51.33	1.2	79.06
		0.4	50.98	0.9	78.76
		0.3	50.46	0.5	78.16
		0.2	47.32	0.3	77.87

				0.2	76.38

Table A.25—Void-phase autocorrelation function of the Ekofisk chalk samples (Fig. 27).

	Sample						
u **(pixel)**	**2**	**3**	**4**	**32**	**35**	**36**	**38**
0	1	1	1	1	1	1	1
1	0.8530233	0.858126	0.850479	0.867084	0.880774	0.875489	0.867261
2	0.71465851	0.737975	0.710674	0.740582	0.767501	0.757405	0.741707
3	0.58749016	0.628238	0.583704	0.623348	0.661738	0.647745	0.62464
4	0.47551698	0.52529	0.474222	0.518324	0.566096	0.549245	0.520066
5	0.381075	0.43511	0.383275	0.426886	0.482233	0.463399	0.429408
6	0.30316429	0.360647	0.309676	0.348899	0.409865	0.39008	0.352769
7	0.24079353	0.297893	0.251597	0.283853	0.34816	0.328323	0.289078
8	0.191438	0.244995	0.206175	0.230335	0.295893	0.276808	0.236953
9	0.15316996	0.203565	0.170789	0.186554	0.252651	0.234139	0.194862
10	0.12370297	0.1707	0.143186	0.151266	0.217118	0.199211	0.160714
11	0.10061662	0.142787	0.121418	0.122596	0.187588	0.170712	0.133037
12	0.08275658	0.120284	0.104115	0.099679	0.163182	0.147475	0.110889
13	0.06875571	0.103115	0.090147	0.08173	0.143113	0.128352	0.093124
14	0.0578448	0.088223	0.079045	0.067572	0.126662	0.112628	0.078949
15	0.04929886	0.075462	0.070362	0.055941	0.112817	0.099459	0.067589
16	0.04250769	0.066383	0.063059	0.04663	0.100878	0.08812	0.058085
17	0.03697359	0.05864	0.056804	0.039058	0.090614	0.078065	0.050583
18	0.0325152	0.050908	0.051437	0.03306	0.081932	0.069072	0.044552
19	0.0286812	0.045223	0.047081	0.028223	0.074573	0.061074	0.039797
20	0.02543521	0.041062	0.043262	0.024441	0.067605	0.053993	0.035828
21	0.02240281	0.036524	0.039977	0.021252	0.060385	0.047797	0.032304
22	0.01968113	0.033077	0.037494	0.018901	0.053932	0.0422	0.029425
23	0.01710416	0.031538	0.035319	0.016997	0.047973	0.037283	0.027202
24	0.0151321	0.029602	0.033387	0.015358	0.04294	0.032771	0.025569
25	0.01363084	0.027685	0.031572	0.014107	0.038085	0.028847	0.023974
26	0.01224797	0.027073	0.029785	0.013197	0.033773	0.025057	0.022243
27	0.01075178	0.026432	0.028073	0.012669	0.029798	0.021282	0.020318
28	0.00912058	0.024833	0.026484	0.012243	0.026184	0.017784	0.01822
29	0.00765369	0.023969	0.02494	0.012042	0.023522	0.014252	0.016346
30	0.00632056	0.023778	0.023536	0.011659	0.021319	0.010653	0.014578
31	0.00526911	0.022014	0.022286	0.011289	0.019058	0.007432	0.013084
32	0.00427987	0.020435	0.02098	0.010536	0.016526	0.004765	0.011757
33	0.00317011	0.0201	0.019285	0.009539	0.014161	0.003013	0.010188
34	0.00202952	0.019071	0.017292	0.007958	0.012188	0.001815	0.008774
35	0.0008665	0.017785	0.015187	0.005687	0.010185	0.001148	0.007345
36	0.00019861	0.017451	0.013461	0.003347	0.008089	0.000932	0.006149
37	-5.517E-05	0.017189	0.012152	0.001098	0.006572	0.001246	0.005189
38	-0.00014527	0.015999	0.011238	-0.00066	0.005307	0.001653	0.004208
39	-0.00018496	0.015385	0.010077	-0.0018	0.004728	0.002398	0.003098
40	-0.00068022	0.015254	0.009047	-0.00251	0.003823	0.003187	0.00225
41	-0.00132607	0.014027	0.008674	-0.0033	0.002526	0.003721	0.00158
42	-0.00193017	0.012372	0.008519	-0.0038	0.001021	0.004179	0.000849
43	-0.00274011	0.011877	0.008448	-0.00418	-0.00041	0.00467	-4.3E-06
44	-0.00339411	0.010918	0.008447	-0.00443	-0.00127	0.005151	-0.00091
45	-0.00402457	0.009149	0.008755	-0.00461	-0.00215	0.005284	-0.00162
46	-0.00437746	0.008184	0.008979	-0.00482	-0.00293	0.005298	-0.00186
47	-0.00454496	0.007499	0.009092	-0.00513	-0.00347	0.005056	-0.00156
48	-0.00479609	0.006231	0.009168	-0.00561	-0.00376	0.004699	-0.00134
49	-0.00537576	0.005594	0.00856	-0.00606	-0.00399	0.004085	-0.00115
50	-0.00608772	0.0057	0.007579	-0.00623	-0.00424	0.003247	-0.00121
51	-0.00693578	0.005061	0.006047	-0.00617	-0.00394	0.002541	-0.0016
52	-0.00781121	0.004096	0.004201	-0.00588	-0.00398	0.001955	-0.00224
53	-0.0083112	0.004142	0.002348	-0.00553	-0.0042	0.001333	-0.00349
54	-0.00843296	0.003735	0.000554	-0.0051	-0.00476	0.00088	-0.00481
55	-0.00846113	0.002676	-0.00083	-0.0047	-0.00543	0.000475	-0.00614
56	-0.00813713	0.002404	-0.00186	-0.00415	-0.0062	0.000164	-0.00742
57	-0.00757333	0.002573	-0.00274	-0.00367	-0.00683	-9.6E-05	-0.00865
58	-0.00692847	0.002235	-0.00347	-0.00341	-0.0076	-0.00018	-0.00956
59	-0.0063928	0.001828	-0.00389	-0.00305	-0.00785	-0.00024	-0.01055

60	-0.00567856	0.002283	-0.0042	-0.00263	-0.00804	-1.3E-05	-0.01121
61	-0.00519341	0.002129	-0.00393	-0.00234	-0.00806	0.000437	-0.01189
62	-0.0049622	0.001548	-0.00342	-0.00232	-0.00799	0.000582	-0.01274
63	-0.00449752	0.001724	-0.00321	-0.0022	-0.00752	0.000743	-0.01329
64	-0.00401436	0.001491	-0.00338	-0.00225	-0.0069	0.000658	-0.01357
65	-0.00341198	0.000388	-0.00389	-0.00249	-0.00627	0.000219	-0.01369
66	-0.00255476	-0.00037	-0.00445	-0.00283	-0.00543	0.000119	-0.01352
67	-0.00143821	-0.00091	-0.00455	-0.00312	-0.00424	0.000243	-0.01313
68	-0.00077528	-0.00211	-0.00417	-0.00333	-0.0033	0.000449	-0.01221
69	-0.00037955	-0.00316	-0.00374	-0.00357	-0.00247	0.000954	-0.01096
70	-0.00055498	-0.00316	-0.00289	-0.00339	-0.00211	0.001428	-0.00973
71	-0.00089706	-0.00324	-0.002	-0.00333	-0.00226	0.001504	-0.00815
72	-0.00170846	-0.00337	-0.0013	-0.00315	-0.00294	0.001527	-0.00701
73	-0.00288387	-0.0026	-0.0008	-0.00292	-0.00387	0.001638	-0.00563
74	-0.00416987	-0.00148	-0.00035	-0.00283	-0.00486	0.002001	-0.00432
75	-0.00526919	-0.00103	-0.0002	-0.00275	-0.00589	0.002245	-0.00298
76	-0.00614754	-0.00057	6.29E-06	-0.00257	-0.007	0.002244	-0.00175
77	-0.00647662	-0.0002	-0.00032	-0.00227	-0.00816	0.002224	-0.00064
78	-0.00686187	-0.00079	-0.00046	-0.00202	-0.00931	0.002204	0.000752
79	-0.00733367	-0.00162	-0.0005	-0.00199	-0.01008	0.002322	0.001966
80	-0.00779965	-0.0018	-0.00029	-0.00156	-0.01047	0.002514	0.003301
81	-0.00803523	-0.00231	0.000342	-0.00085	-0.01046	0.002998	0.004628
82	-0.00822147	-0.00255	0.00083	-0.00041	-0.00998	0.003451	0.00581
83	-0.0081409	-0.00186	0.0016	3.36E-05	-0.00875	0.003982	0.006695
84	-0.00784736	-0.00067	0.002384	0.000453	-0.00685	0.004724	0.007292
85	-0.00760224	0.000211	0.002941	0.000657	-0.00469	0.005763	0.007515
86	-0.00726579	0.001382	0.003376	0.000903	-0.00245	0.006809	0.007517
87	-0.00706368	0.002513	0.003392	0.001189	-0.0007	0.007524	0.007407
88	-0.00702731	0.003126	0.003287	0.00123	0.000478	0.007984	0.007216
89	-0.00760199	0.00333	0.002984	0.00107	0.001471	0.008262	0.006982
90	-0.00818331	0.003538	0.002831	0.000892	0.002115	0.007931	0.006593
91	-0.00893753	0.003461	0.003033	0.000743	0.002483	0.007402	0.006244
92	-0.00909668	0.002809	0.003555	0.000779	0.002758	0.006961	0.005899
93	-0.00874205	0.002028	0.004853	0.001001	0.002564	0.00636	0.005862
94	-0.00821631	0.001457	0.006112	0.001191	0.001762	0.005868	0.005479
95	-0.00801577	0.000596	0.007776	0.001381	0.000976	0.005547	0.005153
96	-0.00803953	-0.00017	0.009389	0.001737	0.000856	0.005273	0.004613
97	-0.0080651	-0.00022	0.010628	0.0021	0.001054	0.005212	0.004125
98	-0.00811092	-0.00018	0.011546	0.002544	0.001843	0.004807	0.003446
99	-0.0084424	-0.00023	0.011953	0.002961	0.002771	0.004566	0.002422
100	-0.00872468	0.00015	0.011789	0.003248	0.0038	0.00413	0.001491
101	-0.00930583	0.000463	0.011069	0.00377	0.00477	0.003846	4.2E-05
102	-0.0097655	0.000342	0.010215	0.00429	0.005886	0.003493	-0.00136
103	-0.00994943	0.00028	0.009316	0.004515	0.007572	0.003106	-0.00282
104	-0.00998277	0.000921	0.008782	0.004817	0.00895	0.002801	-0.00399
105	-0.00956905	0.001023	0.008318	0.004953	0.010205	0.002501	-0.00471
106	-0.00877781	0.000758	0.007862	0.005059	0.011004	0.002261	-0.00493
107	-0.00767009	0.001163	0.007339	0.005029	0.011198	0.00235	-0.00509
108	-0.00649015	0.00138	0.006856	0.005031	0.011146	0.002337	-0.00455
109	-0.00550426	0.001196	0.006317	0.004947	0.010599	0.002444	-0.00382
110	-0.00491607	0.001523	0.005892	0.004779	0.00981	0.002295	-0.00313
111	-0.00462319	0.002203	0.005968	0.004619	0.008775	0.001896	-0.0026
112	-0.00417948	0.002203	0.005993	0.004545	0.007397	0.001492	-0.00187
113	-0.00377236	0.002159	0.006184	0.004533	0.00643	0.001026	-0.00077
114	-0.00350984	0.002592	0.006527	0.004233	0.005447	0.000418	0.000336
115	-0.00298336	0.002375	0.00713	0.003787	0.004602	0.000193	0.001615
116	-0.00251251	0.001351	0.007426	0.003156	0.003933	0.000331	0.002614
117	-0.00170882	0.000802	0.007618	0.002344	0.003312	0.000774	0.003408
118	-0.00102837	0.0002	0.007672	0.001455	0.002716	0.001183	0.004147
119	-0.00051194	-0.00078	0.007392	0.000457	0.001998	0.001489	0.004613
120	-0.00035705	-0.00125	0.007189	-0.0006	0.001723	0.001475	0.004732
121	-0.00029608	-0.00169	0.006815	-0.00169	0.001374	0.001341	0.004613
122	0.00003828	-0.00255	0.006341	-0.00258	0.000844	0.001369	0.004401
123	-4.793E-05	-0.00365	0.005764	-0.00336	0.000274	0.001527	0.004258
124	-0.00043694	-0.00414	0.004913	-0.00378	-0.00013	0.001455	0.004253
125	-0.00105374	-0.00452	0.004287	-0.00383	-0.00019	0.001248	0.004339
126	-0.0015618	-0.00497	0.003217	-0.00368	-0.0003	0.001048	0.004366
127	-0.00175727	-0.00466	0.002267	-0.00322	-4.6E-05	0.00111	0.004739

128	-0.00186864	-0.00408	0.00113	-0.00281	0.000475	0.001569	0.004991
129	-0.00205565	-0.00395	0.000188	-0.00212	0.000708	0.002188	0.005458
130	-0.00257173	-0.00371	-0.00027	-0.00136	0.00063	0.002812	0.006246
131	-0.00291079	-0.00323	-0.00061	-0.00031	-0.00022	0.003609	0.006804
132	-0.00282572	-0.00335	-0.0008	0.000802	-0.00161	0.004005	0.007081
133	-0.00269532	-0.00342	-0.00119	0.002115	-0.00234	0.004295	0.006844
134	-0.0023046	-0.00316	-0.00141	0.003342	-0.00304	0.004375	0.006389
135	-0.00205982	-0.00365	-0.00174	0.004901	-0.00351	0.004219	0.005695
136	-0.00190654	-0.0047	-0.00211	0.006071	-0.00381	0.003773	0.004773
137	-0.00179819	-0.00538	-0.00195	0.006892	-0.00425	0.003367	0.004123
138	-0.00190257	-0.00602	-0.00185	0.007486	-0.00488	0.002829	0.003227
139	-0.00208085	-0.00736	-0.00129	0.007631	-0.0055	0.002286	0.002674
140	-0.00238768	-0.00863	-0.00058	0.007188	-0.00643	0.001717	0.002449
141	-0.00286767	-0.00952	0.000135	0.006491	-0.00703	0.001142	0.002534
142	-0.00333011	-0.01032	0.000966	0.005757	-0.00718	0.000921	0.00325
143	-0.00368237	-0.01062	0.002076	0.005112	-0.00763	0.000552	0.003726
144	-0.00389037	-0.01022	0.003175	0.004697	-0.00807	0.000272	0.004098
145	-0.00409592	-0.00975	0.003969	0.004792	-0.00864	-0.00011	0.004345
146	-0.00383934	-0.00957	0.004328	0.004777	-0.00903	-0.00066	0.004431
147	-0.00337373	-0.00889	0.004501	0.005244	-0.00931	-0.00118	0.004517
148	-0.00301259	-0.00833	0.004436	0.005835	-0.00935	-0.00161	0.004324
149	-0.00250178	-0.00842	0.004539	0.006251	-0.00901	-0.0023	0.004455
150	-0.00222234	-0.00846	0.004373	0.006204	-0.00876	-0.00297	0.004618
151	-0.00225275	-0.0081	0.003909	0.00559	-0.00883	-0.00359	0.004851
152	-0.00247765	-0.00798	0.003114	0.004818	-0.00896	-0.00403	0.00515
153	-0.00288649	-0.00781	0.002093	0.004095	-0.00947	-0.00415	0.005218
154	-0.00332731	-0.00695	0.001359	0.003198	-0.00963	-0.00424	0.005044
155	-0.00401106	-0.00625	0.000875	0.002494	-0.00975	-0.00431	0.004791
156	-0.00475085	-0.00609	0.000266	0.002262	-0.00953	-0.00412	0.004517
157	-0.00523103	-0.00532	-9E-05	0.002097	-0.00904	-0.00363	0.004711
158	-0.00536199	-0.0046	-0.00019	0.002046	-0.00839	-0.00302	0.005108
159	-0.00507075	-0.00475	-0.00033	0.001699	-0.00754	-0.0023	0.005727
160	-0.00437125	-0.00486	-0.0009	0.001385	-0.00636	-0.00185	0.006615
161	-0.00360888	-0.0044	-0.00179	0.001079	-0.00545	-0.00159	0.007676
162	-0.00318872	-0.00423	-0.00252	0.000669	-0.00473	-0.00151	0.008527
163	-0.00252901	-0.00411	-0.00317	0.000277	-0.00426	-0.00167	0.008995
164	-0.00182173	-0.00353	-0.00311	-0.00025	-0.00391	-0.0021	0.009484
165	-0.00116643	-0.00281	-0.00255	-0.00066	-0.00412	-0.00217	0.009639
166	-0.00033672	-0.00268	-0.00156	-0.00091	-0.00469	-0.00213	0.00933
167	0.00035252	-0.00208	-0.00069	-0.00091	-0.00555	-0.00206	0.008807
168	0.00107596	-0.00078	0.000131	-0.00077	-0.00604	-0.00188	0.00812
169	0.00161768	-0.00041	0.000771	-0.00047	-0.00583	-0.00196	0.007218
170	0.00228515	-0.00021	0.000888	1.78E-05	-0.00548	-0.00237	0.00647
171	0.00284244	0.000584	0.00097	0.00054	-0.00481	-0.00286	0.005602
172	0.00365951	0.001166	0.000699	0.001067	-0.00382	-0.00358	0.004804
173	0.00431775	0.001544	0.000697	0.001437	-0.00284	-0.00443	0.003854
174	0.00489559	0.002638	0.000691	0.00197	-0.00209	-0.00489	0.002721
175	0.00539296	0.003737	0.000609	0.002033	-0.00171	-0.00542	0.00161
176	0.00552151	0.003837	0.000151	0.001779	-0.00165	-0.00584	0.000618
177	0.00518593	0.003955	-1.5E-05	0.001583	-0.00203	-0.00625	-0.00016
178	0.00481821	0.004547	-0.00018	0.001452	-0.00238	-0.00654	-0.001
179	0.00450791	0.00457	-0.00046	0.001378	-0.0028	-0.00651	-0.00185
180	0.00434258	0.004137	-0.00111	0.001283	-0.00293	-0.00614	-0.00286
181	0.00417632	0.004052	-0.00171	0.000814	-0.00271	-0.00535	-0.00363
182	0.00371778	0.003754	-0.00256	0.000398	-0.00247	-0.00463	-0.00436
183	0.00395849	0.003216	-0.00335	7.87E-05	-0.00232	-0.00368	-0.00494
184	0.00405855	0.00296	-0.00389	-0.00021	-0.00191	-0.00297	-0.00531
185	0.00427739	0.002538	-0.00414	-0.00061	-0.00191	-0.00214	-0.00597
186	0.00426471	0.001611	-0.00456	-0.00087	-0.00252	-0.00133	-0.00602
187	0.0038894	0.000967	-0.00481	-0.00129	-0.00331	-0.00071	-0.00611
188	0.00321393	0.000691	-0.00491	-0.00188	-0.00427	-0.00023	-0.00606
189	0.00244912	-0.00027	-0.00489	-0.00258	-0.00537	3.5E-05	-0.00576
190	0.00160559	-0.00108	-0.00488	-0.00322	-0.00649	-0.00011	-0.00567
191	0.00105345	-0.00147	-0.00448	-0.00323	-0.00704	-0.00047	-0.00576
192	0.00048002	-0.00191	-0.00448	-0.00341	-0.00756	-0.00079	-0.00603
193	-0.00017603	-0.00261	-0.00439	-0.00376	-0.00758	-0.0009	-0.00635
194	-0.00071524	-0.0028	-0.00426	-0.00419	-0.00696	-0.00109	-0.00658
195	-0.00113468	-0.0032	-0.00417	-0.00498	-0.00614	-0.00141	-0.00671

196	-0.00162139	-0.00419	-0.00441	-0.0058	-0.00512	-0.00165	-0.00636
197	-0.0020143	-0.00513	-0.00458	-0.00649	-0.00464	-0.00203	-0.00598
198	-0.00209471	-0.00555	-0.00485	-0.00689	-0.00432	-0.00233	-0.00555
199	-0.00197723	-0.00654	-0.00503	-0.00732	-0.00435	-0.00259	-0.00538
200	-0.00200608	-0.00737	-0.0047	-0.0077	-0.00424	-0.00284	-0.0056

Table A.26—Void-phase lineal path function of the Ekofisk chalk samples (Fig. 28).

				Sample			
u (pixel)	2	3	4	32	35	36	38
0	0.206897734	0.30064	0.183373	0.334836	0.381083	0.353642	0.351805
1	0.183031511	0.271172	0.161226	0.305631	0.353179	0.32557	0.321919
2	0.160200674	0.244354	0.140165	0.277369	0.326116	0.298405	0.293018
3	0.138869491	0.219511	0.120685	0.250632	0.300269	0.272639	0.265447
4	0.119558164	0.196273	0.103309	0.225839	0.276032	0.248647	0.23977
5	0.102561406	0.174992	0.088209	0.203188	0.253554	0.226626	0.216242
6	0.087741246	0.155954	0.075265	0.182647	0.232861	0.206558	0.194878
7	0.075018951	0.138923	0.064288	0.164156	0.213863	0.188323	0.175604
8	0.064114041	0.123672	0.054948	0.147548	0.196453	0.171745	0.15826
9	0.054796223	0.110161	0.047024	0.132566	0.180547	0.156679	0.142621
10	0.046815471	0.098217	0.040286	0.119108	0.166021	0.14302	0.128518
11	0.039986044	0.087534	0.034558	0.106982	0.152713	0.130602	0.115848
12	0.034150391	0.077995	0.029687	0.096064	0.140523	0.119316	0.104428
13	0.029139137	0.06957	0.025509	0.086299	0.129341	0.109048	0.094179
14	0.024852142	0.062053	0.021921	0.077573	0.119042	0.099711	0.085004
15	0.021215182	0.055315	0.018869	0.069741	0.109555	0.091215	0.076726
16	0.018142406	0.04935	0.016261	0.062737	0.100808	0.083446	0.069255
17	0.015531486	0.044063	0.014028	0.05643	0.092772	0.076363	0.062551
18	0.013314856	0.039312	0.012106	0.050781	0.085378	0.069897	0.056537
19	0.011432318	0.035052	0.010448	0.04572	0.078571	0.063988	0.05113
20	0.009847005	0.031241	0.009015	0.041171	0.072292	0.058611	0.046272
21	0.008494304	0.027842	0.007818	0.037078	0.066519	0.053702	0.041898
22	0.00734096	0.02483	0.006801	0.033414	0.061226	0.049185	0.037946
23	0.006341066	0.022175	0.005924	0.030113	0.056344	0.045044	0.034377
24	0.005479957	0.019805	0.005165	0.02713	0.051892	0.041248	0.031137
25	0.004742443	0.017695	0.004511	0.024451	0.047821	0.037794	0.028208
26	0.004114422	0.015835	0.003951	0.022027	0.044073	0.034623	0.025565
27	0.003576435	0.014176	0.003463	0.019859	0.040626	0.031688	0.023188
28	0.00310805	0.01268	0.003039	0.017909	0.037469	0.029008	0.021026
29	0.002707687	0.011351	0.002667	0.016165	0.034579	0.026533	0.019062
30	0.002356312	0.01017	0.002346	0.014595	0.031946	0.024256	0.017288
31	0.002052609	0.009102	0.002068	0.013202	0.029524	0.022164	0.01568
32	0.001796061	0.008131	0.001828	0.01195	0.027306	0.020251	0.014204
33	0.001569839	0.007267	0.001617	0.01081	0.025252	0.018491	0.01286
34	0.001367596	0.006486	0.001433	0.009783	0.023353	0.016886	0.011634
35	0.001189072	0.005791	0.00127	0.008852	0.021587	0.015415	0.010524
36	0.001029084	0.005163	0.001128	0.008022	0.019949	0.014076	0.009529
37	0.000886923	0.004604	0.001007	0.007272	0.018439	0.012861	0.008636
38	0.000768065	0.004104	0.000895	0.006591	0.017051	0.011746	0.007824
39	0.00066398	0.003656	0.000795	0.005972	0.015765	0.010727	0.007089
40	0.000576007	0.003262	0.000709	0.005405	0.014582	0.009789	0.006424
41	0.000503416	0.002906	0.000634	0.00489	0.013483	0.008933	0.005824
42	0.00044174	0.002588	0.000567	0.004428	0.01247	0.008147	0.005287
43	0.000386461	0.002315	0.000509	0.004017	0.011532	0.007439	0.004804
44	0.000338459	0.002072	0.00046	0.003657	0.010658	0.0068	0.004362
45	0.000297778	0.001852	0.000417	0.00333	0.009849	0.006212	0.003972
46	0.000263211	0.001664	0.000378	0.003034	0.009103	0.00568	0.003623
47	0.000233116	0.001501	0.000347	0.002774	0.008415	0.00519	0.003309
48	0.000203734	0.001349	0.00032	0.002538	0.007786	0.00475	0.003023
49	0.000179284	0.001212	0.000296	0.002325	0.007204	0.004346	0.002759
50	0.000159801	0.001084	0.000274	0.002133	0.006674	0.003974	0.002517
51	0.000141083	0.000968	0.000254	0.00196	0.006194	0.003628	0.002295
52	0.000123133	0.000861	0.000237	0.001807	0.005756	0.003313	0.002097
53	0.000105955	0.000765	0.000221	0.001672	0.005347	0.003028	0.001919
54	0.000090834	0.000676	0.000208	0.001551	0.004965	0.002764	0.00176
55	0.000078638	0.000598	0.000195	0.001439	0.004617	0.002529	0.001618

56	0.000067246	0.00053	0.000183	0.001336	0.004295	0.002321	0.001487
57	0.00005795	0.00047	0.000173	0.001238	0.004005	0.002136	0.001366
58	0.000049472	0.000418	0.000163	0.001146	0.003733	0.00197	0.001251
59	0.000041391	0.000375	0.000153	0.001059	0.003482	0.001816	0.001148
60	0.000034137	0.000339	0.000145	0.00098	0.003246	0.001674	0.001054
61	0.000027282	0.000307	0.000137	0.000908	0.003026	0.001546	0.000966
62	0.000021701	0.000277	0.000129	0.000841	0.002831	0.001428	0.000887
63	0.0000174	0.00025	0.000121	0.000779	0.002645	0.001316	0.000814
64	0.000013515	0.000225	0.000114	0.000723	0.00247	0.001213	0.000746
65	0.000010487	0.000202	0.000109	0.000676	0.002309	0.001117	0.000686
66	0.000007445	0.000181	0.000104	0.000631	0.002158	0.001029	0.000631
67	0.000005267	0.000162	0.0001	0.000592	0.002019	0.000945	0.000581
68	0.000003959	0.000145	9.59E-05	0.000555	0.00189	0.000863	0.000532
69	0.000002645	0.000131	9.17E-05	0.00052	0.001767	0.000785	0.000484
70	0.000001326	0.000119	8.75E-05	0.000489	0.001649	0.000712	0.000439
71	0.000000443	0.000109	8.33E-05	0.000461	0.001544	0.000647	0.000399
72	0	9.9E-05	7.9E-05	0.000435	0.001449	0.000589	0.000364
73	0	8.9E-05	7.47E-05	0.000411	0.00136	0.000534	0.000332
74	0	7.98E-05	7.13E-05	0.000387	0.001278	0.000484	0.000304
75	0	7.06E-05	6.84E-05	0.000365	0.001201	0.00044	0.000278
76	0	6.23E-05	6.54E-05	0.000343	0.001128	0.000402	0.000253
77	0	5.66E-05	6.24E-05	0.000322	0.001058	0.000369	0.000229
78	0	5.13E-05	5.94E-05	0.000301	0.000992	0.000339	0.000209
79	0	4.65E-05	5.64E-05	0.000281	0.000931	0.00031	0.000191
80	0	4.16E-05	5.38E-05	0.000263	0.000875	0.000283	0.000175
81	0	3.67E-05	5.12E-05	0.000248	0.000822	0.000257	0.00016
82	0	3.32E-05	4.86E-05	0.000234	0.00077	0.000233	0.000146
83	0	3.05E-05	4.6E-05	0.000221	0.000723	0.000212	0.000132
84	0	2.83E-05	4.38E-05	0.000209	0.000677	0.000191	0.00012
85	0	2.61E-05	4.16E-05	0.000197	0.000633	0.000172	0.000107
86	0	2.38E-05	3.94E-05	0.000187	0.000592	0.000155	9.63E-05
87	0	2.16E-05	3.72E-05	0.000176	0.000552	0.000138	8.59E-05
88	0	1.93E-05	3.5E-05	0.000166	0.000514	0.000123	7.69E-05
89	0	1.71E-05	3.28E-05	0.000156	0.000479	0.000108	7.02E-05
90	0	1.48E-05	3.05E-05	0.000146	0.000448	9.4E-05	6.39E-05
91	0	1.25E-05	2.83E-05	0.000136	0.000418	8.07E-05	5.85E-05
92	0	1.02E-05	2.65E-05	0.000126	0.000391	6.88E-05	5.44E-05
93	0	8.39E-06	2.47E-05	0.000117	0.000366	5.78E-05	5.08E-05
94	0	7.01E-06	2.29E-05	0.000109	0.000341	4.77E-05	4.77E-05
95	0	5.62E-06	2.15E-05	0.000102	0.000318	3.75E-05	4.45E-05
96	0	4.7E-06	2.02E-05	9.53E-05	0.000295	2.86E-05	4.13E-05
97	0	3.77E-06	1.88E-05	8.9E-05	0.000273	2.12E-05	3.86E-05
98	0	3.3E-06	1.79E-05	8.35E-05	0.000251	1.56E-05	3.68E-05
99	0	2.84E-06	1.7E-05	7.8E-05	0.000229	1.09E-05	3.5E-05
100	0	2.37E-06	1.61E-05	7.25E-05	0.000207	7.58E-06	3.32E-05
101	0	1.9E-06	1.52E-05	6.7E-05	0.000186	5.23E-06	3.14E-05
102	0	1.43E-06	1.43E-05	6.15E-05	0.000167	2.86E-06	2.95E-05
103	0	9.55E-07	1.34E-05	5.59E-05	0.00015	9.55E-07	2.77E-05
104	0	4.79E-07	1.24E-05	5.03E-05	0.000134	4.79E-07	2.59E-05
105	0	0	1.15E-05	4.46E-05	0.000121	0	2.4E-05
106	0	0	1.06E-05	3.9E-05	0.000109	0	2.26E-05
107	0	0	9.65E-06	3.42E-05	9.89E-05	0	2.12E-05
108	0	0	8.7E-06	3.05E-05	8.9E-05	0	2.03E-05
109	0	0	7.75E-06	2.67E-05	7.95E-05	0	1.94E-05
110	0	0	6.8E-06	2.38E-05	7E-05	0	1.85E-05
111	0	0	5.85E-06	2.09E-05	6.23E-05	0	1.75E-05
112	0	0	4.88E-06	1.86E-05	5.52E-05	0	1.66E-05
113	0	0	3.92E-06	1.66E-05	4.85E-05	0	1.57E-05
114	0	0	2.94E-06	1.47E-05	4.22E-05	0	1.47E-05
115	0	0	1.97E-06	1.33E-05	3.59E-05	0	1.38E-05
116	0	0	9.86E-07	1.23E-05	3.01E-05	0	1.28E-05
117	0	0	0	1.14E-05	2.52E-05	0	1.19E-05
118	0	0	0	1.04E-05	2.18E-05	0	1.09E-05
119	0	0	0	9.44E-06	1.84E-05	0	9.94E-06
120	0	0	0	8.47E-06	1.64E-05	0	8.97E-06
121	0	0	0	7.49E-06	1.45E-05	0	7.99E-06
122	0	0	0	6.51E-06	1.25E-05	0	7.01E-06
123	0	0	0	5.52E-06	1.05E-05	0	6.03E-06

124	0	0	0	4.53E-06	8.56E-06	0	5.03E-06
125	0	0	0	3.53E-06	6.56E-06	0	4.04E-06
126	0	0	0	2.53E-06	4.55E-06	0	3.04E-06
127	0	0	0	1.52E-06	2.54E-06	0	2.03E-06
128	0	0	0	5.09E-07	1.02E-06	0	1.02E-06
129	0	0	0	0	0	0	0
130	0	0	0	0	0	0	0

Table A.27—Solid-phase chord distribution function of the Ekofisk chalk samples (Fig. 29).

	Sample						
***u* (pixel)**	**2**	**3**	**4**	**32**	**35**	**36**	**38**
1	0.014813301	0.062170708	0.015477	0.01568	0.019871	0.018612	0.020142
2	0.016400295	0.036363537	0.017554	0.01945	0.02101	0.020354	0.023321
3	0.020648938	0.022366056	0.02386	0.02802	0.029405	0.028745	0.032901
4	0.027235301	0.028638816	0.02628	0.033228	0.037696	0.036285	0.038243
5	0.029362133	0.037734828	0.028467	0.03714	0.039979	0.039791	0.042774
6	0.031794745	0.034572868	0.029784	0.040737	0.042115	0.040579	0.042995
7	0.029706008	0.034093253	0.030707	0.041381	0.041463	0.042197	0.043138
8	0.031678042	0.039386159	0.02979	0.041345	0.042814	0.040667	0.043834
9	0.030762459	0.035374081	0.029078	0.039331	0.040896	0.038832	0.040353
10	0.027182031	0.030053164	0.027273	0.037627	0.038849	0.038723	0.037991
11	0.027760312	0.031265793	0.025506	0.037695	0.037041	0.034697	0.036391
12	0.024463796	0.030835649	0.024616	0.035322	0.034369	0.032088	0.033533
13	0.025194355	0.026197243	0.022619	0.033095	0.032686	0.032316	0.030923
14	0.022917155	0.025804165	0.022808	0.028791	0.028713	0.028407	0.028692
15	0.022175868	0.026788041	0.020567	0.027533	0.027182	0.02719	0.026924
16	0.022308359	0.022106949	0.019676	0.025308	0.025967	0.024745	0.026386
17	0.020537037	0.021678775	0.017896	0.024826	0.024098	0.021852	0.024858
18	0.019744292	0.022445912	0.018318	0.022686	0.022479	0.021498	0.023026
19	0.019062214	0.020403192	0.018795	0.022698	0.021858	0.020916	0.022141
20	0.018854957	0.01787642	0.018583	0.021472	0.019207	0.019838	0.020231
21	0.018334367	0.01787189	0.016034	0.020455	0.018617	0.019014	0.019172
22	0.016610749	0.017349962	0.015574	0.0197	0.017776	0.018216	0.017821
23	0.016058337	0.01521098	0.014483	0.017363	0.017329	0.017696	0.016629
24	0.015981699	0.016041228	0.013965	0.017585	0.016355	0.016444	0.015201
25	0.014123598	0.015787374	0.0132	0.016644	0.01502	0.015216	0.014641
26	0.014271964	0.014262977	0.013589	0.015129	0.014314	0.015142	0.012785
27	0.013151621	0.012182952	0.013303	0.013533	0.013772	0.014024	0.012264
28	0.013835715	0.012391885	0.012576	0.012861	0.01281	0.014037	0.012175
29	0.012048264	0.012187199	0.011843	0.012525	0.011579	0.011919	0.012016
30	0.011866449	0.010331178	0.010283	0.012193	0.011807	0.011801	0.012108
31	0.011856089	0.010929295	0.010765	0.011791	0.010474	0.011633	0.01118
32	0.011401368	0.010485316	0.009588	0.010852	0.010691	0.011071	0.010242
33	0.011395754	0.008886749	0.009682	0.010051	0.009642	0.010218	0.009648
34	0.009964705	0.008769667	0.009765	0.008498	0.008982	0.010254	0.008192
35	0.011135404	0.00878202	0.009777	0.008657	0.008248	0.008612	0.008979
36	0.009805053	0.007839316	0.009514	0.008392	0.008201	0.008661	0.008398
37	0.01023508	0.007848525	0.008803	0.008575	0.007645	0.008763	0.00808
38	0.008829815	0.007703887	0.008938	0.007697	0.008092	0.008468	0.007089
39	0.009217867	0.007925846	0.008498	0.007058	0.007389	0.008309	0.007119
40	0.008049131	0.006722747	0.009094	0.00703	0.007181	0.007169	0.006483
41	0.008384973	0.007128772	0.008538	0.006693	0.006704	0.00715	0.005905
42	0.008735942	0.007506025	0.008291	0.006078	0.00577	0.007037	0.005588
43	0.008737105	0.006450383	0.006933	0.005585	0.005822	0.006692	0.005621
44	0.008405959	0.005989324	0.008203	0.005716	0.005636	0.005944	0.006055
45	0.007102514	0.005383784	0.007132	0.005516	0.005431	0.00527	0.005274
46	0.007100761	0.005313275	0.006788	0.005179	0.005044	0.00566	0.004799
47	0.006578164	0.004896541	0.006844	0.004856	0.004745	0.004974	0.004632
48	0.006392481	0.00531903	0.006004	0.004282	0.00437	0.004747	0.004485
49	0.006217391	0.004814139	0.006264	0.004887	0.004635	0.004637	0.003581
50	0.005990217	0.004232776	0.006481	0.004431	0.004127	0.004415	0.004269
51	0.005693495	0.004592582	0.006035	0.0038	0.004405	0.003917	0.003649
52	0.006129452	0.004695959	0.005818	0.004328	0.003909	0.003615	0.003248

53	0.005720242	0.003873464	0.00563	0.003933	0.003782	0.003404	0.004146
54	0.005775157	0.003446437	0.006049	0.003604	0.003302	0.003457	0.00357
55	0.006003983	0.003672995	0.005887	0.003751	0.003521	0.003402	0.003602
56	0.005358016	0.003738966	0.005626	0.003278	0.00328	0.003299	0.003302
57	0.005124376	0.00329291	0.005807	0.003231	0.003037	0.003845	0.002948
58	0.005260846	0.003244309	0.005382	0.002849	0.003123	0.002831	0.003019
59	0.004964314	0.002905126	0.004101	0.00254	0.002372	0.003212	0.002665
60	0.004679477	0.002818574	0.00541	0.002516	0.002652	0.002642	0.002319
61	0.004540427	0.002690671	0.004789	0.001939	0.00255	0.002602	0.001956
62	0.005259558	0.002650308	0.004078	0.002823	0.002323	0.002252	0.002215
63	0.004172234	0.002632245	0.003933	0.002052	0.002143	0.002166	0.002369
64	0.004188066	0.002728054	0.003957	0.002251	0.002204	0.00228	0.001964
65	0.003608364	0.002502384	0.004463	0.001823	0.001787	0.002198	0.001839
66	0.00353326	0.002263475	0.004966	0.001945	0.002004	0.002279	0.00193
67	0.003314756	0.002252946	0.004924	0.002008	0.001871	0.001803	0.00178
68	0.00302114	0.002161936	0.004434	0.001916	0.001603	0.002307	0.001786
69	0.002841221	0.00234301	0.003685	0.001657	0.001359	0.002001	0.001823
70	0.002488833	0.001949048	0.003568	0.001444	0.001425	0.001981	0.001606
71	0.002888123	0.002002009	0.003702	0.001331	0.00159	0.002027	0.001209
72	0.003182242	0.00188454	0.00305	0.001501	0.001328	0.001473	0.001422
73	0.003229068	0.001723502	0.003575	0.001291	0.001051	0.001269	0.001346
74	0.002972408	0.001585582	0.003243	0.001364	0.001108	0.001322	0.001209
75	0.003206957	0.001458879	0.003396	0.001252	0.001124	0.001025	0.000932
76	0.002820657	0.00144982	0.002739	0.001316	0.000995	0.00101	0.000967
77	0.002918653	0.001439843	0.003242	0.001091	0.000935	0.001172	0.001157
78	0.002382845	0.001437169	0.003059	0.001242	0.001275	0.000917	0.001009
79	0.002794556	0.001099843	0.003331	0.001043	0.001164	0.000865	0.001118
80	0.00248745	0.001276732	0.002849	0.000963	0.000895	0.00098	0.001289
81	0.002312907	0.001305656	0.002462	0.001122	0.000879	0.001179	0.000973
82	0.002330158	0.001179667	0.002354	0.00094	0.000721	0.000959	0.000635
83	0.002291772	0.001160201	0.002098	0.000791	0.000799	0.000908	0.000772
84	0.002124302	0.000965367	0.002477	0.001053	0.00093	0.00064	0.000645
85	0.001677781	0.001048218	0.002396	0.001139	0.001104	0.00072	0.000845
86	0.002075833	0.00086801	0.00238	0.000677	0.000971	0.000718	0.000602
87	0.001707601	0.000818979	0.002242	0.000762	0.000829	0.000577	0.000503
88	0.002015324	0.000923847	0.002348	0.000866	0.000864	0.000711	0.000457
89	0.002171294	0.000880382	0.002482	0.000711	0.000832	0.000644	0.000408
90	0.001740575	0.000955231	0.002356	0.000485	0.000869	0.000827	0.000535
91	0.001850699	0.000865795	0.002054	0.000563	0.000776	0.000509	0.000416
92	0.001785359	0.00083678	0.00211	0.000553	0.000541	0.000524	0.000365
93	0.001478033	0.000767033	0.00192	0.000464	0.000487	0.000543	0.000474
94	0.001486884	0.000991775	0.00208	0.000489	0.00034	0.000671	0.000493
95	0.001322252	0.000835114	0.002141	0.000562	0.000438	0.000402	0.000458
96	0.001632016	0.000844128	0.001929	0.000729	0.000476	0.000466	0.000453
97	0.001374578	0.000621469	0.001792	0.000504	0.000528	0.000503	0.000494
98	0.00137038	0.00075464	0.001818	0.000517	0.000458	0.0004	0.000513
99	0.001439324	0.000676034	0.001712	0.000554	0.000304	0.000285	0.000396
100	0.001237346	0.000501459	0.001824	0.000387	0.000275	0.000347	0.000336
101	0.001300739	0.000498724	0.001529	0.000478	0.000421	0.000301	0.000236
102	0.001136792	0.000531274	0.001493	0.000366	0.000385	0.000301	0.000222
103	0.001385366	0.000378877	0.001081	0.000313	0.000345	0.000375	0.000194
104	0.001305696	0.000495295	0.00156	0.000288	0.00029	0.000183	0.000337
105	0.000867901	0.000511413	0.001449	0.000263	0.000328	0.000246	0.000244
106	0.001137321	0.000337753	0.0011	0.000338	0.000343	0.000281	0.000254
107	0.000846352	0.000692219	0.001148	0.000325	0.000381	0.000173	0.000217
108	0.000842385	0.00048237	0.001006	0.000263	0.000263	0.000265	0.000136
109	0.000765566	0.000469409	0.001185	0.000327	0.00034	0.000185	0.000156
110	0.00082577	0.000411013	0.000901	0.000202	0.000214	0.00024	0.000147
111	0.000788585	0.000468669	0.001222	0.000153	0.000186	0.000278	0.000138
112	0.000862976	0.000325019	0.001138	0.000189	0.000119	0.000247	0.000309
113	0.000655249	0.000387863	0.001597	0.000276	0.000119	0.000197	0.0002
114	0.000880672	0.000437707	0.001305	0.000177	0.000172	0.000159	0.000314
115	0.000795414	0.000249351	0.001199	0.000112	0.000105	0.000172	0.000234
116	0.00072979	0.00032847	0.001349	0.000127	0.000171	0.00017	0.000199
117	0.000805584	0.000238173	0.000992	8.89E-05	0.00017	0.000142	0.000136
118	0.00060565	0.000263264	0.000824	5.02E-05	0.000171	0.000175	0.000184
119	0.000906968	0.000236075	0.001221	7.48E-05	0.000185	0.000157	8.59E-05

120	0.000687794	0.000275673	0.001156	0.000151	0.000132	0.000184	9.73E-05
121	0.000697483	0.000174135	0.001033	0.00015	0.000132	0.000143	9.75E-05
122	0.000647982	0.000150045	0.000962	0.000113	6.7E-05	0.000119	0.000125
123	0.000651045	0.000163381	0.000829	7.55E-05	0.000121	0.000211	0.000211
124	0.000698209	0.000112249	0.000726	8.77E-05	7.88E-05	0.000237	0.000125
125	0.000716369	0.000211907	0.000719	0.000149	2.61E-05	0.000171	0.000123
126	0.000756984	0.000225494	0.000843	0.000113	9.09E-05	0.000155	7.49E-05
127	0.000787437	0.00019913	0.001031	2.49E-05	1.35E-05	0.000137	5.08E-05
128	0.000511519	0.000097914	0.000694	7.49E-05	5.41E-05	0.000105	1.27E-05
129	0.000551203	0.000202777	0.000582	0.000125	3.99E-05	2.66E-05	9.9E-05
130	0.000622185	0.000150867	0.000634	4.9E-05	4.05E-05	0.000107	7.35E-05
131	0.000501567	0.000100961	0.000848	5.05E-05	9.21E-05	0.000133	5.11E-05
132	0.000606235	0.000150434	0.00078	3.74E-05	7.92E-05	0.000198	6.23E-05
133	0.000431591	0.000152277	0.000855	3.76E-05	5.2E-05	0.000106	6.37E-05
134	0.000436208	0.00011458	0.000734	8.75E-05	5.26E-05	9.21E-05	7.63E-05
135	0.000343104	0.000200065	0.000842	6.28E-05	6.51E-05	7.96E-05	7.56E-05
136	0.000289598	0.000129247	0.000601	1.24E-05	1.29E-05	0.00011	9.68E-05
137	0.000528806	0.000061796	0.000481	5.04E-05	0	0.000124	6.38E-05
138	0.000565239	0.000137981	0.00044	8.84E-05	0	9.55E-05	6.36E-05
139	0.000652631	0.000111059	0.000479	1.24E-05	0	9.42E-05	2.54E-05
140	0.000546114	0.000111528	0.000335	2.51E-05	1.27E-05	9.22E-05	3.49E-05
141	0.0004979	0.000103912	0.000619	0	0	5.31E-05	7.11E-05
142	0.000407643	0.000087903	0.000885	4.97E-05	1.29E-05	1.35E-05	2.54E-05
143	0.000279899	0.000116522	0.000522	2.55E-05	2.64E-05	4.01E-05	3.57E-05
144	0.000233561	0.00006236	0.000789	5.11E-05	4.03E-05	3.98E-05	2.46E-05
145	0.000385662	0.000086589	0.000479	3.72E-05	0	5.29E-05	1.23E-05
146	0.00022685	0.000162865	0.000382	1.24E-05	2.61E-05	1.3E-05	0
147	0.000308644	0.000074248	0.000456	4.96E-05	2.56E-05	1.3E-05	0
148	0.000230671	0.000138759	0.000451	2.56E-05	2.57E-05	3.82E-05	3.6E-05
149	0.000369655	0.000050742	0.000429	6.25E-05	3.97E-05	0	1.23E-05
150	0.000316378	0.00007495	0.000394	2.51E-05	5.34E-05	0	2.35E-05
151	0.000273791	0.000038734	0.000332	3.78E-05	3.93E-05	4.24E-05	4.9E-05
152	0.00021001	0.000137797	0.000429	3.75E-05	1.29E-05	0	2.47E-05
153	0.000264362	0.000077063	0.00033	1.24E-05	1.29E-05	0	3.85E-05
154	0.000170836	0.000024982	0.00034	2.5E-05	0	2.66E-05	7.44E-05
155	0.000240492	0.000023159	0.000444	8.81E-05	0	6.74E-05	3.68E-05
156	0.000153081	0.00003834	0.000526	7.8E-05	1.29E-05	4E-05	3.68E-05
157	0.000075151	0.000075581	0.000514	3.9E-05	2.63E-05	2.61E-05	2.39E-05
158	0.000105492	0.00009009	0.000301	0	0	9.15E-05	0
159	0.000119627	0.000076634	0.000359	0	1.34E-05	1.3E-05	0
160	0.000158609	0.000064629	0.000224	2.51E-05	1.29E-05	2.62E-05	2.54E-05
161	0.000107885	0.00008599	0.000179	3.76E-05	3.91E-05	4E-05	1.19E-05
162	0.000091086	0.000062829	0.000166	1.24E-05	1.29E-05	2.58E-05	1.31E-05
163	0.00022199	0.000065985	0.000279	1.25E-05	1.34E-05	1.29E-05	0
164	0.00012142	0.00006243	0.000388	2.49E-05	1.29E-05	2.55E-05	3.86E-05
165	0.000142321	0.000101989	0.000229	0	0	0	0
166	0.000047526	0.000063158	0.000176	1.25E-05	0	0	0
167	0.000154559	0.000025331	0.000212	0	0	1.35E-05	1.24E-05
168	0.000143976	0.000025326	0.000191	0	0	0	1.23E-05
169	0.000074149	0.000037425	0.000231	1.26E-05	0	0	0
170	0.000135705	0.000037959	0.000257	0	1.29E-05	0	2.48E-05
171	0.000122617	0.000048284	0.000198	0	1.29E-05	2.83E-05	6.11E-05
172	0.000117081	0.000037236	0.000145	0	0	0	0
173	0.00016278	0.000037665	0.000162	0	0	1.33E-05	1.23E-05
174	0.000104183	0.000024793	0.000164	0	0	0	1.23E-05
175	0.000058632	0	0.000179	0	0	0	6.2E-05
176	0.000088194	0.000012497	0.000118	0	0	1.41E-05	2.55E-05
177	0.000107124	0.000025326	0.00023	0	1.29E-05	0	2.35E-05
178	0.000073606	0.000039303	0.000161	0	0	0	0
179	0.00010388	0.000013403	0.000131	1.25E-05	0	0	0
180	0.000060628	0	0.000209	2.48E-05	0	2.74E-05	0
181	0.000156525	0	6.63E-05	0	0	1.33E-05	0
182	0.000109021	0.000013403	0.0001	0	2.68E-05	0	0
183	0.000033715	0	0.000241	0	1.34E-05	0	0
184	0.000046303	0	0.000181	2.49E-05	1.34E-05	1.29E-05	0
185	0.000107316	0	0.000133	0	1.34E-05	3.94E-05	0
186	0.000070975	0.000011346	0.000184	0	0	1.29E-05	0

187	0.000057657	0.000013403	0.000215	0	0	2.71E-05	0
188	0.000058226	0.000025776	0.00018	0	0	3.88E-05	0
189	0.000107628	0.000024746	0.000116	1.26E-05	0	1.29E-05	0
190	0.000050573	0.000013403	0.00017	0	0	3.94E-05	0
191	0.000016158	0.000040209	0.00017	0	0	6.99E-05	0
192	0.000016858	0	0.000127	0	3.91E-05	1.41E-05	0
193	0.000031974	0.000013403	9.65E-05	0	0	0	0
194	0.000032845	0	1.6E-05	0	0	1.33E-05	0
195	0.000029437	0	6.53E-05	0	0	1.33E-05	0
196	0.00005733	0	5.02E-05	0	0	5.26E-05	0
197	0.000110311	0	3.31E-05	0	0	1.3E-05	0
198	0.000042808	0	8.49E-05	0	0	1.29E-05	0
199	0.000014116	0	8.09E-05	0	0	0	0
200	0.000047609	0.000012497	0.000149	0	0	0	0
201	0.000162285	0	0.000179	0	0	1.33E-05	0

Table A.28—Void-phase chord distribution function of the Ekofisk chalk samples (Fig. 30).

	Sample						
u **(pixel)**	**2**	**3**	**4**	**32**	**35**	**36**	**38**
1	0.04604381	0.0910488	0.0517833	0.0353504	0.0331077	0.0352839	0.0358691
2	0.064821173	0.0688848	0.0734092	0.0545464	0.0459253	0.0521304	0.046862
3	0.085498949	0.0560939	0.0959259	0.0682181	0.0593603	0.06478	0.0649908
4	0.097149204	0.0673815	0.1028329	0.0743974	0.0642377	0.0711295	0.0729095
5	0.091429868	0.0767422	0.0969454	0.0729118	0.0647303	0.0700816	0.0729654
6	0.087676615	0.068476	0.0881429	0.0705439	0.0612473	0.0655429	0.0703382
7	0.075997186	0.0605881	0.0735122	0.0645678	0.0572464	0.0591972	0.0646445
8	0.066225895	0.0589928	0.0635411	0.0558034	0.0539921	0.0539405	0.0570518
9	0.055778847	0.0531159	0.0532063	0.0521289	0.0495141	0.0501409	0.0511759
10	0.047940986	0.0426863	0.0453692	0.0455188	0.0436895	0.0441457	0.0476995
11	0.041359132	0.0387294	0.0383994	0.0411806	0.0399658	0.0401817	0.0415768
12	0.034286532	0.0375544	0.0310223	0.0391202	0.0360049	0.0360661	0.0388951
13	0.030004401	0.030587	0.0265237	0.0351951	0.0316038	0.0330314	0.0356211
14	0.026750086	0.02617	0.0239799	0.030288	0.0289613	0.0297212	0.0297126
15	0.023257712	0.0259692	0.0198599	0.0279345	0.0263599	0.0256739	0.0267752
16	0.019029557	0.0227066	0.0167034	0.0235093	0.0252324	0.0241367	0.025287
17	0.016237586	0.0178752	0.0138437	0.0221452	0.0227444	0.0217327	0.022672
18	0.013713051	0.016452	0.011731	0.019711	0.020823	0.019511	0.019902
19	0.012222564	0.015009	0.009946	0.017192	0.018633	0.018615	0.018015
20	0.009501481	0.013689	0.010481	0.015282	0.017855	0.016406	0.015851
21	0.00817413	0.012904	0.007977	0.014325	0.016809	0.013702	0.013796
22	0.006275718	0.011817	0.006171	0.012133	0.014478	0.013159	0.012573
23	0.005711782	0.009394	0.005298	0.010576	0.015005	0.011986	0.010758
24	0.005053716	0.008606	0.004695	0.010116	0.013281	0.011907	0.010182
25	0.00444629	0.00819	0.00413	0.00845	0.011284	0.009838	0.009291
26	0.003669604	0.006626	0.003194	0.008463	0.010484	0.008254	0.008594
27	0.002846047	0.005343	0.002837	0.007219	0.010029	0.008804	0.007008
28	0.002767769	0.005496	0.002287	0.00675	0.009237	0.007148	0.006419
29	0.001980025	0.004867	0.002244	0.005726	0.008871	0.006895	0.006147
30	0.00193193	0.003668	0.001897	0.00582	0.007331	0.006322	0.005308
31	0.001887036	0.003215	0.001654	0.004582	0.006997	0.006175	0.004315
32	0.001227501	0.003486	0.001268	0.003717	0.005701	0.005261	0.004245
33	0.000978513	0.002705	0.001181	0.003674	0.005324	0.005309	0.00385
34	0.000959065	0.002764	0.000918	0.003123	0.004607	0.00454	0.003727
35	0.000758348	0.002185	0.000946	0.003302	0.004412	0.004501	0.003674
36	0.000728511	0.002214	0.00092	0.002573	0.004375	0.00419	0.003252
37	0.000940861	0.001909	0.000381	0.002263	0.004171	0.003424	0.002588
38	0.000598303	0.001662	0.00051	0.002002	0.003484	0.003267	0.002432
39	0.000652724	0.001735	0.000608	0.001702	0.0035	0.002704	0.002227
40	0.000608416	0.001228	0.000489	0.001654	0.002863	0.002777	0.002038
41	0.000438946	0.001236	0.000333	0.001718	0.002931	0.00239	0.001976
42	0.000260262	0.001403	0.000391	0.001623	0.002558	0.002608	0.001727
43	0.000287724	0.000952	0.000409	0.001623	0.002177	0.00229	0.001283
44	0.000294375	0.000744	0.000284	0.001076	0.00221	0.001728	0.001646

45	0.000245682	0.000998	0.000141	0.000944	0.002091	0.001825	0.001265
46	0.000175307	0.000799	0.000351	0.001162	0.001967	0.001451	0.00112
47	0.000030329	0.000371	0.000193	0.000768	0.001964	0.001661	0.000858
48	0.000189199	0.00045	0.000107	0.000704	0.001568	0.001229	0.000723
49	0.000187132	0.000329	8.8E-05	0.000677	0.001749	0.001054	0.000665
50	0.000031828	0.000364	0.000104	0.000601	0.001625	0.000895	0.000643
51	0.000031618	0.000314	0.000105	0.000615	0.001421	0.001005	0.00077
52	0.000035255	0.000322	7.03E-05	0.00059	0.000973	0.000998	0.000599
53	0.000086983	0.000254	8.72E-05	0.000399	0.000904	0.000729	0.000578
54	0.000109504	0.000319	3.58E-05	0.000332	0.001129	0.000949	0.000576
55	0.000031358	0.00031	5.31E-05	0.000244	0.000844	0.000881	0.000302
56	0.000085336	0.000248	3.54E-05	0.000168	0.00106	0.000737	0.000322
57	0.00003259	0.000254	3.54E-05	0.000207	0.000593	0.000603	0.000218
58	0.000015848	0.000265	3.54E-05	0.000167	0.000682	0.000428	0.000333
59	0.00003303	0.000205	1.77E-05	0.000243	0.000495	0.000376	0.000308
60	0.00001705	0.000139	3.55E-05	0.000205	0.000563	0.000456	0.000187
61	0.000049097	5.11E-05	0	0.000168	0.00078	0.000307	0.000253
62	0.000048212	8.72E-05	0	0.000165	0.000296	0.000211	0.000206
63	0.000017627	6.16E-05	4.83E-05	0.000179	0.000376	0.000296	0.000165
64	0.000028616	7.59E-05	5.13E-05	0.000243	0.000455	0.000231	0.0002
65	0	5.29E-05	3.36E-05	0.000116	0.000335	0.00027	0.000192
66	0.000028616	6.54E-05	1.68E-05	0.000129	0.000374	0.000107	0.000125
67	0.000034677	6.07E-05	0	9.04E-05	0.000336	9.29E-05	5.03E-05
68	0	9.38E-05	0	7.84E-05	0.000175	0.000144	3.89E-05
69	0	5.26E-05	0	0.000103	0.000189	0.000148	7.9E-05
70	0.000017627	5.24E-05	0	9.1E-05	0.000419	0.000242	0.000168
71	0.000017627	1.35E-05	0	7.77E-05	0.000324	0.000233	0.00015
72	0.000017627	0	0	2.59E-05	0.000162	9.45E-05	6.37E-05
73	0	2.49E-05	3.45E-05	3.94E-05	0.000256	0.000162	0.000133
74	0	0	1.68E-05	3.86E-05	0.000145	0.000203	6.35E-05
75	0	2.58E-05	0	2.57E-05	0.000148	0.000178	5.24E-05
76	0	7.6E-05	0	1.32E-05	8.07E-05	0.000146	2.54E-05
77	0	1.26E-05	0	1.27E-05	0.000121	0.000108	8.77E-05
78	0	1.26E-05	0	2.65E-05	0.000188	1.37E-05	9.24E-05
79	0	0	1.68E-05	5.14E-05	0.000134	6.57E-05	5.2E-05
80	0	0	0	0.000103	9.48E-05	5.2E-05	2.6E-05
81	0	3.59E-05	0	2.6E-05	5.43E-05	5.25E-05	1.26E-05
82	0	2.43E-05	0	2.54E-05	0.00012	8.06E-05	2.55E-05
83	0	1.27E-05	1.68E-05	2.59E-05	6.76E-05	2.82E-05	3.76E-05
84	0	0	0	1.25E-05	5.29E-05	5.48E-05	1.35E-05
85	0	0	0	5.06E-05	0.000107	4.13E-05	2.5E-05
86	0	0	0	0	2.68E-05	1.37E-05	2.6E-05
87	0	0	0	0	6.7E-05	5.51E-05	4.01E-05
88	0	0	0	0	8.06E-05	1.37E-05	6.51E-05
89	0	0	0	0	0.00012	3.94E-05	1.25E-05
90	0	0	0	1.32E-05	5.44E-05	1.33E-05	2.61E-05
91	0	0	1.77E-05	1.32E-05	8.23E-05	3.95E-05	3.88E-05
92	0	1.33E-05	0	1.32E-05	5.36E-05	2.74E-05	1.26E-05
93	0	1.33E-05	0	1.32E-05	1.31E-05	2.82E-05	1.26E-05
94	0	0	1.77E-05	3.97E-05	4.1E-05	0	0
95	0	1.33E-05	0	2.61E-05	3.99E-05	4.11E-05	0
96	0	0	0	0	0	4.34E-05	1.26E-05
97	0	1.26E-05	1.77E-05	2.58E-05	1.39E-05	5.32E-05	2.53E-05
98	0	0	0	0	0	2.66E-05	0
99	0	0	0	0	0	4E-05	0
100	0	0	0	0	5.29E-05	2.78E-05	0
101	0	0	0	0	3.91E-05	0	0
102	0	0	0	0	5.37E-05	1.45E-05	0
103	0	0	0	0	3.97E-05	4.23E-05	0
104	0	0	0	0	7.93E-05	0	0
105	0	1.19E-05	0	0	3.97E-05	1.33E-05	1.26E-05
106	0	0	0	2.49E-05	3.93E-05	0	0
107	0	0	0	2.54E-05	1.3E-05	0	1.26E-05
108	0	0	0	0	1.29E-05	0	0
109	0	0	0	2.54E-05	0	0	0
110	0	0	0	0	5.45E-05	0	0
111	0	0	0	1.25E-05	1.29E-05	0	0
112	0	0	0	1.25E-05	1.3E-05	0	0

113	0	0	0	0	1.31E-05	0	0
114	0	0	0	1.29E-05	0	0	0
115	0	0	0	1.29E-05	1.3E-05	0	0
116	0	0	0	0	2.61E-05	0	0
117	0	0	3.54E-05	0	4.16E-05	0	0
118	0	0	0	0	0	0	0
119	0	0	0	0	4.09E-05	0	0
120	0	0	0	0	0	0	0
121	0	0	0	0	0	0	0
122	0	0	0	0	0	0	0
123	0	0	0	0	0	0	0
124	0	0	0	0	0	0	0
125	0	0	0	0	0	0	0
126	0	0	0	0	0	0	0
127	0	0	0	0	1.29E-05	0	0
128	0	0	0	1.29E-05	1.29E-05	0	0
129	0	0	0	1.29E-05	2.58E-05	0	2.71E-05
130	0	0	0	0	0	0	0
131	0	0	0	0	0	0	0

Paper I

Hysteresis Effects in Capillary Pressure, Relative Permeability and Resistivity Index of North Sea Chalk

M.T. Tweheyo, M.S. Talukdar and O. Torsæter
Department of Petroleum Engineering and Applied Geophysics
Norwegian University of Science and Technology (NTNU), Trondheim.

SCA 2001-65, International Symposium of the Society of Core Analysts, Edinburgh, 17-19 September 2001.

Abstract

Accurate estimation of capillary pressure and relative permeability curves are very important for evaluating hydrocarbon recovery processes. Also, resistivity index data are important in evaluating fluid distributions in reservoirs during these processes. All these parameters are path dependent i.e. different in drainage and imbibition processes, commonly known as hysteresis, which makes them complicated to predict. Laboratory tests have therefore been performed on four North Sea chalk core samples to measure the wettability index and determine the hysteresis in capillary pressure, relative permeability and resistivity index. The cores were extracted using toluene and methanol, and a light oil (*n*-decane) and brine saturation equivalent to the formation water were used in the displacement processes. Varying levels of hysteresis were observed. Hysteresis effects were significant in capillary pressure and relative permeability curves and not so pronounced for the resistivity index.

1. Introduction

Knowledge about the flow paths of wetting and non-wetting phases is basic in understanding multi-phase flow in hydrocarbon reservoirs from initial oil migration in source rocks to primary and tertiary recovery processes. The flow paths of the displacing and displaced fluids are governed by the distribution of the fluids in the pores, the pore size distribution, and the interaction between the fluid and the rocks (wettability), among others.

In order to estimate the *in situ* water and hydrocarbon saturations, resistivity tests are carried out and then combined with a saturation model. Although there exists many saturation models, results in this study have been based on Archie's (1942)-saturation model. The saturation exponent n is determined from log-log plot of I_r versus S_w, which is usually assumed to be linear. Extraction of cores, geological features, wettability, vugs, electrical conductive minerals, microporosity and rugged grain surfaces have been found to cause deviation from the linearity scale (Stalheim and Eidesmo, 1995). This results in either an increased n with decreasing S_w (positive curvature), or a decreasing n with decreasing S_w (negative curvature). Hysteresis effects in the n-value during the drainage and imbibition processes have also been observed by many researchers (Wei and Lile, 1993; Lewis *et al*, 1988).

Relative permeability depends on a combined effect of pore geometry, fluid distribution, wettability, and fluid saturation history, among others. Therefore relative permeability curves will show that during drainage and imbibition processes, the fluids can exchange positions and flow behaviour resulting in hysteresis effects (Geffen *et al*, 1951). Like relative permeability, capillary pressure/saturation relationship depends on the composite interaction of wettability, pore structure, initial saturation and saturation history. Generally there is hysteresis in capillary pressure as the saturation is varied in drainage and imbibition processes.

2. Experimental work

The work included the following in chronological sequence: cleaning and drying, porosity and absolute permeability determination, capillary pressure and Amott wettability index determination, relative permeability determination by the unsteady state technique and resistivity measurements. The procedures for the hysteresis studies are as follows:

Capillary pressure was obtained by the centrifuge method. The cores were saturated with the wetting phase (brine) and rotated in the non-wetting phase (*n*-decane) at increasing speeds. The Hassler and Brunner (1945) corrected water saturations at each speed were calculated. The cores were then removed and submerged in brine for minimum 300 hours and spontaneously produced oil was recorded. The positive part of the imbibition curve was modelled (Hegre, 1992). The cores were then centrifuged in brine and negative capillary pressure data were obtained. The core plugs were submerged in oil for minimum 300 hours to determine the spontaneously taken up oil. The end point saturations were used to calculate the Amott (1959) wettability index.

Relative permeability was measured by the unsteady state method under constant differential pressure (5 bar) during the drainage and imbibition cycles. First, the cores were saturated with 100 per cent water and then desaturated by injecting oil until no more water production was obtained, defining the initial water saturation, S_{wi}. Oil was then displaced by brine until no more oil production was observed. During displacement experiments no measurement points are possible before breakthrough for both drainage and imbibition (see Table 1 for breakthrough saturations). Also, the measurements points after breakthrough are normally scattered. Relative permeability curves consisting of scattered points and no points before breakthrough are not suited for practical applications. Therefore, numerical simulations were conducted using a commercial reservoir simulator and relatively smooth curves covering important range of water saturation were obtained from Corey exponent representation through history matching of the oil and water production data.

Electrical resistance of the cores was determined at laboratory conditions by a two-electrode method using the ratio of voltage decrease between a reference resistor and a core sample in series. The cleaned and dried cores were 100 % saturated with formation brine and placed in the resistivity cell to measure R_o. The cores were then placed in a core holder and the brine was displaced by *n*-decane using a pump. Saturation changes were measured

by weighing and double-checked by the amount of brine produced. At each reduction in saturation, the core was transferred to the resistivity cell and the drainage resistivity indices were determined. Saturation and resistivity indices for the imbibition cycle were achieved similarly, but instead *n*-decane was displaced with brine in steps until S_{or} was reached.

3. Results and discussions

The key rock parameters and results of the multiphase experiments are given in Table 1. The fluid data is as follows: Brine density; 1.05 g/cc, oil density; 0.73 g/cc, brine viscosity; 1.05 cp, oil viscosity, 1.36 cp and brine/oil interfacial tension; 13.56 dynes/cm.

Table 1: Key parameters from displacement experiments on the chalk core samples.

Core number	**2**	**3**	**4**	**6**	**Core number**		**2**	**3**	**4**	**6**
Core length (cm)	4.27	4.22	4.15	3.79	Oil index, r_o		0	0	0	0
Core diameter (cm)	3.74	3.75	3.74	3.71	$I_{Amott} = r_w - r_o$		0.34	0.35	0.39	0.53
Pore volume (cm^3)	8.92	12.26	8.69	12.66	*n*	Drainage	1.6	-	1.4	1.7
Porosity (fraction)	0.19	0.26	0.19	0.31		Imbibition	1.4	-	1.4	1.6
Air permeability (md)	0.20	1.35	0.36	2.60	$S_{wi\ (H\ \&\ B)}$		0.19	0.10	0.19	0.11
Liquid permeability (md)	0.09	0.64	0.12	1.94	$S_{or\ (H\ \&\ B)}$		0.18	0.20	0.17	0.24
Entry pressure (bar)	0.67	0.24	0.42	0.22	k_{ro} at S_{wi}		0.77	0.85	0.74	0.79
Water index, r_w	0.34	0.35	0.39	0.53	k_{rw} at S_{or}		0.17	0.20	0.21	0.29
Water saturation at breakthrough					Drainage		0.48	0.63	0.59	0.53
					Imbibition		0.69	0.49	0.53	0.51

Capillary pressure/saturation relationship results from centrifuge experiments and imbibition cell are shown in Fig. 1 and 2. Capillary hysteresis can clearly be observed from the primary drainage and spontaneous imbibition data. The final hysteresis loop will consist of a spontaneous uptake of oil and the secondary drainage curve. An example of a complete capillary pressure curve is shown in Fig. 2.

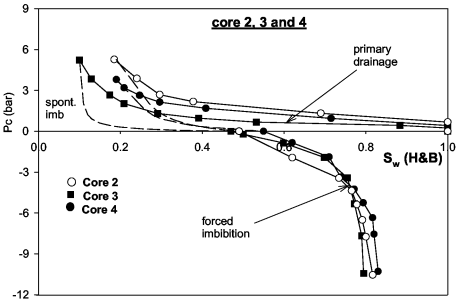

F ig. 1: Water-oil capillary pressure (core 2, 3 and 4).

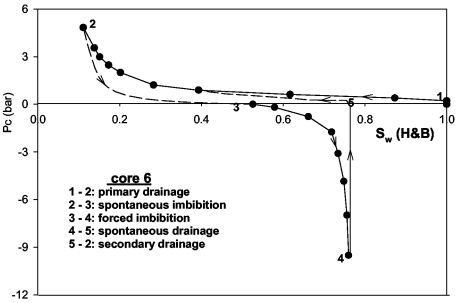

Fig. 2: Water- oil capillary pressure (core 6).

The Amott wettability indices were computed using the data from spontaneous and forced drainage and imbibition tests. The indices (0.34 - 0.53) are shown in Table 1 and reveal

moderately water-wet conditions for all the chalk samples. There was no spontaneous uptake of oil. Since the cores were not aged after cleaning, the use of crude oil and ageing could result in different wettability indices. Tobola (1996) has reported similar low wettability indices in some North Sea chalk samples from tight formations with no visual evidence of fractures. The quartz content of chalks can also affect the capillary pressure/water saturation relationships and hence the wettability (Spinler, 1996), but the composition of the chalk was not investigated in this work. The drainage capillary pressure curves showed low entry pressures (0.22 - 0.67 bars), sharp curvature for drainage near S_{wi} and big saturation changes at slightly negative capillary pressures during the forced imbibition. The shape of the negative capillary pressure curve indicate that the forced imbibition has the potential of being an important production mechanism in chalk. Previous studies on North Sea chalk (Graue *et al*, 1999 and Tobola, 1996) reported similar production characteristics at less water-wet conditions.

Relative permeabilities are graphically shown in Fig. 3 and 4. The key end point saturation and relative permeability values are indicated in Table 1. The end-point values are typical and consistent with earlier tests on chalk reported in literature for water-wet conditions (Graue *et al*, 1999).

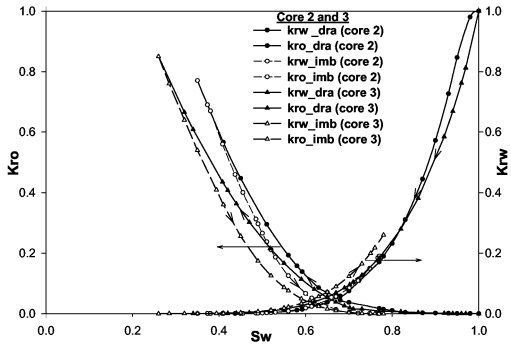

Fig. 3 Water-oil relative permeability (core 2 and 3).

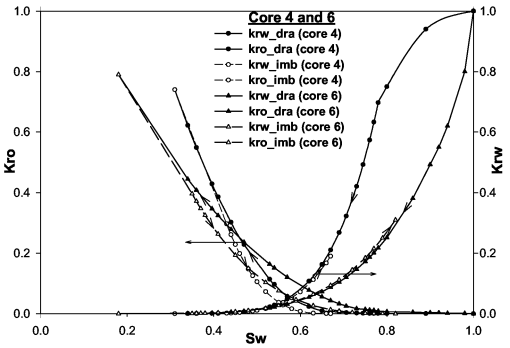

Fig. 4 Water-oil relative permeability (core 4 and 6).

The drainage and imbibition processes show hysteresis effects in the relative permeability curves. The hysteresis is more pronounced in the non-wetting phase than in the wetting phase. In improved recovery projects, we may often encounter a change from one process to another. The flow reversal may occur at any intermediate saturation and the relative permeability will follow an intermediate path.

The saturation exponent (n) was determined from log-log plot of I_r versus S_w for both the drainage and imbibition processes. Values from 1.4 to 1.7 were recorded. These are shown in Table 1 and on log-log graph (Fig. 5). Hysteresis in resistivity index was observed during the drainage/imbibition cycles of core 2 (Fig. 5) and core 6. The computed values of

n for the drainage and imbibition processes in core 2 are 1.6 and 1.4 respectively. Values of *n* for core plug 6 are 1.7 and 1.6 for the drainage and imbibition cycles. Core 3 broke and core 4 had no hysteresis with *n*-value of 1.4. The relatively low values of *n* could be explained by the cleaning of the chalk cores; resulting in reduced oil-wet surface areas within the pore space, and maintaining of the lengths and conducting paths of brine in the sample for a wider range of saturations (Sweeney and Jennings, 1960).

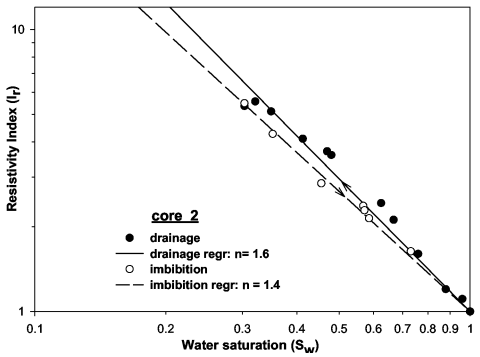

Fig. 5: Log-log plot of I_r versus S_w (core 2).

Other factors causing the variation in the saturation exponent of chalk may include the presence of micropores, irregular surfaces in the samples and the different degrees of wettability, Spinler and Hedges (1995). The presence of fractures have been found to cause negative curvatures as water saturation decreases (Rasmus, 1986). This behaviour can be seen in Fig. 5 for core sample 2 at water saturations below 30%. Although there was no attempt to correlate this variation, some North Sea chalk fields are highly fractured. Such variations could have significant effect on predictions of initial hydrocarbon estimates in place and on subsequent reservoir performance.

4. Conclusions

1. The North Sea chalk samples analysed with n-decane and simulated formation brine without ageing showed a moderately water-wet tendency. This was revealed by the positive wettability indices, the curvature of k_{rw} and k_{ro} curves and saturation and relative permeability end-points in the drainage and imbibition processes.
2. Significant capillary hysteresis effects have been observed in the drainage and imbibition capillary pressure curves for all the core samples. The forced imbibition is an important production mechanism for oil production from the tested chalk material.
3. The effect of saturation history on the distribution of fluids was also reflected in the hysteresis effect in drainage and imbibition relative permeability curves. However, hysteresis in the wetting phase (water) relative permeability was generally negligible.
4. A minor hysteresis in resistivity has been observed between drainage and imbibition in the tested chalk core samples.

Nomenclature

I_r: resistivity index
k_{ro}: relative permeability of oil
k_{rw}: relative permeability of water
n: Archie's saturation exponent
P_c: capillary pressure

R_o: resistivity of core 100 % saturated with brine
r_w, r_o: water and oil indices respectively
$\overline{S}_w$: average water saturation
S_w(H&B): Hassler and Brunner corrected saturation
S_{or}: residual oil saturation
S_w: water saturation
S_{wi}: initial water saturation

Acknowledgements

We are grateful to Philips Petroleum Company Norway for providing the cores and financial support for this study and for permission to publish this extended abstract.

References.

Amott, E.: "Observations Relating the Wettability of Porous Rocks," *Trans. AIME*, (1959) **216**, 156-162.

Archie, G.E.: "The Electrical Resistivity Log as an Aid in Determining some Reservoir Characteristics," *Trans. AIME*, (1942) **146**, 54.

Graue, A., Bognø, T., Moe, R.W., Baldwin, B.A., Spinler, E.A., Maloney, D., and Tobola, D.P.: "Impacts of Wettability on Capillary Pressure and Relative Permeability," *SCA 9515, Int. Symposium of Core Analysts, Colorado* (August 1-4, 1999).

Geffen, T.M.: "Experimental Investigation of Factors Affecting Laboratory Relative Permeability Measurements," *Trans. AIME*, (1951) **192**, 99-110.

Hassler, G.L., and Brunner, E.: "Measurement of Capillary Pressure in Small Core Samples," *Trans. AIME*, (1945) **160**, 114-123.

Hegre, T.M.: "Fractured Reservoir Simulation," Technical Report (1992), PETEC 8/93.930210.

Lewis, M.G., Sharma, M.M, Dunlap, H.F. and Dorfman, M.H.: " Techniques for Measuring the Electrical Properties of Sandstone Cores," *SPE 18178 presented at the 63rd An. Tech. Conf. and Exhibition of the SPE held in Houston*, TX, Oct. 2-5, 1988.

Rasmus, J.C.: "A Summary of the Effect of Various Pore Geometries and their Wettabilities on Measurement of in situ Values of Cementation and Saturation Exponent," *SPWLA Trans.* vol. **II** (June 9-13,1986).

Spinler, E.A.: "Methodology for Determining the Distribution of Wettability from Laboratory and Well Log Measurements for a Microcrystalline/Microfossiliferous Carbonate Field," SCA 9617, *Int. Symp. of Core Analysts, Montpellier* (Sept. 8-10, 1996).

Spinler, E.A. and Hedges, J.M.: "Variations in the Electrical Behaviour of the Ekofisk Field in the North Sea," SCA 9516, *Int. Symp. of Core Analysts, San Francisco* (Sept. 8-10, 1995).

Stalheim, S.O. and Eidesmo, T.: "Is the Saturation Exponent *n* a Constant?" In: *SPWLA 36th Annual Logging Symposium*, New Orlearns, (June 26-29, 1995).

Sweeney, S.A., Jennings, Jr.: "Effect of Wettability on the Electrical Resistivity of Carbonate Rock from a Petroleum Reservoir," *J. of Phys. Chem*, (May 1960) **64**, 551.

Tobola, D.P.: "The Contribution of Oil Production Mechanisms as Determined by a Novel Centrifuge Technique," *SCA 9617, Int. Symp. of Core Analysts, Montpellier* (Sept. 8-10, 1996).

Wei, J.Z. and Lile, O.B.: "Resistivity Index Hysteresis and Its Significance in Electrical Well Log Interpretation," *SPWLA*, Stavanger (May 5-7, 1993).

Paper II

Improvement of Experimental Relative Permeability of North Sea Chalk Through Simulation

M.T. Tweheyo, M.S. Talukdar[1], O. Torsæter and Y. Vafaeinezhad
Department of Petroleum Engineering and Applied Geophysics
Norwegian University of Science and Technology (NTNU), 7491 Trondheim, Norway.

Paper presented at the 11th Oil, Gas and Petrochemical Congress & Exhibition, Tehran, Iran, 29-31 October 2001.

ABSTRACT

Laboratory measurements have been conducted on three North Sea chalk samples having porosities ranging from 0.36 to 0.40. The measurements include relative permeability, capillary pressure and wettability. In drainage and imbibition relative permeability curves, no points are possible before breakthrough. Also, the measured points after breakthrough are normally scattered. Relative permeability curves consisting of scattered points and no points before breakthrough are not suited for practical applications. A numerical simulation approach has been adopted and relatively smoother curves covering important range of water saturation are obtained from Corey exponent representation through history matching of the oil and water production data.

1. INTRODUCTION

Reservoir simulation studies are routinely carried out to design a first development plan, to support ongoing reservoir management, to assess the potential and progress of any improved recovery scheme or to enable the screening of options reviving mature fields. To perform such a simulation, basic equilibrium and flow properties need to be known in each and every location in the reservoir, and the properties of the reservoir rock and fluids must be specified. For multiphase situations, this implies that relative permeability and capillary pressure functions are to be specified at all locations throughout the reservoir [1]. Consequently, accurate determination of multiphase flow functions is an issue of great concern to the oil industry. As there is typically insufficient information to determine reliable estimates of these functions from data gathered from field tests or production history, they are generally determined through laboratory core-flood experiments which are thought to mimic what could happen in the history of any hydrocarbon reservoir and during subsequent recovery processes; for example displacement of water by oil during initial hydrocarbon migration and displacement of oil by mud filtrate during drilling and by water during water flooding. Unfortunately, laboratory experiments have pitfalls/artefacts, for example, fairly low water saturations observed during imbibition experiments at water-wet conditions could be artefacts resulting from early water breakthrough caused by heterogeneities (e.g., fractures) in the core samples. Also, the interference of capillary pressure on the measurement of relative permeability, the so-called capillary end effect, is a long standing issue. Therefore, quality control of the experimental data is a matter of great practical significance. Numerical

[1] Corresponding author. Email: talukdar@ipt.ntnu.no

simulations of the experiments have proved to be an excellent tool to interpret the experimental data and to produce reliable and fit-for-purpose results [2].

The routine core-flood experiments employ unsteady-state or Welge's method [3] and the derived drainage and imbibition relative permeability curves consist of few points only after breakthrough. Also, the measured points are normally scattered. This problem is more pronounced for tight carbonate rocks [4]. The relative permeability curves consisting of scattered points and no points before breakthrough are not suited for practical applications. In this work, we have adopted a numerical simulation technique to obtain relatively smooth curves covering important range of water saturation. This has been achieved by fitting Corey exponent representation [1, 5] with experimental data through history matching of the oil and water production data.

2. LABORATORY EXPERIMENTS

Core flood experiments at laboratory conditions were conducted on three North Sea chalk samples numbered as CH32, CH36 and CH38. The cores were extracted using toluene and methanol, and a light oil (*n*-decane) doped with a colouring agent (*Sedan red*) and formation brine (saturated with calcite) were used in the displacement processes. The samples were not aged. Drainage and imbibition relative permeability curves were calculated using Welge's method [3] and capillary pressure curves were obtained by the centrifuge method. Amott wettability indices [6] were calculated from end-point saturations. Experiments and calculation procedures of the aforementioned parameters for different set of North Sea chalk samples have been presented elsewhere [4] and will not be repeated here. The key parameters for the three samples obtained from the experiments are listed in Table 1. Amott wettability indices close to 1.0 indicate that the samples are strongly water-wet.

Table 1: Key parameters from experiments on the chalk core samples.

Core number	**CH32**	**CH36**	**CH38**	**Core number**		**CH32**	**CH36**	**CH38**
Core length (cm)	4.56	2.63	4.27	Water index, r_w		0.96	0.86	0.91
Core diameter (cm)	3.75	3.77	3.77	$I_{Amott} = r_w - r_o$		0.92	0.84	0.85
Pore volume (cm^3)	17.23	11.05	16.55	k_{ro} at S_{wi}		0.79	0.66	0.66
Porosity (fraction)	0.36	0.40	0.37	k_{rw} at S_{or}		0.34	0.35	0.30
Air permeability (md)	1.64	3.05	0.84	S_w at breakthrough	Drainage	0.55	0.59	0.59
Liquid permeability (md)	0.35	1.88	0.40		Imbibition	0.52	0.55	0.52
Entry pressure (bar)	1.01	0.66	0.97	λ	Experimental	2.91	3.04	3.56
Oil index, r_o	0.04	0.02	0.06		History-matched	3.22	3.31	4.00

3. SIMULATION OF CORE FLOOD EXPERIMENTS

Simulation Model: In the core-flood simulation, a one-dimensional black-oil model consisting of 108 grid blocks of square cross-section has been considered. Similar models have been used by other researchers for history matching of gas-oil injection sequences [5] and water-alternating-gas (WAG) injection sequences [1, 7]. The circular cross-section of the cylindrical core is converted into equivalent square cross-section. To account for the capillary end effects, one block at inlet and one block at outlet are sub-divided into four with lengths *1/15L*, 2*/15L*, 4*/15L* and 8*/15L* (see Fig. 1) where *L* is the length of a regular grid block. The inlet and outlet pipes of the core holder are simulated as the injection and production wells respectively. The pipes are connected to the core plug via two dummy blocks added at the

two ends. The length of the dummy block is equal to the adjacent core block, which is *1/15L*. These blocks can be considered as fluid banks having porosity 1.0, zero capillary pressure and very high permeability. Therefore, they are treated as separate region in the simulation model.

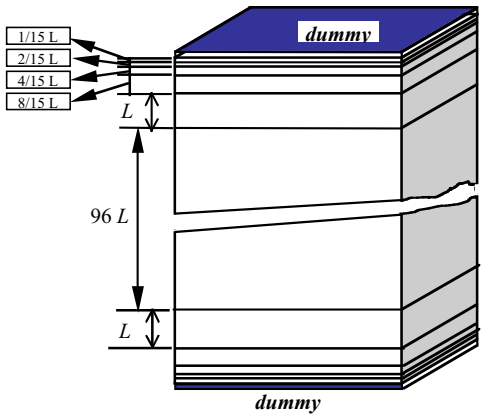

Fig. 1—Simulation model of the core.

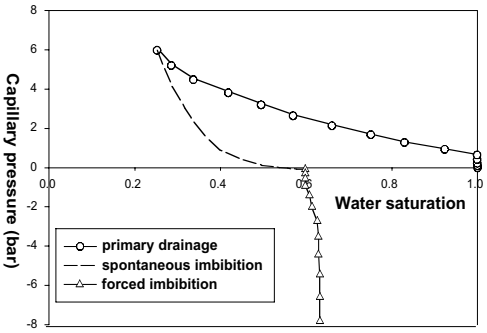

Fig. 2—Water-oil capillary pressure (core CH38).

Since the experiments were conducted at atmospheric pressure, the simulation model was equilibrated at atmospheric pressure referenced at the centre of the core. Both injection and production wells were controlled by bottom hole pressures and set at pressures such that pressure difference between wells equals the differential pressure used in the injection experiments. Diameter of the wells was taken to be 0.16 cm (diameter of the inlet/outlet pipes). Separate saturation tables were used for drainage and imbibition cycles.

Capillary pressure and relative permeability: In excess of core dimensions and equilibration data, relative permeability and capillary pressure functions are important input parameters for reservoir simulation. It should be mentioned that the oil-water capillary curve for our chalk samples has three separate parts (see Fig. 2 for sample CH38). Primary drainage and forced imbibition parts were obtained from centrifuge measurements. In the centrifuge, many measurement points are possible by stepping up the speed at small increments and hence smooth curves. Spontaneous imbibition is obtained in one step by decreasing the capillary pressure from the maximum positive value to zero immediately after primary drainage. The spontaneous imbibition curve was modelled from initial water saturation (S_{wi}) and water saturation after spontaneous imbibition ($S_{w,Pc0}$) using Eq. 1 [8].

$$P_{c,pi}(S_w) = P_{c,e}\left[\frac{S_w - S_{wi}}{S_{w,Pc0} - S_{wi}}\right]^{-\frac{1}{\ddot{e}}} - P_{c,e} \qquad (1)$$

The pore size distribution index (λ) characterises the range of the pore sizes in a rock and was determined using Eq. 2 proposed by Brooks and Corey [9].

$$\left[\frac{P_c}{P_{c,e}}\right]^{-\ddot{e}} = S_w^* \qquad (2)$$

where, $S_w^* = \left[\frac{S_w - S_{wi}}{1 - S_{wi}}\right]$ is the effective water saturation. The calculated pore size distribution indices for the three samples are listed in Table 1.

The initial functions of relative permeability were generated using the modified Corey exponent representation incorporating oil and water end-point relative permeability values [1, 5]:

$$k_{ro} = k_{roe}\left[\frac{1 - S_w - S_{or}}{1 - S_{or} - S_{wi}}\right]^{n_o} \tag{3}$$

and

$$k_{rw} = k_{rwe}\left[\frac{S_w - S_{wi}}{1 - S_{or} - S_{wi}}\right]^{n_w} \tag{4}$$

where, $n_w = \frac{2 + 3\ddot{e}}{\ddot{e}}$ and $n_o = \frac{2 + \ddot{e}}{\ddot{e}}$ for water-wet cases. While end-point relative permeability values define the extent of the relative permeability curves, n_w and n_o define their curvatures. The end-point values used in these equations were those obtained from experiments. During core flood experiments the fluid phase productions were recorded at regular intervals. The water and oil production data during drainage and imbibition are the history matching parameters. Starting from an educated guess λ (and hence n_w and n_o) was gradually changed in order to match the production profiles. The relative permeability curves corresponding to the history-matched λ is the representative smooth curves that cover important range of water saturation. The history-matched λ values are compared with experimental values (Eq. 2) in Table 1. The simulated values correspond very well with the experimental values. The history-matched production profiles and the corresponding relative permeability curves for sample CH38 are shown in Figs. 3 and 4 respectively. Similar or better match in production profiles and relative permeability curves was obtained for other samples and are not shown.

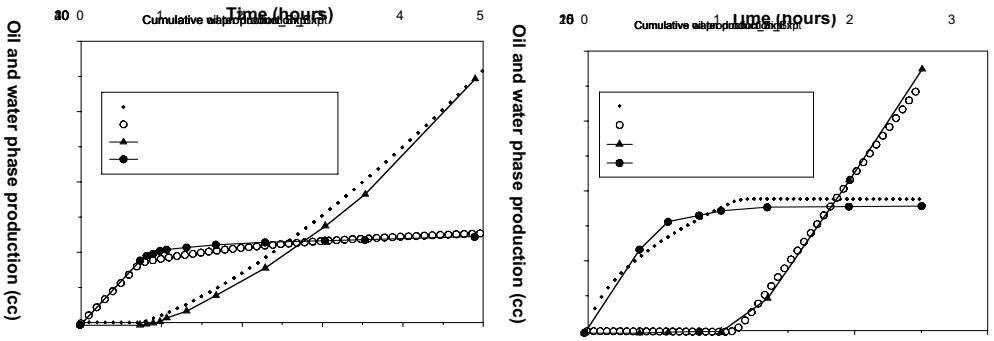

Fig. 3—Experimental and simulated production profiles (core CH38); (a) drainage, (b) imbibition.

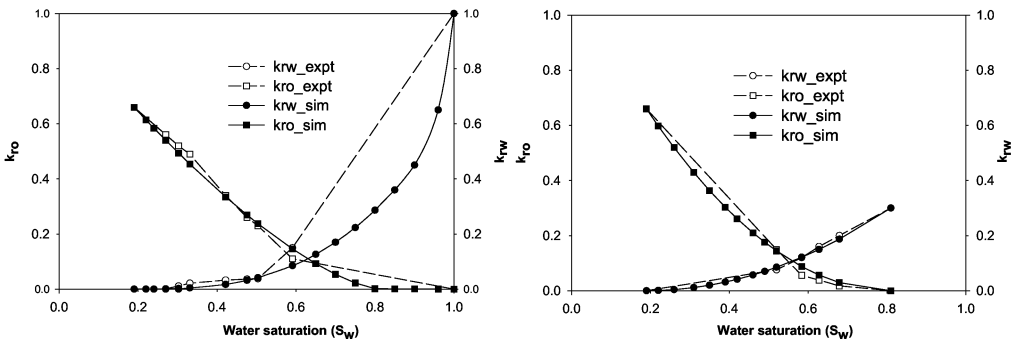

Fig. 4—Oil-water relative permeability curves (core CH38); (a) primary drainage, (b) imbibition.

4. DISCUSSIONS

History matching of the fluid (oil and water) production profiles was successful for drainage and imbibition processes. A match within ±4% for oil and ±6% for water was possible for all measurement points. The pore size distribution index at history match corresponds well with the experimental value. It suggests that Brooks and Corey relationship [9] is well suited for this type of chalk samples at least for oil-water system. The history-matched relative permeability curves also compare very favourable with the experimental curves at measurement points. The simulated curves demonstrate how successful this simulation approach is to obtain smooth relatively permeability curves consisting of points before breakthrough. Another advantage of this approach is that in case of water-wet samples, where there is little or no oil production after breakthrough during the imbibition process, useful data can be obtained. While the experimental curves consist of only few points, the simulated curves may consist of as many data points as needed. This procedure can also be useful in analyzing hysteresis effects. This is because few experimental data points are not adequate to show complete trend of the drainage and imbibition relative permeability curves. In this work, only production profiles have been used as history matching parameters. This prediction technique may be made even more accurate by using more history matching parameters, such as, saturation profile along the length of the core [1, 5, 7].

5. CONCLUSIONS

Core-flood experiments have been conducted on three strongly water-wet North Sea chalk samples with *n*-decane and simulated formation brine without ageing. The samples have porosities and permeabilities ranging from 0.36-0.4 and 1.64-3.05 md respectively. Because of the tight nature of the samples, the relative permeability curves measured by unsteady-state method consist of few scattered data points, which are not suited for practical applications. It has been demonstrated that relatively smoother curves covering important range of water saturation can be obtained from Corey exponent representation through reservoir simulation and history matching of the oil and water production data.

NOMENCLATURE

I_{Amott}=Amott wettability index
k_{ro}=Relative permeability of oil
k_{roe}=Oil relative permeability at S_{wi}
k_{rw}=Relative permeability of water
k_{rwe}=Water relative permeability at S_{or}
n_o=Corey exponent for oil
n_w=Corey exponent for water
P_c=Capillary pressure
$P_{c,e}$=Entry capillary pressure
$P_{c,pi}$=Positive capillary pressure of imbibition curve
S_{or}=Residual oil saturation after water injection
S_w=Water saturation
S_{wi}=Iinitial water saturation
$S_{w,Pc0}$=Water saturation at zero capillary pressure after spontaneous imbibition
λ=Pore size distribution index

ACKNOWLEDGMENTS

We are grateful to Philips Petroleum Company Norway for providing the cores and financial support for this study and for permission to publish this paper.

REFERENCES

1. Akervoll, I., Talukdar, M.S., Midtlyng, S.H., Stensen, J.Å., and Torsæter, O.: "WAG Injection Experiments With In-Situ Saturation Measurements at Reservoir Conditions and Simulations," paper SPE 59323 presented at the 2000 SPE/DOE Improved Oil Recovery Symp. in Tulsa, Oklahoma, USA, 3-5 April 2000.
2. Kokkedee, J.A., Boom, W., Frens, A.M. and Maas, J.C.: "Improved Special Core Analysis: Scope for a Reduced Residual Oil Saturation," paper SCA 9601 presented at the Intl. SCA Symp. in Montpellier, France, 8-10 Sept. 1996.
3. Welge, H.J.: "A Simplified Method for Computing Oil Recovery by Gas or Water Drive," *Trans. AIME*, (1952) **19**, 91-98.
4. Tweheyo, M.T., Talukdar, M.S. and Torsæter, O.: "Hysteresis Effects in Capillary Pressure, Relative Permeability and Resistivity Index of North Sea Chalk," paper SCA 66 presented at the Intl. SCA Symp. in Edinburgh, Scotland, 17-19 Sept. 2001.
5. Yu, S.Y., Akervoll, I., Torsæter, O., Stensen, J.A., Kleppe, J., and Midtlyng, S.H.: "History Matching Gas Injection Processes with In-Situ Saturation Measurements and Process Hysteresis," paper SPE 48842 presented at the SPE Int. Conf. and Exhib. in Beijing, China, 2-6 Nov. 1998.
6. Amott, E.: "Observations Relating the Wettability of Porous Rocks," *Trans. AIME*, (1959) **216**, 156-162.
7. Akervoll, I., Talukdar, M.S., Midtlyng, S.H., Torsæter, O. and Stensen, J.Å.: "History Matching WAG Injection Experiments Performed Under CT Surveillance to Obtain Relative Permeability and Capillary Pressure," paper no. 17 presented at the 20th Annual Intl. Energy Agency Workshop and Symp. in Paris, France, 21-24 Sept. 1999.
8. da Silva, F.V.: "Primary and Enhanced Recovery of Ekofisk Field: A Single- and Double-Porosity Numerical Simulation Study," paper SPE 19840 presented at the SPE Annual Technical Conference and Exhibition, San Antonio, TX, USA, 8-11 Oct. 1989.
9. Brooks, R.H., and Corey, A.T.: "Properties of Porous Media Affecting Fluid Flow," *J. of Irrigation and Drainage Division, Proc. of ASEC* (1966) **92** (IR2), 61-88.

Paper III

Stochastic Reconstruction, 3D Characterization and Network Modeling of Chalk

M.S. Talukdar[1] and O. Torsaeter
Department of Petroleum Engineering and Applied Geophysics,
Norwegian University of Science and Technology, Norway

M.A. Ioannidis
Porous Media Research Institute, Department of Chemical Engineering,
University of Waterloo, Canada

J.J. Howard
Geoscience Building, Phillips Petroleum Company, OK, USA

Journal of Petroleum Science and Engineering, in press

Abstract

Systematic studies involving stochastic reconstruction, geometric and topological characterization, and network modeling of chalk, aiming at computation of petrophysical properties, are reported. The numerical chalk models are constructed exclusively from limited morphological information obtained from 2D backscatter scanning electron microscope images of the microstructure. Two different stochastic reconstruction methods are considered: conditioning and truncation of Gaussian random fields and simulated annealing. The potential of initializing the simulated annealing reconstruction with input generated using the Gaussian random fields method is evaluated and found to accelerate significantly the rate of convergence of simulated annealing reconstruction. This finding is important because the main advantage of simulated annealing method, namely its ability to impose a variety of reconstruction constraints, is usually compromised by its very slow rate of convergence.

A detailed description of the chalk microstructure in the form of 3D volume data is essential for the prediction of petrophysical properties from first principles. The prediction of absolute permeability and formation factor directly are considered first from such information. The prediction of absolute permeability, formation factor, and mercury-air capillary pressure curves are then considered using approximate network models constrained by information (pore and throat size distributions, coordination number) obtained from geometric and topological analysis of the reconstructed pore networks. Such information is extracted from the 3D volume data using morphological skeletonization and pore space partitioning methods. Very good agreement between the predicted and measured data is found for samples of North Sea chalk. On the basis of this study, it is concluded that (a) stochastic

[1] Corresponding author. E-mail: talukdar@ipt.ntnu.no

reconstruction from limited morphological information reproduces the essential features of pore geometry and connectivity of chalk, and (b) network modeling techniques can be used to predict petrophysical properties of chalk based on geometric and topological information of the stochastically reconstructed media.

Keywords: stochastic reconstruction, chalk, autocorrelation function, simulated annealing, 3D characterization, network modeling.

1. Introduction

Network modeling techniques have emerged in the recent years as an alternate tool to predict a variety of petrophysical properties from pore structure information. Macroscopic properties (e.g., fluid permeability, electrical conductivity, capillary pressure curves, etc.) are computed either directly by simulating fluid or electric current flow in complex geometric models of the pore space or by converting the porous media into geometrically simpler resistor-type networks. The requisite geometric and topological information for developing an equivalent network model (pore and throat shape and size distributions, pore-to-pore connectivity and spatial correlation) is, however, quite difficult to determine. X-ray computed microtomography (Spanne et al., 1994; Coles et al., 1994; Hazlett, 1995; Coles et al., 1996) and scanning laser confocal microscopy (Fredrich et al., 1995) can provide good quality volume images of the pore space. Unfortunately, these techniques are not suited for routine application. Most importantly, their resolution is not sufficient to image the sub-micron size pores that are abundant in chalk. In the absence of experimental 3D volume data, 3D stochastic reconstruction from limited statistical information obtainable from 2D microscopic images is a viable alternative. For the case of chalk, whose microstructure is too complex to reproduce by explicit modeling of the grain depositional and diagenetic processes (Bakke and Øren, 1997), stochastic reconstruction is also the only alternative.

The conditioning and truncation of Gaussian random fields (GRF) is a widely used stochastic reconstruction technique (Quiblier 1984; Adler et al., 1990; Ioannidis et al., 1997; Levitz, 1998; Liang et al., 2000a; Bekri et al., 2000; Kainourgiakis et al., 2000). The approach is mathematically elegant and computationally efficient, but unfortunately limited to imposing the void fraction (porosity) and pore-pore autocorrelation function of the reference (real) medium as the only reconstruction constraints. Much greater flexibility is offered by the simulated annealing (SA) method. SA is a global optimization technique, which can be constrained by an arbitrary number of correlation functions conveying morphological information of the microstructure. The algorithm minimizes an objective function, defined as the sum of square differences between a set of experimentally determined

correlation functions and that of the simulated medium, by a Monte Carlo type simulation. Using this method, Yeong and Torquato (1998a, 1998b) imposed the void-phase two-point correlation and lineal path functions as constraints in the reconstruction of a Fontainebleau sandstone sample. Manwart et al. (2000) reconstructed Berea and Fontainebleau sandstone samples from information on the void-phase two-point correlation function, void-phase lineal path function, and pore size distribution function. Liang et al. (2000b) imposed the so-called "neighborhood rank" distribution together with two-point correlation function, where neighborhood rank of a void pixel was defined as the number of void pixels in the neighborhood of that pixel. In a recent study using the SA technique, Talukdar et al. (2001a) showed that the solid phase chord distribution function contains additional information that is critical for the reconstruction of the morphology of *particulate* media exhibiting short-range order. They confirmed this finding by successfully reconstructing the microstructure of a pack of irregular silica particles. In another study, Talukdar et al. (2001b) reconstructed *chalk* samples imposing different combinations of void- and solid-phase autocorrelation and chord distribution functions. Quantitative analysis of 2D reconstructions revealed that imposing chord distribution functions had resulted only in minor improvement over what was achieved by using the void-phase autocorrelation function as the only constraint. This result was further verified by geometric and topological characterization of a 3D replica of the sample generated using only autocorrelation function constraints.

Despite its flexibility to include an arbitrary number of reconstruction constraints, the SA method is limited by slow convergence. This makes the reconstruction of large samples (256^3 or more voxels) impractical on single-processor computers. It is therefore, very important to find a way to accelerate the rate of convergence of SA method while reconstructing large samples with more than one constraints. One possibility may be to parallelize the SA algorithm and take advantage of several processors simultaneously. Unfortunately, no suitable parallel algorithm for the purpose of reconstructing porous media is available to date. Here, an alternative way to accelerate the rate of convergence, in which the SA reconstruction is initialized with input generated using the GRF method, is introduced.

With the exception of a recent study by Bekri et al. (2000), stochastic reconstruction and network modeling techniques have not been previously used in the study of chalk reservoirs. These authors employed a GRF technique to reconstruct the microstructure of a suite on North Sea chalk samples and computed their permeability and formation factor by pore network simulation and by direct numerical solution of the Stokes and Laplace equations. Agreement with experimental data within a factor of 4 for permeability and a factor of 2 for formation factor was observed for samples with no appreciable amount of vuggy porosity. Bekri *et al*. (2000) were not successful in modeling the microstructure and transport properties of samples containing vuggy porosity in the form of hollow Foraminifer shells; a fact

indicative of the limitations of the GRF method. In view of recent advances in stochastic reconstruction using the SA method and morphological characterization using a pore space partitioning technique (Liang et al., 2000c), it is important to consider whether or not further refinement is possible.

2. Stochastic reconstruction from limited morphological information

2.1 Morphological descriptors of the porous microstructure

The structure of a porous material is completely defined in terms of the binary phase function $Z(\vec{r})$, which takes the value of unity if a point $\vec{r}$ in space belongs to the void phase and the value of zero otherwise. For a statistically homogeneous medium, the void fraction (porosity), φ, and the autocorrelation function of the void phase, $R_z(\vec{u})$, are formally defined as the first two statistical moments of the function $Z(\vec{r})$,

$$\varphi = \langle Z(\vec{r}) \rangle, \qquad [1]$$

$$R_z(\vec{u}) = \frac{\langle [Z(\vec{r}) - \varphi] \cdot [Z(\vec{r} + \vec{u}) - \varphi] \rangle}{\varphi - \varphi^2}, \qquad [2]$$

where angular brackets denote statistical averages and $\vec{u}$ is a lag vector. For an isotropic porous medium, ϕ is a constant and $R_z(\vec{u})$ is only a function of the modulus of the lag vector, *i.e.*, $R_z(\vec{u}) = R_z(u)$. The function $R_z(u)$ may be determined from cross-sectional images of the pore space or from small-angle scattering experiments. Its slope at the origin is related to the specific surface area (the interfacial area per unit volume) *s*, which for digitized media is given by (Yeong and Torquato, 1998a):

$$s = -2D(\varphi - \varphi^2)\left.\frac{dR_z}{du}\right|_{u=0}, \qquad [3]$$

where *D* is the dimensionality of the space. Another important morphological descriptor is the correlation length $\bar{\lambda}$, which is defined as the integral of the autocorrelation function,

$$\bar{\lambda} = \int_0^\infty R_z(u)du\,. \qquad [4]$$

The assumption underlying this work is that the values of the phase function at different positions in space are independent realizations of random functions with mean and variance which are not dependent on position, and a correlation structure which depends only on the magnitude of the distance separating the different points. In other words, a weakly stationary process and finite variance are assumed (Journel and Huijbregts, 1978).

2.2 Reconstruction of porous media by the Gaussian Random Field method

Detailed descriptions of the GRF technique may be found elsewhere (e.g., Quiblier, 1984; Adler at al., 1990; Ioannidis et al., 1997). Briefly, the method utilizes as input the target porosity φ and the void phase autocorrelation function $R_z(\vec{u})$, calculated from binary 2D images of the real chalk sample (cf. Eqs. [1]-[2]). The latter function is computed along the two orthogonal directions only. The basic idea behind the GRF method is to generate values of the phase function $Z(\vec{r})$ on a cubic grid of fixed size (e.g., 256^3 voxels) in a manner that satisfies the target porosity and autocorrelation function. The reconstruction starts from a realization of a continuous 3D uncorrelated Gaussian field. This uncorrelated field is subsequently passed through a linear filter that introduces spatial correlation. The linear filter is constructed from the target porosity and autocorrelation function so that the requisite binary field $Z(\vec{r})$ is obtained by a final thresholding operation.

2.3 Reconstruction of porous media by the Simulated Annealing method

Simulated annealing, a global optimization technique, has a rich history in geostatistical applications (see Farmer, 1992 and Ouenes *et al.*, 1994, for a review). Hazlett (1997) first implemented this technique to reconstruct a 3D Berea sandstone sample using the extended variogram statistics. In order to account for the local porosity variation, the sample was divided into subdomains and the variogram for each subdomain was computed independently. A family of variograms representing the entire sample was referred to as the extended variogram. Since then, this technique has been used by others for stochastic reconstruction of porous media (Yeong and Torquato, 1998a; Yeong and Torquato 1998b; Manwart et al., 2000; Liang et al., 2000b, Talukdar et al., 2001a, Talukdar et al., 2001b). The main idea behind this simple but powerful technique is to gradually transform an unstructured ("high-energy") configuration of solid and void pixels into a "minimum-energy" configuration, where "energy" is measured in terms of deviations from a set of target, experimentally determined, functions conveying morphological information, *e.g.*, $R_z(u)$. This is a stochastic optimization problem with an objective function generally defined in terms of *n* reference functions as:

$$E = \sum_{n} \sum_{u=0}^{u_n^{max}} \left[f_n(u) - \widetilde{f}_n(u) \right]^2, \qquad [5]$$

where, f_n and $\widetilde{f}_n$ are the simulated and reference functions, respectively. The reference functions imposed are the pore-pore autocorrelation functions along the three orthogonal directions, $R_{z_x}(u)$, $R_{z_y}(u)$ and $R_{z_Z}(u)$. Each reference function $\widetilde{f}_n$ is matched to a maximum lag u_n^{max}.

The algorithm is based on an analogy with thermodynamics, specifically with the way that metals cool and anneal. Metropolis et al. (1953) employed the so-called Boltzmann probability distribution to simulate this process numerically. The Boltzmann probability distribution, $p(E) \approx e^{\frac{-E}{bt}}$ expresses the idea that a system in thermal equilibrium at temperature *t* has its energy probabilistically distributed among all different energy states *E*. The constant *b* is termed the Boltzmann constant. When offered a succession of options, a simulated thermodynamic system was assumed to change its configuration from energy E_1 to energy E_2 with probability, $p = e^{\frac{-\Delta E}{bt}}$ where, $\Delta E = E_2 - E_1$. Note that if $E_2 < E_1$ (decreasing energy), this probability is greater than unity; in such cases the change is arbitrarily assigned a probability $p = 1$, i.e., the system always takes such an option.

The simulation begins by randomly designating fractions ϕ and $(1-\phi)$ of void and solid phase voxels, respectively, on a grid of size N^3. At each iteration step *k*, a void and a solid voxel are chosen at random and their phase function values are interchanged. This interchange slightly modifies the functions f_n and therefore changes the energy of the system while preserving the porosity. A voxel interchange is accepted with a probability p_a given by the Metropolis rule (Metropolis et al., 1953),

$$p_a^{(k)} = \begin{cases} 1 & if\ \Delta E^{(k)} \le 0 \\ e^{-\Delta E^{(k)}/T^{(k)}} & if\ \Delta E^{(k)} > 0 \end{cases}, \qquad [6]$$

where $\Delta E^{(k)} = E^{(k+1)} - E^{(k)}$ and $T^{(k)}$ is a control parameter representing the "*temperature*" of the system. Notice that the product *bt* has been replaced by *T* which has the same unit as the energy. Further, *E* is not same as the Gibb's free energy in thermodynamic systems. Therefore, conventional units for energy and temperature are not appropriate for *E* and *T*. The energy is measured as the difference between reference and simulated correlation functions and is unitless. The starting value and the rate of reduction of *T* are

governed by an *annealing schedule*. This schedule should be such that a global optimum is achieved as quickly as possible. In practice, T is reduced by a factor λ after a predefined number of interchanges, referred to as a *Markov chain*. If rapid convergence is expected, a dynamic schedule, which takes into account the rapid fluctuations in the evolving energy in updating the system temperature T should be preferred over a static one where T decreases monotonically. Otherwise, there is a real possibility that the system will be trapped at a local energy minimum, unless T is decreased very slowly. The following formula for updating T was adopted in this work (Ouenes et al., 1994):

$$\lambda = Max\left[\lambda_{min}, Min\left(\lambda_{max}, \frac{E_{min}}{\overline{E}}\right)\right], \qquad [7]$$

where λ_{min} and λ_{max} are the minimum and maximum allowable reduction factors, respectively, and are specified by the user. In this approach, for each *Markov chain*, the lowest and average energy values reached, E_{min} and $\overline{E}$, are used to compute the reduction factor λ. The system temperature is then updated as,

$$T = T_o e^{(\lambda-1)(m+1)}, \qquad [8]$$

where, T_o is the starting temperature and m is the number of Markov chains after a total of k interchanges. This approach permits estimation of the starting temperature from the initial behavior of the energy function. Accordingly, the mean change in the energy function for k_o initial iterations is first evaluated:

$$\overline{\Delta E} = \frac{1}{k_o}\sum_{k=1}^{k_o} \Delta E^{(k)}. \qquad [9]$$

The starting temperature T_o is then estimated from the following expression for a given initial acceptance probability p_a^o,

$$p_a^o = e^{-\overline{\Delta E}/T_o}. \qquad [10]$$

All results obtained in this work were obtained with $k_o = 100$, $p_a^o = 0.5$ and $m = 11500$. It should be kept in mind that the choice of these parameters is highly system-specific (Ouenes et al., 1994).

2.4 Hybrid GRF/SA reconstruction

The simulated annealing algorithm is very slow because of the large number of unsuccessful voxel interchanges, especially at low temperatures. For comparison, a GRF reconstruction of size 256^3 takes only a little more than an hour on a lightly loaded IBM RS 6000 UNIX workstation, whereas a SA reconstruction of this size takes several days. From the point of view of obtaining a realistic replica of a microstructure, the SA method is, however, preferred because it can accommodate additional reconstruction constraints. It is therefore worth exploring the potential time saving that may arise from initiating the SA reconstruction with a GRF-generated instead of a random configuration.

3. Laboratory measurements

3. 1 Target images and morphological parameters

The GRF and SA methods were used to reconstruct 3D samples of a high porosity, low permeability North Sea chalk. The reference (target) porosity and autocorrelation function were obtained from a single backscatter SEM image of size 512x512 pixels, acquired at 1500x magnification and providing a pixel resolution of 0.136x0.136 μm^2. The image was captured from a thin section of approximate size 10x10x1 mm^3 that was cut off from a cleaned and dried core sample and then impregnated with epoxy under vacuum. A binary image was obtained by setting all pixels above a threshold value to zero (Fig. 1(a)). The porosity of the binary image was 0.309. The target autocorrelation function was calculated from the two-point correlation function $S_2(u)$ from the equation:

$$R_Z(u) = \frac{S_2(u) - \varphi^2}{(\varphi - \varphi^2)}. \qquad [11]$$

This function was calculated along the two orthogonal directions. The *x*- and *y*-direction autocorrelation functions are shown in Fig. 1(b) together with the average. The average autocorrelation function for this sample corresponds well with those reported by Bekri et al. (2000) for similar North Sea chalk samples.

The correlation length was calculated using Eq. [4] and found equal to 6.68 pixels or 0.91 μm, a value close to those reported by Bekri et al. (2000). The specific surface area of the sample calculated from the binary image using Eq. [3] is 1.3 μm^{-1}. This value differs significantly from the value obtained by mercury intrusion porosimetry (MIP), which is 4.75 μm^{-1}. This discrepancy is expected, considering the limited resolution (0.136 μm/pixel) of the image

data. The magnitude of specific surface area is dependent on the size of the "probe" used to measure it. Since MIP detects pore volume invaded at capillary pressures corresponding to equivalent cylindrical pore radii smaller than 0.136 μm, it is expected that MIP will yield a higher specific surface area.

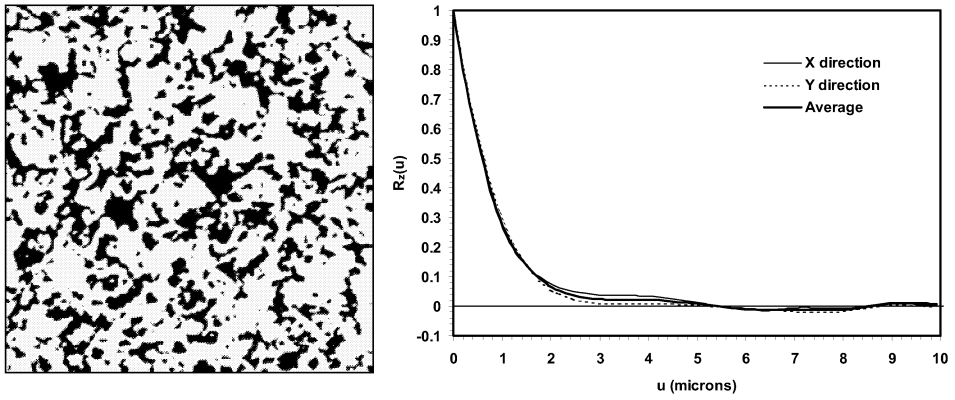

(a) **(b)**

Fig. 1—(a) Backscatter scanning electron microscope image of a North Sea chalk sample. Image size is 512x512 pixels (70x70 μm^2). The image is thresholded segmenting pore (black) and solid (white). Image porosity is 0.309. (b) Pore-pore autocorrelation function of the image.

3.2 Petrophysical properties

Several laboratory measurements were conducted on chalk sample used for 3D reconstruction and subsequent prediction of petrophysical properties. Porosity, absolute permeability and capillary pressure were measured using standard laboratory equipment. Chalk sample porosity was measured on a standard size dry core using a helium porosimeter and found equal to 0.3, in good agreement with the image data. A constant head permeameter with a Hassler cell was used to measure the permeability to air and brine. The absolute air and brine permeabilities were 1.35 mD and 0.64 mD, respectively. The brine permeability was measured using filtered formation brine saturated with calcite to avoid dissolution of chalk in the brine. One of the most important parameters regarding the electrical properties of rocks and is of fundamental importance in electrical well logging is the formation factor *F*. This parameter shows a relationship between water saturated rock conductivity and bulk water conductivity, and represents the factor by which the resistivity increases due to tortuosity of electric flow path in the rock sample. Formation factor was measured at laboratory conditions by a two-electrode method using the ratio of voltage decrease between a reference resistor and a core sample in series. The cleaned and dried core was 100%

URN:NBN:no-2347

saturated with formation brine and placed in the resistivity cell to measure R_o. The measured formation factor was 10.4.

The oil (decane)-water (formation brine) capillary pressure was measured in a centrifuge (Beckman Model LH-M Ultracentrifuge). The drainage capillary pressure curve is shown in Fig. 2. The residual water saturation is shown to be about 0.3 at $P_c \approx 5\text{x}10^5$ Pa, the maximum capillary pressure reached in the centrifuge without core damage. This value is considerably higher than 0.1, the value typical attributed to the "irreducible" water saturation of North Sea chalk. Mercury porosimetry measurements were conducted using a Carlo Erba Porosimeter 2000. Before the measurement, the chalk sample was dried for a day at 60°C and then evacuated to a pressure below 10^{-4} mm Hg until a constant weight at room temperature was observed. The mercury-air capillary pressure was calculated from intrusion mercury volume versus pressure data and is included in Fig. 2. The two curves cannot be brought into coincidence by scaling with the ratio of the product $\sigma\cos\theta$ of the two fluid pairs. This indicates significant differences in fluid distribution at the pore scale for the same value of wetting fluid saturation (Dullien, 1992).

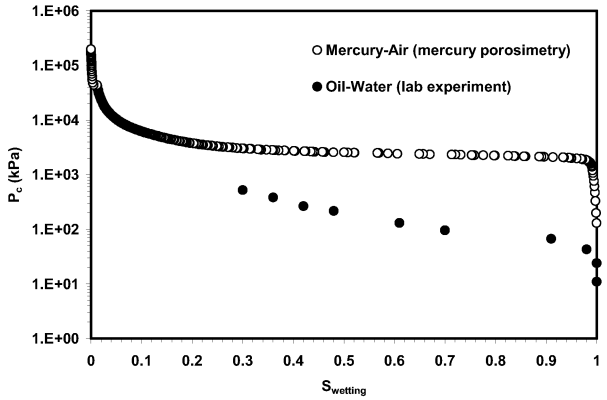

Fig. 2—Oil-water and mercury-air capillary pressures of the target chalk sample (ϕ=0.3) obtained from centrifuge and mercury porosimetry measurements, respectively.

Mercury intrusion and extrusion data provide information about the sizes of throats and pores in the chalk sample. The cumulative distribution of pore volume by pore throat size is obtained from the intrusion data. Similarly, the retraction data provide an estimate of the cumulative distribution of pore volume by pore size. As such, they are volume weighted. It is also understood that these estimates are compromised by pore space accessibility limitations - large pores are not invaded at the pressure corresponding to their size if they are shielded by smaller pores and, for the case of retraction data, permanent trapping of mercury (Ioannidis and Chatzis, 1993a). An equivalent cylindrical capillary radius is obtained from capillary pressure. The

relationship of radius of pore or throat with capillary pressure is expressed by the well-known Young-Laplace equation of capillarity,

$$P_c = \frac{2\,\sigma\,\cos\theta}{r}, \qquad [12]$$

where, r is the pore or throat radius, σ is the mercury surface tension, θ is the contact angle and P_c is the retraction or intrusion capillary pressure. The pore and throat radius distributions are calculated considering a surface tension of 480 mN/m and a contact angle of 140° for intrusion and 120° for extrusion. The resulting distributions are shown in Fig. 3. There is considerable overlap between the pore and throat sizes. The mean radius of the throat size distribution is 0.27 μm and that for pore size distribution is 0.73 μm.

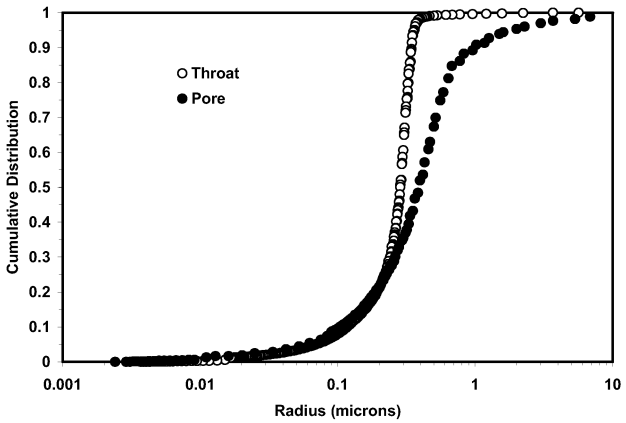

Fig. 3—Pore and throat size distributions of the target chalk sample (ϕ=0.3) obtained from mercury porosimetry measurement assuming pores and throats have cylindrical shape. Mean throat and pore radii are 0.27 and 0.73 μm respectively.

4. Reconstruction results

4. 1 GRF and SA reconstructions of a 100^3 voxels sample

The potential of hybrid GRF/SA reconstruction was tested on a sample containing 100^3 voxels. In Case 1, the SA method is used with an initial configuration that corresponds to a cube of size 100^3 voxels extracted from a GRF-generated realization of size 256^3 voxels. In this case annealing was started at high initial temperature allowing the system to "melt". Case 2 differs from Case 1 in that annealing was started at low initial temperature preventing "melting" of the system. The initial energy for Cases 1 and 2 was

0.322 and the reconstruction was completed as soon as the energy fell below 10^{-5} (see Table 1). In Case 3, the conventional SA method was applied, with the annealing process starting at high initial temperature from a random, uncorrelated configuration.

As a result of further reduction of energy in the system by SA method, improved match of the autocorrelation functions in all directions is observed for Cases 1 and 2 by comparison to the initial, GRF-generated configuration (see Fig. 4). Fig. 4 shows the result in the *x*-direction. Similar results were obtained in other directions and are not shown. Note that the initial configuration (a sub-volume from a GRF-generated realization of size 256^3 voxels) does not match the target functions, whereas the complete (256^3 voxels) GRF realization does (see below).

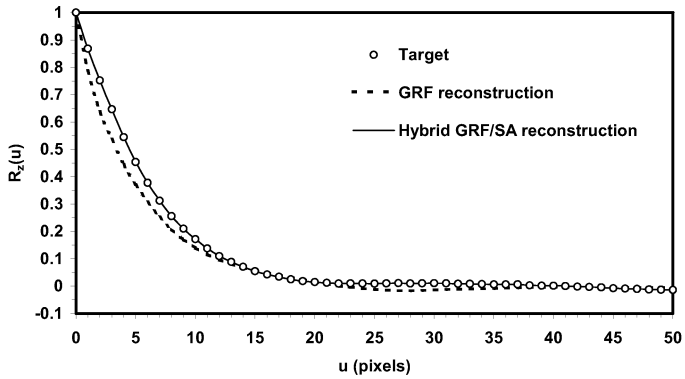

Fig. 4—Target and simulated (100^3 voxels sample) autocorrelation functions in *x*-direction. Empty circles represent target autocorrelation function, broken and solid lines represent autocorrelation functions of the GRF-generated and hybrid GRF/SA-generated (Case 2) media, respectively. Similar results were obtained in other directions and hence are not shown.

The reduction of energy in the system by SA yields a better reconstruction. Fig. 5(a) presents a section through the GRF-generated image while a section of the target image [taken from Fig. 1(a)] is shown in Fig. 5(b) for comparison. Visually, the images look alike, but closer inspection reveals subtle differences in the shape of the rock-pore interface and the number of small void and solid features. The hybrid GRF/SA reconstruction improves the quality of the image slightly (not shown).

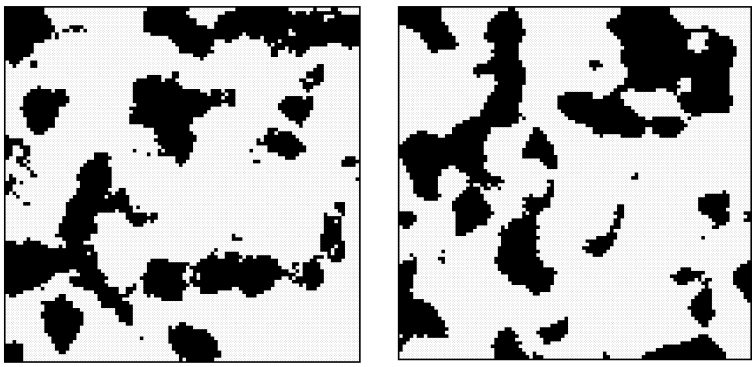

(a) (b)

Fig. 5—Reconstruction of 100^3 voxels sample; (a) a section through the GRF-generated image, (b) target image [100x100 pixels taken from Fig. 1(a)]. Pores are in black.

The evolution of energy and temperature for the three cases is presented in Fig. 6. For Case 2 and Case 3, a nearly exponential decrease in energy and temperature is observed. For Case 1, however, energy initially builds up in the system as the system "melts" during cooling. Temperature fluctuates during the energy build up due to the dynamic nature of the annealing schedule, which takes into account the abrupt changes in the evolving energy function.

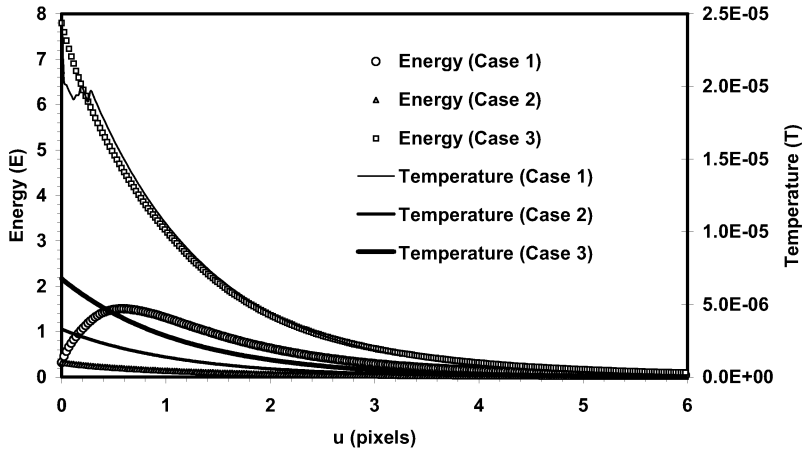

Fig. 6—Evolution of energy and temperature for the three simulated annealing reconstruction cases (Case 1, 2 and 3). For clarity, volume of data has been reduced.

From the point of view of computational efficiency, initialization of SA with a GRF-generated, instead of an uncorrelated random configuration, seems promising. Table 1 shows some of the important simulated annealing

parameters. The simulations were performed on an IBM RS6000 SP Model 9076-260 computer. The conventional SA reconstruction required 5.89 CPU hours (22.7 million iterations) to reconstruct a 100^3 sample, but only 3.88 hours (15.7 million iterations) when the annealing process was started from GRF reconstruction at low initial temperature. For a larger model (e.g., 256^3 voxels), the savings in CPU time would be considerably more significant. There is no gain if the annealing process is started at high initial temperature. Seeding SA with imperfect but not random image and then not to destroy that seed image by overheating is also suggested by others (e.g., Deusch and Journel, 1992; Farmer, 1992).

Table 1—Comparison of the SA parameters for construction of a 100^3 voxels sample.

	Simulated annealing reconstruction cases (target energy 10^{-5})		
	Case 1	**Case 2**	**Case 3**
Energy at start	0.322	0.322	7.80
Temperature at start	2.52E-05	3.30E-06	6.76E-06
CPU time (hours)	5.68	3.88	5.89
Total iterations (millions)	22.37	15.70	22.70
Convergence temperature	7.27E-17	1.29E-14	3.64E-17

4. 2 GRF and SA reconstructions of a 256^3 voxels sample

A reconstructed porous medium of size 100^3 voxels is not sufficiently large for obtaining reliable estimates of macroscopic properties, such as the permeability, formation factor, etc. For this reason, two realizations of size 256^3 voxels were generated. The first one (Case 4) was reconstructed using the GRF method. Reconstruction of this size using the SA method even using only the autocorrelation function seems impractical at the present time due to limitations in computer speed, therefore a new hybrid technique [described in Section 2.4 and exemplified in Section 4.1 (Case 2)] was adopted. This realization is referred to as Case 5. The starting energy (after GRF reconstruction) calculated from Eq. 4 was 0.0283. This energy was reduced by an order of magnitude (0.0026) in about 9 hours on an IBM RS6000 SP Model 9076-260 computer. The annealing was started at low initial temperature, therefore, the energy decreased gradually and no "melting" took place. An improved match of the autocorrelation function (see Fig. 7 for *x*-direction) and a "smoother" image [compare Figs. 8(a) and 8(b)] was observed for this modest reduction of energy. A 3D representation of the reconstructed chalk (Case 5) is shown in Fig. 9.

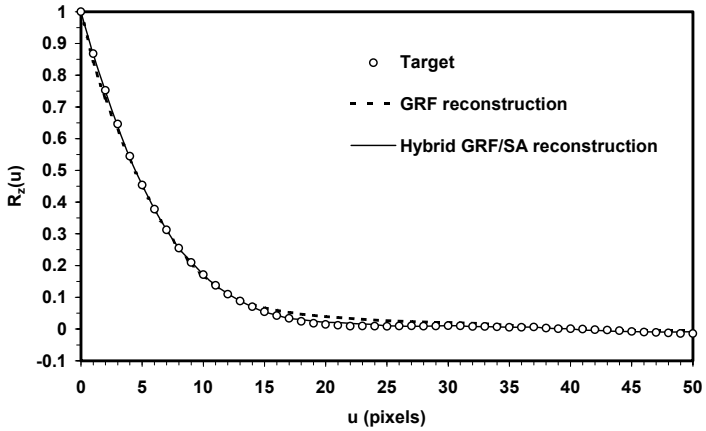

Fig. 7—Target and simulated (256^3 voxels sample) autocorrelation functions in x-direction. Empty circles represent target autocorrelation function, broken and solid lines represent autocorrelation functions of the GRF-generated (Case 4) and hybrid GRF/SA-generated (Case 5) media, respectively. Similar results were obtained in other directions and hence are not shown.

It is interesting to note how other measures of the morphology of the chalk microstructure, not imposed as constraints on the reconstruction process, are reproduced in the models. Application of the SA method provided a better match between the chord distribution functions of the target image and the reconstructed sample. Figure 10 shows solid- and pore-phase chord distribution functions along the *x*-direction for the target image and the two reconstructed samples (Cases 4 and 5). Similar results were obtained in other directions and are not shown.

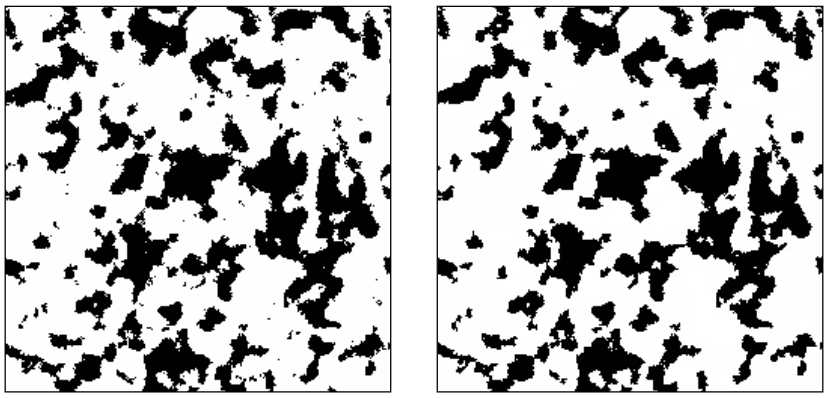

(a) **(b)**

Fig. 8—Reconstruction of 256^3 voxels sample; (a) a section through GRF-generated (Case 4) image, (b) a section through hybrid GRF/SA-generated (Case 5) image. Pores are in black.

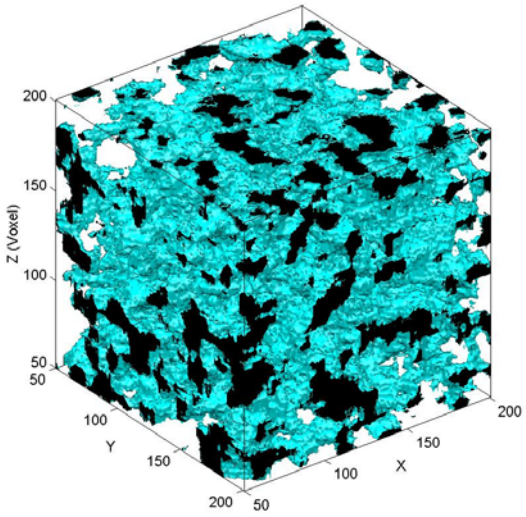

Fig. 9—Microstructure of the reconstructed 3D chalk sample (Case 5). A subvolume of 150^3 voxels has been shown. The pore space is shown opaque with ends in black. The solid is transparent.

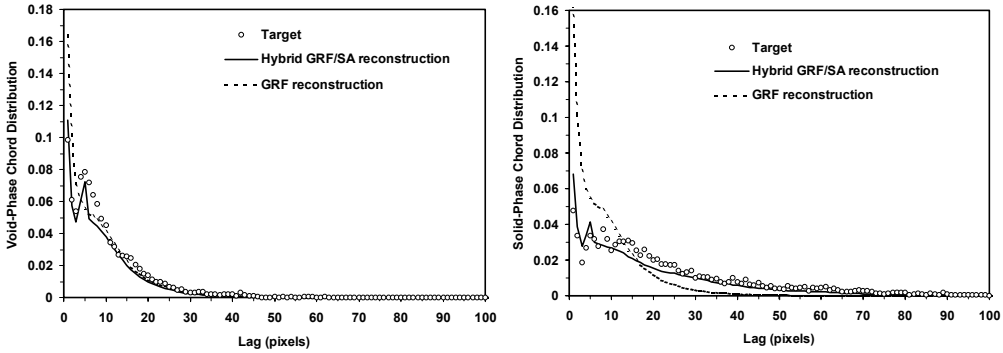

(a) **(b)**

Fig. 10—Chord distribution functions of the reconstructed sample (256^3 voxels) in x-direction; (a) solid phase, (b) void phase. Empty circles represent target chord distribution, broken and solid lines represent chord distributions of the GRF-generated (Case 4) and hybrid GRF/SA-generated (Case 5) media, respectively.

5. Network modeling for petrophysical property estimation

5. 1 Characterization of the reconstructed media

The stochastic reconstruction techniques do not impose any connectivity constraints. Therefore, the reconstructed media may contain clusters of isolated pore and solid voxels. These isolated clusters contribute to the correlation functions and their removal by filtering results in deviations from

the target functions. This afflicts reconstructed media for which $\phi < 0.2$ (Ioannidis et al., 1997) and is not a matter of concern in the reconstruction of chalk. Nonetheless, the cluster reconnection algorithm of Liang et al. (2000b) was implemented to establish the connectivity of the void phase. The algorithm conserves porosity and causes negligible changes to the morphology of the solid-void interface and autocorrelation function. Isolated pore pixels in the medium reconstructed by the GRF technique (Case 4) were 0.3%, and 0.1% in the medium reconstructed by the hybrid GRF/SA technique (Case 5).

The fully connected media were characterized using the pore space partitioning algorithms developed by Liang et al. (2000c). The method is based on partitioning of pore space into nodal pores by identifying local minima in the cross-sectional area of the pore space channels using a skeleton link scanning procedure. The methodology takes advantage of a 3D, connectivity preserving, fully parallel thinning algorithm developed by Ma and Sonka (1996). The thinning algorithm is used to extract the skeleton (medial axis) of the pore space. The skeleton serves as the basis for characterization of the reconstructed media. The characterization provides the distributions of pore volume V_p, throat area A_t, throat hydraulic radius R_H and coordination number, as well as the distributions of hydraulic and electrical conductance of distinct pore space channels.

Assuming that the pores are cubic and that the throats have a square cross-section, the pore volume and throat area distributions were converted to equivalent pore and throat sizes using the following relationships,

$$R_p = \left(\frac{V_p}{8} \right)^{1/3} \qquad [13]$$

$$R_t = \left(\frac{A_t}{4} \right)^{1/2} \qquad [14]$$

The pore-size, throat-size and coordination number distributions obtained from 3D characterization of the reconstructed 256^3 sample (Case 4) are shown in Figs. 11, 12 and 13, respectively. Pore and throat radii were calculated using Eq. 13 and 14, respectively. Throat-size and coordination number distributions obtained from 3D characterization of sample reconstructed in Case 5 are included in Figs. 12 and 13, respectively. Pore- and throat-size distributions calculated from mercury intrusion and extrusion data are also included in Figs. 11 and 12, respectively. As expected, the throat-size and coordination number distribution of the reconstructed sample in Case 4 differs only slightly from those of the reconstructed sample in Case 5.

The range of pore and throat sizes found in the reconstructed chalk sample agrees very well with the range of pore and throat sizes estimated from mercury porosimetry. This finding further supports the conclusion that

stochastic reconstruction has provided a faithful replica of the chalk microstructure. As stated previously, there is no expectation that the distributions shown in Figs. 11 and Fig. 12 should overlap in anything but the range of pore and throat sizes. Further, it has been observed (Knackstedt et al., 1998) from rate-controlled mercury injection experiments on Berea sandstone that correlated heterogeneity may exists at the pore-scale upto several pore lengths which has a marked effect on the behavior of capillary pressure curve. In our reconstructions, the rock is assumed to be macroscopically homogeneous. The correlations considered are at the pixel (sub-pore) scale, which may have contributed to the mismatch in Figs. 11 and 12.

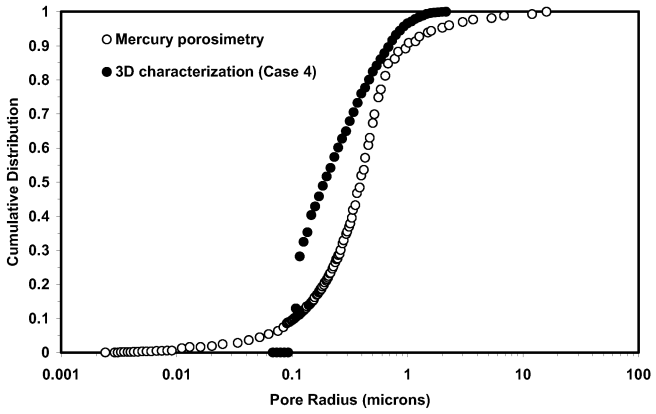

Fig. 11—Pore size distributions from mercury porosimetry and from 3D characterization of the reconstructed medium (Case 4).

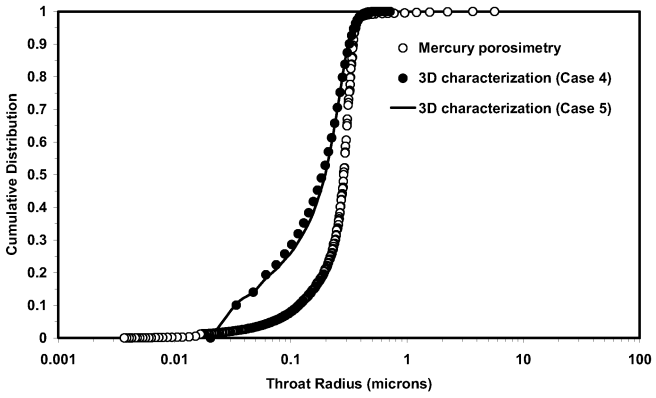

Fig. 12—Throat size distributions from mercury porosimetry and from 3D characterization of the reconstructed media (Case 4 and 5).

The mean throat and pore radii of the reconstructed medium (Case 4) obtained from 3D characterization are 0.182 and 0.31 μm, respectively. These values are somewhat lower than those obtained from mercury porosimetry data (0.27 and 0.73 μm, respectively). The mean throat radius of the reconstructed medium (Case 5) is 0.184. Samples reconstructed in Case 4 and 5 have slightly different coordination number distributions (see Fig. 13) and average values of the distributions (4.8 for Case 4 while 5.1 for Case 5). The average coordination numbers are much higher than that obtained by Bekri et al. (2000) for similar chalk (approximately 3.2). This discrepancy is probably due to limitations of the characterization methodology employed in the previous study. There are few pores having coordination number as high as 28. The 3D characterization of the reconstructed chalk (Case 4) estimated 2264 pores and 7916 necks in a sample of 35x35x35 μm^3.

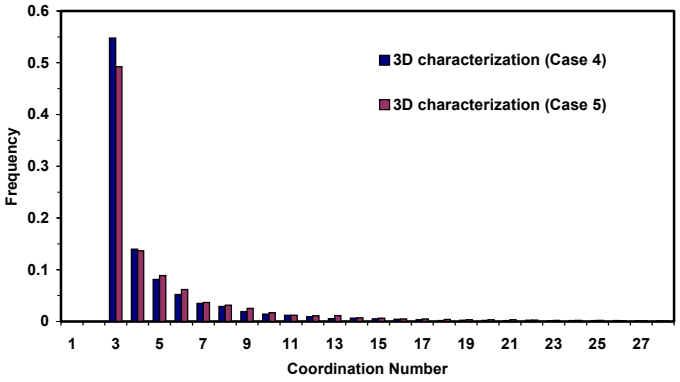

Fig. 13—Coordination number distributions of the reconstructed media (Case 4 and 5) obtained from 3D characterization.

5. 2 Network model

In order to estimate petrophysical properties, an equivalent network model of chalk pore structure was constructed based on bond-correlated site percolation concepts detailed by Ioannidis and Chatzis (1993a, 1993b). The network model is constructed from input on porosity, average coordination number, pore- and throat-size distributions, specific surface area and shape of pores and throats. Its distinguishing features are explained below.

The network model is an approximation of the irregular 3D microstructure shown in Fig. 9. An irregular porous medium [see Fig. 14(a)] is represented by a network of cubes (pores) occupying the sites of a regular cubic lattice. The cubic pores are interconnected through volumeless throats of rectangular cross-section (see Fig. 14(b)). Prior to assignment of sizes to the sites and bonds of the lattice, site percolation is used to remove sites and associated bonds until the desired average coordination number is achieved. Next, pore

sizes are randomly assigned to the lattice size from the known pore volume distribution. In agreement with detailed studies of the geometry of stochastically reconstructed porous media (Ioannidis and Chatzis, 2000), a bias is introduced on the assignment of pore sizes so that larger pores preferentially occupy sites of greater coordination number. Assignment of throat sizes follows the bond-correlated site percolation scheme, whereby larger throats are assigned to bonds connecting larger pores. This introduces short-range spatial correlation of pore throat sizes and is also in agreement with detailed studies of the geometry of stochastically reconstructed porous media (Liang et al., 2000a). The node-to-node distance or lattice constant (l_c) is adjusted to obtain the required porosity. Note that the network model matches the average coordination number accurately, but not the coordination number distribution.

In the construction of the network model, it is realized that the shape of actual pores is in fact irregular (see Ioannidis and Chatzis, 2000). Thus, although the measured pore volume distribution is precisely matched in the network model, the model is actually smoother than the medium it is taken to represent (i.e., the specific surface area of the network model is smaller). For the sample under study the specific surface area of the equivalent network is 0.9 μm^{-1}, by comparison to 1.3 μm^{-1} for the reconstructed medium and 4.75 μm^{-1} for the real sample (MIP result). Realistic simulation of immiscible displacement using the network model requires at least an approximate account of late pore filling (i.e. filling of the crevices and pore surface roughness). Several possibilities exist and the one considered here is based on a fractal "decoration" of the pores. A fractal decoration (see Fig. 14(c)) is assigned to the pore cross-section in order to match the model specific surface area (S_m) with the one measured by mercury porosimetry (S_f). It is shown (Lowell and Shields, 1991) that the number of levels of fractal decoration (n_f) required to match this specific surface area can be expressed by,

$$n_f = \frac{log\left(\frac{S_f}{S_m}\right)}{log\left(\frac{4}{3}\right)} \qquad [15]$$

Addition of fractal decoration increases the model pore volume. As a result, it is necessary to adjust the equivalent pore radii (Eq. 13). The volume adjustment necessary may be calculated as follows:

$$\frac{V_f}{V_p} = 1 + \frac{3}{5}cos\left(\frac{\pi}{6}\right)\left[1 - \left(\frac{4}{9}\right)^{n_f}\right] \qquad [16]$$

where V_f is the volume of each pore after n_f levels of fractal decoration.

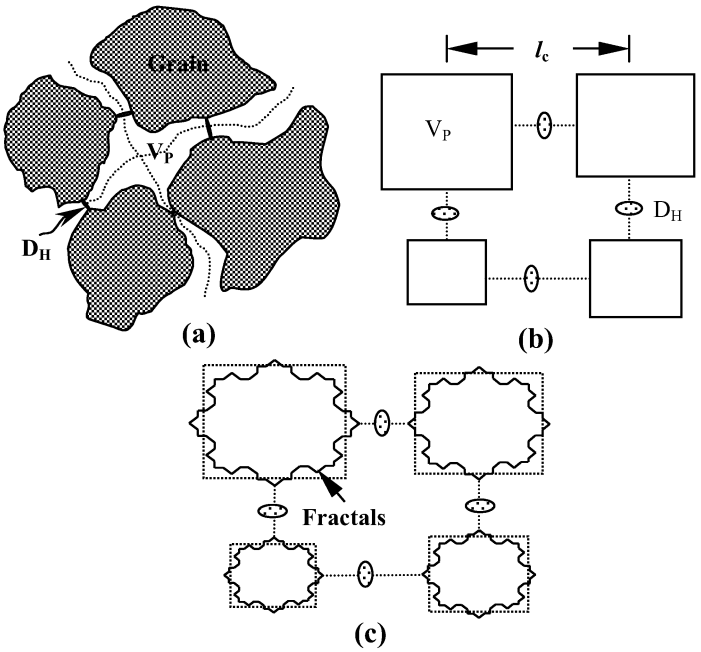

Fig. 14—Construction of a network model; (a) real porous medium, (b) equivalent network model, (c) fractal decoration in order to match specific surface area.

5. 3 Computation of petrophysical properties

Computation of absolute permeability and formation factor is based on an electric analogue-linear network concept detailed by Ioannidis and Chatzis (1993a, 1993b). To simulate fluid or current flow, one needs to compute the overall hydraulic or electric conductance of the network by applying the principle of mass or electric current balance at all nodes. In the network model the throats have no volume as they correspond to local minima in the hydraulic radius of distinct, irregularly shaped pore space channels. The equivalent hydraulic or electrical conductance of the each resistor in the network model is calculated from the following equations:

$$g_h = \frac{\xi R_t^4}{8 l_e} f(\xi) \qquad [17]$$

$$g_e = \frac{4 \xi R_t^2}{l_e} \qquad [18]$$

where l_e is an equivalent length estimated as

$$l_{e_{m-n}} = l_c - (R_{p_m} + R_{p_n}) \quad [19]$$

In these equations, $f(\xi)$ is a function of the throat aspect ratio ($\xi = 1$ here, see also Ioannidis and Chatzis, 1993) and R_{p_m}, R_{p_n} are the sizes of adjacent pores.

The mass (or electric current) balance requires that the algebraic sum of flows at all nodes in the network be zero, i.e.,

$$\sum q_{mn} = g_{mn}(P_n - P_m) = 0 \quad [20]$$

where g_{mn} is the effective hydraulic conductance of a throat connecting pores m and n, and P_m and P_n are the corresponding pore pressures. These equations, together with appropriate initial and boundary conditions, constitute a set of linear equations, which can be solved by a linear solver. A preconditioned conjugate gradients method was employed.

The pressure differential (ΔP) (or voltage differential, ΔV) across the model can be computed for a given volumetric flow rate (Q) (or electric current, I), enabling the calculation of the absolute permeability (k) and formation factor (F) of the network. Absolute permeability is calculated from Darcy's equation:

$$k = \frac{\mu L Q}{A \Delta P} \quad [21]$$

where L is the network length and A is the network cross-sectional area. The formation factor is calculated in a similar manner.

It is emphasized that the network model is only an approximation of the pore space in chalk. The quality of this approximation must be judged not only by comparing the predicted petrophysical properties with experimental data, but also by comparing them with predictions obtained using the reconstructed microstructure itself. For this reason, the permeability of the reconstructed chalk is also calculated by solving the equivalent resistor network problem as described in Liang *et al.* (2000a) and the formation factor by random-walk simulation (Ioannidis et al., 1997).

6. Network modeling results

6. 1 Drainage capillary pressure

The network was constructed based on the 3D characterization data for the reconstructed chalk sample corresponding to Case 4. The mercury-air drainage capillary pressure computed using the network model is compared to the experimental one in Fig. 15. The network model predicts a breakthrough

capillary pressure and radius of 24.5×10^5 Pa and 0.29 μm respectively. The agreement is remarkably good considering the approximate nature of the network model and the fact that no adjustable parameters were used. The discrepancy in the range 30×10^5 - 100×10^5 Pa is most likely due to the fact that the fraction of the volume of each pore that is contributed by fractal decoration (and therefore contributes to late filling) is small.

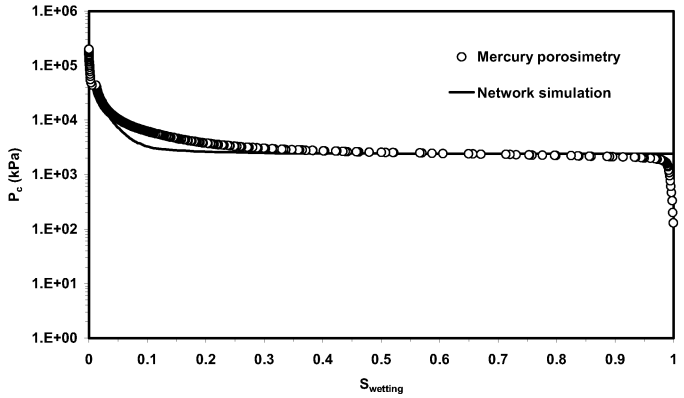

Fig. 15—Experimental and simulated mercury-air drainage capillary pressure curves.

As stated previously, correlated heterogeneity at the pore-scale has an effect on the rate-controlled mercury-air capillary pressure curve for Berea sandstone (Knackstedt et al., 1998). Ioannidis and Chatzis (1993a) modeled the effect of spatial correlations among the pore sizes on pressure-controlled porosimetry. Such correlations were shown to make the mercury intrusion curve more gradual, without affecting the breakthrough pressure. Unfortunately, no rate-controlled mercury porosimetry data are available for chalk for estimating the range of pore size correlations. It is expected (see Ioannidis and Chatzis, 1993a) that an even better match would be obtained in Fig. 15 if spatial structure among the pores were included in the network model. Note however that the network model involves several approximations and such a match could not be used conclusively as evidence for the presence of long-range correlations.

6. 2 Absolute permeability and formation factor

Computations of absolute permeability and formation factor performed directly on the reconstructed microstructure yielded the values 1.73 mD and 12.3, respectively. The computed values are remarkably close to the experimental values (1.35 mD and 10.4, respectively), supporting the conclusion that stochastic reconstruction has rendered the microstructure of the real sample with sufficient accuracy. Predictions of permeability and

formation factor from the network model are 0.643 mD and 13.5, respectively, also in good agreement. Permeability and formation factor predicted from simulation directly on the reconstructed microstructure should be considered more reliable, because the convergent-divergent geometry and exact spatial arrangement of all flow paths is taken into account. On the other hand, the network model considers flow paths as channels of uniform cross-section and slightly underestimates the hydraulic and electrical conductivity.

Finally, it is instructive to check whether the following formula, relating the values of k and F in stochastically reconstructed media to image statistical properties (ϕ and s) (Liang et al., 2000a), also holds for the reconstructed chalk:

$$k = \frac{64\varphi^2}{226Fs^2} \qquad [22]$$

Using $\phi = 0.309$, $s = 1.3\ \mu m^{-1}$ and $F = 12.3$, we obtain $k = 1.3$ mD in excellent agreement with the measured permeability.

7. Conclusions

Hybrid GRF/SA reconstruction was shown to lead to refinement of the simulated microstructure and considerable acceleration of the convergence of the SA method. Morphological, geometric and topological characterization showed that the resulting stochastic replica is a reasonably accurate model of the microstructure of the real sample. This was further confirmed by computing the permeability and formation factor of the simulated microstructure.

A network model capable of incorporating the essential geometric, topological and correlational aspects of stochastically reconstructed porous media was constructed and used to estimate the petrophysical properties of North Sea chalk. The predictions of permeability, formation factor, and mercury-air capillary pressure curves were found to be in good agreement with experimental data.

Acknowledgments

Saifullah Talukdar gratefully acknowledges the financial support by Phillips Petroleum Company Norway for his Ph.D. studies. He also acknowledges the warm reception he received from the Department of Chemical Engineering (Porous Media Laboratory), University of Waterloo, Canada during his three months research stay in 2001.

Nomenclature

A	=	*Network cross-sectional area*
A_t	=	*Throat area*
D	=	*Dimensionality of the space*
E	=	*Energy*
E_{min}	=	*Minimum energy*
$\overline{E}$	=	*Average energy*
F	=	*Formation factor*
$\widetilde{f}_n$	=	*Reference (target) correlation function*
f_n	=	*Simulated correlation function*
g_e	=	*Electric conductance*
g_h	=	*Hydraulic conductance*
I	=	*Current flow rate across the network*
k	=	*Permeability*
L	=	*Network length*
l_c	=	*lattice constant*
l_e	=	*Equivalent length*
m	=	*Markov chain length*
N	=	*Model size (voxels) in x, y and z directions*
n	=	*No. of correlation functions*
n_f	=	*Levels of fractal decoration*
p_a	=	*Acceptance probability*
p_a^o	=	*Initial acceptance probability*
P_c	=	*Capillary pressure*
ΔP	=	*Pressure differential*
Q	=	*Volumetric flow rate across the model*
q_{ij}	=	*Flow rate between nodes i and j*
r	=	*Pore or throat radius*
R_H	=	*Hydraulic radius*
R_o	=	*Resistivity of core saturated with 100% brine*
R_p	=	*Pore radius*
R_t	=	*Throat radius*
$R_z(\vec{u})$	=	*Autocorrelation function at a lag vector* $\vec{u}$
s	=	*Specific surface area*
$S_2(u)$	=	*Two-point correlation function at lag u*
S_f	=	*Specific surface area from mercury porosimetry*
S_m	=	*Specific surface area of the model*
T	=	*Temperature*
T_o	=	*Starting temperature*
u_n^{max}	=	*Maximum lag*

V_f = *Volume of each pore after n_f levels of fractal decoration*
V_p = *Pore volume*
ΔV = *Voltage differential*
$Z(\vec{r})$ = *Binary phase function at a point vector* $\vec{r}$

Greek
θ = *Contact angle*
$\bar{\lambda}$ = *Correlation length*
μ = *Fluid viscosity*
σ = *Interfacial tension*
ξ = *Aspect ratio*
λ = *Temperature reduction factor*
λ_{max} = *Maximum allowable reduction factor*
λ_{min} = *Minimum allowable reduction factor*
φ = *Porosity*

Acronym
GRF = *Gaussian random fields*
SA = *Simulated annealing*
MIP = *Mercury intrusion porosimetry*

References

Adler, P.M., Jacquin, C.G. and Quiblier, J.A., 1990. Flow in simulated porous media. Int. J. of Multiphase Flow, 16 (4): 691-712.

Bakke, S. and Øren, P.E., 1997. 3D Pore-scale modeling of sandstones and flow simulations in the pore networks. SPEJ, 2: 136-149.

Bekri, S., Xu, K., Yousefian, F., Adler, P.M., Thovert, J.-F., Muller, J., Iden, K., Psyllos, A., Stubos, A.K., and Ioannidis, M.A., 2000. Pore geometry and transport properties in North Sea chalk. J. Petrol. Sci. Eng., 25: 107.

Coles, M.E., Spanne, P., Muegge, E.L., and Jones, K.W., 1994. Computed microtomography of reservoir core samples. Proc. 1994 Int. Symp. of the Society of Core Analyst, Stavanger, Norway.

Coles, M.E., Hazlett, R.D., Muegge, E.L., Jones, K.W., Andrews, B., Dowd, B., Siddons, P., Peskin, A., Spanne, P. and Soll, W.E., 1996. Developments in synchrotron X-ray microtomography with applications to flow in porous media. SPE 36531, 1996 Ann. Tech. Conf. , Denver, Colorado, USA, 6-9 October.

Deusch, C.V. and Journel, A.G., 1992. GSLIB: Geostatistical Software Library user guide. *Oxford Univ. Press*, New York.

Dullien, F.A.L., 1992. Porous media-fluid transport and pore structure. Second edition, *Academic Press Inc.*, San Diego, California.

Farmer, C.L., 1992. Numerical rocks. *In* The Mathematical Generation of Reservoir Geology, *Clerendon Press*, ed. P.R. King.

Fredrich, J., Menendez, B., and Wong, T.-F., 1995. Imaging the pore structure of geomaterials. Science, 268: 276-279.

Journel, A.G. and Huijbregts, C.J., 1978. Mining Geostatistics. *Academic Press*, New York.

Hazlett, R.D., 1995. Simulation of capillary-dominated displacements in microtomographic images of reservoir rocks. Transport in Porous Media, 20: 21-35.

Hazlett, R.D., 1997. Statistical characterization and stochastic modeling of pore networks in relation to fluid flow. Math. Geology, 29: 801-822.

Ioannidis, M.A. and Chatzis, I., 1993a. A mixed-percolation model of capillary hysteresis and entrapment in mercury porosimetry. J. of Colloid and Interface Science, 161: 278.

Ioannidis, M.A. and Chatzis, I., 1993b. Network modeling of pore structure and transport properties of porous media. Chem. Eng. Sci., 48: 951.

Ioannidis, M.A., Kwiecien, M.J., and Chatzis, I., 1997. Electrical conductivity and percolation aspects of statistically homogeneous porous media. Transport in Porous Media, 29: 61.

Ioannidis, M.A. and Chatzis, I., 2000. On the geometry and topology of 3D stochastic porous media. J. of Colloid and Interface Science, 229: 323.

Kainourgiakis, M.E., Kikkinides, E.S., Steriotis, Th.A., Stubos, A.K., Tzevelekos, K.P., and Kanellopoulos, N.K., 2000. Structural and transport properties of alumina porous membranes from process-based and statistical reconstruction techniques. J. Colloid Interface Science, 231: 158.

Knackstedt, M.A., Sheppard, A.P. and Pinczewski, W.V., 1998. Simulation of mercury porosimetry on correlated grids: Evidence for extended correlated heterogeneity at the pore scale in rocks, *Physical Review E* **58**, 6923-6926.

Levitz, P., 1998. Off-lattice reconstruction of porous media: critical evaluation, geometrical confinement and molecular transport. Advances in Colloid and Interface Science, 76/77: 71-106.

Liang, Z., Ioannidis, M.A., and Chatzis, I., 2000a. Permeability and electrical conductivity of porous media from 3D stochastic replicas of the microstructure. Chem. Eng. Sci., 55: 5247.

Liang, Z., Ioannidis, M.A. and Chatzis, I., 2000b. Reconstruction of 3D porous media using simulated annealing. Proc. of the XIII Int. Con. on Computational Methods in Water Resources, Alberta, Canada: 25-29.

Liang, Z., Ioannidis, M.A. and Chatzis, I., 2000c. Geometric and topological analysis of three-dimensional porous media: pore space partitioning based on morphological skeletonization. J. of Colloid and Interface Science, 221: 13-24.

Lowell, S. and Shields, J.E., 1991. *Powder surface area and porosity*. 3rd edition, Chapman & Hall.

Ma, C.M. and Sonka, M., 1996. A fully parallel 3D thinning algorithm and its applications. Comput. Vision Image Understanding, 64: 420.

Manwart, C., Torquato, S., and Hilfer, R., 2000. Stochastic reconstruction of sandstones. Phys. Rev. E, 62: 893.

Metropolis, N., Rosenbluth, A., Rosenbluth, M., Teller, A. and Teller, E., 1953. Equation of state calculations by fast computing machines. J. Chem. Phys., 21: 1087-1092.

Ouenes, A., Bhagavan, S., Bunge, P.H. and Travis, B.J., 1994. Application of simulated annealing and other global optimization methods to reservoir description: myths and realities. SPE 28415, 69th Ann. Tech. Conf., New Orleans, LA, USA, 25-26 September.

Quiblier, J.A., 1984. A new three-dimensional modeling technique for studying porous media. J. of Colloid and Interface Science, 98: 84-102.

Spanne, P., Thovert, J., Jacquin, C., Lindquist, W., Jones, K. and Adler, P., 1994. Synchrotron computed microtomography of porous media: topology and transports. Phys. Rev. Lett., 73: 2001-2004.

Talukdar, M.S., Torsaeter, O. and Ioannidis, M.A., 2001a. Stochastic reconstruction of particulate media from 2D images. J. of Colloid and Interface Science, In press.

Talukdar, M.S., Torsaeter, O., Ioannidis, M.A. and Howard, J.J., 2001b. Stochastic reconstruction of chalk from 2D images. Transport in Porous Media, In press.

Yeong, C.L.Y., and Torquato, S., 1998a. Reconstructing random media. Physical Review E, 57: 495-506.

Yeong, C.L.Y. and Torquato, S., 1998b. Reconstructing random media. II. Three-dimensional media from two-dimensional cuts. Physical Review E, 58: 224-233.

Paper IV

Stochastic Reconstruction of Particulate Media from 2D Images

M.S. Talukdar and O. Torsaeter
Department of Petroleum Engineering and Applied Geophysics,
Norwegian University of Science and Technology, Norway

M.A. Ioannidis[1]
Porous Media Research Institute, Department of Chemical Engineering,
University of Waterloo, Canada

Journal of Colloid and Interface Science, vol. 246 (2002)

Abstract

In this contribution we address the problem of reconstructing particulate media from limited morphological information that may be readily extracted from 2D images of their microstructure. Sixty-five backscatter SEM images of the microstructure of a lightly consolidated pack of glass spheres are analyzed to determine morphological descriptors, such as the pore-pore autocorrelation function and pore and solid phase chord distributions. This information is then used to constrain the stochastic reconstruction of the glass sphere packing in 2D using a simulated annealing method. The results obtained demonstrate that the *solid phase chord distribution* contains additional information that is critical for the reconstruction of the morphology of particulate media exhibiting short-range order. We further confirm this finding by successfully reconstructing the microstructure of a pack of irregular silica particles.

Keywords: stochastic reconstruction, porous media, correlation function, chord distribution, simulated annealing.

1. Introduction

Reconstructing the microstructure of disordered porous materials from limited microstructural information is a challenging problem of great practical significance. The significance of this problem stems from the fact that the effective (macroscopic) properties of porous materials cannot be predicted from knowledge of the volume fraction of the constituent phases alone. Instead, details of the geometry and topology of the convoluted 3D boundary surface separating the solid and void phases must be considered (1,2). Sufficiently high-resolution 3D images of the microstructure of real porous materials are generally very difficult to obtain by microtomographic methods

[1] Corresponding author. E-mail: mario@opa.uwaterloo.ca

(*e.g.*, 3-5). For this reason, detailed studies of the effects of geometric confinement on flow and transport are usually based on 3D digitized models of the microstructure obtained by a variety of stochastic reconstruction techniques on the basis of 2D information (*e.g.*, 6-13). For these models to have predictive power, it is necessary that they accurately reflect the morphology of the microstructure under study. Given that only 2D micrographs of the pore space are usually available, the challenge is then to identify 2D morphological descriptors that are essential for reproducing the microstructure of different classes of porous materials.

Insofar as particulate media are concerned, stochastic reconstruction from limited morphological information has been largely unsuccessful. Levitz (9) attempted off-lattice 2D reconstruction of a section through a pack of clay-coated silica particles using a method based on conditioning and truncation of Gaussian random fields. This is a mathematically elegant reconstruction approach, which unfortunately can be constrained only by the void fraction (porosity) and pore-pore autocorrelation function of the reference (real) medium. Levitz (9) observed that these constraints are insufficient to reproduce the granular appearance of the real medium. He further showed that although the reconstructed image matched the pore-pore autocorrelation function and pore chord distribution, it did not match the solid phase chord distribution of the reference microstructure. In a recent study, Manwart *et al*. (12) used a simulated annealing method to reconstruct the 3D microstructure of a Fontainebleau sandstone sample. In addition to imposing the pore-pore autocorrelation function, these authors also imposed the lineal path function of the void phase (a surrogate of the pore chord distribution function) as an additional reconstruction constraint. They also found that the reconstructed images failed to reproduce the granular appearance of the solid matrix. Recently, Kainourgiakis *et al*. (13) used an on-lattice stochastic reconstruction technique, originally proposed by Quiblier (6) and Adler *et al*. (7), in an attempt to reconstruct the microstructure of a random pack of spherical particles generated by a sequential deposition algorithm. These authors also noted large differences in the chord distribution function of the solid phase for the reconstructed and reference microstructures, despite the fact that the pore-pore autocorrelation function and pore chord distributions were matched with reasonable accuracy. The appearance of the solid matrix in the reconstructed random pack was amorphous and showed none of the distinct morphology of the solid-void interfaces that characterize sphere aggregates. Importantly, Kainourgiakis *et al*. (13) noted large differences in the Knudsen diffusivity of the reference and reconstructed media - an observation attesting to the fact that transport through disordered porous media is rather sensitive to the morphology of the boundary surface between the solid and void phases.

To this date, realistic models of the internal structure of particulate media have only been obtained by explicit simulation of the processes of grain deposition, compaction and (possibly) consolidation (14-16 and references therein). While such models have provided valuable insight into the

dependence of effective flow and transport properties on microstructure, they cannot be readily tailored to specific media using experimentally available information. Furthermore, they are limited to simulating the packing of regularly shaped particles (*e.g.*, spheres, ellipsoids) and their success hinges on adequate understanding of the physicochemical processes responsible for the formation of the porous microstructure, something that is attainable only in the simplest of cases. This is not so with stochastic reconstruction, which is solely based on the requirement that a 3D model microstructure matches a number of reference functions determined from 2D images of the real pore space. Of course, the challenge here is to establish reference functions suitable for the reconstruction of particulate media.

This work is motivated by recent observations (9,13) and its purpose is to examine the hypothesis that the solid phase chord distribution function contains sufficient additional information to reconstruct the microstructure of particulate porous media by stochastic optimization methods. The paper is organized as follows. In Section 2 we briefly review the definitions of statistical functions used to describe the morphology of a microstructure and describe the simulated annealing algorithm used to reconstruct the porous microstructure from limited morphological information. In Section 3 we describe results confirming that the solid phase chord distribution contains information essential in reproducing the morphology of microstructures exhibiting short-range order. These results concern the reconstruction of 2D sections through (i) a lightly consolidated aggregate of glass spheres for which an extensive set of backscatter SEM image data is available and (ii) a 2D section through a packing of irregularly shaped, clay-coated silica grains, previously studied by Levitz (9). We summarize in Section 4 with concluding remarks on the significance of our findings.

2. Stochastic reconstruction from limited morphological information

2.1. Morphological descriptors of the porous microstructure

The structure of a porous material is completely defined in terms of the binary phase function $Z(\vec{r})$, which takes the value of unity if a point $\vec{r}$ in space belongs to the void phase and the value of zero otherwise. For a statistically homogeneous medium, the void fraction (porosity), ϕ, and the autocorrelation function of the void phase, $R_z(\vec{u})$, are formally defined as the first two statistical moments of the function $Z(\vec{r})$,

$$\phi = \langle Z(\vec{r}) \rangle , \qquad [1]$$

$$R_z(\vec{u}) = \frac{\langle [Z(\vec{r}) - \phi] \cdot [Z(\vec{r} + \vec{u}) - \phi] \rangle}{\phi - \phi^2}, \quad [2]$$

where, angular brackets denote statistical averages and $\vec{u}$ is a lag vector. For an isotropic porous medium, ϕ is a constant and $R_z(\vec{u})$ is only a function of the modulus of the lag vector, *i.e.*, $R_z(\vec{u}) = R_z(u)$. The function $R_z(u)$ may be determined from cross-sectional images of the pore space or from small-angle scattering experiments. Its slope at the origin is related to the specific surface area (the interfacial area per unit volume) *s*, which for digitized media is given by (17):

$$s = -6(\phi - \phi^2)\left.\frac{dR_z}{du}\right|_{u=0} \quad [3]$$

Higher-order moments of the phase function may also be defined (2). Their determination is, however, rather complicated (18) and they are seldom computed (19). Another useful characteristic of microstructure is the chord distribution function, $P_i(u)$, where the subscript *i* refers to either void or solid) (20). A chord is the length *u* between intersections of a line with the two-phase interface. Closely related is the so-called lineal path function $L_i(u)$ (21). The latter quantity measures the probability that a line segment of length *u* lies entirely within phase *i*. The chord distribution function can be directly interpreted in terms of microstructural features, as it contains phase connectedness and correlation information along a lineal path (20). That is, if $P_i(u) \neq 0$ for large values of *u*, there exist connected regions of phase *i* at scale *u*. Importantly, the value of *u* at which $P_i(u)$ is maximum provides an estimate of the length scale associated with phase *i*. It is therefore expected that the solid phase chord distribution of particulate media should exhibit a peak at a value of *u* characteristic of the particle size. This is not the case for the pore chord distribution function, even in the extreme case of a random pack of uniform spheres (13). Failure of its surrogate void phase lineal path function to improve the reconstruction of a visibly granular sandstone sample (12) may be attributed to this fact.

2.2. Reconstruction of Porous Media by Simulated Annealing

The reconstruction of porous media by simulated annealing was first investigated by Hazlett (22) and further advanced by Yeong and Torquato (17, 23). The main idea behind this simple but powerful technique is to gradually transform an unstructured ("high-energy") configuration of solid and void pixels into a "minimum-energy" configuration, where "energy" is measured in terms of deviations from a set of target, experimentally determined, functions

conveying morphological information, *e.g.*, $R_z(u)$ and/or $P_i(u)$. This is a stochastic optimization problem with an objective function generally defined in terms of *n* reference functions as:

$$E = \sum_n \sum_{u=0}^{u_n^{\max}} \left[f_n(u) - \widetilde{f}_n(u) \right]^2, \qquad [4]$$

where, f_n and $\widetilde{f}_n$ are the simulated and reference functions, respectively. For the purposes of this work, the reference functions imposed are the pore-pore autocorrelation functions along the two orthogonal directions, $R_{z_x}(u)$ and $R_{z_y}(u)$, and the solid-phase chord distribution functions along the two orthogonal directions, $P_{s_x}(u)$ and $P_{s_y}(u)$. Each reference function $\widetilde{f}_n$ is matched to a maximum lag $u_n^{\max}$.

The simulation begins by randomly designating fractions ϕ and $(1-\phi)$ of void and solid phase pixels, respectively, on a grid of size $M \times N$. At each iteration step *k*, a void and a solid pixel are chosen at random and their phase function values are interchanged. This interchange slightly modifies the functions f_n and therefore changes the energy of the system while preserving the porosity. A pixel interchange is accepted with a probability p_a given by the Metropolis rule (24),

$$p_a^{(k)} = \begin{cases} 1 & if\ \Delta E^{(k)} \le 0 \\ e^{-\Delta E^{(k)} / T^{(k)}} & if\ \Delta E^{(k)} > 0 \end{cases} \qquad [5]$$

where, $\Delta E^{(k)} = E^{(k+1)} - E^{(k)}$ and $T^{(k)}$ is a control parameter representing the "temperature" of the system. The starting value and the rate of reduction of *T* are governed by an annealing schedule. This schedule should be such that a global optimum is achieved as quickly as possible. In practice, *T* is reduced by a factor λ after a predefined number of interchanges, referred to as a *Markov* chain. If rapid convergence is expected, a dynamic schedule, which takes into account the rapid fluctuations in the evolving energy in updating the system temperature *T* should be preferred over a static one where *T* decreases monotonically. Otherwise, there is a real possibility that the system will be trapped at a local energy minimum, unless *T* is decreased very slowly. The following formula for updating *T* was adopted in this work (25):

$$\lambda = Max\left[\lambda_{\min}, Min\left(\lambda_{\max}, \frac{E_{\min}}{\overline{E}} \right) \right], \qquad [6]$$

where, λ_{min} and λ_{max} are the minimum and maximum allowable reduction factors, respectively, and are specified by the user. In this approach, for each Markov chain, the lowest and average energy values reached, $E_{\min}$ and $\overline{E}$, are used to compute the reduction factor λ. The system temperature is then updated as,

$$T = T_o e^{(\lambda-1)(m+1)} \quad [7]$$

where, T_o is the starting temperature and m is the number of Markov chains after a total of k interchanges. This approach permits estimation of the starting temperature from the initial behavior of the energy function. Accordingly, the mean change in the energy function for k_o initial iterations is first evaluated:

$$\overline{\Delta E} = \frac{1}{k_o}\sum_{k=1}^{k_o}\Delta E^{(k)} \quad [8]$$

The starting temperature T_o is then estimated from the following expression for a given initial acceptance probability p_a^o,

$$p_a^o = e^{-\overline{\Delta E}/T_o} \quad [9]$$

All results obtained in this work were obtained with k_o = 100, p_a^o = 0.5 and m = 11500. It should be kept in mind that the choice of these parameters is highly system-specific (25).

3. Results and discussion

3.1. Reconstruction of an aggregate of glass spheres

A thin section through a pack of lightly fused glass spheres of average radius $R \cong 90\ \mu m$ was examined by backscatter SEM. A total of 65 high-contrast gray scale images of size 768x576 pixels were obtained at a resolution of 2.1 μm per pixel. These images were readily segmented and average properties of the phase function were determined. A representative image is shown in Fig. 1. The average porosity of the pack was found to be 0.335. The average pore-pore autocorrelation functions along each of the two principal directions are plotted in Fig. 2. These functions display the characteristic features of a model of non-overlapping spheres (26). That is, a first zero crossing is observed around r/R = 1, followed by negative correlation up to r/R =2 and essentially complete decay of correlations for r/R > 3.

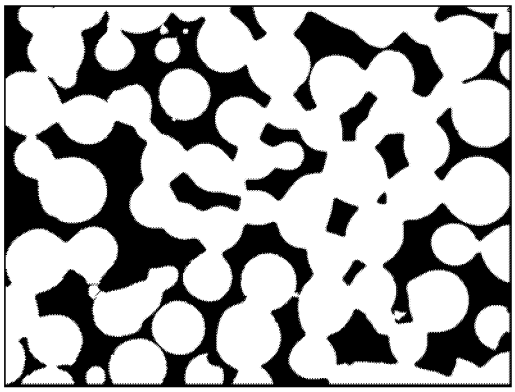

Fig. 1. A representative image of real aggregate of glass spheres. Image size is 768x576 pixels. Pixel size is 2.1x2.1 μm^2. Pore space is shown in black.

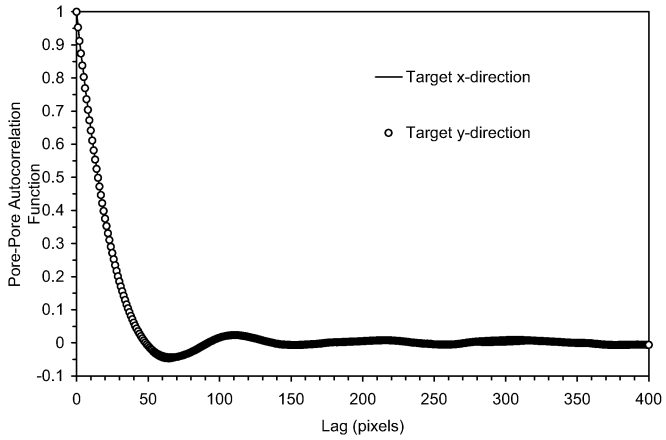

Fig. 2. Average pore-pore autocorrelation functions along each of the two principal directions. These functions display the characteristic features of a model of non-overlapping spheres.

Three reconstruction cases were examined. Case 1 concerns reconstruction from the pore-pore autocorrelation function and the chord length distribution function of the solid phase. In Case 2 only the chord length distribution function of the solid phase was used, whereas in Case 3 reconstruction was attempted using only the pore-pore autocorrelation function. In all cases, optimization was carried out using reference functions measured along the two orthogonal directions and was terminated as soon as the energy of the system became less than 10^{-4}. Approximate CPU times for reconstructions of size 384 x 288 pixels (4.2 μm /pixel) were 30 h (Case 1), 5 h (Case 2) and 22 h (Case 3) on a lightly loaded IBM RS/6000 workstation.

For Case 1 the initial energy of the system was 36.31. Its evolution with temperature T is shown in Fig. 3. The evolution of the system structure at

selected energy levels (see Fig. 3) is shown in Fig. 4. As shown in Fig. 5(a), the pore-pore autocorrelation functions of the reconstructed medium along each of the principal directions match the respective reference functions remarkably well. This is also the case for the chord length distribution functions of the solid phase, as shown in Fig. 5(b). Most importantly, the reconstruction essentially reproduces the distinct appearance of a sphere pack. The roundness of the solid-void interface is clearly visible, as are the shapes of pore space features seen in the real medium. It is noted that the extreme regularity of the solid-void interface in the real aggregate of spheres is not perfectly reproduced in the reconstruction. This is in part due to the fact that the reference functions were optimized only along the two orthogonal directions. While this is a standard approach aimed at reducing computational costs, some artificial anisotropy along the non-optimized directions is introduced for the case of media exhibiting short-range order. This anisotropy can be removed by optimizing in more directions (27).

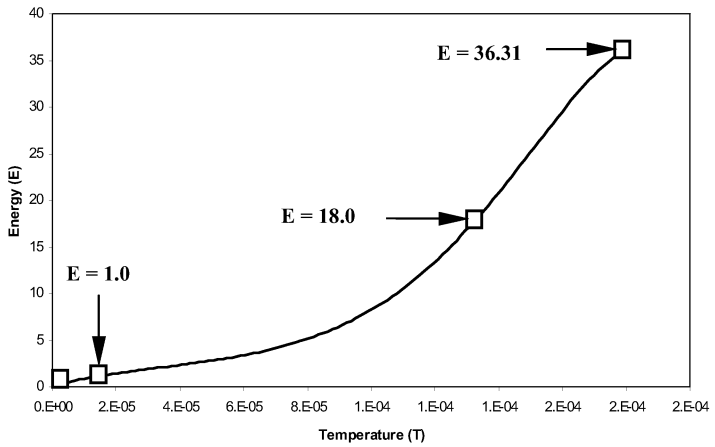

Fig. 3. Evolution of the system "energy" with temperature *T* for Case 1 (reconstruction of glass sphere aggregate from the pore-pore autocorrelation function and the solid-phase chord distribution function). Squares mark the energy of the configurations shown in Figs. 4(a) through 4(d).

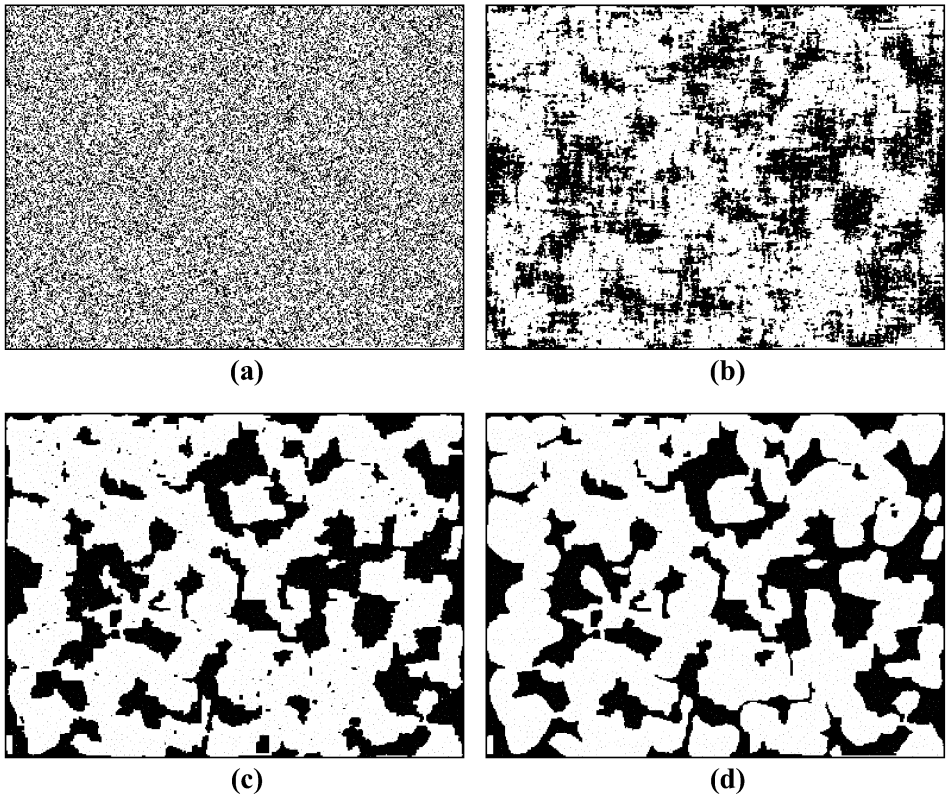

Fig. 4. Case 1: Reconstruction of glass sphere aggregate from the pore-pore autocorrelation function and the solid-phase chord distribution function. Pore space is shown in black. (a) Initial random structure (E = 36.31), (b) intermediate structure (E = 18.0), (c) intermediate structure (E = 1.0), and (d) final structure ($E = 10^{-4}$).

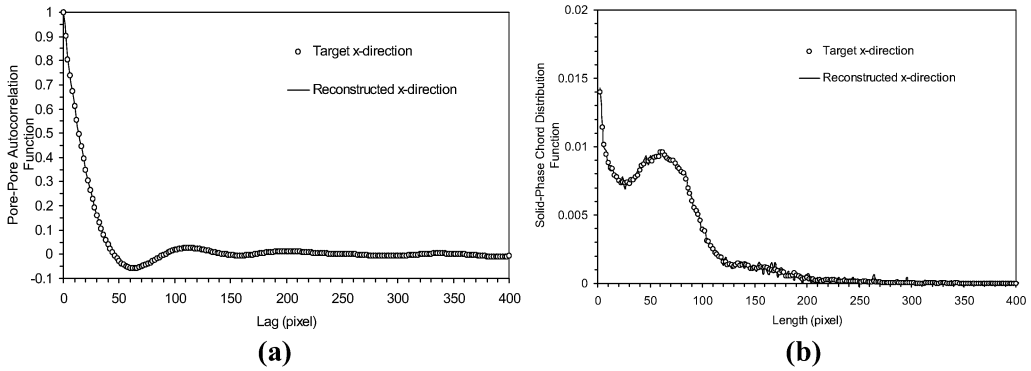

Fig. 5. Morphological properties of reference (target) and reconstructed glass sphere aggregate (Case 1). (a) Pore-pore autocorrelation function and (b) solid-phase chord distribution function. Agreement along the y-direction is similar and is not shown.

For Case 2 the initial energy of the system was 27.9. Excellent agreement of the solid phase chord length distribution functions is observed in Fig. 6(a), but deviations from the reference pore-pore autocorrelation functions are also evident, mainly at large lag distances (see Fig. 6(b)). This can be understood by considering that significant correlation information is, in fact, contained in the chord length distribution function. This information is limited to *connected* regions along a lineal path. As can be seen in Fig. 6(b), the chord distribution function contains sufficient information to reproduce the pore-pore autocorrelation function for lags up to about one sphere diameter. The reconstructed image at an intermediate and the final stage is shown in Fig. 7(a) and 7(b), respectively. Interestingly, the general morphology of the sphere aggregate is evident in the reconstructed medium. However, a distinct difference can also be observed, namely the reconstructed medium appears to contain somewhat smaller particle features than the target microstructure (see Fig. 1). Because the chord length distribution function contains correlation information from connected regions along a lineal path, the simulated microstructure begins to form as a collection of smaller, but more numerous particle features (see Fig. 7(a)). Contrary to this, Case 1 reconstruction produces larger particle features during the initial stages of the annealing process (see Fig. 4(b)).

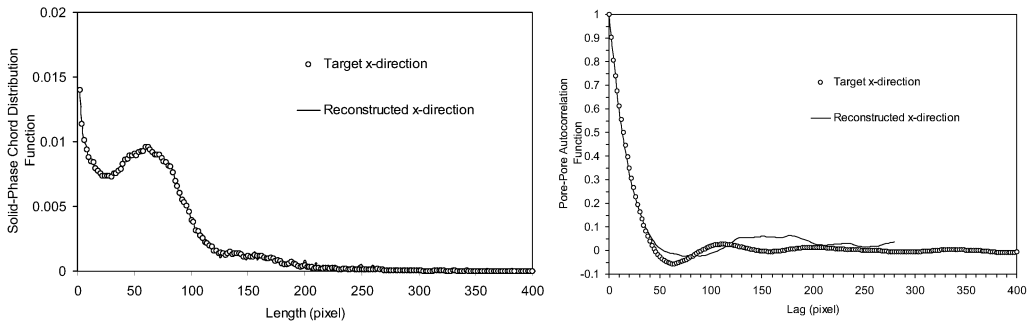

(a) **(b)**

Fig. 6. Morphological properties of reference (target) and reconstructed media (Case 2: reconstruction of glass sphere aggregate from the solid-phase chord distribution function only). (a) Solid-phase chord distribution function and (b) pore-pore autocorrelation function.

For Case 3 the initial energy of the system was 8.4. As shown in Fig. 8(a), the simulated autocorrelation functions along the two perpendicular directions match perfectly the reference functions, but considerable disagreement is observed between the simulated and reference chord length distribution for the solid phase (see Fig. 8(b)). The reconstructed medium is shown in Fig. 9. As also observed elsewhere (17), the pore-pore autocorrelation function is inadequate to reproduce the morphology of the sphere aggregate, since the solid phase in the reconstructed medium appears completely amorphous. In

addition, numerous small void-phase features appear in the reconstructed image. This has also been observed in the reconstruction of an interpenetrating ceramic-metal composite which displayed no short-range order (27) and points to a general limitation of the pore-pore autocorrelation function to capture fine details of the microstructure (see also (10)).

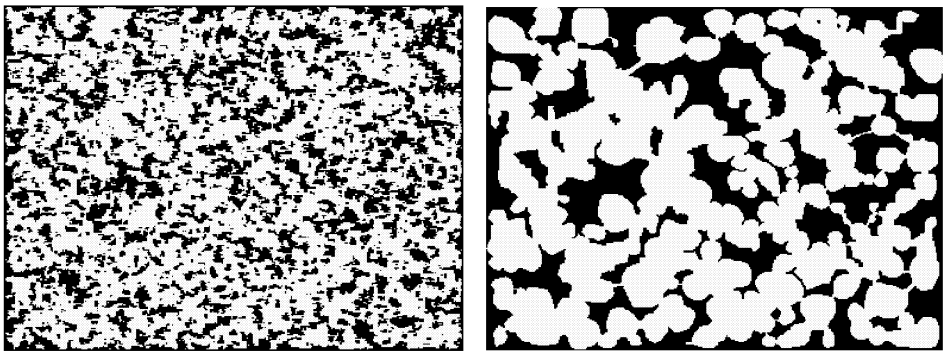

(a) (b)

Fig. 7. Case 2: reconstruction of glass sphere aggregate from the solid-phase chord distribution function only. Pore space is shown in black. (a) Intermediate structure at an energy equivalent to that of the configuration shown in Fig. 4(b), and (b) final structure ($E = 10^{-4}$).

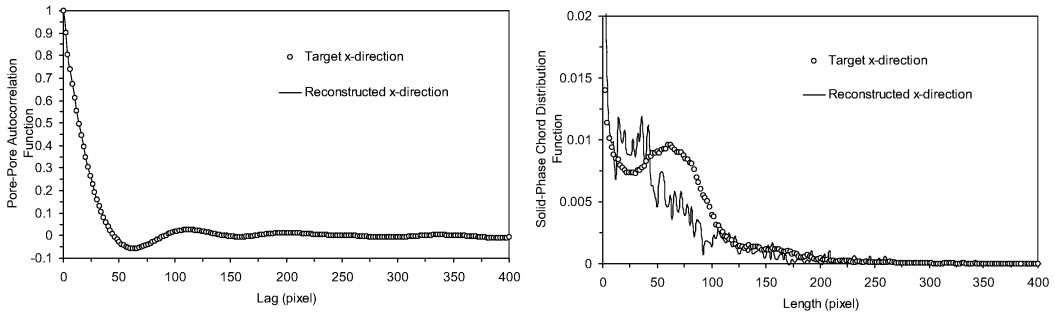

(a) (b)

Fig. 8. Case 3: reconstruction of glass sphere aggregate from the pore-pore autocorrelation function only. Reference (target) and reconstructed (a) pore-pore autocorrelation function and (b) solid-phase chord distribution function.

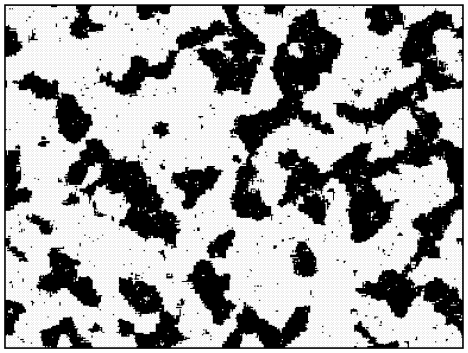

Fig. 9. Case 3: Reconstruction of glass sphere aggregate from the pore-pore autocorrelation function only. Final reconstructed structure ($E = 10^{-4}$). Pore space is shown in black.

3.2. Reconstruction of a packing of clay-coated irregular silica particles

The necessity of the solid-phase chord length distribution for the stochastic reconstruction of particulate media was further verified by reconstructing the microstructure of a pack of irregular silica particles, peviously considered by Levitz (9). This microstructure would be extremely difficult, if not impossible, to simulate using any of the currently known particle deposition algorithms. Two cases were considered. In the first case (Case 4) the pore-pore autocorrelation function and the solid-phase chord distribution function were chosen as the reference functions. In the second case (Case 5), only the chord distribution functions of the solid and void phases were used. As before, optimization was carried out only along the two orthogonal directions. In both cases, the reconstruction was terminated as soon as the energy became less than 10^{-2}. Approximate CPU times for reconstructions of size 500 x 500 pixels were 220 h (Case 4) and 55 h (Case 5) on a lightly loaded IBM RS/6000 workstation.

The initial energy of the system for Case 4 was 44.89. As shown in Fig. 10(a), the pore-pore autocorrelation functions of the reconstructed medium along each of the principal directions match the respective reference functions remarkably well. The chord length distribution functions of the solid phase also agree quite well (see Fig. 10(b)). The original and reconstructed images are compared in Fig. 11. A significant improvement in the visual appearance of the reconstructed microstructure is easily recognizable. The reconstruction might be further improved if the chord length distribution were optimized along more than the two orthogonal directions.

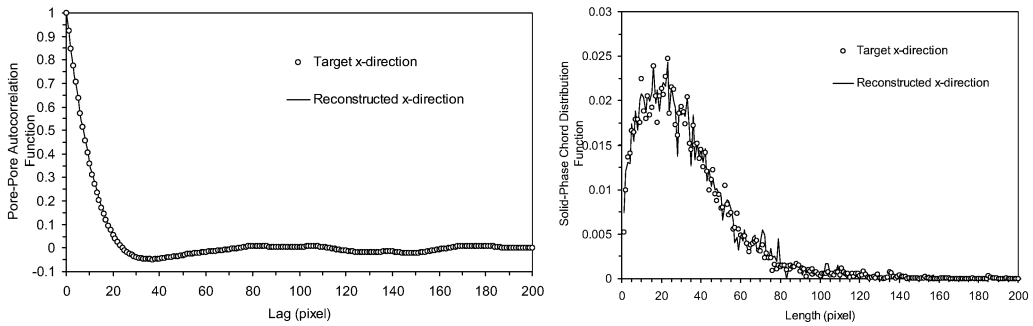

(a) **(b)**

Fig. 10. Case 4: Reconstruction of clay-coated silica particle aggregate from the pore-pore autocorrelation function and solid-phase chord distribution function. Morphological properties of the reference (target) and reconstructed media. (a) Pore-pore autocorrelation function and (b) solid-phase chord distribution function. Agreement along the *y*-direction is similar and is not shown.

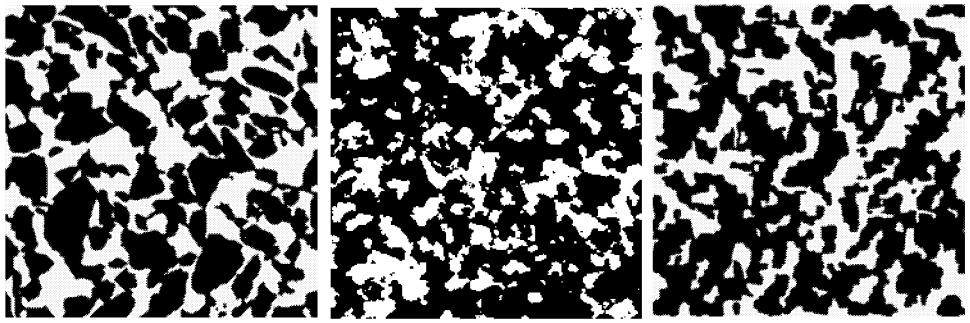

(a) **(b)** **(c)**

Fig. 11. (a) Microstructure of an aggregate of clay-coated irregular silica particles (after Levitz (9)). (b) Off-lattice reconstruction of the image in (a) (after Levitz (9)). (c) Reconstruction by simulated annealing (this work) from the pore-pore autocorrelation function and solid-phase chord distribution function (Case 4). Solid grains are shown in black.

The initial energy of the system for Case 5 was 55.96. As shown in Fig. 12(a) and Fig. 12(b), the solid- and void-phase chord distribution functions of the reconstructed medium along each of the principal directions match the respective reference functions quite well. Reconstruction using exclusively chord length information produces a microstructure remarkably similar to the one in Case 4 (compare Fig. 13 and Fig. 11(c)). This finding supports the conclusion that imposing the pore-phase chord distribution function (or its surrogate lineal path function) as an additional constraint is largely redundant if the pore-pore autocorrelation function is also imposed as a constraint. To further illustrate this point, the non-optimized functions (void-phase chord

distribution function in Case 4 and pore-pore autocorrelation function in Case 5) are compared to the reference functions in Fig. 14(a) and Fig. 14(b), respectively. Reasonably close agreement is observed.

The significance of obtaining accurate descriptions of the morphology of real porous media by stochastic reconstruction cannot be overemphasized. As recently demonstrated (28), the size distribution and connectivity of pore space channels is very sensitive to the morphology of the solid-void interface. This should be kept in mind when the success or failure of stochastic reconstruction is judged on the basis of agreement between measured and predicted transport properties (*e.g.*, 10-13). Finally, further development of the simulated annealing method, aimed at accelerating its convergence in the presence of multiple constraints, is highly desirable.

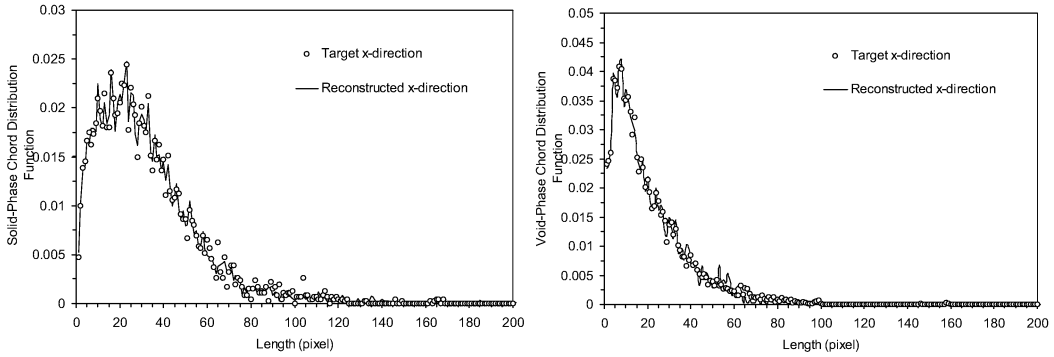

(a) **(b)**

Fig. 12. Case 5: Reconstruction of an aggregate of clay-coated silica particles from the solid- and void-phase chord distribution functions. Comparison of the reference (target) and reconstructed functions: (a) solid-phase chord distribution function and (b) void-phase chord distribution function.

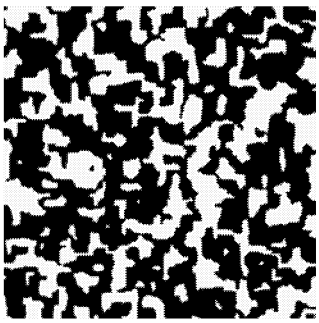

Fig. 13. Case 5: Reconstruction of an aggregate of clay-coated silica particles from the solid- and void-phase chord distribution functions. Final microstructure ($E = 10^{-2}$). Solid grains are shown in black.

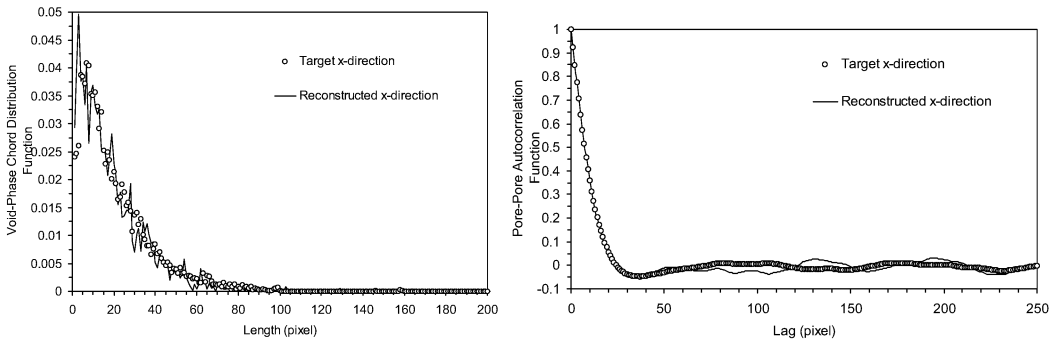

(a) **(b)**

Fig. 14. (a) Comparison of the non-optimized void-phase chord distribution function (Case 4 reconstruction) to the respective function of the reference medium. (b) Comparison of the non-optimized pore-pore autocorrelation function (Case 5 reconstruction) to the respective function of the reference medium.

4. Conclusions

Morphological analysis and reconstruction of the microstructure of packs of lightly fused glass spheres and clay-coated irregular silica particles were used to demonstrate that realistic stochastic models of these media could be generated from knowledge of the pore-pore autocorrelation function (or pore chord distribution function) *and* the chord length distribution function of the solid phase. These results indicate that the chord distribution function of the solid phase is a necessary morphological constraint in the reconstruction of particulate media by stochastic methods. Imposing this additional constraint cannot be achieved using reconstruction methods based on conditioning and truncation of Gaussian random fields, but is possible using simulated annealing methods. The findings of this work have important implications for the study of particulate media whose morphology may not be realistically simulated using particle deposition models, but may be easily quantified through analysis of 2D images.

Acknowledgments

Financial support for this work from the Natural Sciences and Engineering Research Council of Canada (NSERC) is gratefully acknowledged. One of the authors (S. Talukdar) also acknowledges financial support from the Phillips Petroleum Company Norway for his Ph.D. studies. He also acknowledges the warm reception he received at the Porous Media Laboratory, Department of Chemical Engineering, University of Waterloo, Canada, during his three-month research stay in 2001.

References

1. Dullien, F.A.L., "Porous Media: Fluid Transport and Pore Structure," 2nd ed., Academic Press, San Diego, 1992.
2. Torquato, S., *Appl. Mech. Rev.* **44**, 37 (1991).
3. Lymberopoulos, D.P. and Payatakes, A.C., *J. Colloid Interface Sci.* **150**, 61 (1992).
4. Spanne, P., Thovert, J.F., Jacquin, J.C., Lindquist, W.B., Jones, K.W., and Adler, P.M., *Phys. Rev. Lett.* **73**, 2001 (1994).
5. Baldwin, C.A., Sederman, A.J., Mantle, M.D., Alexander, P., and Gladden, L.F., *J. Colloid Interface Sci.* **181**, 79 (1996)
6. Quiblier, J.A., *J. Colloid Interface Sci.*, **98**, 84 (1984).
7. Adler, P.M., Jacquin, C.G., and Quiblier, J.A., *Int. J. Multiphase Flow* **16**, 691 (1990).
8. Ioannidis, M.A., Kwiecien, M.J., and Chatzis, I., *Transp. Porous Media* **29**, 61 (1997).
9. Levitz, P., *Adv. Colloid Interface Sci.*, **76/77**, 71 (1998).
10. Liang, Z., Ioannidis, M.A., and Chatzis, I., *Chem. Eng. Sci.* **55**, 5247 (2000)
11. Bekri, S., Xu, K., Yousefian, F., Adler, P.M., Thovert, J.-F., Muller, J., Iden, K., Psyllos, A., Stubos, A.K., and Ioannidis, M.A., *J. Petrol. Sci. Eng.* **25**, 107 (2000).
12. Manwart, C., Torquato, S., and Hilfer, R., *Phys. Rev. E* **62**, 893 (2000).
13. Kainourgiakis, M.E., Kikkinides, E.S., Steriotis, Th.A., Stubos, A.K., Tzevelekos, K.P., and Kanellopoulos, N.K., *J. Colloid Interface Sci.* **231**, 158 (2000).
14. Yang, A., Miller, C.T., and Turcoliver, L.D., *Phys. Rev. E.* **53**, 1516 (1996).
15. Bakke, S., and Oren, P.-E., *SPE J.* **2**, 136 (1997).
16. Coelho, D., Thovert, J.-F. and Adler, P.M., *Phys. Rev. E* **55**, 1959 (1997).
17. Yeong, C.L.Y., and Torquato, S., *Phys. Rev. E.* **57**, 495 (1998).
18. Berryman, J.G., *J. Appl. Phys.* **57**, 2374 (1985).
19. Yao, J., Frykman, P., Kalaydjian, F., Thovert, J.-F., and Adler, P.M., *J. Colloid Interface Sci.* **156**, 478 (1993).
20. Roberts, A.P., and Torquato, S., *Phys. Rev. E* **59**, 4953 (1999).
21. Coker, D.A., and Torquato, S., *J. Appl. Phys.* **77**, 6087 (1995).
22. Hazlett, R.D., *Math. Geol.* **29**, 801 (1997).
23. Yeong, C.L.Y., and Torquato, S., *Phys. Rev. E* **58**, 224 (1998).
24. Metropolis, N., Rosenbluth, A., Rosenbluth, M., Teller, A. and Teller, E., *J. Chem. Phys.* **21**, 1087 (1953).
25. Ouenes, A., Bhagavan, S., Bunge, P.H., and Travis, B.J., SPE Paper 28415, Proceedings of the 69th SPE Annual Technical Conference and Exhibition, New Orleans, LA, Sept. 25-26, 1994.
26. Torquato, S., and Stell, G., *J. Chem. Phys.* **82**, 980 (1985).
27. Sheehan, N., and Torquato, S., *J. Appl. Phys.* **89**, 53 (2001).

28. Liang, Z., Ioannidis, M.A., and Chatzis, I., *J. Colloid Interface Sci.* **221**, 13 (2000).

Paper V:

Talukdar, M.S., Torsæter, O., Ioannidis, M.A. and Howard, J.J.:

"Stochastic Reconstruction of Chalk from Two-Dimensional Images," *Transport in Porous Media*, 48, 101-123 (2002).

Paper VI

Reconstruction of Chalk Pore Networks from 2D Backscatter Electron Micrographs Using A Simulated Annealing Technique

M.S. Talukdar[1] and O. Torsaeter
Department of Petroleum Engineering and Applied Geophysics,
Norwegian University of Science and Technology, Norway

Journal of Petroleum Science and Engineering, in press

Abstract

We report the stochastic reconstruction of chalk pore networks from limited morphological information that may be readily extracted from 2D backscatter electron (BSE) images of the pore space. The reconstruction technique employs a simulated annealing algorithm, which can be constrained by an arbitrary number of morphological descriptors. Backscatter electron images of a high porosity North Sea chalk sample are analyzed and the morphological descriptors of the pore space are determined. The morphological descriptors considered are the void-phase two-point probability function and lineal path function computed with or without the application of periodic boundary conditions. 2D and 3D samples have been reconstructed with different combinations of the descriptors and the reconstructed pore networks have been analyzed quantitatively to evaluate the quality of reconstructions. The results demonstrate that simulated annealing technique may be used to reconstruct chalk pore networks with reasonable accuracy using the void-phase two-point probability function and/or void-phase lineal path function. Void-phase two-point probability function produces slightly better reconstruction than the void-phase lineal path function. Imposing void-phase lineal path function results in slight improvement over what is achieved by using the void-phase two-point probability function as the only constraint. Application of periodic boundary conditions appears to be not critically important when reasonably large samples are reconstructed.

Keywords: chalk reconstruction, simulated annealing, two-point probability function, lineal path function, backscatter electron micrograph.

1. Introduction

Network modeling techniques have been used in the recent years as an alternate tool to predict a variety of petrophysical properties (e.g., fluid permeability, electrical conductivity, capillary pressure, etc.) from pore structure information. The model to be predictive, the pore network model

[1] Corresponding author. E-mail: talukdar@ipt.ntnu.no

must represent the pore space geometry and topology of the real medium as closely as possible. The requisite information for building an equivalent pore network model (e.g., pore and throat shape and size distributions, pore-to-pore connectivity, spatial correlation, etc.) is quite difficult to determine. Statistical information about pore and throat size distributions is often obtained from: (1) mercury injection data (Dullien, 1991); (2) a combination of thin sections and capillary pressure data (Davies and Vessell, 1996); and (3) pore casts (Wardlaw, 1976). These techniques do not provide all requisite information to develop 3D network replica of the porous media, which is essential for detailed studies of the effects of geometric confinement on flow and transport. Advanced techniques, such as, (1) X-ray computed microtomography (e.g., Spanne et al., 1994; Coles et al., 1994; Hazlett, 1995; Coles et al., 1996); (2) scanning laser confocal microscopy (Fredrich et al., 1995); and (3) serial sectioning (Kwiecien et al., 1990; Lymberopoulos and Payatakes, 1992) can provide good quality volume images of the pore space. Unfortunately, these techniques are not suited for routine application. Most importantly, its resolution is not sufficient to image the sub-micron size pores that are abundant in chalk. In the absence of experimental 3D volume data, 3D stochastic reconstruction from limited statistical information, accessible by analysis of 2D BSE images, is a viable alternative. For the case of chalk, whose microstructure is too complex to reproduce by explicit modeling of the grain depositional and diagenetic processes (e.g., Bryant et al., 1993; Bakke and Øren, 1997), stochastic reconstruction is the only alternative.

The most widely studied stochastic reconstruction technique is based on conditioning and truncation of Gaussian random fields (GRF) (Quiblier, 1984; Adler et al., 1990; Ioannidis et al., 1997). This technique is mathematically elegant and computationally efficient, but unfortunately can be constrained only by the porosity and two-point probability function of the reference (real) medium. These constraints have been found to be insufficient to reproduce the microstructure of particulate media, such as grain or sphere packs (Levitz, 1998; Kainourgiakis et al., 2000). Insofar as stochastic reconstruction of chalk is concerned, the only published study appears to be the work of Bekri et al. (2000). These authors also employed a GRF technique to reconstruct the pore networks of a suite on North Sea chalk samples. The technique was not successful in reconstructing chalk samples containing vuggy porosity in the form of hollow Foraminifer shells. Clearly, the stochastically reconstructed porous media to have predictive power, a more robust reconstruction technique is necessary. Much greater flexibility is offered by the simulated annealing (SA) method (Yeong and Torquato, 1998a; Yeong and Torquato, 1998b; Manwart et al., 2000; Liang et al., 2000, Talukdar et al., 2001a). Using this method, Yeong and Torquato (1998b) imposed the void-phase two-point probability and lineal path functions as constraints in the reconstruction of a Fontainebleau sandstone sample. Manwart et al. (2000) reconstructed Berea and Fontainebleau sandstone samples from information on the void-phase two-point probability and lineal path functions, and pore size distribution

function. Liang et al. (2000) imposed the neighborhood rank distribution together with two-point correlation function. Talukdar et al. (2001a) applied void-phase two-point correlation function and solid-phase chord distribution function to obtain reliable reconstruction of *particulate* media. It has been shown that materials (results did not include chalk) with practically identical porosity, two-point correlation functions and/or lineal path functions can have very different morphologies and transport properties (Roberts, 1997, Manwart et al., 2000). However, to the best of our knowledge, simulated annealing technique has not been applied previously for reconstruction of chalk samples. It is, therefore, interesting to see as to what extent chalk pore networks can be reproduced from these information. The use of periodic boundary conditions allows us to approximate a finite volume of the simulation model as an infinite volume of the periodic medium. The effect of periodic boundary condition in stochastic reconstruction of chalk has not been studied previously. The objectives of this work are: (1) to evaluate the effectiveness of two-point correlation function and lineal path function in reconstructing chalk pore networks; and (2) to assess the effect of periodic boundary conditions. These objectives will be achieved by reconstructing 2D and 3D samples with different combinations of the correlation functions and the quality of reconstructions will be evaluated in terms of several quantitative measures.

The paper is organized as follows: In Section 2 we review the definitions of various morphological descriptors used to reconstruct chalk pore networks. We also describe the simulated annealing algorithm and the quantitative measures applied to evaluate the quality of reconstructions. In Section 3 we briefly describe the acquisition and processing of 2D BSE images and the measurement of morphological descriptors for a high porosity North Sea chalk sample. The results from a series of 2D reconstructions using different combinations of constraints are presented and discussed in Section 4. In Section 5 we present and discuss the results of 3D reconstructions. We summarize in Section 6 with concluding remarks on the significance of our findings.

2. Review of theory

2.1. Morphological Descriptors

The structure of a porous medium is completely defined in terms of the binary phase function $Z(\vec{r})$ given below (Adler *et al.*, 1990),

$$Z(\vec{r}) = \begin{cases} 1, & \vec{r} \text{ points to pore space} \\ 0, & \text{otherwise} \end{cases}. \qquad [1]$$

The void fraction (porosity), φ, and the two-point probability function of the void phase, $S_2(\vec{u})$, are formally defined as the first two statistical moments of the function $Z(\vec{r})$,

$$\varphi = \langle Z(\vec{r}) \rangle, \quad [2]$$

$$S_2(\vec{u}) = \langle [Z(\vec{r})] \cdot [Z(\vec{r}+\vec{u})] \rangle, \quad [3]$$

where, angular brackets denote statistical averages and $\vec{u}$ is a lag vector. For statistically homogeneous and isotropic porous media, φ is a constant and $S_2(\vec{u})$ is only a function of the modulus of the lag vector, *i.e.*, $S_2(\vec{u}) = S_2(u)$. The quantity $S_2(\vec{u})$ can be interpreted as the probability of finding two points at positions $\vec{r}$ and $\vec{r}+\vec{u}$ both in void phase. For all isotropic media without long-range order, $S_2(u=0) = \varphi$ and $\lim_{u \to \infty} S_2(u) = \varphi^2$. The limitation of two-point probability function is that it cannot distinguish between void and solid phases since $S_2^p(u) - \varphi^2 = S_2^g(u) - (1-\varphi)^2$, where *p* and *g* represent void and solid, respectively. This function also does not reflect information about the connectedness of the phases (Yeong and Torquato, 1998a).

The void-phase lineal path function $L(\vec{u})$ is another useful characteristic of microstructure. This quantity measures the probability that a line segment spanning from $\vec{r}$ to $\vec{r}+\vec{u}$ lies entirely within void phase. Unlike the two-point probability function, a lineal path function can distinguish between different phases of a medium, in the sense that the lineal path function for a particular phase is not uniquely determined by simply knowing that of the complementary phase(s). Therefore, for efficient reconstructions using lineal path functions, it is important to identify which phase in the porous medium is the target phase to be reconstructed. Also unlike two-point probability function, this function contains some connectedness information, at least along a lineal path, and hence reflects certain long-range information about the system. For statistically isotropic media, the lineal-path function depends only on the distance *u* between the two end-points and can be expressed simply as $L(u)$. For a porous medium with porosity φ, $L(u)$ at $u=0$ is equal to φ (Yeong and Torquato, 1998a).

Following the procedure adopted by Yeong and Torquato (1998a), we calculated $S_2(u)$ and $L(u)$ by successively translating a sampling probe of *u* pixels in length (along a row of pixels) a distance of one pixel at a time, spanning the whole image, counting the number of occurrences that the two end-points of the probe fall in void spaces or the probe entirely fall in void spaces, respectively, and finally, dividing the number of occurrences by the total number of trials. This sampling procedure is more accurate and produces

smoother $S_2(u)$ and $L(u)$ profiles than that by random sampling (throwing random points into the system), because the former exhaustively incorporates information from every pixel in the entire system (Yeong and Torquato, 1998a). The sampling regions for the functions should be chosen to encompass the ranges before $S_2(u)$ gets its long-range value of φ^2 and $L(u)$ becomes negligibly small. The functions were calculated along the orthogonal directions with or without the application of periodic boundary conditions. Better results may be expected through sampling in more directions, but at an expense of high computational costs (Manwart and Hilfer, 1999). It might be the right point here to define a periodic medium and the periodic boundary conditions. A periodic medium is one which repeats itself after certain intervals. The use of periodic boundary conditions allows us to approximate a finite volume of the simulation model as an infinite volume of the periodic medium. In a periodic boundary condition, the far end of the sampling probe wraps around to the start when it goes past the boundary.

2.2. Simulated Annealing

Simulated annealing, a global optimization technique, has a rich history in geostatistical applications (see Ouenes *et al.*, 1994, for a review). Hazlett (1997) first implemented this technique to reconstruct a 3D Berea sandstone sample using the extended variogram statistics. Ever since this technique has been used by others for stochastic reconstruction of porous media (e.g., Yeong and Torquato, 1998a; Yeong and Torquato 1998b; Manwart and Hilfer, 1999; Manwart et al., 2000; Liang et al., 2000, Talukdar et al., 2001a). The main idea behind this simple but powerful technique is to gradually transform an initial uncorrelated ("high-energy") configuration of void and solid voxels (pixels in 2D) into a correlated ("low-energy") configuration, which allows a certain target function commonly known as an "objective function" to approach a global optimum. The "energy" is measured in terms of deviations from a set of target, experimentally determined, functions conveying morphological information, *e.g.*, $S_2(u)$ and/or $L(u)$. The "objective function" is generally defined in terms of an arbitrary number (n) of user-defined target functions as:

$$E = \sum_{n} \sum_{u=0}^{u_n^{max}} \left[f_n(u) - \tilde{f}_n(u) \right]^2, \qquad [4]$$

where, f_n and $\tilde{f}_n$ are the simulated and target functions, respectively. For the purposes of this work, the function $\tilde{f}_n$ is the void-phase two-point probability function (along any orthogonal direction) or the void-phase lineal path function (along any orthogonal direction) computed with or without the

application of periodic boundary conditions. The functions are used either independently or as a combination. Each target function $\tilde{f}_n$ is matched to a maximum lag u_n^{max}.

At the heart of the algorithm is an analogy with thermodynamics, specifically with the way that metals cool and anneal. The essence of the process is slow cooling, allowing ample time for redistribution of the atoms as they lose mobility to ensure that a low energy state will be achieved. Metropolis et al. (1953) first introduced the so-called Boltzmann probability distribution to simulate this kind of principles numerically. The Boltzmann probability distribution,

$$Prob(E) \approx e^{\frac{-E}{bt}}, \qquad [5]$$

expresses the idea that a system in thermal equilibrium at temperature *t* has its energy probabilistically distributed among all different energy states *E*. The constant *b* is termed as the Boltzmann constant. When offered a succession of options, a simulated thermodynamic system was assumed to change its configuration from energy E_1 to energy E_2 with probability $p = e^{\frac{-\Delta E}{kt}}$, where, $\Delta E = E_2 - E_1$. Notice that if $E_2<E_1$ (decreasing energy), this probability is greater than unity; in such cases the change is arbitrarily assigned a probability $p = 1$, i.e., the system always takes such an option. If $E_2>E_1$ (increasing energy), the system also takes an option with probability $p = e^{\frac{-\Delta E}{kt}}$.

Surprisingly, the implementation of the algorithm is relatively simple. The simulation begins by randomly designating fractions φ and $(1-\varphi)$ of void and solid phase voxels, respectively, on a grid of size $L \times M \times N$ ($L \times M$ in 2D). At each iteration step *k*, a void and a solid voxel are chosen at random and their phase function values are interchanged. This interchange slightly modifies the functions f_n and therefore changes the energy of the system while preserving the porosity. A pixel interchange is accepted with a probability p_a given by the Metropolis rule (Metropolis *et al.*, 1953),

$$p_a^{(k)} = \begin{cases} 1 & if\ \Delta E^{(k)} \le 0 \\ e^{-\Delta E^{(k)}/T^{(k)}} & if\ \Delta E^{(k)} > 0 \end{cases} \qquad [6]$$

where $\Delta E^{(k)} = E^{(k+1)} - E^{(k)}$ and $T^{(k)}$ is a control parameter representing the "temperature" of the system. Notice that the product *bt* in Eq. [5] has been replaced by *T* in Eq. [6] which has the same unit as the energy. The starting value and the rate of reduction of *T* are governed by an annealing schedule. This schedule should be such that a global optimum is achieved as quickly as possible. In practice, *T* is reduced by a factor λ after a predefined number of interchanges, referred to as a *Markov chain*. If rapid convergence is expected, a dynamic schedule, which takes into account the rapid fluctuations in the evolving energy in updating the system temperature *T* should be preferred over a static one where *T* decreases monotonically. Otherwise, there is danger that the system will be trapped at a local energy minimum, unless *T* is decreased very slowly. The following formula for updating *T* was adopted in this work (Ouenes *et al.*, 1994):

$$\lambda = Max\left[\lambda_{min}, Min\left(\lambda_{max}, \frac{E_{min}}{\overline{E}}\right)\right], \qquad [7]$$

where λ_{min} and λ_{max} are the minimum and maximum allowable reduction factors, respectively, and are specified by the user. In this approach, for each *Markov chain*, the lowest and average energy values reached, E_{min} and $\overline{E}$, are used to compute the reduction factor λ. The system temperature is then updated as,

$$T = T_o e^{(\lambda-1)(m+1)} \qquad [8]$$

where, T_o is the starting temperature and *m* is the number of *Markov chains* after a total of *k* interchanges. This approach permits estimation of the starting temperature from the initial behavior of the energy function. Accordingly, the mean change in the energy function for k_o initial iterations is first evaluated:

$$\overline{\Delta E} = \frac{1}{k_o}\sum_{k=1}^{k_o} \Delta E^{(k)} \qquad [9]$$

The starting temperature T_o is then estimated from the following expression for a given initial acceptance probability p_a^o,

$$p_a^o = e^{-\overline{\Delta E}/T_o} \qquad [10]$$

All results obtained in this work were obtained with k_o = 100, p_a^o = 0.5 and *m* = 11500. It should be kept in mind that the choice of these parameters is highly system-specific (Ouenes *et al.*, 1994).

2.3. Quantitative Measures

The quantitative measures used to evaluate the quality of 2D and 3D reconstructions are as follows:

Specific surface area: The slope of $S_2(u)$ at the origin is related to the specific surface area (the interfacial area per unit volume), s, which for digitized media is given by (Yeong and Torquato, 1998a):

$$s = -2D\left.\frac{dS_2(u)}{du}\right|_{u=0}, \qquad [11]$$

where, D is the dimensionality of the space. The quantity s is an indicative of how accurately the void-solid interface has been reproduced. It also indicates to what extent the initial part (small lags) of the two-point probability function has been captured.

Correlation length: The correlation length $\bar{\lambda}$, provides a characteristic length scale of the pore space defined as the integral of the two-point probability function:

$$\bar{\lambda} = \int_0^\infty (\varphi - \varphi^2) S_2(u)\,du\,. \qquad [12]$$

Cluster size distribution: The cluster size distribution is an indicative of how well the pore clusters of different sizes have been reproduced. Clusters of size equal to one voxel represent the number of isolated pores. A burning algorithm was used to calculate the distribution of distinct void-phase clusters. The algorithm scans for a pore pixel along the rows or columns of the image and sets fire at a pore location. The fire iteratively burns all connected pore pixels and extinguishes when there are no more pore pixels connected to this cluster. Each time a pore pixel is burnt, the size of the pixel is added to the cluster size. The process is then repeated at a new cluster site. The number of clusters of a given size is dividing by the total number of clusters to obtain the distribution.

Local porosity distribution: The local porosity distribution $\mu(\varphi, L)$ is a useful quantity in describing the porous microstructures. $\mu(\varphi, L)$ measures the probability of finding the porosity $\varphi(\vec{u}, L)$ in the range $(\varphi, \varphi + \Delta\varphi)$ within a square box of side length L centred at position $\vec{u}$. The local porosity distribution can be easily calculated from the phase function $Z(\vec{r})$ (Eq. [1]).

If $\varphi(\vec{u}, L) = \langle Z(\vec{r}) \rangle_{\mathrm{M}}$ denotes the porosity of a measurement cell $\mathrm{M}(\vec{u}, L)$, then

$$\mu(\varphi, L) = \frac{1}{n} \sum_{\vec{u}} \delta(\varphi - \varphi(\vec{u}, L)), \qquad [13]$$

where,

$$\delta(\varphi - \varphi(\vec{u}, L)) = \begin{cases} 1 \text{ if } |\varphi - \varphi(\vec{u}, L)| \le \Delta\varphi \\ 0 \text{ otherwise} \end{cases}, \qquad [14]$$

and n is the total number of measurement cells. If the porosity of a cell is found to be equal to or greater than a specified value, the cell is counted (cf. Eq. [14]). In principle, the measurement cells should not overlap but, to avoid bad statistics, we placed $\mathrm{M}(\vec{u}, L)$ on all pixels, which are at least a distance $L/2$ away from the boundaries of the sample.

Local percolation probability: Another useful quantity in describing the porous microstructures is the local percolation probability, $P_i(L)(i = x, y, z)$, which provides a quantitative characterization of local connectivity. Since connectivity is a 3D parameter, this quantity will be measured only on 3D samples. $P_i(L)$ is defined as the probability of finding a measurement cell $\mathrm{M}(\vec{u}, L)$ that percolates in direction i. Mathematically,

$$P_i(L) = \frac{1}{n} \sum_{\vec{u}} \Lambda_i(\vec{u}, L), \qquad [15]$$

where,

$$\Lambda_i(\vec{u}, L) = \begin{cases} 1 \text{ if } \mathrm{M}(\vec{u}, L) \text{ percolates} \\ 0 \text{ otherwise} \end{cases}, \qquad [16]$$

The local percolation probabilities were calculated using a burning algorithm. The algorithm seeks for a pore pixel (voxel in 3D) along an edge of a measurement cell. If it finds a pore pixel, it sets a fire and iteratively burns all connected pore pixels until it crosses the boundaries of the cell or the fire extinguishes if no more connected pore pixels are found. The measurement cell is said to percolate in the i-direction if the fire reaches a boundary started from its opposite boundary in direction i

Unoptimized correlation functions: The reproduction of unoptimized correlation functions (correlation functions which are not constrained in the simulated annealing algorithm) is a strong indicative of the quality of

reconstructions. Two-point probability function and lineal path function are computed and compared for the cases where these functions are not used in the optimization process.

Chord distribution function: The chord distribution function, $C_i(u)$, where the subscript *i* refers to either void or solid, is another useful parameter to describe the quality of reconstructions. This function can be directly interpreted in terms of microstructural features, as it contains phase connectedness and correlation information along a lineal path (Roberts and Torquato, 1999). That is, if $C_i(u) \neq 0$ for large values of *u*, there exist connected regions of phase *i* at scale *u*. Importantly, the value of *u* at which $C_i(u)$ is maximum provides an estimate of the length scale associated with phase *i*.

3. Analysis of BSE images and calculation of morphological descriptions

3.1. Image acquisition and processing

A high porosity ($\varphi = 0.38$ by helium porosimetry) North Sea chalk sample from the Greater Ekofisk Region was used for this study. A total of five BSE microscopic images were captured from thin sections (polished surfaces) of approximate size 15x15x1 mm^3 that were cut from a cleaned and dried core sample and then impregnated with epoxy resin under vacuum. Images of size 512x512 pixels were taken at a pixel resolution of 0.136 x 0.136 μm^2. This pixel resolution was selected in order to capture the sub-micron size pores that are abundant in chalk. In BSE imaging, a narrow beam of monochromatic electrons is focused on a tiny area (dwell point) of the polished surface. Elastic collisions take place between the incident electrons and the atoms of the specimen and the incident electrons scatter "backward" 180 degrees with no appreciable loss of energy. The backscattered electrons are then counted using a semiconductor device mounted on the bottom of the objective lens. This quantity is translated into gray intensity (0 to 255) and a pixel is displayed on a cathode ray tube (CRT) with the appropriate gray level. The beam is then moved to its next dwell point and the process is repeated for the required number of pixels. The intensity of the pixel varies directly with the atomic number of the specimen at the dwell point. Higher atomic number elements (more collisions) appear brighter than lower atomic number elements.

Thresholding was used to segment each image into objects of interest (void) and background (solid) on the base of gray level. The binarization sets all thresholded pixels (pore) to black (a phase value 1) and all background pixels (solid) to white (a phase value 0). Here, thresholding was based on an

analysis of the histogram of the gray values. The histograms for all five images were found to be bimodal. A threshold value was selected between the peaks, such that the porosity of the thresholded image was close to the measured porosity of the chalk sample. A sample image and its binary counterpart are shown in Fig. 1(a) and 1(b) respectively. The average porosity of the binary images is 0.38108 in very good agreement with the measured porosity. All target properties (porosity, correlation functions, and relevant quantitative measures) reported hereafter correspond to averages over five images.

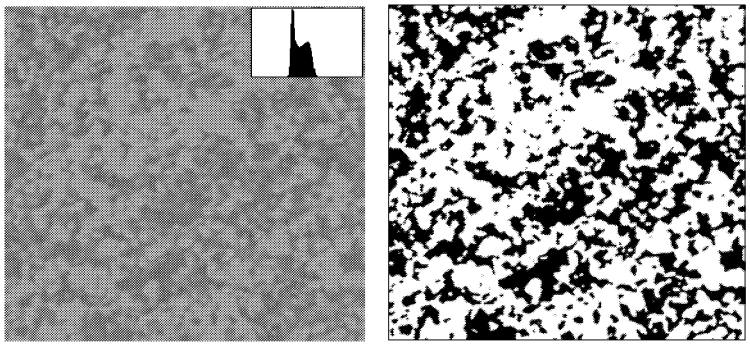

(a) **(b)**

Fig. 1—(a) One of the five BSE micrographs (gray scale) taken from a North Sea chalk sample of the Greater Ekofisk Region. Image size is 512x512 pixels (70x70 μm^2). Inset is a gray-value histogram of the image. (b) The image is thresholded and binarized segmenting void and solid phases shown in black and white, respectively.

3.2. Target Correlation Functions

Following the procedures described in Section 2.1, the target two-point probability function and lineal path function have been computed for void phase along the orthogonal directions with or without the application of periodic boundary conditions (PBC). The target two-point probability functions are shown in Fig. 2(a). This function is virtually identical along the two orthogonal directions, indicating sample isotropy. Periodic boundary conditions do not appear to have any significant effect on this function. The function gets its long-range value of ϕ^2=0.145 at a lag of approximately 60 pixels or 8.16 μm. No appreciable correlation exits beyond this lag. For this sample, the correlation length $\overline{\lambda}$ calculated using Eq. [12] (considering an integral upto 10.2 μm or 75 pixels) is 0.408 μm or 3 pixels. The specific surface area s calculated from Eq. [11] is 1.25 μm^{-1}. Average of x- and y-directional two-point probability functions is used in the calculations. The target lineal path functions are shown in Fig. 2(b). This function neither

differs in orthogonal directions nor is affected by the periodic boundary conditions. The correlation is negligible beyond a lag of approximately 80 pixels or 10.88 μm.

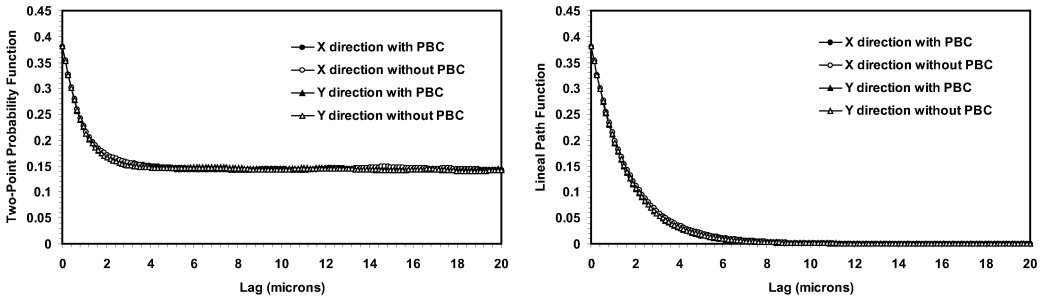

Fig. 2—Target correlation functions along the orthogonal directions; (a) void-phase two-point probability function, (b) void-phase lineal path function. PBC represents periodic boundary conditions.

4. Reconstruction results

4.1. 2D Reconstructions

To evaluate the effectiveness of different morphological descriptors in reproducing the chalk pore networks, we reconstructed five 2D samples of size 300 x 300 pixels each. Case 1 concerns reconstruction using the two-point probability functions, computed with the application of periodic boundary conditions, as the only constraints. Case 2 differs from Case 1 in that the functions were calculated without the application of periodic boundary conditions. In Case 3 and 4, lineal path functions were used with and without periodic boundary conditions, respectively. In Case 5, we applied a hybrid reconstruction in which both two-point probability functions and lineal path functions were used. Periodic boundary conditions were not used. In all five cases, the target functions were optimized along the two orthogonal directions and the simulations were terminated as soon as the energy of the systems became less than 10^{-4}. The initial energy (E_o) and temperature (T_o) for each case are listed in Table 1. Also listed are the specific surface area, correlation length and characteristic cluster statistics.

Table 1. Summary of 2D reconstruction results (300x300 pixels).

Case	E_o	T_o	s μm^{-1}	$\overline{\lambda}$ (μm)	Single-Pixel Pore Cluster (fraction)	Average Size of Pore Clusters (μm^2)	Single-Pixel Solid Chord (fraction)
1	0.329	7.13E-7	1.53	0.402	0.302	0.56	0.1470
2	0.334	1.38E-6	1.51	0.400	0.323	0.55	0.1444
3	1.341	1.11E-5	1.49	0.406	0.275	0.60	0.1317
4	1.362	1.07E-5	1.52	0.413	0.193	0.65	0.1095
5	1.696	1.21E-5	1.38	0.401	0.214	0.69	0.0573
Target			1.25	0.408	0.104	1.05	0.0199

A visual comparison of the reconstructed pore networks is given in Fig 3. It may appear from a cursory comparison of Fig. 3 to Fig. 1(b) that the general features of the target chalk sample are reproduced in all cases. However, the shape of the pore clusters is better reproduced by the use of two-point probability function than the lineal path function. A distinct difference between the target image and the reconstructed images is that a higher number of isolated pore clusters (single-pixel clusters) are present in the reconstructed samples (see Table 1). It must be emphasized here that further decrease in the final energy (less than 10^{-4}) could reduce the number of isolated pore clusters significantly. As a result of higher fractions of isolated pore clusters, the specific surface areas, which are related to the origin of $S_2(u)$ (cf. Eq. [11]), are higher and the average cluster sizes are less than the target values (see Fig. 4 for cluster size distributions). However, the values of $\overline{\lambda}$ (cf. Eq. [12]) are reproduced with an error less than ±2% in all cases. This demonstrates that the target $S_2(u)$ function is reasonably reproduced at higher lags. The void-phase lineal path function $L(u)$ contains correlation information only along *connected* regions within the void phase. It is, therefore, not surprising that the two-point correlation function is slightly mismatched in Case 3 and 4 where $S_2(u)$ is not used as a constraint (see Fig. 5(a)). This is also the case for void-phase lineal path function. In Case 1 and 2, $L(u)$ is not used as a constraint and consequently, it is poorly reproduced (see Fig. 5(b)). However, both $S_2(u)$ and $L(u)$ are accurately reproduced in Case 5 where both of them are optimized.

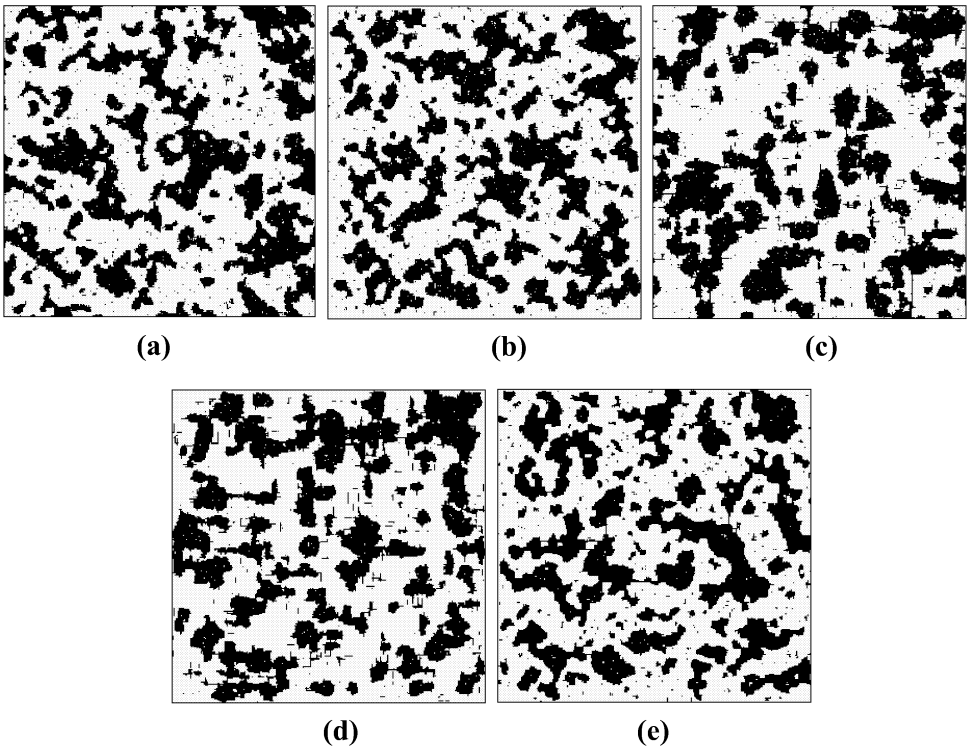

Fig. 3—2D reconstructed images (300x300 pixels); (a) void-phase two-point probability function with periodic boundary conditions (Case 1), (b) void-phase two-point probability function without periodic boundary conditions (Case 2), (c) void-phase lineal path function with periodic boundary conditions (Case 3), (d) void-phase lineal path function without periodic boundary conditions (Case 4), (e) combination of void-phase two-point probability function and lineal path function both without periodic boundary conditions (Case 5).

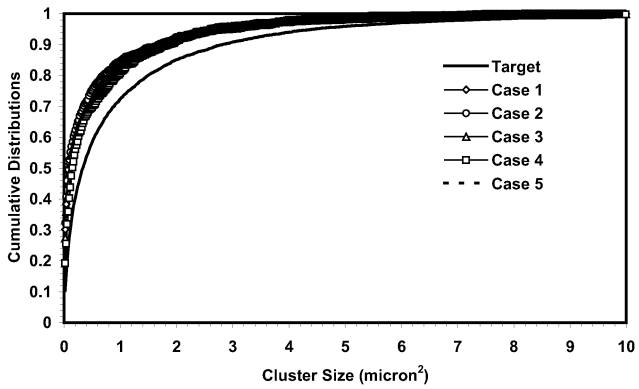

Fig. 4—Cluster size distributions of the 2D target images and 2D reconstructed samples (Cases 1 through 5).

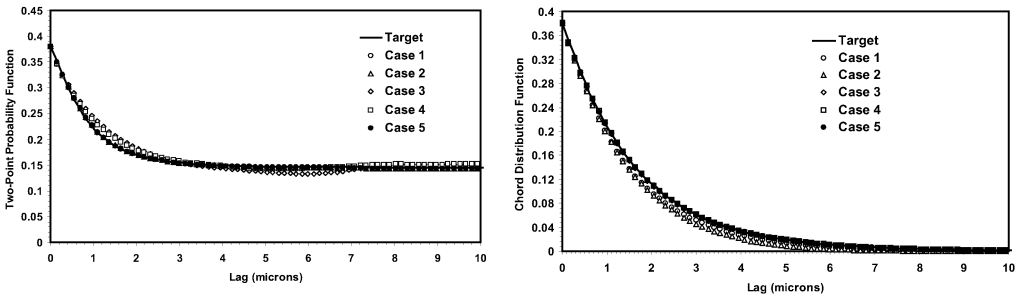

(a) **(b)**

Fig. 5—Comparison between target and simulated correlation functions (Cases 1 through 5); (a) void-phase two-point probability functions, (b) void-phase lineal path functions.

The solid-phase chord distribution functions $C_s(u)$ of the reconstructed samples are compared with the target function in Fig. 6. The peak of target $C_s(u)$ is at about 8 pixels (0.816 μm), which is reasonably reproduced in the reconstructed samples. The match beyond the peak is also reasonable. The match before the peak is poor specially, for Cases 3 and 4 where $L(u)$ alone is optimized. As shown in Table 1, the fractions of isolated solid chords (single-pixel chords) are much higher in the reconstructed samples than the target value. Use of both $S_2(u)$ and $L(u)$ in Case 5 has, however, improved the overall match slightly. The local porosity distributions of reconstructed samples are compared to the target distribution in Fig. 7. The agreement between the target and the reconstructed local porosity distributions is reasonable.

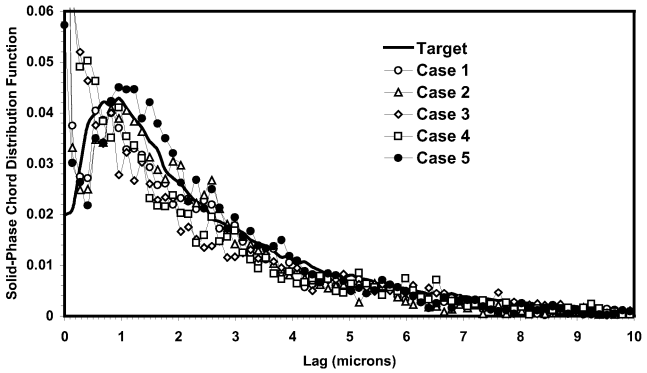

Fig. 6—Comparison between target and simulated solid-phase chord distribution functions (Cases 1 through 5).

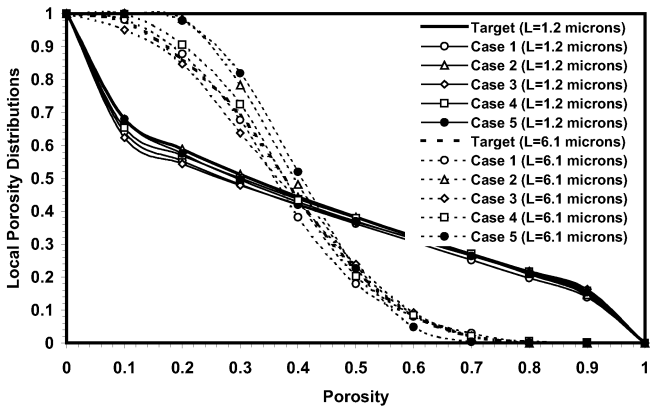

Fig. 7—Local porosity distributions of the 2D reconstructed samples (Cases 1 through 5) and comparison to the target images (at cell side lengths of 1.2 μm (9 pixels) and 6.1 μm (45 pixels)).

Qualitative (visual observation) and quantitative analysis of 2D reconstructions using different morphological constraints reveals that stochastic reconstruction of chalk pore networks using a simulated annealing algorithm constrained by either void-phase two-point probability function or lineal path function is possible with reasonable accuracy. Void-phase two-point probability function appears to be superior to the void-phase lineal path function. Imposing void-phase lineal path function (hybrid reconstruction in Case 5) results in slightly better reconstruction over what is achieved by using the void-phase two-point probability function as the only constraint (compare Case 2 and 5) but at an expense of higher computational cost (a factor of 2).

The use of periodic boundary conditions has only a minor impact on the quality of the 2D reconstructed samples (300x300 pixels). However, it may have some effects if the sample size is small. To analyze it further, Case 6 where a sample of 100x100 pixels is reconstructed using void-phase two-point probability function with periodic boundary conditions and Case 7 where a similar size sample is reconstructed using the same correlation function but without periodic boundary conditions, are studied. The initial energy, temperature, specific surface area, correlation length and characteristic cluster statistics for each case are given in Table 2. In these two cases the target function was matched upto a maximum lag 50 and hence target $\bar{\lambda}$ is different from that reported in Table 1.

Table 2. Summary of 2D reconstruction results (100 x 100 pixels).

Case	E_o	T_o	S μm^{-1}	$\overline{\lambda}$ (μm)	Single-Pixel Pore Cluster (fraction)	Average Size of Pore Clusters (μm^2)	Single-Pixel Solid Chord (fraction)
6	0.332	3.57E-5	1.52	0.286	0.3750	0.489	0.3750
7	0.339	4.82E-5	1.49	0.285	0.3800	0.430	0.3800
Target			1.25	0.289	0.104	1.05	0.0199

The match between target and simulated void-phase two-point probability function and lineal path function is very similar to that in Cases 1 and 2 and hence not shown here. For similar reasons, the solid-phase chord distribution function and cluster size distribution function are also not shown. The reconstructed images and the local porosity distribution function are shown in Fig. 8 and 9 respectively. From quantitative comparisons, it appears that slightly improved results are obtained when two-point probability function is used with periodic boundary conditions.

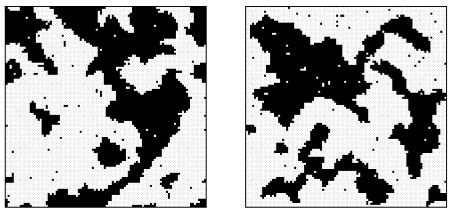

(a) (b)

Fig. 8—2D reconstructed images (100x100 pixels); (a) void-phase two-point probability function with periodic boundary conditions (Case 6), (b) void-phase two-point probability function without periodic boundary conditions (Case 7).

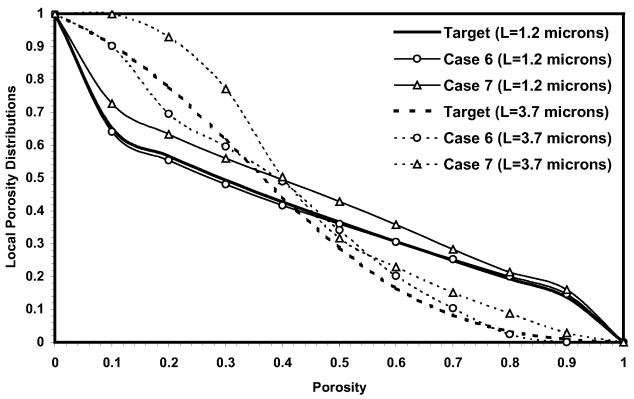

Fig. 9—Local porosity distributions of the 2D reconstructed samples (Cases 6 and 7) and comparison to the target images (at cell side lengths of 1.2 μm (9 pixels) and 3.7 μm (27 pixels)).

4.2. 3D Reconstructions

3D samples are required for detailed study of transport phenomena in chalk. It is therefore essential to investigate as to what extend the 3D chalk pore networks can be reproduced from limited morphological descriptors. Two samples (Cases 8 and 9) of size 150^3 voxels each have been reconstructed and the quality of reconstructions is analyzed in terms of two quantitative measures, namely, local porosity distributions and local percolation probabilities. Case 8 concerns reconstruction using void-phase two-point probability functions, computed in three orthogonal directions with the application of periodic boundary conditions, as the only constraints. In Case 9, a hybrid reconstruction using void-phase two-point probability functions and lineal path functions is considered. Lineal path function was also computed in three orthogonal directions but without the application of periodic boundary conditions. The simulations were terminated as soon as the energy of the systems became less than 10^{-4}.

The agreement between the target and simulated $S_2(u)$, $L(u)$ and $C_s(u)$ is very similar to the respective 2D cases and therefore the function plots are not repeated here. The reconstructed chalk pore networks are shown in Fig. 10. From a visual inspection, we see some differences in the reconstructed microstructures. The black areas of the pore space represent mouths of the pores belong to the outer boundaries. Sample reconstructed in Case 8 has more such mouths than the sample in Case 9. This, however, does not imply that sample in Case 9 has less connectivity than the sample in Case 8. It is not possible to recognize the degree of connectivity inside the samples from a visual inspection. A quantitative characterization of the connectivity is provided by the local percolation probabilities shown in Fig. 11. The figure shows that the sample in Case 9 has slightly higher connectivity than the sample in Case 8. Both samples show some anisotropy in their connectivities. The connectivity is higher in x-direction than y- and z-directions. Sample in Case 9 shows relatively less anisotropy than the sample in Case 8. Therefore, it is evident that a slightly better connectivity is achieved by imposing void-phase lineal path function together with the void-phase two-point probability function.

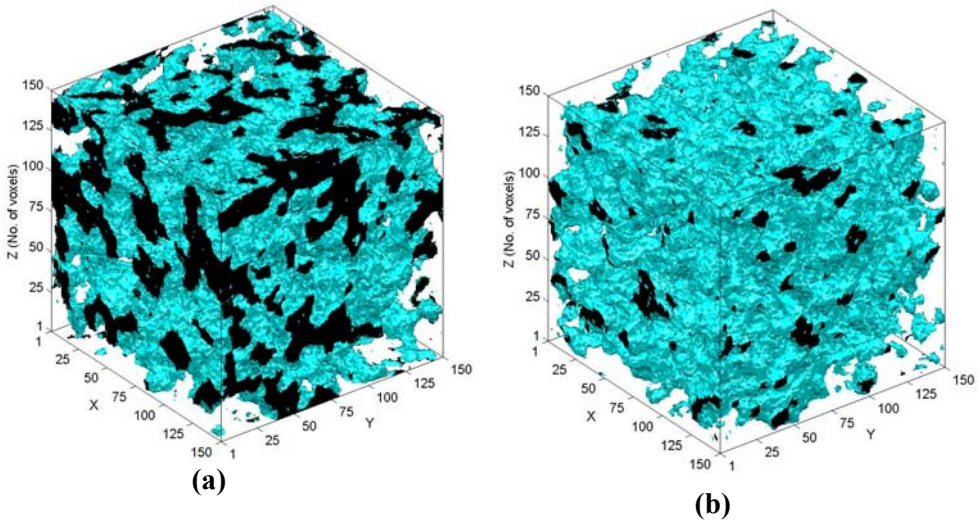

Fig. 10—Microstructure of the reconstructed 3D chalk samples (150^3 voxels); (a) void-phase two-point probability function with periodic boundary conditions (Case 8), (b) combination of void-phase two-point probability function and lineal path function both without periodic boundary conditions (Case 9). The pore space is shown opaque with ends in black. The solid is transparent.

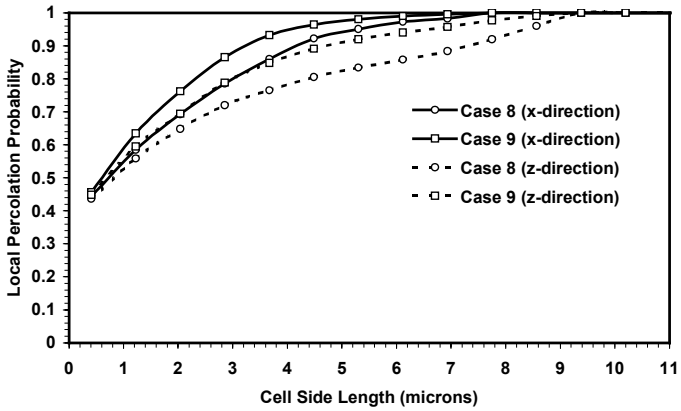

Fig. 11—Local percolation probabilities of the 3D reconstructed samples (Cases 8 and 9). The probabilities denote fraction of the measurement cells that percolate in *i* (*i*=*x*, *y*, *z*) direction. Local percolation probabilities in *y*-direction are similar to those in *z*-direction and hence not shown.

Local porosity distributions of the reconstructed samples are shown in Fig. 12. Due to lack of a 3D target medium, the local porosity distributions obtained from 2D target images is included in Fig. 12 for comparison purpose. These results (also the results from respective 2D cases) show that addition of void-phase lineal path function together with void-phase two-point probability

function does not necessarily improve the local porosity distributions. Further investigation of the geometric and transport properties of the reconstructed chalk pore networks is necessary and will be reported in a forthcoming communication (Talukdar et al., 2001b).

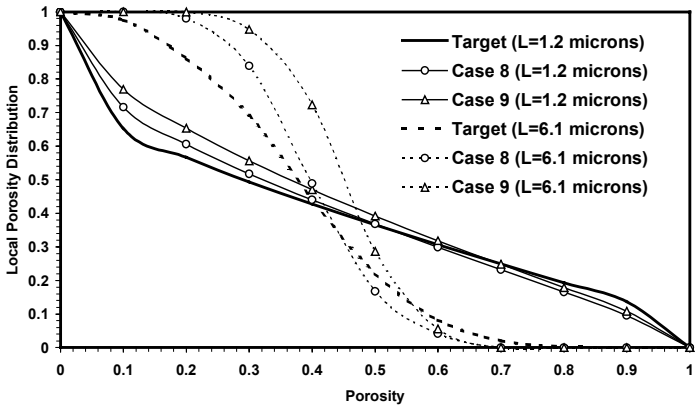

Fig. 12—Local porosity distributions of the 3D reconstructed samples (Cases 8 and 9) and comparison to the 2D target images (at cell side lengths of 1.2 μm (9 pixels) and 6.1 μm (45 pixels)).

5. Conclusions

Stochastic reconstruction of a high porosity North Sea chalk from limited morphological information has been investigated using a simulated annealing algorithm. Quantitative analysis of reconstructed pore networks (2D and 3D) in terms of various morphological parameters shows the following:

(a) The microstructure of chalk may be modeled with reasonable accuracy using the void-phase two-point probability function and/or void-phase lineal path function. Void-phase two-point probability function produces slightly better reconstruction than the void-phase lineal path function. It is probably due to the fact that lineal path function does not contain morphological information for length scales larger than the maximum cluster size in the system. On the other hand, two-point probability function provides short-range information about different clusters.

(b) A combination of void-phase two-point probability function and lineal path function results in slight improvement over what is achieved by using the void-phase two-point probability function as the only constraint, but at an expense of higher computational cost.

(c) For large sample size, use of periodic boundary condition is not crucial. However, for small sample size, the correlation functions are to be

computed with the application of periodic boundary conditions to avoid finite size effects.

Acknowledgment

This work has been fully financed by Phillips Petroleum Co. Norway (PPCoN) as part of a Ph.D. fellowship program. The financial support from PPCoN is gratefully acknowledged.

References

Adler, P.M., Jacquin, C.G. and Quiblier, J.A., 1990. Flow in Simulated Porous Media. Int. J. of Multiphase Flow, 16 (4), 691-712.

Bakke, S. and Øren, P.E., 1997. 3D Pore-Scale Modeling of Sandstones and Flow Simulations in the Pore Networks. SPEJ, 2, 136-149.

Bekri, S., Xu, K., Yousefian, F., Adler, P.M., Thovert, J.-F., Muller, J., Iden, K., Psyllos, A., Stubos, A.K., and Ioannidis, M.A., 2000. Pore Geometry and Transport Properties in North Sea Chalk. J. Petrol. Sci. Eng., 25, 107.

Bryant, S., Cade, C. and Mellor, D., 1993. Permeability Prediction from Geologic Models, AAPG Bull. 77(8), 1338-1350.

Coles, M.E., Hazlett, R.D., Muegge, E.L., Jones, K.W., Andrews, B., Dowd, B., Siddons, P., Peskin, A., Spanne, P. and Soll, W.E., 1996. Developments in Synchrotron X-Ray Microtomography with Applications to Flow in Porous Media. Paper SPE 36531 presented at the 1996 Annual Technical Conference and Exhibition, Denver, Colorado, USA, 6-9 October.

Coles, M.E., Spanne, P., Muegge, E.L., and Jones, K.W., 1994. Computed Microtomography of Reservoir Core Samples. Proc. 1994 Int. Symp. of SCA, Stavanger, Norway.

Davies, D.K. and Vessell, R.K., 1996. Flow Unit Characterization of a Shallow Shelf Carbonate Reservoir: North Robertson Unit, West Texas. Paper SPE 35433 presented at the SPE/DOE Symposium on Improved Oil Recovery, Tulsa, Oklahoma, 21-24 April 1996.

Dullien, F.A.L., 1991. Characterization of Porous Media-Pore Level. Transp. Porous Media, 6, 581.

Fredrich, J., Menendez, B., and Wong, T.-F., 1995. Imaging the Pore Structure of Geomaterials. Science, 268, 276-279.

Hazlett, R.D., 1995. Simulation of Capillary-Dominated Displacements in Microtomographic Images of Reservoir Rocks. Transport in Porous Media, 20, 21-35.

Hazlett, R.D., 1997. Statistical Characterization and Stochastic Modeling of Pore Networks in Relation to Fluid Flow. Math. Geology, 29, 801-822.

Ioannidis, M.A., Kwiecien, M.J., and Chatzis, I., 1997. Electrical Conductivity and Percolation Aspects of Statistically Homogeneous Porous Media. Transport in Porous Media, 29, 61.

Kainourgiakis, M.E., Kikkinides, E.S., Steriotis, Th.A., Stubos, A.K., Tzevelekos, K.P., and Kanellopoulos, N.K., 2000. Structural and Transport Properties of Alumina Porous Membranes from Process-Based and Statistical Reconstruction Techniques. J. Colloid Interface Sci., 231, 158.

Kwiecien, M.J., Macdonald, I.F. and Dullien, F.A.L., 1990. Three-Dimensional Reconstruction of Porous Media from Serial Section Data. J. Microsc., 159, 343-359.

Levitz, P., 1998. Off-lattice reconstruction of porous media: critical evaluation, geometrical confinement and molecular transport. Advances in Colloid and Interface Science, 76/77, 71-106.

Liang, Z., Ioannidis, M.A. and Chatzis, I., 2000. Reconstruction of 3D Porous Media Using Simulated Annealing. Proc. of the XIII Int. Con. on Computational Methods in Water Resources, Alberta, Canada, 25-29.

Lymberopoulos, D.P. and Payatakes, A.C., 1992. Derivation of Topological, Geometrical and Correlation Properties of Porous Media from Void-Chart Analysis of Serial Section Data. J. Colloid Interface Sci. 150, 61-80.

Manwart, C. and Hilfer, R., 1999. Reconstruction of random media using Monte Carlo methods. Physical Review E, 59, 5596-5599.

Manwart, C., Torquato, S., and Hilfer, R., 2000. Stochastic Reconstruction of Sandstones. Phys. Rev. E, 62, 893.

Metropolis, N., Rosenbluth, A., Rosenbluth, M., Teller, A. and Teller, E., 1953. Equation of State Calculations by Fast Computing Machines. J. Chem. Phys., 21, 1087-1092.

Ouenes, A., Bhagavan, S., Bunge, P.H. and Travis, B.J., 1994. Application of Simulated Annealing and Other Global Optimization Methods to Reservoir Description: Myths and Realities. Paper SPE 28415 presented at the 69th Annual Technical Conference and Exhibition, New Orleans, LA, USA, 25-26 September.

Quiblier, J.A., 1984. A New Three-Dimensional Modeling Technique for Studying Porous Media. J. of Colloid and Interface Science, 98, 84-102.

Roberts, A.P. and Torquato, S., 1999. Chord-distribution functions of three-dimensional random media: Approximate first-passage times of Gaussian process. Phys. Rev. E 59, 4953-4963.

Roberts, A.P., 1997. Statistical Reconstruction of Three-Dimensional Porous Media from Two-Dimensional Images. Physical Review E, 56, 3203-3212.

Spanne, P., Thovert, J., Jacquin, C., Lindquist, W., Jones, K. and Adler, P., 1994. Synchrotron Computed Microtomography of Porous Media: Topology and Transports. Phys. Rev. Lett., 73, 2001-2004.

Talukdar, M.S., Torsaeter, O. and Ioannidis, M.A., 2001a. Stochastic Reconstruction of Particulate Media from 2D Images. J. of Colloid and Interface Science, in press.

Talukdar, M.S., Torsæter, O., Ioannidis, M.A. and Howard, J.J., 2001b. Stochastic Reconstruction, 3D Characterization and Network Modeling of Chalk. J. of Petroleum Science and Engineering, in press.

Wardlaw, N.C., 1976. Pore Geometry of Carbonate Rocks as Revealed by Pore Casts and Capillary Pressure. AAPG Bull., 60, 245.

Yeong, C.L.Y. and Torquato, S., 1998b. Reconstructing Random Media. II. Three-Dimensional Media from Two-Dimensional Cuts. Physical Review E, 58, 224-233.

Yeong, C.L.Y., and Torquato, S., 1998a. Reconstructing Random Media. Physical Review E, 57, 495-506.

Paper VII:

Talukdar, M.S., Torsæter, O. and Howard, J.J.: "Stochastic Reconstruction of Chalk Samples Containing Vuggy Porosity Using A Conditional Simulated Annealing Technique," *Transport in Porous Media*, under review.

Paper VIII

URN:NBN:no-2347

A Network Model for Two-Phase Flow in Chalk

M.S. Talukdar and O. Torsæter
Norwegian University of Science and Technology, Trondheim, Norway

Unpublished

Abstract

A network model of drainage and imbibition has been developed for chalk incorporating important pore-level displacement phenomena (e.g., corner flow, wettability alteration, trapping, etc.) and realistic description of pore space geometry and topology. Limited results from very simple pore network demonstrate its applicability in computing absolute and relative permeabilities, capillary pressure, formation factor and resistivity index. However, for the model to be predictive, realistic description of pore space geometry and topology is to be given as input, which is accessible through characterization of the stochastically reconstructed (e.g., using a simulated annealing technique) 3D chalk samples.

Keywords: network model, two-phase flow, corner flow, primary drainage, wettability alteration, piston-type displacement, snap-off, pore-body filling, chalk.

1. Introduction

The prediction of macroscopic transport properties of porous sedimentary rocks is of great theoretical and practical interest in many fields of technology particularly in petroleum reservoir engineering and hydrology. Some of the properties with great practical applications to these fields include absolute and relative permeabilities, capillary pressure, formation factor, and formation resistivity index. In petroleum reservoir engineering, knowledge of these properties at each and every location of reservoir is indispensable for exploration and estimation of oil and gas reserves, to design a first development plan, to support ongoing reservoir management, and to assess the potential and progress of any improved recovery scheme or to enable the screening of options reviving mature fields. In hydrology, one important application, among others, is pollutant transport and cleanup. Consequently, tremendous efforts have been made over the last two decades for accurate prediction of the aforementioned properties.

Traditioanlly, the macroscopic properties are determined through laboratory core-flood experiments which are thought to mimic what could happen in the formation of any hydrocarbon reservoir and during subsequent recovery processes; for example displacement of water by oil during initial hydrocarbon migration and displacement of oil by mud filtrate during drilling

URN:NBN:no-2347

and by water during water flooding. Unfortunately, experimental measurements have limitations, for example, they are laborious, time consuming and not always accurate. Reliable experimental procedure is nonexistent for heterogeneous rock samples, and practically very difficult for three-phase flow. Experiments are conducted on fairly small size core plugs which obviously has pitfalls/artefacts, for example, fairly low water saturations observed during imbibition experiments at water-wet conditions could be artefacts resulting from early water breakthrough caused by heterogeneities (e.g., fractures) in the core samples. Also, the interference of capillary pressure on the measurement of relative permeability, the so-called capillary end effect, is a long standing and yet unresolved issue. Furthermore, subtle complicacy arises for brittle and tight rocks, for example, achieving true irreducible water saturation may not be possible for tight chalk during measurement of drainage capillary pressure in the centrifuge due to crushing of the core at high speed. It is, therefore, not surprising that an alternative technique, such as, theoretical prediction through numerical means would immerge. Network modeling offers an appealing alternative to experimental measurements of single and multi-phase transport properties.

Network modeling began with the pioneering work of Fatt [1-3] who computed capillary pressure, relative permeability and resistivity index curves in two-dimensional networks of interconnected cylindrical pores. Since the work of Fatt, our physical understanding of two- and three-phase pore-scale displacement mechanisms has increased significantly, e.g., [4-13]. Consequently, more sophisticated network models incorporating realistic flow physics have immerged with different predictive capabilities, such as relative permeability and capillary pressure hysteresis [14-15], the effects of wettability [16-27], three-phase flow [11, 25, 28-38], modeling multiphase flow in fractures and matrix/fracture transfer [39], and prediction of relative permeability for an internal gas drive process (gas liberation during depressurization) [40]. However, with an exception to handful of studies, e.g., [37, 41-43], most of the network models use idealized pore networks, which do not adequately represent the complex pore space morphology and thus greatly limit their application in the petroleum industry.

The pores of real porous media consist of angular corners, which retain wetting fluid and allow two or more fluids to flow simultaneously through the same pore. This flow characteristic has important role on oil recovery and therefore, must be accounted for in a network model. Another important aspect of oil recovery is the wettability of reservoir rock. The wettability has a profound effect on displacement efficiency and as a result on ultimate oil recovery. Experimental measurements have demonstrated that most mineral surfaces become oil-wet after prolonged contact with crude oil [44-46]. Salathiel [47] established experimentally that the reservoirs with mixed wettability display low residual oil and consequently high displacement efficiency. Kovscek *et al.* [48] explained Salathiel's results using a pore level scenario for the development of mixed wettability where portions of the solid

surface contacted by oil during primary drainage become oil-wet by the deposition of asphaltenes. This physical scenario for wettability changes at the pore level has been incorporated in several network models, e.g., [19-20, 23-25, 43] and has shown to have significant impact on oil recovery, capillary pressure, relative permeability and resistivity index.

Despite significant share of world's petroleum reside in chalk (carbonate) reservoirs, surprisingly, this rock type has received little attention from network modeling researchers. With the exception of Bekri *et al.* [49] and Xu *et al.* [50] network modeling techniques have been previously used in the study of sandstone reservoirs. While Bekri *et al.* have demonstrated the feasibility of this approach for predicting absolute permeability, formation factor and drainage air-mercury capillary pressure of homogeneous chalks, Xu *et al.* have used this tool to improve the analysis of core-flood experiments in heterogeneous (vugular) chalks. These authors neither used realistic description of the pore space geometry and topology nor all aspects of pore-level displacement phenomena e.g., corner flow, wettability alteration, trapping, etc. Clearly, there are enormous scopes to extent predictive capabilities of a network model for chalk through incorporating all the above aspects. Development of such a model has been pursued in this study in light of recent advances in this area [19, 25, 43, 51-52].

2. Pore network

Direct flow simulations on the complex and chaotic pore space of chalk as obtained from a stochastic reconstruction, e.g., using a simulated annealing technique (see Fig. 1 for an example) either by numerically solving the Navier-Stokes equation [53] or by applying a Lattice Boltzmann simulation [54] is computationally very expensive. It is convenient to construct an equivalent pore network that captures essential features of the pore space and yet simple to deal with mathematically and numerically. Before transformation of the reconstructed pore space into equivalent pore network, the essential task is the topological and geometrical characterization of the reconstructed sample. The characterization technique must calculate the following: (1) location, length, average cross-sectional area and corresponding perimeter length of each pore-body within the sample; (2) number of connected pore-bodies and their locations to each pore-body; (3) length, average cross-sectional area and corresponding perimeter length of all pore-throats connected to each of the pore-bodies; and (4) list of boundary pore-bodies and pore-throats. Characterization of the reconstructed sample is not within the scope of this study and will not be discussed further. For future work on this topic, the readers are referred to Liang *et al.* [55], Bakke and Øren [41] and the public domain software and literature by Lindquist [56].

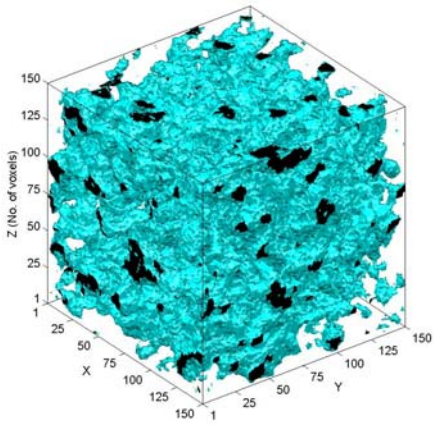

Fig. 1—Microstructure of a reconstructed 3D chalk sample (150^3 voxels) using a simulated annealing technique. The pore space is shown opaque with ends in black. The solid is transparent.

After having the aforementioned pore space characterization data known, the next step is to construct an equivalent pore network model. An important aspect of real pore network is the angular corners that retain wetting fluid and allow two or more fluids to flow simultaneously through the same pore. Use of cylindrical pores nullifies that possibility. Therefore, pore shapes other than cylindrical is recommended. We adopt the procedure by Øren *et al.* [43] and Patzek [51]. Here, the irregular pore space (pore-body and pore-throat) is converted to translationally symmetric pore channels of triangular shapes. However, the triangular pore geometry is variable and is dictated by the so-called shape factor G and the inscribed circle radius r of the pore space under consideration. The shape factor is defined by [57],

$$G = \frac{A}{P^2} = \frac{r}{2P} = \frac{1}{4\sum_{i=1}^{3} \cot\beta_i} = \frac{1}{4}\tan\beta_1 \tan\beta_2 \cot(\beta_1 + \beta_2) \qquad [1]$$

where, A is the pore cross-sectional area, P is the corresponding perimeter length and β_i (i=1, 2, 3) are the corner half-angles ($0 \le \beta_1 \le \beta_2 \le \beta_3 \le \pi/2$). The shape factor ranges from zero for a slit-shaped pore to 0.048 for an equilateral triangular pore. Therefore, depending on its value, the triangular pore geometry may take different shapes, two of which are shown in Fig. 2.

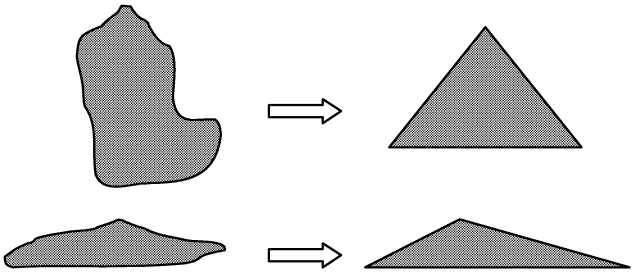

Fig. 2—Shape of triangular pore geometry depending on the shape factor of the pore space.

It is obvious from Eq. 1 that a single value of G corresponds to a range of triangular geometries. However, the following guideline is adopted to select the non-unique corner half-angles [51]: First, the minimum and maximum bounds on β_2 is calculated from Eqs. 2 and 3, respectively. Second, a value for β_2 is selected at random from $\beta_{2,min} \le \beta_2 \le \beta_{2,max}$. Third, an appropriate value for β_1 is calculated from Eq. 4, and finally β_3 is calculated from $\beta_3 = \pi/2 - \beta_1 - \beta_2$.

$$\beta_{2,min} = tan^{-1}\left\{\frac{2}{\sqrt{3}}cos\left[\frac{cos^{-1}\left(-12\sqrt{3}G\right)}{3}+\frac{4\pi}{3}\right]\right\} \quad [2]$$

$$\beta_{2,max} = tan^{-1}\left\{\frac{2}{\sqrt{3}}cos\left[\frac{cos^{-1}\left(-12\sqrt{3}G\right)}{3}\right]\right\} \quad [3]$$

$$\beta_1 = -\frac{1}{2}\beta_2 + \frac{1}{2}\sin^{-1}\left(\frac{\tan\beta_2 + 4G}{\tan\beta_2 - 4G}\sin\beta_2\right) \quad [4]$$

3. Displacement mechanisms and controlling equations

The rock is assumed to be water-wet, therefore, water displacement by oil is a drainage process and the reverse is the imbibition process. The displacing fluid is injected from an external reservoir through the throats connected to the inlet face of the model. The displaced fluid escapes through the outlet face on the opposite side. The main assumption regarding displacement is that the capillary force dominate at the pore-scale which is reasonable for low capillary number, N_c (10^{-6} or less, see Paper 9 for a definition of N_c). The important pore-scale displacement mechanisms during primary drainage and

imbibition and the controlling equations for each of the mechanisms are briefly described below.

3.1 Primary Drainage

Primary drainage process represents the migration of oil into water-filled reservoir. Initially the model is 100% saturated with water. Primary drainage is a pure bond invasion-percolation process [58]. Percolation is about connectedness and in invasion-percolation, the invading fluid must be connected to the inlet to continue invading and the defending fluid must be connected to the outlet to be displaced. In drainage simulation, the calculations are performed in order of increasing threshold capillary entry-pressures; only the accessible pore-throats (adjacent to an oil-filled pore-body) and associated pore-bodies are invaded at each step. Primary drainage continues until some maximum capillary pressure $P_{c,max}$ is reached. We use Øren *et al.*'s [43] generalization of Mason and Morrow's [57] expression for the threshold capillary entry-pressure where the Mayer and Stowe [59], and Prinsen [60-62] (MS-P) method is utilized. The MS-P method relies on equating the curvature of the corner arc-menisci (AM's) to the curvature of the invading interface. The threshold capillary entry-pressure in primary drainage $P^e_{c,pd}$ in a triangular pore is expressed as

$$P^e_{c,pd} = \frac{\sigma}{r_{pd}} = \frac{\sigma}{r} cos\,\theta_r \left(1 + 2\sqrt{\pi G}\right) F_d\left(\theta_r, G, C\right) \qquad [5]$$

where, θ_r is the receding contact angle, r_{pd} is the radius of curvature in primary drainage, and F_d is a function of corner half-angles through C where F_d and C are expressed as follows

$$F_d\left(\theta_r, G, C\right) = \frac{1 + \sqrt{1 - 4GC / cos^2\,\theta_r}}{\left(1 + 2\sqrt{\pi G}\right)} \qquad [6]$$

$$C = \sum_{i=1}^{3} \left[cos\,\theta_r \frac{cos\left(\theta_r + \beta_i\right)}{sin\,\beta_i} - \left(\frac{\pi}{2} - \theta_r - \beta_i\right) \right] \qquad [7]$$

C is not universal for a given G if the AM's are not present in all pore corners. However, for strongly water-wet system (i.e., θ_r = 0), F_d = 1, regardless of how many pore corners have the water AM.

3.2 *Wettability Alteration*

It has been shown experimentally that most mineral surfaces become oil-wet after prolonged contact with crude oil [44-46]. When oil initially invades a water-filled pore-throat or pore-body, a thick water film coats all the solid surfaces and the oil-water contact angle is zero. This thick film is stable until some threshold capillary pressure P_{thresh} is reached and the film collapses to molecular thickness. This allows the surface active components in the oil (e.g., asphaltenes) to adsorb on the pore wall. As a result, the surface becomes oil-wet and the contact angle is no longer zero. The capillary pressure at which the water layer collapses depends on the fluid system, the mineralogy of the solid surface and the curvature of the pore wall. Kovscek *et al.* [48] performed a detailed analysis of this scenario for star-shaped pores. Practically it is very difficult to quantify the curvature and mineralogy of pore surfaces. Blunt [19] extended the analysis to square-shaped pores and proposed a parametric model for P_{thresh}. A similar model is used in this study. For a pore-body or pore-throat *i*, P_{thresh} is calculated from

$$P_{thresh,i} = P_{low,i} + \Omega_i x_i \qquad [8]$$

where, P_{low} and Ω are input parameters and x is a random number between 0 and 1. The first term on the right side of the equation represents the disjoining pressure, whereas, the second term represents the film curvature. This parametric model should not be used if experimental P_{thresh} is available for each pore-body and pore-throat. If $P_{c,max} > P_{thresh}$ in an oil-filled pore-body or pore-throat, the contact angle must change to a new value [48]. This pore-body or pore-throat is termed as having mixed-wettability because the corners contain bulk water and remain water-wet while away from the corners, the pore wall is oil-wet (see Fig. 3). We assume a new value of $\theta_r < \frac{\pi}{2} - max(\beta_i, i = 1,2,3)$ so that water is always present in all corners. Pore-body or pore-throat where $P_{c,max} < P_{thresh}$ remains water-wet.

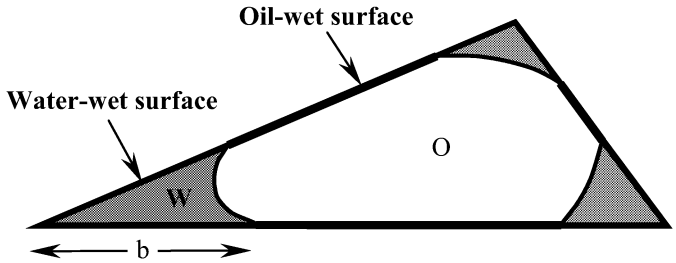

Fig. 3—A mixed-wet pore showing the oil-wet and water-wet surfaces, and the meniscus-apex distance *b* along the wall.

3.3 Imbibition

Imbibition is a problem in mixed invasion-percolation and percolation with trapping. In percolation with trapping, clusters of the defending fluid can be disconnected from the outlet. Imbibition is a much more complicated process than primary drainage and is very slow. The invading wetting fluid spans the entire medium through corners and crevices while the clusters of non-wetting fluid become trapped when their escape paths are cut off by the bond-breaking mechanisms.

The capillary pressure drops during imbibition and as capillary pressure decreases, the pore-throats fill in the order of increasing radius, with the narrowest filling first. The throat filling starts by snap-off [if initially there are no main terminal arc menisci (MTAM)], and then by piston-type imbibition. At the same time, the pore-bodies attached to the invaded throats are subject to cooperative pore-body filling by the I_n events. These mechanisms have been described by Lenormand *et al.* [4] for water-wet pores and Blunt [19] for mixed-wet pores. The behavior and threshold capillary pressures for each of the three mechanisms are briefly described below (see Paper 9 for a sketch of the mechanisms):

Piston-Type Imbibition

This refers to the displacement of oil from a pore-throat by an invading interface initially located in an adjoining water-filled pore-body. If the advancing contact angle θ_a is equal to θ_r (i.e., no contact angle hysteresis), the threshold capillary pressure is the same as for drainage, i.e., Eq. 5. With contact angle hysteresis ($\theta_a > \theta_r$), each corner AM hinges about its contact line, pinned at a distance b_i from the corner apex (Fig. 3), until the hinging contact angle $\theta_{h,i}$ exceeds θ_a. $\theta_{h,i}$ can acquire any value between θ_r and θ_a. Thereafter, the AM slides at θ_a while decreasing its radius of curvature r_{pt} to accommodate the current capillary pressure in imbibition. The AM in sharpest corner slides first while the AM in the widest corner slides last.

Spontaneous imbibition ($P_c > 0$) by piston-type displacement always occurs for $\theta_a < \frac{\pi}{2}$ and may occur for θ_a much greater than $\frac{\pi}{2}$. The maximum contact angle $\theta_{a,max}$ at which spontaneous piston-type imbibition can occur is defined by the requirement that the effective perimeter wetted by oil be zero [43]:

$$\theta_{a,max} = cos^{-1}\left[\frac{-4G\sum_{i=1}^{3}cos(\theta_r+\beta_i)}{rP_{c,max}/\sigma - cos\theta_r + 12G\,sin\theta_r}\right] \quad [9]$$

Thus, $\theta_{a,max}$ depends on $P_{c,max}$, G and θ_r. In triangular pore, the threshold capillary pressure in spontaneous inbibition (i.e., $\theta_a \le \theta_{a,max}$), with contact-angle hysteresis, is calculated by solving the following system of nonlinear algebraic equations [51]:

$$\theta_{h,i} = min\left\{cos^{-1}\left[\frac{r_{pd}}{r_{pt}}cos(\theta_r+\beta_i)\right]-\beta_i\ ,\theta_a\right\};\ i = 1, 2, 3 \quad [10]$$

$$b_i = \begin{cases} r_{pd}\dfrac{cos(\theta_r+\beta_i)}{sin\,\beta_i},\ if\ \theta_{h,i} \le \theta_a \\ r_{pt}\dfrac{cos(\theta_a+\beta_i)}{sin\,\beta_i},\ if\ \theta_{h,i} > \theta_a \end{cases};\ i = 1, 2, 3 \quad [11]$$

$$\alpha_i = \begin{cases} sin^{-1}\left(\dfrac{b_i}{r_{pt}}sin\,\beta_i\right),\ if\ \theta_{h,i} \le \theta_a \\ \dfrac{\pi}{2}-\theta_a-\beta_i,\ if\ \theta_{h,i} > \theta_a \end{cases};\ i = 1, 2, 3 \quad [12]$$

and

$$r_{pt} = \frac{\dfrac{r^2}{4G} - r_{pt}\sum_{i=1}^{3}b_i\,cos\theta_{h,i} + r_{pt}^2\sum_{i=1}^{3}\left(\dfrac{\pi}{2}-\theta_{h,i}-\beta_i\right)}{2r_{pt}\sum_{i=1}^{3}\alpha_i + \left(\dfrac{r}{2G}-2\sum_{i=1}^{3}b_i\right)cos\,\theta_a} \quad [13]$$

The above nonlinear system of equations can be solved numerically (e.g., Newton-Raphson method) for the radius of curvature r_{pt} and, thus, the threshold capillary pressure in piston-type imbibition $P_{c,pt}^{e} = \dfrac{\sigma}{r_{pt}}$.

For very large contact-angle hysteresis ($\theta_a > \theta_{a,max}$), the corner menisci remain pinned, while the MTAM is forced into the pore at a negative capillary pressure, as in primary drainage. When $\theta_a \ge \dfrac{\pi}{2} + max(\beta_i) > \theta_{a,max}$, imbibition is forced and a film of oil may be left sandwiched between the water in the

corner(s) and the water in the center (see Fig. 4). In this case, the threshold capillary pressure in piston-type is obtained from Eq. 5 with θ_r replaced with θ_a. When $\theta_{a,max} < \theta_a < \frac{\pi}{2} + max(\beta_i)$, geometry prevents the creation of intermediate film and the MTAM is forced into the pore when each of its radii of curvature equals $\frac{r}{cos\,\theta_a}$. The threshold capillary pressure is then given by $P^e_{c,pt} = \frac{2\sigma\, cos\,\theta_a}{r}$.

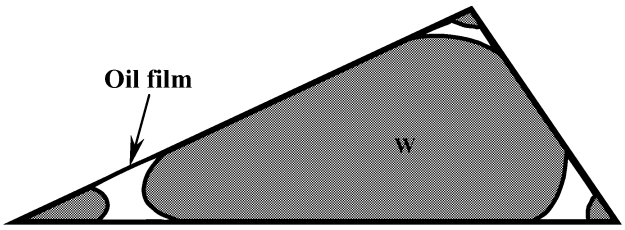

Fig. 4—Formation of oil films in piston-type imbibition with extreme contact-angle hysteresis.

Similar to Blunt [19], the oil film in a corner is assumed to be stable until the two oil-water interfaces on either side of the film meet. The critical capillary pressure at which an oil film in a corner *i* collapses is given by

$$\frac{P_c}{-P_{c,max}} = \frac{sin\,\beta_i}{cos(\theta_r + \beta_i)}\left(\frac{1-d^2}{d\,cos\,\beta_i + \sqrt{1-d^2\,sin^2\,\beta_i}}\right) \qquad [14]$$

where, $d = 2 + \frac{cos\,\theta_a}{sin\,\beta_i}$.

Cooperative Pore-Body Filling

The largest radius of curvature of water-oil interface in a pore-body and its oil-filled pore-throats defines the threshold capillary pressure necessary to fill that pore-body. The required radius of curvature depends on the size of the pore-body and on the number and spatial distribution of connecting pore-throats filled with oil. For a pore-body with coordination number *z*, there are *z*-1 such pore-body filling mechanisms (see Paper 9). If only one of the connecting throats contain oil (i.e., I_1 mechanism), the pore-body filling is similar to that

of a piston-type invasion and the threshold capillary pressure is almost the same.

The threshold capillary pressure for the I_2 to I_{z-1} mechanisms are more complex and no accurate expression is available to date. Blunt [19] presented a parametric model for these mechanisms, which was also used by others [43]. If $\theta_a < \theta_{a,\max}$, the mean radius of curvature for filling by an I_n mechanism is calculated from

$$R_n = \frac{1}{\cos\theta_a}\left(r_p + \sum_{i=1}^{3} b_i r_i x_i\right) \qquad [15]$$

where, r_p is the pore-body radius, r_i is the radii of the oil-filled throats and x_i is a random number between 0 and 1. The threshold pore-filling capillary pressure for the I_n mechanism is then $P_{c,n}^e = \frac{2\sigma}{R_n}$. If $\theta_a > \theta_{a,\max}$, the water invasion is forced, and the threshold capillary pressure is the same as for the I_1 mechanism.

Snap-Off

Snap-off is the invasion of an oil-filled pore by water AM's, which always exist in the corners of pore-bodies and pore-throats. If there is no contact-angle hysteresis, the AM's advance smoothly along the pore walls as the capillary pressure decreases. At a critical point, the AM's fuse and become unstable; and the entire cross-section of the pore fills with water cutting the oil filament into two parts (see Paper 9). The threshold capillary entry-pressure in piston-type displacement is always higher than that for snap-off; therefore, snap-off occurs only when piston-type displacement is impossible for topological reasons (i.e., when there is no water-oil MTAM waiting at the pore end) [51].

For a strongly water-wet system, the snap-off instability occurs at a threshold capillary pressure of

$$P_{c,so}^e = \frac{\sigma}{r} \qquad [16]$$

With contact-angle hysteresis, the AM's remain pinned at the position established at $P_{c,max}$ until the hinging contact angle in the sharpest corner equals θ_a. Further decrease of capillary pressure causes the sharpest corner's AM to advance towards the center of the pore. Eventually the advancing AM meets another one in the second sharpest corner, causing snap-off. If

$\theta_a < \frac{\pi}{2} + min(\beta_i)$, the curvatures of the AM's are positive and snap-off takes place at a positive capillary pressure (spontaneous snap-off).

We follow the steps described by Patzek [51] to calculate the threshold capillary entry-pressure for snap-off with contact-angle hysteresis, and $\theta_a < \frac{\pi}{2} + min(\beta_i) = \frac{\pi}{2} + min(\beta_i)$ by starting from the threshold capillary pressure in piston-type imbibition. Given the initial values of $r_{so} = r_{pt}$ and $\theta_{h,i}$, obtained from Eqs. 10-13, the capillary pressure is gradually lowered by increasing r_{so} and the corresponding $\theta_{h,i}$ and b_i are calculated using Eqs. 10-11. The following checks are performed:

$$b_1(r_{so1}, \theta_{h,1}) + b_2(r_{so1}, \theta_{h,2}) < l_1 = r(cot\,\beta_1 + cot\,\beta_2) \quad [17]$$

$$b_2(r_{so2}, \theta_{h,2}) + b_3(r_{so2}, \theta_{h,3}) < l_2 = r(cot\,\beta_2 + cot\,\beta_3) \quad [18]$$

$$b_1(r_{so3}, \theta_{h,1}) + b_3(r_{so3}, \theta_{h,3}) < l_3 = r(cot\,\beta_1 + cot\,\beta_3) \quad [19]$$

where l_i (i=1,2,3) are the lengths of triangle sides expressed through the inscribed circle radius and the corner half-angles. If one or more of the conditions in Eqs. 17-19 is violated, two or three of the AM's have met and snap-off has occurred. Solving for the equality signs in each of the conditions in Eqs. 17-19, yields three different radii of the menisci, $r_{so_i}(i = 1,2,3)$. The threshold capillary entry-pressure for snap-off occurs at the minimum radius (i.e., at the highest possible capillary pressure). Note that for $\theta_a = \frac{\pi}{2} - \beta_{min}$, the threshold capillary entry-pressure for snap-off is zero (a flat meniscus in the sharpest corner advances). Therefore, in contrast to piston-type imbibition, spontaneous imbibition by snap-off occurs only for $\theta_a < \frac{\pi}{2} - \beta_{min}$.

If $\theta_a > \frac{\pi}{2} - min(\beta_i) = \frac{\pi}{2} - \beta_{min}$, all three AM's are convex, their curvatures are negative and water invasion is forced. Once the hinging angle in the sharpest corner has increased to θ_a, its AM advances towards the center of the pore and the absolute value of its curvature decreases. This situation is analogous to the cause of instability of three concave menisci that meet. The convex AM is thus unstable and the part of the pore in which the instability has occurred immediately fills with water. The threshold pressure for this snap-off event depends on the curvature of the AM when it begins to move:

$$r_{so}\,cos(\theta_a + \beta_{min}) = r_{pd}\,cos(\theta_r + \beta_{min}) \quad [20]$$

and the threshold capillary entry-pressure is given by

$$P_{c,so}^{e} = \frac{\sigma}{r_{so}} = P_{c,max}\frac{cos(\theta_a + \beta_{min})}{cos(\theta_r + \beta_{min})},\ \theta_a < \pi - \beta_{min} \qquad [21]$$

otherwise, the numerator in Eq. 21 is replaced by its smallest possible value ($cos\pi = -1$) and

$$P_{c,so}^{e} = \frac{\sigma}{r_{so}} = P_{c,max}\frac{-1}{cos(\theta_r + \beta_{min})},\ \theta_a \geq \pi - \beta_{min} \qquad [22]$$

4. Pore occupancy and hydraulic conductance

The triangular cross-sectional area of a pore is given by

$$A = \frac{r^2}{4G} \qquad [23]$$

When a pore is filled with a single fluid, the area occupied by that fluid is calculated from Eq. 23. If water is present as AM's in the corners, the area occupied by water is given by

$$A_w = \left(\frac{\sigma}{P_c}\right)^2 \sum_{i=1}^{3}\left[\frac{cos\,\theta\, cos(\theta + \beta_i)}{sin\,\beta_i} - \frac{\pi}{2}\left(1 - \frac{\theta + \beta_i}{\pi/2}\right)\right], \qquad [24]$$

where θ is θ_r, θ_h or θ_a depending on the circumstances and the area occupied by oil is given by $A_o = A - A_w$. When oil films are present in the corners, the area occupied by oil is

$$A_o = \left(\frac{\sigma}{P_c}\right)^2 \sum_{i=1}^{3}\left[\frac{cos\,\theta_a\, cos(\theta_a - \beta_i)}{sin\,\beta_i} - \frac{\pi}{2}\left(\frac{\theta_a - \beta_i}{\pi/2} - 1\right)\right] - A_w \qquad [25]$$

In the above equation, the sum includes only the corners where oil films exist.

The volume of each phase in a pore-body or pore-throat is obtained by multiplying the corresponding area with the pore length. The overall saturation of each phase is found by adding the volume of each phase in every pore-body and pore-throat and dividing by the total volume of the network.

For a pore-body or pore-throat containing a single fluid, the hydraulic conductance *g* is approximated from Poiseuille's law [43]

$$g = \frac{3r^2 A}{20\mu} \qquad [26]$$

If oil occupies the center of a pore with water present as AM's in the corners, the oil conductance is found from Eq. 26 with A replaced by A_o.

When water is present as AM's in a corner i with a contact angle less than $\frac{\pi}{2} - \beta_i$, the water conductance for the corner is

$$g_{w,i} = \frac{\left(\frac{\sigma}{P_c}\right)^2 A_{w,i}}{C_{w,i}\mu_w} \qquad [27]$$

The total conductance is the sum of all the corner conductances. In the equation, C_w is a dimensionless flow resistance factor that accounts for the reduction in water conductance close to the pore wall and is a function of corner geometry, contact angle and boundary condition at the oil-water interface. C_w can be calculated from an approximate expression due to Zhou *et al.* [52].

$$C_{w,i} = \frac{12\sin^2\beta_i(1-\phi_3)^2(\phi_2+\phi_1)^2}{(1-\sin\beta_i)^2(\phi_2\cos\theta-\phi_1)\phi_3^2} \qquad [28]$$

where $\varphi_1 = \frac{\pi}{2} - \beta_i - \theta$, $\varphi_2 = cot\,\beta_i\, cos\,\theta - sin\,\theta$ and $\varphi_3 = \left(\frac{\pi}{2} - \beta_i\right) tan\,\beta_i$.

If the contact angle is greater than $\frac{\pi}{2} - \beta_i$, the curvature of the AM is negative and the water conductance for the corner may be calculated from an approximate equation [43],

$$g_{w,i} = \frac{A_{w,i}^2}{C_{w,i}\kappa_i\mu_w} \qquad [29]$$

where C_w is evaluated from Eq. 28 at $\theta = 0$, i.e.,

$$C_{w,i} = \frac{12\,sin^2\beta_i(1-\varphi_3)(1+\varphi_3)^2}{tan\,\beta_i(1-sin\,\beta_i)^2\varphi_3^2} \qquad [30]$$

and

$$\kappa_i = \frac{\cos\beta_i}{\sin\beta_i} - \frac{\pi}{2} + \beta_i \qquad [31]$$

If oil films are present in the corners of a pore-body or pore-throat, the oil conductance is obtained from Eq. 29, but with A_w replaced by A_o. This is again an approximation because the geometry of the oil film is different from that of a water AM.

5. Computation of macroscopic properties

In laminar flow of two immiscible fluids, the flow rate of fluid i (i = oil, water) between two connecting pore-bodies j and k is given by (see Fig. 5):

$$q_{i,jk} = \frac{g_{i,jk}}{l_{jk}}\left(p_{i,j} - p_{i,k}\right), \quad i = o, w \qquad [32]$$

where l_{jk} is the spacing between the pore-body centers and $g_{i,jk}$ [$m^4/Pa.s$] is the effective hydraulic conductance of phase i between the two pore-bodies. To calculate the absolute permeability and formation factor, the network is filled with a single fluid and index i disappears. We calculate the relative permeabilities of water and oil by performing two separate calculations at several level of capillary pressure (average wetting phase saturation). The first calculation is done for water, which spans the entire network, and the second one is restricted to the pore-bodies and pore-throats invaded by oil.

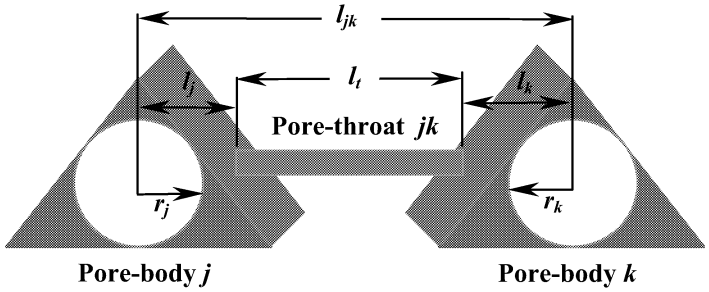

Fig. 5—Geometry of a unit-flow channel. The inscribed circles are the cross-sections of the largest spheres that can pass through each pore-body.

Flow resistances R_i add; therefore, the overall flow conductance is the harmonic mean of the conductances of the connecting pore-throats and its two

pore-bodies (only one-half of each pore-body resistance is allocated to the unit-flow channel):

$$R_{jk} = R_t + \frac{1}{2}R_j + \frac{1}{2}R_k \qquad [33]$$

and

$$\frac{l_{jk}}{g_{i,jk}} = \frac{l_t}{g_{i,t}} + \frac{1}{2}\left(\frac{l_j}{g_{i,j}} + \frac{l_k}{g_{i,k}}\right), \quad i = o, w \qquad [34]$$

In steady-state flow of incompressible immiscible fluids, mass conservation in each pore-body is imposed:

$$\sum_k q_{i,jk} = \frac{g_{i,jk}}{l_{jk}}\left(p_{i,j} - p_{i,k}\right) = 0, \quad i = o, w \qquad [35]$$

where k runs over all the pore-throats that are connected to pore-body j. The index j runs over all pore-bodies that do not belong to the inlet and outlet faces of the model, i.e., internal pore-bodies. Eqs. 34 and 35 together with appropriate initial and boundary conditions constitute a complete set of linear equations, which can be solved by a linear solver for the unknown pore-body pressures. To write the set of linear equations in a matrix form, the boundary pressures (constant) are moved to the right hand side of Eq. 35. The matrix equation may be written as [63]

$$\sum_k D_{jk} p_k = B_j \qquad [36]$$

where the indices j and k only run over the internal pore-bodies. D is a sparse matrix whose elements D_{jk} contain effective conductances (g's), p_k are the elements of the pore-body pressure vector (internal pore-bodies only) which are unknown and B_j contains the pressure at the boundaries. We are seeking solution of internal pore-body pressures at a given computation step, i.e.,

$$p_k = \sum_j \left(D^{-1}\right)_{jk} B_j \qquad [37]$$

The equation is solved by a Conjugate Gradient (CG) method of Hestenes and Stiefel as outlined by Batrouni and Hansen [63]. The algorithm is briefly described below:

We start by choosing some initial set of pressures p_j^o and calculate

$$v_j^o = r_j^o = B_j - \sum_k D_{jk} p_k^o \qquad [38]$$

If it turns out that $p_j^o = 0$ (for all j), the initial guess is in fact the correct solution. Otherwise, for m = 1, 2, 3 …, we compute

$$a^m = \frac{\sum_j r_j^m r_j^m}{\sum_j \sum_k v_j^m D_{jk} v_k^m} \qquad [39]$$

$$p_j^{m+1} = p_j^m + a^m v_j^m \qquad [40]$$

$$r_j^{m+1} = r_j^m - a^m \sum_k D_{jk} v_k^m \qquad [41]$$

$$b^m = \frac{\sum_j r_j^{m+1} r_j^{m+1}}{\sum_k r_k^m r_k^m} \qquad [42]$$

and

$$v_j^{m+1} = r_j^{m+1} + b^m v_j^m \qquad [43]$$

The natural error criterion is the norm of r_j^m. If ε is the desired accuracy, then we stop the iteration of Eqs. 39-43 when $\sum_k r_k^m r_k^m \le \varepsilon$. The theoretical maximum number of iterations necessary for this algorithm to converge is the square of the total number of internal pore-bodies.

The absolute permeability of the network is computed by imposing a constant pressure differential across the network ΔP (see Fig. 6) and letting the system relax by use of the CG method described above. From the pressure distribution, the total flow rate Q (through the inlet pore-throats) is calculated and, thus, the absolute permeability from Darcy's equation

$$k = \frac{\mu L Q}{A \Delta P} \qquad [44]$$

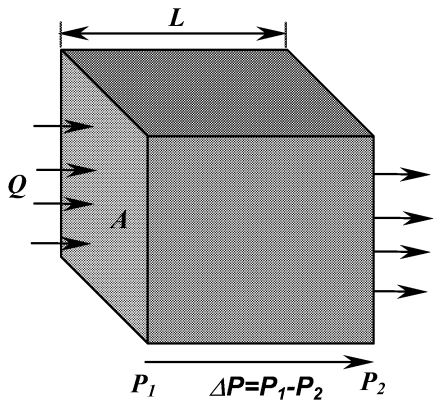

Fig. 6—3D model for flow simulation.

The relative permeabilities k_r are computed similarly. As stated previously, separate calculations are performed on water and oil at various stages of the displacement (average water saturation) and Darcy's law is applied for each of the phases:

$$k_{r,i}(S_w) = \frac{\mu_i \, L \, Q_i}{kA \, \Delta P_i} \qquad [45]$$

Because of the analogy between Poiseuille's law and Ohm's law, the flow of electric current can also be described by Eqs. 34 and 35 but with pressure replaced by voltage, Q by current I, ΔP by voltage difference ΔV and g by electric conductance g_e. The electrical conductance g_e is assumed to be dependant only on the pore geometry, i.e., pore walls are non-conductors and is given by

$$g_e = \sigma_w A \qquad [46]$$

where σ_w is the electrical conductivity of water which is known. The electrical conductivity σ of the pore network is computed by applying a constant voltage drop across the model and then applying Eqs. 34 and 35 to find the current flow between each of the connecting pore-bodies and hence the total current flow through the model. The formation factor is then calculated simply from

$$F = \frac{\sigma_w}{\sigma} \qquad [47]$$

Resistivity index I_r is also calculated at various stages of the displacement but, unlike for relative permeabilities, the calculation is performed only on

water because oil is a non-conductor. Contrary to the calculation of F, we only consider pore cross-sectional A_w which is occupied by water and, thus, $g_e = \sigma_w A_w$.

6. Implementation

The drainage part of the model has been implemented in Fortran 90 (see Appendix A for the codes). As stated previously, the descriptors of the network model are: (1) pore-body locations and their cross-sectional area, perimeter and length; (2) number of pore-bodies and their exact locations connected to each of the pore-bodies, and the cross-sectional area, perimeter and length of the connecting pore-throats; and (3) the pore-throats connected to the inlet and outlet faces of the sample. The displacing fluid is injected from an external reservoir through the throats connected to the inlet face while the displaced fluid escapes through the outlet face on the opposite side. The pore-body locations may be expressed by their *i*-, *j*- and *k*-indices or simply by designating them with numbers. In this study, the inlet fluid reservoir is designated with zero, a single number for each of the internal pore-bodies (ascending order from inlet to the outlet) and a number '*n+1*' for the outlet fluid reservoir where *n* is the total number of internal pore-bodies (see Fig. 7 for a 2D example). This numbering allows to use a *do loop* in Fortran to run over the pore-bodies. A second *do loop* is used to run over all pore-throats (1 to *z* where *z* is the coordination number) attached to each of the pore-bodies.

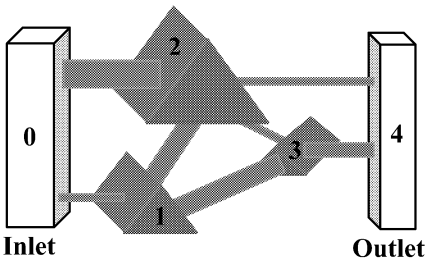

Fig. 7—A simple 2D network model showing the numbering convention.

7. Results and discussion

The drainage part of the flow model is tested on a regular cubic-lattice model of 3x3x3 pore-bodies (see Appendix B for input data). The pore cross-sectional areas and corresponding perimeter lengths are selected randomly which correspond to an equivalent cylindrical pore-body and pore-throat radii range from 0.5 - 1.0 μm and 0.2 - 0.4 μm, respectively and the geometric shape factor G ranges from 0.03 – 0.048. For L = 13.6 μm, A = 13.62 μm^2 and

ΔP = 2 μPa, we calculated absolute permeability k = 0.055 mD and formation factor F = 72.34. The capillary pressure, relative permeability and resistivity index curves are shown in Figs. 8 through 10. A value of 0.93 is calculated for the Archie's saturation exponent n from the I_r vs. S_w plot.

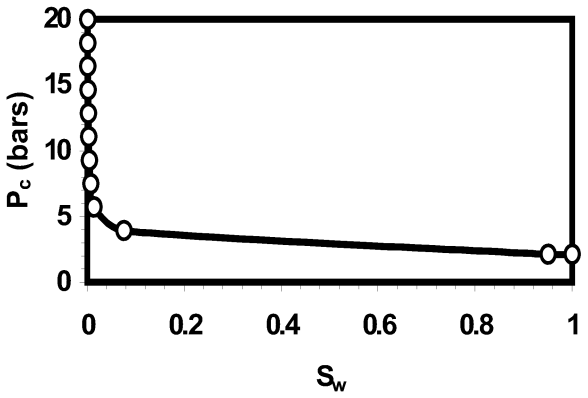

Fig. 8—Computed capillary pressure curve for a regular cubic-lattice model of 3x3x3 pore-bodies.

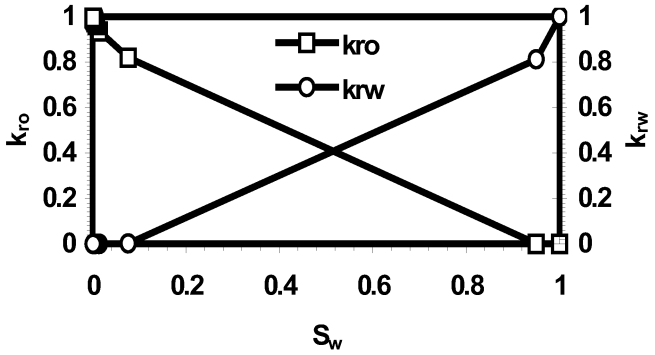

Fig. 9—Computed relative permeability curves for a regular cubic-lattice model of 3x3x3 pore-bodies.

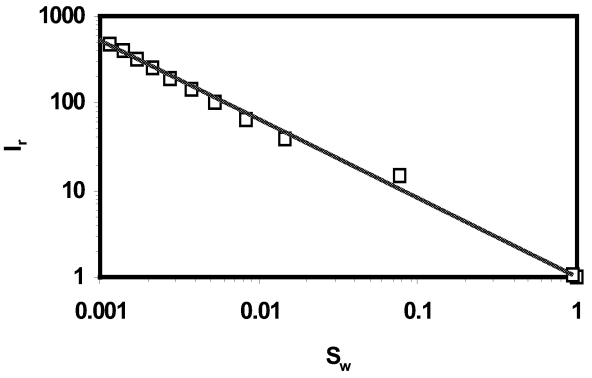

Fig. 6.6—Computed resistivity index curve for a regular cubic-lattice model of 3x3x3 pore-bodies.

As can be observed, the usual shapes of the capillary pressure, relative permeability and resistivity index curves are conceived even for this simple network model. Clearly, for the model to be predictive, the realistic variations of the chalk pores are to be included. It is important to note that the network modeling technique may be used to compute the above curves for the whole range of water saturations, specially, at very low water saturations. This is important in evaluating improved oil recovery processes but is usually not measurable by standard laboratory experiments.

8. Conclusions

A network model of drainage and imbibition has been developed for chalk in light of recent advances in this area. The model incorporates important pore-level displacement phenomena and uses realistic description of pore space geometry and topology. The drainage part of the model is tested for a regular cubic-lattice network of 3x3x3 pore-bodies. Results from this simple model demonstrate its applicability in computing absolute and relative permeabilities, capillary pressure, formation factor, resistivity index and Archie's saturation exponent. Further works are necessary to make this model predictive for Ekofisk Field through implementing the imbibition part of the model and providing realistic description of pore space geometry and topology which is accessible by characterization of the stochastically reconstructed 3D chalk samples.

9. Further works

- Future works will require implementation of the imbibition displacement processes, and characterization of the reconstructed 3D chalk samples to acquire pore space descriptors (described previously).
- Instead of using parametric models for wettability alteration and cooperative pore-body filling, improved models need to be developed.
- The approximate expressions for some of the hydraulic conductances (e.g., oil conductance in the oil films) are to be replaced by accurate expressions.

Acknowledgment

Saifullah Talukdar gratefully acknowledges the financial support from Phillips Petroleum Company Norway for his Ph.D. studies.

Nomenclature

A	*Cross-sectional area (pore, network model)*
A_o	*Cross-sectional area of a pore occupied by oil*
A_w	*Cross-sectional area of a pore occupied by water*
b	*Meniscus-apex distance along the wall*
F	*Formation factor*
g	*Hydraulic conductance*
G	*Geometric shape factor*
g_e	*Electric conductance*
I_r	*Resistivity index*
k	*Absolute permeability*
k_r	*Relative permeability*
l	*Length of a pore-body*
L	*Length of the network model*
l_t	*Length of a pore-throat*
N_c	*Capillary number*
P	*Perimeter length*
P_c	*Capillary pressure*
$P^e_{c,pt}$	*Capillary entry-pressure for piston-type imbibition*
$P^e_{c,pd}$	*Capillary entry-pressure for primary drainage*
$P^e_{c,so}$	*Capillary entry-pressure for snap-off imbibition*
$P_{c,max}$	*Maximum capillary pressure in primary drainage*
P_{thresh}	*Threshold capillary pressure for wettability alteration*
ΔP	*Pressure differential across the network model*
Q	*Fluid flow rate across the network model*
q	*Fluid flow rate through a pore*
r	*Inscribed circle radius*
r_{pd}	*Radius of curvature in primary drainage*
r_{pt}	*Radius of curvature in piston-type imbibition*
r_{so}	*Radius of curvature in snap-off imbibition*
S_w	*Water saturation*
σ	*Interfacial tension, electrical conductivity*

μ *Fluid viscosity*

θ_r *Receding contact angle*

θ_a *Advancing contact angle*

θ_h *Hinging contact angle*

β_i *Corner half-angles (i=1, 2, 3)*

References

1. Fatt, I.: "The Network Model of Porous Media I. Capillary Pressure Characteristics," *Trans. AIME* **207**, 144-159 (1956).
2. Fatt, I.: "The Network Model of Porous Media II. Dynamic Properties of a Single Size Tube Network," *Trans. AIME* **207**, 160-163 (1956).
3. Fatt, I.: "The Network Model of Porous Media III. Dynamic Properties of Networks with Tube Radius Distribution," *Trans. AIME* **207**, 164-181 (1956).
4. Lenormand, R., Zarcone, C. and Sarr, A.: "Mechanisms of the Displacement of One Fluid by Another in a Network of Capillary Ducts," *J. Fluid. Mech.* **135**, 337-353 (1983).
5. Lenormand, R. and Zarcone, C.: "Role of Roughness and Edges During Imbibition in Square Capillaries," SPE 13264, 59th Annual Tech. Conf. and Exhib., Houston, Texas, 16-19 September 1984.
6. Li, Y. and Wardlaw, N.C.: "The Influence of Wettability and Critical Pore-Throat Size Ratio on Snap-Off," *J. Colloid Interface Sci.* **109**(2), 461-472 (1986).
7. Chatzis, I., Kantzas, A. and Dullien, F.A.L.: "On the Investigation of Gravity-Assisted Inert Gas Injection Using Micromodels, Long Berea Sandstone Cores, and Computer-Assisted Tomography," SPE 18284, 63rd Annual Tech. Conf. and Exhib., Houston, TX, 2-5 October 1988.
8. Øren, P.E., Billiotte, J. and Pinczewski, W.V.: "Mobilization of Waterflood Residual Oil by Gas Injection for Water-Wet Conditions," *SPE Formation Evaluation* **7**, 70-78 (March 1992).
9. Soll, W.E., Celia, M.A. and Wilson, J.L.: "Micromodel Studies of Three-Fluid Porous Media Systems: Pore-Scale Processes Relating to Capillary Pressure-Saturation Relationships," *Water Resources Research* **29**(9), 2963-2974 (1993).
10. Øren, P.E. and Pinczewski, W.V.: "Effect of Wettability and Spreading on Recovery of Waterflood Residual Oil by Immiscible Gasflooding," *SPE Formation Evaluation* **9** (June 1994), 149-156.
11. Øren, P.E. and Pinczewski, W.V.: "Fluid Distribution and Pore-Scale Displacement Mechanisms in Drainage Dominated Three-Phase Flow," *Transport in Porous Media* **20**, 105-133 (1995).

12. Dong, M. Dullien, F.A.L. and Chatzis, I.: "Imbibition of Oil in Film Form Over Water Present in Edges of Capillaries with an Angular Cross-Section," *J. Colloid Interface Sci.* **172**, 278-288 (1995).
13. Keller, A.A., Blunt, M. J. and Roberts, P.V.: "Micromodel Observation of the Role of Oil Layers in Three-Phase Flow," *Transport in Porous Media* **26**(3), 277-297 (1997).
14. Jerauld, G.R. and Salter, S.J.: "The Effect of Pore Structure on Hysteresis in Relative Permeability and Capillary Pressure: Pore Level Modeling," *Transport in Porous Media* **5**, 103-151 (1990).
15. Dixit, A.B., McDougall, S.R. and Sorbie, K.S.: "A Pore-Level Investigation of Relative Permeability Hysteresis in Water-Wet Systems," *SPE Journal* (June 1998), 115-123.
16. McDougall, S.R. and Sorbie, K.S.: "The Impact of Wettability on Waterflooding: Pore-Scale Simulation," *SPE Reservoir Engineering* **10** (August 1995), 208-213.
17. Heiba, A.A., Davis, H.T. and Scriven, L.E.: "Effect of Wettability on Two-Phase Relative Permeabilities and Capillary Pressures," SPE 12172, 58th Annual Tech. Conf. and Exhib., San Francisco, CA, 5-8 October 1983.
18. Blunt, M.J.: "Effect of Heterogeneity and Wetting on Relative Permeability Using Pore Level Modeling," *SPE Journal* **2** (March 1997), 70-87.
19. Blunt, M.J.: "Pore Level Modeling of the Effects of Wettability," *SPE Journal* **2** (December 1997), 494-510.
20. Blunt, M.J.: "Physically-Based Network Modeling of Multiphase Flow in Intermediate-Wet Porous Media," *J. Petroleum Science and Engineering* **20**, 117-125 (1998).
21. Mohanty, K.K. and Salter, S.J.: "Multiphase Flow in Porous Media: III. Oil Mobilization, Transverse Dispersion, and Wettability," SPE 12127, 58th Annual Tech. Conf. and Exhib., San Francisco, CA, 5-8 October 1983.
22. Dixit, A.B., McDougall, S.R., Sorbie, K.S. and Buckley, J.S.: "Pore-Scale Modeling of Wettability Effects and Their Influence on Oil Recovery," *SPE Reservoir Evaluation and Engineering* **2** (February 1999), 25-36.
23. Man, H.N. and Jing, X.D.: "Pore Network Modeling of Electrical Resistivity and Capillary Pressure Characteristics," *Transport in Porous Media* **41**, 263-286 (2000).
24. Man, H.N. and Jing, X.D.: "Network Modeling of Mixed-Wettability on Electrical Resistivity, Capillary Pressure and Wettability Indices," Proc. 6th Int. Symp. on Evaluation of Reservoir Wettability and its Effect on Oil Recovery, Socorro, NM, 27-28 September 2000.
25. Hui, M.H. and Blunt, M.J.: "Pore-Scale Modeling of Three-Phase Flow and the Effects of Wettability," SPE 59309, SPE/DOE Improved Oil Recovery Symp., Tulsa, OK, 3-5 April 2000.

26. Dixit, A.B., Buckley, J.S., McDougall, S.R. and Sorbie, K.S.: "Empirical Measures of Wettability in Porous Media and the Relationship between Them Derived From Pore-Scale Modeling," *Transport in Porous Media* **40**, 27-54 (2000).
27. Laroche, C., Vizika, O., and Kalaydjian, F.: "Network Modeling to Predict the Effect of Wettability Heterogeneities on Multiphase Flow," SPE 56674, SPE Annual Tech. Conf. and Exhib., Houston, TX, Oct. 3-6, 1999.
28. Soll, W.E. and Celia, M.A.: "A Modified Percolation Approach to Simulating Three-Fluid Capillary Pressure-Saturation Relationships," *Advances in Water Resources* **16** (2), 107-126 (1993).
29. Øren, P.E., Billiotte, J. and Pinczewski, W.V.: "Pore-Scale Network Modeling of Waterflood Residual Oil Recovery by Immiscible Gas Flooding," SPE 27814, SPE/DOE 9th Symp. on Improved Oil Recovery, Tulsa, Oklahoma, 17-20 April 1994.
30. Øren, P.E. and Pinczewski, W.V.: "Fluid Distribution and Pore-Scale Displacement Mechanisms in Drainage Dominated Three-Phase Flow," *Transport in Porous Media* **20**, 105-133 (1995).
31. Fenwick, D.H. and Blunt, M.J.: "Network Modeling of Three-Phase Flow in Porous Media," *SPE Journal* **3**, 86-97 (1998).
32. Fenwick, D.H. and Blunt, M.J.: "Three-Dimensional Modeling of Three-Phase Imbibition and Drainage," *Advances in Water Resources* **25**(2), 121-143 (1998).
33. Pereira, G.G., Pinczewski, W.V., Chan, D.Y.C., Paterson, L. and Øren, P.E.: "Pore-Scale Network Model for Drainage-Dominated Three-Phase Flow in Porous Media," *Transport in Porous Media* **24**, 167-201 (1996).
34. Mani, V. and Mohanty, K.K.: "Effect of the Spreading Coefficient on Three-Phase Flow in Porous Media," *J. Colloid Interface Sci.* **187**, 45 (1997).
35. Mani, V. and Mohanty, K.K.: "Pore-Level Network Modeling of Three-Phase Capillary Pressure and Relative Permeability Curves," *SPE Journal* **3** (September 1998), 238-248.
36. Heiba, A.A., Davis, H.T. and Scriven, L.E.: "Statistical Network Theory of Three-Phase Relative Permeabilities," SPE 12690, SPE/DOE 4th Symp. on Enhanced Oil Recovery, Tulsa, OK, 15-18 April 1984.
37. Lerdahl, T.R. and Øren, P.E.: "A predictive network model for three-phase flow in porous media," SPE 59311, SPE/DOE Improved Oil Recovery Symposium, Tulsa, OK, 3-5 April 2000.
38. Van Dijke, M.I.J., McDougall, S.R. and Sorbie, K.S.: "Three-Phase Capillary Pressure and Relative Permeability Relationships in Mixed-Wet Systems," *Transport in Porous Media* **44**, 1-32 (2001).
39. Hughes, R.G. and Blunt, M.J.: "pore-Scale Modeling of Multiphase Flow in Fractures and Matrix/Fracture Transfer," SPE 56411, SPE Annual Tech. Conf. and Exhib., Houston, TX, 3-6 October 1999.
40. Poulsen, S., McDougall, S.R., Sorbie, K.S., and Skauge, A.: "Network Modeling of Internal and External Gas Drive," SCA 2001-17, Proc. Int.

Symp. of the Society of Core Analysts, Edinburgh, Scotland, 17-19 September 2001.
41. Bakke, S. and Øren, P.E.: "3-D Pore-Scale Modeling of Sandstones and Flow Simulations in the Pore Networks," *SPE Journal* **2**(June 1997), 136-149.
42. Nilsen, L.S., Øren, P.E., Bakke, S. and Henriquez, A.: "Prediction of Relative Permeability and Capillary Pressure From a Pore Model," paper SPE 35531 presented at the European 3-D Reservoir Modeling Conference, Stavanger, Norway, 16-17 April (1996).
43. Øren, P.E., Bakke, S. and Arntzen, O.J.: "Extending Predictive Capabilities to Network Models," *SPE Journal* (December 1998), 324-336.
44. Dullien, F.A.L: "Porous Media, Fluid Transport and Pore Structure," *Academic Press*, San Diego, California (1992).
45. Craig, F.R.: "The Reservoir Engineering Aspects of Waterflooding," *Society of Petroleum Engineers*, New York (1993).
46. Legens, C., Toulhoat, H., Cuiec, L., Villieras, F. and Palermo, T.: "Wettability Change Related to Adsorption of Organic Acids on Calcite: Experimental and *Ab Initio* Computational Studies," SPE *Journal* **4**(4), 328-333 (December 1999).
47. Salathiel, R.A.: "Oil Recovery by Surface Film Drainage in Mixed-Wettability Rocks," *JPT* **25**, 1216 (1973).
48. Kovscek, A.R., Wong, H. and Radke, C.J.: "A Pore-Level Scenario for the Development of Mixed Wettability in Oil Reservoirs," *AIChE Journal* **39**(6), 1072-1085 (1993).
49. Bekri, S., Xu, K., Yousefian, F., Adler, P.M., Thovert, J.-F., Muller, J., Iden, K., Psyllos, A., Stubos, A.K., and Ioannidis, M.A.: "Pore Geometry and Transport Properties in North Sea Chalk," *J. Pet. Sci. and Eng.* **25**, 107-134 (2000).
50. Xu, B., Kamath, J., Yortsos, Y.C. and Lee, S.H.: "Use of Pore Network Models to Simulate Laboratory Corefloods in a Heterogeneous Carbonate Sample," *SPE Journal* **4**(3), 179-186 (September 1999).
51. Patzek, T.W.: "Verification of a Complete Pore Network Simulator of Drainage and Imbibition," *SPE Journal* (June 2001), 144-156.
52. Zhou, D., Blunt, M. and Orr Jr., F.M.: "Hydrocarbon Drainage along Corners of Noncircular Capillaries," *J. Colloid and Interface Science* **187**, 11-21 (1997).
53. Adler, P.M., Jacquin, C.G. and Quiblier, J.A.: "Flow in Simulated Porous Media," *Int. J. of Multiphase Flow* **16**(4), 691-712 (1990).
54. Ferreol, B. and Rothman, D.H.: "Lattice-Boltzmann Simulations of Flow Through Fontainebleau Sandstone," *Transport in Porous Media* **22**, 53 (1996).
55. Liang, Z., Ioannidis, M.A. and Chatzis, I.: Geometric and Topological Analysis of Three-Dimensional Porous Media: Pore Space Partitioning

Based on Morphological Skeletonization. *J. of Colloid and Interface Science* **221**, 13 (2000).
56. Lindquist, W.B.: "3DMA: A Package for Geometric Analysis of 2- and 3D Biphase Images," http://www.ams.sunysb.edu/~lindquis/3dma/3dma.html for literature and ftp://ams.sunysb.edu/pub/lindquis/ for public domain software.
57. Mason, G. and Morrow, N.R.: "Capillary Behavior of a Perfectly Wetting Liquid in Irregular Triangular Tubes," *J. Colloid and Interface Science* **141**, 262 (1991).
58. Wilkinson, D. and Willemsen, J.F.: "Invasion Percolation: A New Form of Percolation Theory," *J. Physics A* **16**, 3365 (1983).
59. Mayer, R.P. and Stowe, R.A.: "Mercury Porosimetry-Breakthrough Pressure for Penetration Between Packed Spheres," *J. Colloid and Interface Science* **20**, 893 (1965).
60. Princen, H.M.: "Capillary Phenomena in Assemblies of Parallel Cylinders. I. Capillary Rise Between Two Cylinders," *J. Colloid and Interface Science* **30**, 60 (1969).
61. Princen, H.M.: "Capillary Phenomena in Assemblies of Parallel Cylinders. II. Capillary Rise in Systems With More Than Two Cylinders," *J. Colloid and Interface Science* **30**, 359 (1969).
62. Princen, H.M.: "Capillary Phenomena in Assemblies of Parallel Cylinders. III. Liquid Columns Between Horizontal Parallel Cylinders," *J. Colloid and Interface Science* **34**, 171 (1970).
63. Batrouni, G.G. and Hansen, A.: "Fourier Acceleration of Iterative Processes in Disordered Systems," *J. Statistical Physics* **52** (3/4), 747 (1988).

Appendix A

Fortran 90 codes for the drainage model.

```
!---------------------------------------------------------------------
!                  Program PoreSimDrain.f90
! A 3D network simulator for drainage process to calculates absolute
! and relative permeabilities, formation factor and resistivity index.
! The network model uses exact pore space topology and connectivity
! where the pore spaces (pore-body and pore-throat) are converted
! into equivalent triangular-shaped prisms with varying geometries.
!---------------------------------------------------------------------
!                       copyright:
! Saifullah Talukdar, Norwegian University of Science and Technology
! Email: talukdar@ipt.ntnu.no, talukdar66@hotmail.com
!---------------------------------------------------------------------

    program PoreSimDrain

    implicit none

!-----------------------------------------------------------------
!          Parameter declaration
!-----------------------------------------------------------------
! nt: number of internal nodes in the model (excluding inlet and
!     outlet reservoirs)
! sigmaow: oil-water interfacial tension [N/m]
! pi: value of pie
! pcmax: maximum capillary pressure to be reached [Pa]
! pinlet: inlet pressure [microPa] for calculation of k
! poutlet: outlet pressure [microPa] for calculation of k
! pwinlet: inlet water-phase pressure [microPa] for calculation of krw
! pwoutlet: outlet water-phase pressure [microPa] for calculation of krw
! poinlet: inlet oil-phase pressure [microPa] for calculation of kro
! pooutlet: outlet oil-phase pressure [microPa] for calculation of kro
! voltinlet: inlet voltage [microVolt] for calculation of F
! voltoutlet: outlet voltage [microVolt] for calculation of F
! voltinletn: inlet voltage [microVolt] for calculation of RI
! voltoutletn: outlet voltage [microVolt] for calculation of RI
! cw: conductivity of water [1/(ohm-m)]
! eps: accuracy in the conjugate gradient method
! viscw: viscosity of water [Pa.s]
! visco: viscosity of oil [Pa.s]
! mlength: model length (micron)
! marea: model area (micron^2)

    integer nt
    parameter(nt=27)
    real*8 sigmaow
    parameter(sigmaow=24.034e-03)
    real*8 pi
    parameter (pi=3.141592654)
    real*8 pcmax
    parameter(pcmax=20.e+5)
    real*8 pinlet,poutlet
    parameter(pinlet=2.e+0,poutlet=0.e+0)
    real*8 pwinlet,pwoutlet
    parameter(pwinlet=2.e+0,pwoutlet=0.e+0)
    real*8 poinlet,pooutlet
    parameter(poinlet=2.e+0,pooutlet=0.e+0)
    real*8 voltinlet,voltoutlet
    parameter(voltinlet=2.e+0,voltoutlet=0.e+0)
    real*8 voltinletn,voltoutletn
    parameter(voltinletn=2.e+0,voltoutletn=0.e+0)
    real*8 cw
    parameter(cw=5.88e+0)
    real*8 epsk,epsf,epsri
    parameter(epsk=1.e-10,epsf=1.e-10,epsri=1.e-10)
```

```
    real*8 epskrw,epskro
    parameter(epskrw=1.e-15,epskro=1.e-15)
    real*8 viscw,visco
    parameter(viscw=1.05e+03,visco=0.9e+03)
    real*8 mlength,marea
    parameter(mlength=13.6,marea=13.6**2)

!-----------------------------------------------------------------
!          Array declaration
!-----------------------------------------------------------------
! iz(i): coordination number of node i
! nii: node invasion index (1 invaded by oil, 0 not invaded by oil)
! nn(i,j): node numbers (j=1,iz) connected to node i
! rn(i): inscribed radius of node i
! ln(i): length of node i
! gfn(i): geometric shape factor of node i (G=A/P^2)
! an(i,j): cross-sectional area of node i
! vn(i): volume of node i
! perin(i): perimeter of node i
! thetarn(i): contact angle of node i
! hangn(i,k): corner half-angles (k=1,2,3) of node i
! pn(i): water-phase pressure in node i for calculation of k
! pwn(i): water-phase pressure in node i for calculation of krw
! pon(i): oil-phase pressure in node i for calculation of kro
! voltn(i): voltage in node i (for calculation of F)
! voltnn(i): voltage in node i (for calculation of RI)
! hcwn(i): hyhraulic conductance of water in node i
! hcon(i): hyhraulic conductance of oil in node i
! ecn(i): electric conductance of node i

    integer,dimension(:),allocatable::iz,nii
    integer,dimension(:,:),allocatable::nn
    real*8,dimension(:),allocatable::rn,ln,gfn,an,vn,perin
    real*8,dimension(:),allocatable::thetarn
    real*8,dimension(:,:),allocatable::hangn
    real*8,dimension(:),allocatable::pn
    real*8,dimension(:),allocatable::pwn
    real*8,dimension(:),allocatable::pon
    real*8,dimension(:),allocatable::voltn
    real*8,dimension(:),allocatable::voltnn
    real*8,dimension(:),allocatable::hcwn
    real*8,dimension(:),allocatable::hcon
    real*8,dimension(:),allocatable::ecn

! rl(i,j): inscribed radius of link connecting nodes i and j
! ll(i,j): length of link connecting nodes i and j
! gfl(i,j): geometric shape factor of link connecting nodes i and j
! al(i,j): cross-sectional area of link connecting nodes i and j
! vl(i,j): volume of link connecting nodes i and j
! peril(i,j): perimeter of link connecting nodes i and j
! thetarl(i,j): contact angle of link connecting nodes i and j
! hangl(i,j,k): corner half-angles (k=1,2,3) of link between nodes i and j
! lai: link accessibility index (1 accessible, 0 not accessible for oil)
! lii: link invasion index (1 invaded by oil, 0 not invaded by oil)
! hcwl(i,j): hyhraulic conductance of water in link connecting nodes i and j
! hcol(i,j): hyhraulic conductance of oil in link connecting nodes i and j
! ecl(i,j): electric conductance of the link connecting nodes i and j

    real*8,dimension(:,:),allocatable::rl,ll,gfl,al,vl,peril
    real*8,dimension(:,:),allocatable::thetarl
    real*8,dimension(:,:,:),allocatable::hangl
    real*8,dimension(:,:),allocatable::hcwl
    real*8,dimension(:,:),allocatable::hcol
    real*8,dimension(:,:),allocatable::ecl
    integer,dimension(:,:),allocatable::lai,lii
```

```
!-------------------------------------------------------------------
!          Other variables
!-------------------------------------------------------------------
! vnt: total node volume
! vlt: total link volume
! vmt: total model volume
! rw: radius of curvature of the arc meniscii
! pc: capillary pressure
! pcentry: capillary entry-pressure
! beta(1,2,3): corner half-angles of a triangle
! vom: volume of oil in the model
! swavg: average water saturation in the model
! qw: flow rate of water
! qo: flow rate of oil
! absperm: absolute permeability
! ef: electricity flow rate [Amp]
! formfact: formation factor
! cmfw: conductivity of the model when 100% saturated with water
! cm: conductivity of the model when partially saturated with water
! awn: water area of partially saturated node
! awl: water area of partially saturated link
! hcwn: hydraulic conductance of water in node
! hcwl: hydraulic conductance of water in link
! ri: resistivity index
! kwd: effective permeability of water in drainage process
! krwd: relative permeability of water in drainage process
! kod: effective permeability of oil in drainage process
! krod: relative permeability of oil in drainage process

    integer i,j,k,it
    real*8 ant,vnt,alt,vlt,amt,vmt
    real*8 rw,pc,pcentry
    real*8 beta1,beta2,beta3
    real*8 vom,swavg
    real*8 pclmin,pcedl,pcstep,pcalmax
    integer ialmax,jalmax
    integer idum3
    real*8 almax
    logical ans
    real*8 qw,qo,absperm
    real*8 ef,formfact,cmfw,cm
    real*8 awn,awl,hcwns,hcwls
    real*8 ri
    real*8 kwd,krwd,kod,krod
    real*8 ran3

!-------------------------------------------------------------------
!   Allocate memory spaces for node variables
!-------------------------------------------------------------------

    allocate(iz(0:nt+1),nii(0:nt+1))
    allocate(nn(0:nt+1,0:nt+1))
    allocate(rn(0:nt+1),ln(0:nt+1),gfn(0:nt+1),an(0:nt+1))
    allocate(vn(0:nt+1),perin(0:nt+1))
    allocate(thetarn(0:nt+1))
    allocate(hangn(0:nt+1,3))
    allocate(pn(0:nt+1))
    allocate(pwn(0:nt+1))
    allocate(pon(0:nt+1))
    allocate(voltn(0:nt+1))
    allocate(voltnn(0:nt+1))
    allocate(hcwn(0:nt+1))
    allocate(hcon(0:nt+1))
    allocate(ecn(0:nt+1))
```

```
!-----------------------------------------------------------------
!   Allocate memory space for link variables
!-----------------------------------------------------------------

    allocate(rl(0:nt+1,0:nt+1),ll(0:nt+1,0:nt+1),gfl(0:nt+1,0:nt+1))
    allocate(al(0:nt+1,0:nt+1),vl(0:nt+1,0:nt+1),peril(0:nt+1,0:nt+1))
    allocate(thetarl(0:nt+1,0:nt+1),hangl(0:nt+1,0:nt+1,3))
    allocate(lai(0:nt+1,0:nt+1),lii(0:nt+1,0:nt+1))
    allocate(lwai(0:nt+1,0:nt+1))
    allocate(lwii(0:nt+1,0:nt+1))
    allocate(hcwl(0:nt+1,0:nt+1))
    allocate(hcol(0:nt+1,0:nt+1))
    allocate(ecl(0:nt+1,0:nt+1))

!-----------------------------------------------------------------
!   Open input files
!-----------------------------------------------------------------

    open(unit=1,file='nodeinput_cubic.dat',status='old')
    open(unit=2,file='neighborinput_cubic.dat',status='old')
    open(unit=3,file='linkinput_cubic.dat',status='old')

!-----------------------------------------------------------------
!   Open output files
!-----------------------------------------------------------------

    open(unit=13, file='output.out', status='unknown')

!-----------------------------------------------------------------
!   Randon seed for random number generator
!-----------------------------------------------------------------

    idum3=-1

!-----------------------------------------------------------------
!   Read input data for the model nodes
!-----------------------------------------------------------------
! Read:
! iz: coordination numbers
! an: average cross-sectional area
! pn: corresponding perimeter length
! ln: length

    read(1,*)
    read(1,*)
    do i=0,nt
        read(1,*) iz(i),an(i),perin(i),ln(i)
    end do

!-----------------------------------------------------------------
!   Calculate parameters for the model nodes
!-----------------------------------------------------------------
! Calculate:
! gfn: geometric shape factor
! rn: inscribed radius
! vn: volume
! hangn: corner half-angles of the nodes
! vnt: total node volume
    vnt=0.e0
    do i=1,nt
        gfn(i)=an(i)/perin(i)**2
        rn(i)=2.e0*perin(i)*gfn(i)
        vn(i)=an(i)*ln(i)
        vnt=vnt+vn(i)
        call halfangles(gfn(i),beta1,beta2,beta3)
            hangn(i,1)=beta1
            hangn(i,2)=beta2
            hangn(i,3)=beta3
    end do
```

```
!-------------------------------------------------------------------
!   Read input data for the model links
!   Calculate parameters for the model links
!-------------------------------------------------------------------

! Read:
! nn(i,j): node numbers (j=1,iz) connected to node i
! al(i,j): average cross-sectional area of link connecting node i and j
! peril(i,j): corresponding perimeter
! ll(i,j): length of link connecting node i and j

    read(2,*)
    do i=0,nt
      read(2,*)
       do j=1,iz(i)
           read(2,*) nn(i,j)
       end do
    end do

    read(3,*)
    read(3,*)
    do i=0,nt
      read(3,*)
       do j=1,iz(i)
           read(3,*) al(i,nn(i,j)),peril(i,nn(i,j)),ll(i,nn(i,j))
       end do
    end do

!-------------------------------------------------------------------
!   Calculate parameters for the model links
!-------------------------------------------------------------------
! Calculate:
! gfl: geometric shape factor
! rl: inscribed radius
! vl: volume
! hangl: corner half-angles of the links
! vlt: total link volume

    vlt=0.e0
    do i=0,nt
        do j=1,iz(i)
            gfl(i,nn(i,j))=al(i,nn(i,j))/peril(i,nn(i,j))**2
            rl(i,nn(i,j))=2.e0*peril(i,nn(i,j))*gfl(i,nn(i,j))
            vl(i,nn(i,j))=al(i,nn(i,j))*ll(i,nn(i,j))
            vlt=vlt+vl(i,nn(i,j))
            call halfangles(gfl(i,nn(i,j)),beta1,beta2,beta3)
                hangl(i,nn(i,j),1)=beta1
                hangl(i,nn(i,j),2)=beta2
                hangl(i,nn(i,j),3)=beta3
        end do
    end do

! Deduct the links that have been counted twice:

    do i=1,nt
        do j=1,iz(i)
            if(nn(i,j).lt.i) then
                vlt=vlt-vl(i,nn(i,j))
            end if
        end do
    end do

! Calculate total model volume:

    vmt=vnt+vlt
```

```
!---------------------------------------------------------------------
!   Initialize nodes and links with zero receding contact angle
!---------------------------------------------------------------------

    do i=1,nt
        thetarn(i)=0.e0
    end do

    do i=0,nt
        do j=1,iz(i)
            thetarl(i,nn(i,j))=0.e0
        end do
    end do

!---------------------------------------------------------------------
!              Calculate absolute permeability
!---------------------------------------------------------------------

! Initialize the model with random nodal pressures (between inlet
! and outlet pressures):

    pn(0)=pinlet
    pn(nt+1)=poutlet

    do i=1,nt
        pn(i)=poutlet+(pinlet-poutlet)*ran3(idum3)
    end do

! Make sure that connected nodes do not have same pressure:

    do i=1,nt
        do j=1,iz(i)
            if (pn(i).eq.pn(nn(i,j))) then
                if (nn(i,j).ne.0.and.nn(i,j).ne.nt+1) then
                    pn(nn(i,j))=1.01*pn(nn(i,j))
                end if
            end if
        end do
    end do

! Calculate hydraulic conductances of the nodes and links:

    ln(0)=0.e0
    ln(nt+1)=0.e0
    hcwn(0)=1.0e+20
    hcwn(nt+1)=1.0e+20

    do i=1,nt
        hcwn(i)=3.e0*rn(i)**2*an(i)/(20.e0*viscw)
    end do

    do i=0,nt
        do j=1,iz(i)
            hcwl(i,nn(i,j))=3.e0*rl(i,nn(i,j))**2*al(i,nn(i,j))/(20.e0*viscw)
        end do
    end do

    do i=0,nt
        do j=1,iz(i)
            hcwl(i,nn(i,j))=1.e0/(ll(i,nn(i,j))/hcwl(i,nn(i,j))+ &
                                  0.5e0*(ln(i)/hcwn(i)+ln(nn(i,j))    &
                                  /hcwn(nn(i,j))))
        end do
    end do

! Calculate absperm:

    call ConjGrad(pn,nt,iz,nn,hcwl,epsk,it)
```

```
    qw=0.e0
        i=0
            do j=1,iz(i)
                qw=qw+hcwl(i,nn(i,j))*(pn(i)-pn(nn(i,j)))
            end do

    absperm=qw*viscw*mlength/(marea*(pinlet-poutlet))
    absperm=absperm*1.e-12*1000.e0/(9.86923*1.e-13)

    write(13,*)'Absolute Permeability [mD]= ',absperm

!-------------------------------------------------------------------
!              Calculate formation factor
!-------------------------------------------------------------------

! Initialize the model with random nodal voltages (between inlet
! and outlet voltages):

    voltn(0)=voltinlet
    voltn(nt+1)=voltoutlet

    do i=1,nt
        voltn(i)=voltoutlet+(voltinlet-voltoutlet)*ran3(idum3)
    end do

! Make sure that connected nodes do not have same voltage:

    do i=1,nt
        do j=1,iz(i)
            if (voltn(i).eq.voltn(nn(i,j))) then
                if (nn(i,j).ne.0.and.nn(i,j).ne.nt+1) then
                    voltn(nn(i,j))=1.01*voltn(nn(i,j))
                end if
            end if
        end do
    end do

! Calculate electric conductances of the nodes and links:

    ecn(0)=1.0e+20
    ecn(nt+1)=1.0e+20

    do i=1,nt
        ecn(i)=cw*an(i)
    end do

    do i=0,nt
        do j=1,iz(i)
            ecl(i,nn(i,j))=cw*al(i,nn(i,j))
        end do
    end do

    do i=0,nt
        do j=1,iz(i)
            ecl(i,nn(i,j))=1.e0/(ll(i,nn(i,j))/ecl(i,nn(i,j))+   &
                                 0.5e0*(ln(i)/ecn(i)+ln(nn(i,j)) &
                                 /ecn(nn(i,j))))
        end do
    end do

! Calculate formfact:

    call ConjGrad(voltn,nt,iz,nn,ecl,epsf,it)

    ef=0.e0
        i=0
            do j=1,iz(i)
                ef=ef+ecl(i,nn(i,j))*(voltn(i)-voltn(nn(i,j)))
            end do
```

```
    cmfw=ef*mlength/(marea*(voltinlet-voltoutlet))

    formfact=cw/cmfw

    write(13,*)'Formation Factor= ',formfact

!-------------------------------------------------------------------
! Simulate drainage displacement by increasing Pc in steps and calculate
! resistivity index and relative permeabilities
!-------------------------------------------------------------------

! Initialize nodes and links with 0 invasion index:
! nii(i): node invasion index (1 invaded, 0 not-invaded by oil)
! lii(i,j): link invasion index (1 invaded, 0 not-invaded by oil)

    do i=1,nt
        nii(i)=0
    end do

    do i=0,nt
        do j=1,iz(i)
            lii(i,nn(i,j))=0
        end do
    end do

! Initialize links with invading fluid accessibility index:
! lai(i,j): link accecibility index (1 accessible, 0 non-accessible)
! A link is accessible to oil if it is adjacent to an oil-filled node
! nn(i,j): node numbers (j=1,iz) connected to node i

    do i=0,0
        do j=1,iz(i)
            lai(i,nn(i,j))=1
        end do
    end do

    do i=1,nt
        do j=1,iz(i)
            lai(i,nn(i,j))=0
        end do
    end do

! Calculate minimum capilary pressure increment, which corresponds to
! the entry capillary pressure for the biggest link present in the model:

    almax=0.e0
    do i=1,nt
        do j=1,iz(i)
            if(al(i,nn(i,j)).gt.almax) then
                almax=al(i,nn(i,j))
                    ialmax=i
                    jalmax=nn(i,j)
            end if
        end do
    end do

    call PcEntryD(gfl(ialmax,jalmax),thetarl(ialmax,jalmax),&
         rl(ialmax,jalmax),sigmaow,hangl(ialmax,jalmax,1),       &
         hangl(ialmax,jalmax,2),hangl(ialmax,jalmax,3),pcalmax)
    pcstep=pcalmax

! Find entry capillary pressure for the model, which corresponds to the
! minimum entry pressure for the links connected to the inlet boundary:

    pclmin=1.e+20
    do i=0,0
        do j=1,iz(i)
            call PcEntryD(gfl(i,nn(i,j)),thetarl(i,nn(i,j)), &
```

```
                    rl(i,nn(i,j)),sigmaow,hangl(i,nn(i,j),1),&
                    hangl(i,nn(i,j),2),hangl(i,nn(i,j),3),pcedl)
            pclmin=min(pclmin,pcedl)
        end do
    end do
    pcentry=pclmin

! Report entry capillary pressure, and initial resistivity index and
! relative permeabilities:
    swavg=1.e0
    ri=1.e0
    krwd=1.e0
    krod=0.e0
    write(13,104) swavg,pcentry*1.e-05,ri,krwd,krod

! Initialize the model with random nodal pressures for water and
! oil phases between inlet and outlet pressures and voltages
! between inlet and outlet voltages:

! Voltages:

    voltnn(0)=voltinletn
    voltnn(nt+1)=voltoutletn

    do i=1,nt
        voltnn(i)=voltoutletn+(voltinletn-voltoutletn)*ran3(idum3)
    end do

! Make sure that connected nodes do not have same voltage:

    do i=1,nt
        do j=1,iz(i)
            if (voltnn(i).eq.voltnn(nn(i,j))) then
                if (nn(i,j).ne.0.and.nn(i,j).ne.nt+1) then
                    voltnn(nn(i,j))=1.01*voltnn(nn(i,j))
                end if
            end if
        end do
    end do

! Water pressures:

    pwn(0)=pwinlet
    pwn(nt+1)=pwoutlet

    do i=1,nt
        pwn(i)=pwoutlet+(pwinlet-pwoutlet)*ran3(idum3)
    end do

! Make sure that connected nodes do not have same water pressure:

    do i=1,nt
        do j=1,iz(i)
            if (pwn(i).eq.pwn(nn(i,j))) then
                if (nn(i,j).ne.0.and.nn(i,j).ne.nt+1) then
                    pwn(nn(i,j))=1.01*pwn(nn(i,j))
                end if
            end if
        end do
    end do

! Oil pressures:

    pon(0)=poinlet
    pon(nt+1)=pooutlet

    do i=1,nt
        if(nii(i).eq.1) then
            pon(i)=1.01*pooutlet+(poinlet-pooutlet)*ran3(idum3)
```

```
        else
            pon(i)=pooutlet
        end if
    end do

! Make sure that connected nodes (invaded) do not have same oil pressure:

    do i=1,nt
        do j=1,iz(i)
            if (pon(i).eq.pon(nn(i,j))) then
                if(nii(i).eq.1.and.nii(nn(i,j)).eq.1) then
                    if (nn(i,j).ne.0.and.nn(i,j).ne.nt+1) then
                        pon(nn(i,j))=1.01*pon(nn(i,j))
                    end if
                end if
            end if
        end do
    end do

    hcon(0)=1.0e+20
    hcon(nt+1)=1.0e+20

! Start simulation. Increase Pc in steps until PcMax is reached. Report
! average water saturation and corresponding Pc, RI, krwd and krod:

    do pc=pcentry+1.e-01,pcmax,pcstep
        do i=0,nt
            do j=1,iz(i)
                if(lai(i,nn(i,j)).eq.1.and.lii(i,nn(i,j)).ne.1) then
                    call PcEntryD(gfl(i,nn(i,j)),thetarl(i,nn(i,j)), &
                            rl(i,nn(i,j)),sigmaow,hangl(i,nn(i,j),1), &
                            hangl(i,nn(i,j),2),hangl(i,nn(i,j),3),pcedl)
                    if(pc.gt.pcedl) then
                        lii(i,nn(i,j))=1
                        lii(nn(i,j),i)=1
                        if(nii(nn(i,j)).ne.1) then
                            nii(nn(i,j))=1
                            do k=1,iz(nn(i,j))
                                if(lii(nn(i,j),nn(nn(i,j),k)).ne.1) then
                                    lai(nn(i,j),nn(nn(i,j),k))=1
                                end if
                            end do
                        end if
                    end if
                end if
            end do
        end do

        rw=(sigmaow/pc)*1.e+6
        call VolumeOil(rw,thetarn,thetarl,hangn,hangl,an,    &
                        al,ln,ll,nt,iz,nii,lii,nn,vom)
        swavg=(vmt-vom)/vmt

! Calculate resistivity index:

    do i=1,nt
        if(nii(i).eq.1) then
            call AreawD(rw,thetarn(i),hangn(i,1),hangn(i,2),hangn(i,3),awn)
                ecn(i)=cw*awn
        else
                ecn(i)=cw*an(i)
        end if
    end do

    do i=0,nt
        do j=1,iz(i)
            if(lii(i,nn(i,j)).eq.1) then
                call AreawD(rw,thetarl(i,nn(i,j)),hangl(i,nn(i,j),1),    &
                            hangl(i,nn(i,j),2),hangl(i,nn(i,j),3),awl)
```

```
                ecl(i,nn(i,j))=cw*awl
            else
                ecl(i,nn(i,j))=cw*al(i,nn(i,j))
            end if
        end do
    end do

    do i=0,nt
        do j=1,iz(i)
            ecl(i,nn(i,j))=1.e0/(ll(i,nn(i,j))/ecl(i,nn(i,j))+      &
                                 0.5e0*(ln(i)/ecn(i)+ln(nn(i,j)) &
                                 /ecn(nn(i,j))))
        end do
    end do

    call ConjGrad(voltnn,nt,iz,nn,ecl,epsri,it)

    ef=0.e0
        i=0
            do j=1,iz(i)
                ef=ef+ecl(i,nn(i,j))*(voltnn(i)-voltnn(nn(i,j)))
            end do

    cm=ef*mlength/(marea*(voltinletn-voltoutletn))

    ri=cmfw/cm

! Calculate relative permeability of water:

    do i=1,nt
        if(nii(i).eq.1) then
            call hcwd(rw,thetarn(i),hangn(i,1),hangn(i,2),hangn(i,3),   &
                      viscw,hcwns)
                hcwn(i)=hcwns
        else
                hcwn(i)=3.e0*rn(i)**2*an(i)/(20.e0*viscw)
        end if
    end do

    do i=0,nt
        do j=1,iz(i)
            if(lii(i,nn(i,j)).eq.1) then
                call hcwd(rw,thetarl(i,nn(i,j)),hangl(i,nn(i,j),1),  &
                          hangl(i,nn(i,j),2),hangl(i,nn(i,j),3),viscw,hcwls)
                    hcwl(i,nn(i,j))=hcwls
            else
                    hcwl(i,nn(i,j))=3.e0*rl(i,nn(i,j))**2*al(i,nn(i,j))/   &
                       (20.e0*viscw)
            end if
        end do
    end do

    do i=0,nt
        do j=1,iz(i)
            hcwl(i,nn(i,j))=1.e0/(ll(i,nn(i,j))/hcwl(i,nn(i,j))+ &
                                 0.5e0*(ln(i)/hcwn(i)+ln(nn(i,j))    &
                                 /hcwn(nn(i,j))))
        end do
    end do

    call ConjGrad(pwn,nt,iz,nn,hcwl,epskrw,it)

    qw=0.e0
        i=0
            do j=1,iz(i)
                qw=qw+hcwl(i,nn(i,j))*(pwn(i)-pwn(nn(i,j)))
            end do

    kwd=qw*viscw*mlength/(marea*(pwinlet-pwoutlet))
```

```
    kwd=kwd*1.e-12*1000.e0/(9.86923*1.e-13)

    krwd=kwd/absperm

! Calculate relative permeability of oil:

    do i=1,nt
        if(nii(i).eq.1) then
            call AreawD(rw,thetarn(i),hangn(i,1),hangn(i,2),hangn(i,3),awn)
                hcon(i)=3.e0*rn(i)**2*(an(i)-awn)/(20.e0*visco)
        else
                hcon(i)=0.e0
        end if
    end do

    do i=0,nt
        do j=1,iz(i)
            if(lii(i,nn(i,j)).eq.1) then
                call AreawD(rw,thetarl(i,nn(i,j)),hangl(i,nn(i,j),1),    &
                           hangl(i,nn(i,j),2),hangl(i,nn(i,j),3),awl)
                   hcol(i,nn(i,j))=3.e0*rl(i,nn(i,j))**2*                &
                      (al(i,nn(i,j))-awl)/(20.e0*visco)
            else
                   hcol(i,nn(i,j))=0.e0
            end if
        end do
    end do

    do i=0,nt
        do j=1,iz(i)
            if(lii(i,nn(i,j)).eq.1) then
                hcol(i,nn(i,j))=1.e0/(ll(i,nn(i,j))/hcol(i,nn(i,j))+ &
                                0.5e0*(ln(i)/hcon(i)+ln(nn(i,j))       &
                                /hcon(nn(i,j))))
            else
                hcol(i,nn(i,j))=0.e0
            end if
        end do
    end do

    call ConjGradO(pon,nt,iz,nn,nii,hcol,epskro,it)

    qo=0.e0
        i=0
            do j=1,iz(i)
                qo=qo+hcol(i,nn(i,j))*(pon(i)-pon(nn(i,j)))
            end do

    kod=qo*visco*mlength/(marea*(poinlet-pooutlet))
    kod=kod*1.e-12*1000.e0/(9.86923*1.e-13)

    krod=kod/absperm

    write(13,104) swavg,pc*1.e-05,ri,krwd,krod

! End of drainage process
    end do

    stop
104 format(f20.15,5x,f16.7,5x,e12.5,5x,e12.5,5x,e12.5)
    close(1)
    close(2)
    close(3)
    close(13)
    end program PoreSimDrain
```

```
! ========================================================================
!              Subroutine halfangles
! Calculates corner half angles of a triangle in radian
! ========================================================================
! Given: shape factor g=a/p^2 (a=cross-sectional area, p=perimeter)
! Output: three half angles of a triangle (beta1,beta2 and beta3)
! beta1<45 deg (pi/4 rad) and beta2<45 deg are the two corner half
! angles subtended at the longest side of the triangle (its base)
! (beta1<beta2<beta3).

    subroutine halfangles(gsf,beta1,beta2,beta3)

    implicit none

    real*8 pi
    parameter (pi=3.141592654)
    integer idum3
    real*8 beta2min,beta2max
    real*8 gsf,ran3
    real*8 beta1,beta2,beta3
    idum3=-1
    beta2min=datan((2.e0/sqrt(3.e0))*cos(dacos(-12.e0*   &
                sqrt(3.e0)*gsf)/3.e0+4.e0*pi/3.e0))
    beta2max=datan((2.e0/sqrt(3.e0))*cos(dacos(-12.e0*   &
                sqrt(3.e0)*gsf)/3.e0))
    beta2=beta2min+(beta2max-beta2min)*ran3(idum3)
    beta1=-0.5e0*beta2+0.5e0*dasin((tan(beta2)+4.e0*gsf)*    &
                sin(beta2)/(tan(beta2)-4.e0*gsf))
    beta3=pi/2-beta1-beta2
    return
    end subroutine halfangles

! ========================================================================
!              Function for random number generation
! ========================================================================
! ran3 returns a uniform random deviate between 0.0 and 1.0. Set
! idum3 to any negative value to initialize or reinitialize the
! sequence.

      function ran3(idum3)
      implicit none
      integer idum3
      integer mbig,mseed,mz
      real*8 ran3,fac
      parameter (mbig=1000000000,mseed=161803398,mz=0,fac=1.0/mbig)

! Any large mbig, and any smaller (but still large) mseed can
! be substituted for the above values.

      integer i,iff,ii,inext,inextp,k
      integer mj,mk,ma(55)

! The value 55 is special and should not be modified.

      save iff,inext,inextp,ma
      data iff /0/

! Initialization. Initialize ma(55) using the seed idum3 and
! the large number mseed.

      IF (idum3 .lt. 0 .or. iff .eq. 0) THEN
         iff=1
         mj=mseed-iabs(idum3)
         mj=mod(mj,mbig)
         ma(55)=mj
         mk=1

! Now initialize the rest of the table, in a slightly random
! order, with numbers that are not especially random.
```

```
         do 11 i=1,54
            ii=mod(21*i,55)
            ma(ii)=mk
            mk=mj-mk
            if (mk .lt. mz) mk=mk+mbig
            mj=ma(ii)
 11      continue

         do 13 k=1,4
            do 12 i=1,55
               ma(i)=ma(i)-ma(1+mod(i+30,55))
               if (ma(i) .lt. mz) ma(i)=ma(i)+mbig
 12         continue
 13      continue

! Prepare indices for our first generated number.
! The constant 31 is special.

         inext=0
         inextp=31
         idum3=1

      end if

! Here is where we start, except on initialization.
! Increment inext, wrapping around 56 to 1.

      inext=inext+1
      if (inext .eq. 56) inext=1
      inextp=inextp+1
      if (inextp .eq. 56) inextp=1

! Now generate a new random number subtractively. Be sure
! it is in range. Store it and output the derived uniform derivate.

      mj=ma(inext)-ma(inextp)
      if (mj .lt. mz) mj=mj+mbig
      ma(inext)=mj
      ran3=mj*fac

      return
      end function ran3

! ========================================================================
!   Subroutine to calculate drainage entry capillary pressure
! ========================================================================
! pced: drainage capillary entry pressure
! gsf: geometric shape factor
! thetar: receding contact angle
! r: inscribed circle radius
! sigmaow: oil-water interfacial tension
! beta(1,2,3): corner half-angles
! r in [micron]
! sigmaow in [N/m]
! Pc in [Pa]

    subroutine PcEntryD(gsf,thetar,r,sigmaow,beta1,beta2,beta3,pced)

    implicit none

    real*8 pi
    parameter (pi=3.141592654)
    real*8 gsf,thetar,r,sigmaow,beta1,beta2,beta3,pced,d,fd
    integer i

    if(thetar.eq.0.e0) then
        d=1.e0/(4.e0*gsf)-pi
    else
```

```
    d=cos(thetar)*cos(thetar+beta1)/sin(beta1)-(pi/2.e0-thetar-beta1) &
     +cos(thetar)*cos(thetar+beta2)/sin(beta2)-(pi/2.e0-thetar-beta2) &
     +cos(thetar)*cos(thetar+beta3)/sin(beta3)-(pi/2.e0-thetar-beta3)
    end if

    fd=(1.e0+sqrt(1.e0-4.e0*gsf*d/(cos(thetar))**2 ))/   &
       (1.e0+2.e0*sqrt(pi*gsf))

    pced=(1.e+6)*(sigmaow/r)*(cos(thetar))*(1.e0+2.e0*sqrt(pi*gsf))*fd

    return
    end subroutine PcEntryD

! ========================================================================
!   Subroutine to calculate drainage area of water when oil is present
!   in the middle and water is present in the corners
! ========================================================================
! rw: radius of curvature of the arc-menisci
! thetar: receding contact angle
! beta(1,2,3): corner half angles
! aw: area of water

    subroutine AreawD(rw,thetar,beta1,beta2,beta3,aw)

    implicit none

    real*8 pi
    parameter (pi=3.141592654)
    real*8 rw,thetar,beta1,beta2,beta3,aw

    aw=rw**2*(cos(thetar)*cos(thetar+beta1)/sin(beta1)-pi/2.e0*(1.e0-   &
             2.e0*(thetar+beta1)/pi)+cos(thetar)*cos(thetar+beta2)/     &
            sin(beta2)-pi/2.e0*(1.e0-2.e0*(thetar+beta2)/pi)            &
            +cos(thetar)*cos(thetar+beta3)/sin(beta3)-pi/2.e0*          &
            (1.e0-2.e0*(thetar+beta3)/pi))

    return
    end subroutine AreawD

!--------------------------------------------------------------------
!       Subroutine to calculate invaded oil volume
!--------------------------------------------------------------------

    subroutine VolumeOil(rw,thetarn,thetarl,hangn,hangl,an,  &
                         al,ln,ll,nt,iz,nii,lii,nn,vom)

    implicit none

    integer nt,i,j
    integer iz(0:nt+1),nii(0:nt+1),lii(0:nt+1,0:nt+1),nn(0:nt+1,0:nt+1)
    real*8 ln(0:nt+1),ll(0:nt+1,0:nt+1),an(0:nt+1),al(0:nt+1,0:nt+1)
    real*8 thetarn(0:nt+1),thetarl(0:nt+1,0:nt+1),hangn(0:nt+1,3)
    real*8 hangl(0:nt+1,0:nt+1,3)
    real*8 rw,vom,awn,awl
    logical ans

    vom=0.e0
    do i=1,nt
        if(nii(i).eq.1) then
            call AreawD(rw,thetarn(i),hangn(i,1),  &
                        hangn(i,2),hangn(i,3),awn)
               vom=vom+(an(i)-awn)*ln(i)
        end if
    end do

    do i=0,nt
        do j=1,iz(i)
            if(lii(i,nn(i,j)).eq.1) then
                call AreawD(rw,thetarl(i,nn(i,j)),           &
```

```
                    hangl(i,nn(i,j),1),hangl(i,nn(i,j),2),    &
                    hangl(i,nn(i,j),3),awl)
                    vom=vom+(al(i,nn(i,j))-awl)*ll(i,nn(i,j))
            end if
        end do
    end do

! Deduct the links that have been counted twice:
    do i=1,nt
        do j=1,iz(i)
            if(lii(i,nn(i,j)).eq.1.and.nn(i,j).lt.i) then
                call AreawD(rw,thetarl(i,nn(i,j)),hangl(i,nn(i,j),1),  &
                            hangl(i,nn(i,j),2),hangl(i,nn(i,j),3),awl)
                vom=vom-(al(i,nn(i,j))-awl)*ll(i,nn(i,j))
            end if
        end do
    end do

    return
    end subroutine VolumeOil

! ========================================================================
! Subroutine to calculate hydraulic conductance of water of the oil-
! invaded pore/link during drainage
! ========================================================================
! rw: radius of curvature of the arc meniscii
! thetar: receding contact angle
! beta(1,2,3): corner half angles
! viscw: viscosity of water
! hcw: hydraulic conductance of water

    subroutine hcwd(rw,thetar,beta1,beta2,beta3,viscw,hcw)

    implicit none

    real*8 pi
    parameter (pi=3.141592654)

    real*8 rw,thetar,beta1,beta2,beta3,viscw,hcw
    real*8 hc1,hc2,hc3,hc
    real*8 drf1,drf2,drf3
    real*8 chi11,chi21,chi31,chi12,chi22,chi32,chi13,chi23,chi33
    real*8 aw1,aw2,aw3,kappa1,kappa2,kappa3


! Angle-1:
    aw1=rw**2*(cos(thetar)*cos(thetar+beta1)/sin(beta1)-pi/2.e0*        &
        (1.e0-2.e0*(thetar+beta1)/pi))
    chi11=(pi/2.e0-beta1-thetar)
    chi21=(1.e0/tan(beta1))*cos(thetar)-sin(thetar)
    chi31=(pi/2.e0-beta1)*tan(beta1)
    if(thetar.lt.(pi/2.e0-beta1)) then
        drf1=(12.e0*(sin(beta1))**2*(1.e0-chi31)**2*(chi21+chi11)**2)/  &
            ((1.e0-sin(beta1))**2*(chi21*cos(thetar)-chi11)*chi31**2)
        hc1=rw**2*aw1/(drf1*viscw)
    else
        drf1=(12.e0*(sin(beta1))**2*(1.e0-chi31)*(1.e0+chi31)**2)/      &
                (tan(beta1)*(1.e0-sin(beta1))**2*chi31**2)
        kappa1=cos(beta1)/sin(beta1)-pi/2.e0+beta1
        hc1=aw1**2/(drf1*kappa1*viscw)
    endif

! Angle-2:
    aw2=rw**2*(cos(thetar)*cos(thetar+beta2)/sin(beta2)-pi/2.e0*        &
        (1.e0-2.e0*(thetar+beta2)/pi))
    chi12=(pi/2.e0-beta2-thetar)
    chi22=(1.e0/tan(beta2))*cos(thetar)-sin(thetar)
    chi32=(pi/2.e0-beta2)*tan(beta2)
    if(thetar.lt.(pi/2.e0-beta2)) then
```

```
          drf2=(12.e0*(sin(beta2))**2*(1.e0-chi32)**2*(chi22+chi12)**2)/  &
              ((1.e0-sin(beta2))**2*(chi22*cos(thetar)-chi12)*chi32**2)
          hc2=rw**2*aw2/(drf2*viscw)
        else
          drf2=(12.e0*(sin(beta2))**2*(1.e0-chi32)*(1.e0+chi32)**2)/      &
                 (tan(beta2)*(1.e0-sin(beta2))**2*chi32**2)
          kappa2=cos(beta2)/sin(beta2)-pi/2.e0+beta2
          hc2=aw2**2/(drf2*kappa2*viscw)
        endif

! Angle-3:
        aw3=rw**2*(cos(thetar)*cos(thetar+beta3)/sin(beta3)-pi/2.e0*       &
            (1.e0-2.e0*(thetar+beta3)/pi))
        chi13=(pi/2.e0-beta3-thetar)
        chi23=(1.e0/tan(beta3))*cos(thetar)-sin(thetar)
        chi33=(pi/2.e0-beta3)*tan(beta3)
        if(thetar.lt.(pi/2.e0-beta3)) then
          drf3=(12.e0*(sin(beta3))**2*(1.e0-chi33)**2*(chi23+chi13)**2)/  &
              ((1.e0-sin(beta3))**2*(chi23*cos(thetar)-chi13)*chi33**2)
          hc3=rw**2*aw3/(drf3*viscw)
        else
          drf3=(12.e0*(sin(beta3))**2*(1.e0-chi33)*(1.e0+chi33)**2)/      &
                 (tan(beta3)*(1.e0-sin(beta3))**2*chi33**2)
          kappa3=cos(beta3)/sin(beta3)-pi/2.e0+beta3
          hc3=aw3**2/(drf3*kappa3*viscw)
        endif

        hcw=hc1+hc2+hc3

        return
        end subroutine hcwd

! ========================================================================
! Subroutine to solve a set of linear equations by Conjugate Gradient
!               method (Hestenes-Stiefel version)
! Solves Eqs. 32 to 38 in Batrouni and Hansen, J. Stat. Phys. 52, 747 (1988)
! ========================================================================
! pn(i): pressure at node i
! v(i),r(i),av(i): necessary variables for the CG method
! g(i,j): conductance of the link between nodes i and j
! Note: it is assumed that no meniscus exists in the links

        subroutine ConjGrad(pn,nt,iz,nn,g,eps,it)

        implicit none

        integer nt,iz(0:nt+1),nn(0:nt+1,0:nt+1),it
        integer i,j,itmax
        real*8 pn(0:nt+1),g(0:nt+1,0:nt+1),eps
        real v(0:nt+1),r(0:nt+1),av(0:nt+1),rvs,am,rvn,bm

! Initialization (Eq. 32):
        v(0)=0.e0
        v(nt+1)=0.e0
        r(0)=0.e0
        r(nt+1)=0.e0

        do i=1,nt
          v(i)=0.e0
            do j=1,iz(i)
              v(i)=v(i)+g(i,nn(i,j))*(pn(i)-pn(nn(i,j)))
            end do
          r(i)=v(i)
        end do

! Begin iteration:
! (Theoretical maximum number of iterations necessary is nt*nt.
! Due to roundoff, we double this number)
```

```
    itmax=2*(nt+1)
    do it=1,itmax

! Determining whether we have the solution or not (Eq. 38):
       rvs=0.e0
       do i=1,nt
           rvs=rvs+r(i)*r(i)
       end do

       if(rvs.le.eps**2) goto 1001

! Eq. 33:
       do i=1,nt
           av(i)=0.e0
               do j=1,iz(i)
                   av(i)=av(i)+g(i,nn(i,j))*(v(nn(i,j))-v(i))
               end do
       end do

       am=0.e0
       do i=1,nt
           am=am+v(i)*av(i)
       end do
       am=rvs/am

! Eq. 34:
       do i=1,nt
           pn(i)=pn(i)+am*v(i)
       end do

! Eq. 35:
       do i=1,nt
           r(i)=r(i)-am*av(i)
       end do

! Eq. 36:
       rvn=0.e0
       do i=1,nt
           rvn=rvn+r(i)*r(i)
       end do

       bm=rvn/rvs

! Eq. 37:
       do i=1,nt
           v(i)=r(i)+bm*v(i)
       end do

! End of iteration
    enddo

 1001 continue
      if(it.ge.itmax) then
       write(*,*) 'CG Error: it equals itmax, it=',itmax
      end if

      return
      end subroutine ConjGrad
```

```
! ========================================================================
! Subroutine to solve a set of linear equations by Conjugate Gradient
!              method (Hestenes-Stiefel version)
! Designed for oil-phase (pores invaded by oil)
! Solves Eqs. 32 to 38 in Batrouni and Hansen, J. Stat. Phys. 52, 747 (1988)
! ========================================================================
! pn(i): pressure at node i
! v(i),r(i),av(i): necessary variables for the CG method
! g(i,j): conductance of the link between nodes i and j
! Note: it is assumed that no meniscus exists in the links

    subroutine ConjGradO(pn,nt,iz,nn,nii,g,eps,it)

    implicit none

    integer nt,iz(0:nt+1),nn(0:nt+1,0:nt+1),nii (0:nt+1),it
    integer i,j,itmax
    real*8 pn(0:nt+1),g(0:nt+1,0:nt+1),eps
    real v(0:nt+1),r(0:nt+1),av(0:nt+1),rvs,am,rvn,bm

! Initialization (Eq. 32):
    v(0)=0.e0
    v(nt+1)=0.e0
    r(0)=0.e0
    r(nt+1)=0.e0

    do i=1,nt
        if(nii(i).eq.1) then
            v(i)=0.e0
                do j=1,iz(i)
                    v(i)=v(i)+g(i,nn(i,j))*(pn(i)-pn(nn(i,j)))
                end do
            r(i)=v(i)
        else
            v(i)=0.e0
            r(i)=0.e0
        end if
    end do

! Begin iteration:
! (Theoretical maximum number of iterations necessary is nt*nt.
! Due to roundoff, we double this number)
    itmax=2*(nt+1)
    do it=1,itmax

! Determining whether we have the solution or not (Eq. 38):
        rvs=0.e0
        do i=1,nt
            if(nii(i).eq.1) then
                rvs=rvs+r(i)*r(i)
            end if
        end do

        if(rvs.le.eps**2) goto 1001

! Eq. 33:
        do i=1,nt
            av(i)=0.e0
                if(nii(i).eq.1) then
                    do j=1,iz(i)
                        av(i)=av(i)+g(i,nn(i,j))*(v(nn(i,j))-v(i))
                    end do
                end if
        end do

        am=0.e0
        do i=1,nt
            if(nii(i).eq.1) then
                am=am+v(i)*av(i)
```

```
            end if
        end do

        am=rvs/am

! Eq. 34:
        do i=1,nt
            if(nii(i).eq.1) then
                pn(i)=pn(i)+am*v(i)
            end if
        end do

! Eq. 35:
        do i=1,nt
            if(nii(i).eq.1) then
                r(i)=r(i)-am*av(i)
            end if
        end do

! Eq. 36:
        rvn=0.e0
        do i=1,nt
            if(nii(i).eq.1) then
                rvn=rvn+r(i)*r(i)
            end if
        end do

        bm=rvn/rvs

! Eq. 37:
        do i=1,nt
            if(nii(i).eq.1) then
                v(i)=r(i)+bm*v(i)
            end if
        end do

! End of iteration
    enddo

 1001 continue

      if(it.ge.itmax) then
        write(*,*) 'CG Error: it equals itmax, it=',itmax
      end if

      return
      end subroutine ConjGradO
```

Appendix B

Input data for a regular cubic-lattice network model of 3x3x3 pore-bodies.

Data for pore-bodies (no data is required for the outlet fluid reservoir):

Pore-body	*z*	Area(μm^2)	Perimeter(μm)	Length(μm)
0	9	0	0	0
1	4	1.4587	5.8330	1.5
2	5	0.7349	4.0084	1.5
3	4	2.4074	7.6285	1.5
4	5	4.5082	11.4088	1.5
5	6	4.8049	11.7184	1.5
6	5	3.3676	9.3282	1.5
7	4	2.3928	8.4766	1.5
8	5	1.3699	5.7906	1.5
9	4	4.1084	10.9756	1.5
10	4	3.0960	8.8506	1.5
11	5	2.4073	8.5749	1.5
12	4	0.8401	4.6052	1.5
13	5	3.6419	9.0735	1.5
14	6	3.1393	9.2224	1.5
15	5	1.2963	5.4792	1.5
16	4	0.9727	4.9700	1.5
17	5	1.6353	5.8388	1.5
18	4	1.7696	6.2929	1.5
19	4	2.8210	7.9770	1.5
20	5	4.8215	12.5569	1.5
21	4	5.2806	10.6452	1.5
22	5	4.8894	12.5053	1.5
23	6	0.8092	4.1905	1.5
24	5	4.0950	11.3797	1.5
25	4	0.9538	4.8116	1.5
26	5	0.7275	4.0073	1.5
27	4	5.0058	10.7506	1.5

Data for pore-throats:

Neighbor pore-bodies	Area(μm^2)	Perimeter(μm)	Length(μm)
Pore-throats connecting pore-bodies 0 and			
1	0.1420	1.7964	1.5
2	0.1089	1.8854	1.5
3	0.1411	1.8128	1.5
4	0.0445	1.1847	1.5
5	0.0990	1.4637	1.5
6	0.0903	1.4279	1.5
7	0.1560	2.0183	1.5
8	0.0594	1.2707	1.5
9	0.2373	2.3387	1.5
Pore-throats connecting pore-bodies 1 and			
0	0.1420	1.7964	1.5
2	0.1439	1.8439	1.5
10	0.0726	1.4178	1.5
4	0.0481	1.0045	1.5
Pore-throats connecting pore-bodies 2 and			
0	0.1089	1.8854	1.5
3	0.2899	2.7079	1.5
11	0.2163	2.6541	1.5
1	0.1439	1.8439	1.5
5	0.2150	2.3001	1.5
Pore-throats connecting pore-bodies 3 and			
0	0.1411	1.8128	1.5
12	0.2021	2.2478	1.5
2	0.2899	2.7079	1.5
6	0.2576	2.3629	1.5
Pore-throats connecting pore-bodies 4 and			
0	0.0445	1.1847	1.5
5	0.2094	2.3223	1.5

13	0.0493	1.2297	1.5
7	0.0733	1.4079	1.5
1	0.0481	1.0045	1.5
Pore-throats connecting pore-bodies 5 and			
0	0.0990	1.4637	1.5
6	0.1683	1.9020	1.5
14	0.0982	1.4584	1.5
4	0.2094	2.3223	1.5
8	0.1209	1.6614	1.5
2	0.2150	2.3001	1.5
Pore-throats connecting pore-bodies 6 and			
0	0.0903	1.4279	1.5
15	0.2881	2.5819	1.5
5	0.1683	1.9020	1.5
9	0.2075	2.0956	1.5
3	0.2576	2.3629	1.5
Pore-throats connecting pore-bodies 7 and			
0	0.1560	2.0183	1.5
8	0.0979	1.5533	1.5
16	0.1181	1.7373	1.5
4	0.0733	1.4079	1.5
Pore-throats connecting pore-bodies 8 and			
0	0.0594	1.2707	1.5
9	0.1828	2.2010	1.5
17	0.2531	2.4473	1.5
7	0.0979	1.5533	1.5
5	0.1209	1.6614	1.5
Pore-throats connecting pore-bodies 9 and			
0	0.2373	2.3387	1.5
18	0.1607	1.8788	1.5
8	0.1828	2.2010	1.5
6	0.2075	2.0956	1.5
Pore-throats connecting pore-bodies 10 and			
1	0.0726	1.4178	1.5
11	0.2243	2.2992	1.5
19	0.0519	1.0471	1.5
13	0.1030	1.7691	1.5
Pore-throats connecting pore-bodies 11 and			
2	0.2163	2.6541	1.5
12	0.0579	1.1811	1.5
20	0.0896	1.4174	1.5
10	0.2243	2.2992	1.5
14	0.2880	2.6226	1.5
Pore-throats connecting pore-bodies 12 and			
3	0.2021	2.2478	1.5
21	0.1733	2.1428	1.5
11	0.0579	1.1811	1.5
15	0.0582	1.3045	1.5
Pore-throats connecting pore-bodies 13 and			
4	0.0493	1.2297	1.5
14	0.0486	1.0530	1.5
22	0.1233	1.9376	1.5
16	0.2320	2.5904	1.5
10	0.1030	1.7691	1.5
Pore-throats connecting pore-bodies 14 and			
5	0.0982	1.4584	1.5
15	0.0873	1.6322	1.5
23	0.1558	2.1822	1.5
13	0.0486	1.0530	1.5
17	0.0474	1.0261	1.5
11	0.2880	2.6226	1.5
Pore-throats connecting pore-bodies 15 and			
6	0.2881	2.5819	1.5
24	0.1892	2.0275	1.5
14	0.0873	1.6322	1.5
18	0.1467	2.2024	1.5
12	0.0582	1.3045	1.5
Pore-throats connecting pore-bodies 16 and			
7	0.1181	1.7373	1.5

17	0.0826	1.6273	1.5
25	0.2887	2.6173	1.5
13	0.2320	2.5904	1.5
Pore-throats connecting pore-bodies 17 and			
8	0.2531	2.4473	1.5
18	0.2387	2.3405	1.5
26	0.1759	2.0080	1.5
16	0.0826	1.6273	1.5
14	0.0474	1.0261	1.5
Pore-throats connecting pore-bodies 18 and			
9	0.1607	1.8788	1.5
27	0.0804	1.5920	1.5
17	0.2387	2.3405	1.5
15	0.1467	2.2024	1.5
Pore-throats connecting pore-bodies 19 and			
10	0.0519	1.0471	1.5
20	0.0867	1.6585	1.5
28	0.1894	2.2329	1.5
22	0.0822	1.3231	1.5
Pore-throats connecting pore-bodies 20 and			
11	0.0896	1.4174	1.5
21	0.1592	1.9001	1.5
28	0.1078	1.8691	1.5
19	0.0867	1.6585	1.5
23	0.2576	2.4721	1.5
Pore-throats connecting pore-bodies 21 and			
12	0.1733	2.1428	1.5
28	0.2460	2.3038	1.5
20	0.1592	1.9001	1.5
24	0.1089	1.8248	1.5
Pore-throats connecting pore-bodies 22 and			
13	0.1233	1.9376	1.5
23	0.2665	2.4267	1.5
28	0.0635	1.3377	1.5
25	0.1636	2.1093	1.5
19	0.0822	1.3231	1.5
Pore-throats connecting pore-bodies 23 and			
14	0.1558	2.1822	1.5
24	0.2216	2.4149	1.5
28	0.3086	2.5702	1.5
22	0.2665	2.4267	1.5
26	0.1077	1.6400	1.5
20	0.2576	2.4721	1.5
Pore-throats connecting pore-bodies 24 and			
15	0.1892	2.0275	1.5
28	0.1043	1.4997	1.5
23	0.2216	2.4149	1.5
27	0.1489	2.0954	1.5
21	0.1089	1.8248	1.5
Pore-throats connecting pore-bodies 25 and			
16	0.2887	2.6173	1.5
26	0.2697	2.4377	1.5
28	0.0756	1.5618	1.5
22	0.1636	2.1093	1.5
Pore-throats connecting pore-bodies 26 and			
17	0.1759	2.0080	1.5
27	0.2045	2.2996	1.5
28	0.1912	2.1828	1.5
25	0.2697	2.4377	1.5
23	0.1077	1.6400	1.5
Pore-throats connecting pore-bodies 27 and			
18	0.0804	1.5920	1.5
28	0.0814	1.5779	1.5
26	0.2045	2.2996	1.5
24	0.1489	2.0954	1.5

Paper IX

2000 International Symposium of the Society of Core Analysts
October 18-22, 2000, Abu Dhabi, UAE

Pore-Scale Studies of Mobilization and Recovery of Oil by Waterflooding

Saifullah Talukdar, Martha Semere and Ole Torsaeter

Norwegian University of Science and Technology, Trondheim, Norway

NTNU

Abstract

Mechanisms by which oil is mobilized and recovered during waterflooding at strongly water-wet conditions have been investigated with 2D glass micromodels using distilled water and refined oil. Two groups of experiments have been performed. In group-1, the capillary number was increased through decreasing interfacial tension by adding more isopropanol to the distilled water. In group-2, the capillary number was increased by increasing flow velocity. The movement of phase interface and the distribution of phase saturations were monitored under a microscope having variable magnification lens and were recorded continuously by a video camera.

Analysis of the Capillary Desaturation Curves (CDC) and microscopic photographs for the two groups of experiments reveal that the displacement process is more efficient when the capillary force is reduced (group-1) rather than when viscous force is increased (group-2). The reason is that the slow displacement in group-1, where piston- and *I1*-type mechanisms dominate, causes less distortion of the displacement fronts, whereas, the rapid displacement in group-2, where snap-off and *I2* mechanisms dominate, causes both viscous fingering and frequent breaking of oil into small blobs. The isolated blobs mostly remain trapped.

Introduction

One important physical relationship during immiscible displacement is the Capillary Desaturation Curve (CDC). The CDC is the relation between residual phase saturation and the capillary number, $N_C = \frac{q\mu}{A\sigma}$, which is the ratio of viscous to capillary forces. It has been found from laboratory experiments[1] and from theoretical considerations[2] that CDC curves for water-wet rocks depend on whether the residual oil phase is hydraulically continuous or discontinuous. The critical capillary number, the minimum capillary number at which the residual oil saturation begins to decrease, is much higher for the discontinuous case than for the continuous case. The concern is how to change the capillary number. For a particular geometry and wetting condition, the capillary number can be increased either by increasing the viscous force (increase flow velocity or viscosity of the injected fluid) or by lowering the capillary force (decrease in the interfacial tension between the two fluids). It must be interesting to see whether the increase in viscous force or decrease in capillary force have any impact on the overall CDC curves, in other words, on displacement mechanisms and recovery efficiencies. Micromodel experiments have been conducted in this work to investigate the above phenomena at pore level.

Experimental Procedure

The experimental setup is shown in Fig.1. The experiments were done using a 2D glass micromodel consisting of 4388 pore bodies and 8970 pore throats in a regular square network. The pore throats are approximately rectangular in cross section with a depth of 150μm and the width ranges from 100 to 300μm. The pore bodies are approximately cylindrical with a depth of 150μm and the diameter varies between 300 and 400μm. The experiments were conducted at room conditions and the movement of phase interface and the distribution of phase saturations were monitored under a microscope having variable magnification lens and were recorded continuously by a video camera.

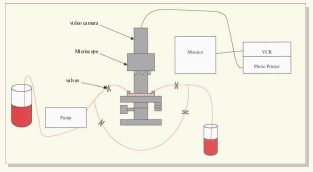

Figure 1 Experimental setup

Distilled water (viscosity 1.002 cp), oil (Soltrol 130^{TM}) and isopropanol (viscosity 2.3 cp) were used. The interfacial tension (IFT) between oil and water was varied through adding variable amount of isopropanol. The addition of small amount of dyes to the fluids (red to oil and blue to water) was also found to decrease the IFT. The experiments were divided into two groups, where each group consists of six experiments at six increasing capillary numbers. Experiments in group-1 were conducted at a constant flow rate of 0.01 ml/min and the capillary number was increased through decreasing interfacial tension by adding more isopropanol to the distilled water. Group-2 experiments were carried out at a fixed IFT of 20.3 dyne/cm, but the same capillary numbers as in group-1 were obtained by increasing flow velocity. The micromodel was initially filled with water by pumping water at high flow rate. Oil was then pumped at high capillary number (≈10^{-4}) to displace water to irreducible water saturation. Finally, water was injected (imbibition process) until there was no more production of oil. The residual oil saturations were determined by counting the number of pores and throats after the imbibition and are reported in table 1 together with capillary number, IFT and flow rate.

Table 1 Residual oil saturation vs. capillary number for the two groups of experiments

Experiment No.	Capillary Number, N_c	Group-1 (q=0.01 ml/min)		Group-2 (σ=20.3 dyne/cm)	
		σ(dyne/cm)	S_{or}	q (ml/min)	S_{or}
1	3.36E- 06	20.30	33.9	0.010	33.9
2	7.12E- 06	16.23	33.9	0.023	33.9
3	1.30E- 05	11.10	22.5	0.039	29.3
4	3.14E- 05	6.20	18.2	0.093	25.5
5	5.15E- 05	4.26	10.3	0.153	22.4
6	1.13E- 04	2.24	5.8	0.337	15.0

Results and Discussion

The CDC curves obtained from plotting the residual oil saturations vs. capillary numbers for the two groups of experiments (table 1) are compared in Fig. 2.

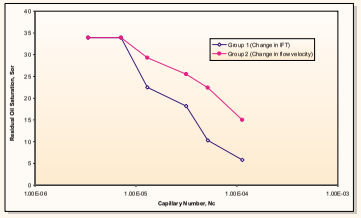

Figure 2 CDC for the two groups of experiments

As can be observed from the figure, the critical capillary number is approximately same (≈10^{-5}) for both cases. After this capillary number the residual oil saturation begins to decrease, and between the two cases, group-1 experiments have higher decrease rate than group-2. It is therefore, evident that increase in capillary number by decreasing interfacial tension is more efficient than by increasing flow velocity.

To find out the root for this difference, we have to investigate the underlying flow mechanisms for the two cases. The nice thing about micromodel experiments is that we practically see the displacement phenomena at pore-scale. From microscopic photographs we observed a general trend for both groups as we increased the capillary number. With increase in capillary number, the displacement becomes more and more piston type resulting in less trapping and also the blob size of the trapped oil decreases. At the lowest capillary number (e.g. experiment-1), the residual oil occupies many pore bodies (as high as 200) and at the highest capillary number (e.g. experiment-6), the residual oil occupies only single pores. Photographs in Fig. 3 illustrate this point.

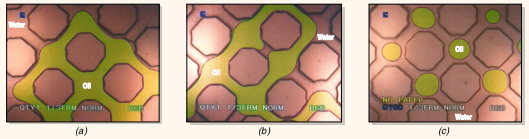

Figure 3 Residual oil saturation (group-2); (a) experiment-1 (b) experiment-3 (c) experiment-6

Different flow mechanisms are responsible for lower residual oil saturations in group-1 compared to group-2. At the beginning of the displacement, the displacing fluid advances faster in the middle than at the sides. In group-2, this leads to viscous fingering and frequent breaking of oil (both by snap-off and *I2*) into small blobs. These blobs remain trapped, as they cannot be mobilized by the small viscous-pressure gradient acting across them. In group-1, the displacement is slow and relatively sharp front is observed. Lateral imbibition by *I1* and piston-type mechanism dampened the tendency for viscous fingering. Less snap-off events are observed probably due to local surface tension gradients, which lead to substantial shear viscosity effects at the oil-water interfaces. This increases the flow resistance in the wetting films and makes it difficult for snap-off events to proceed. As a result of all these phenomena, residual oil saturation in the water-swept region is substantially low. The different imbibition flow mechanisms are schematically illustrated in Fig. 4.

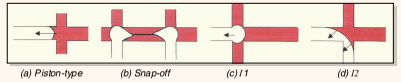

Figure 4 Two-phase imbibition displacement mechanisms[3]

Conclusions

1. In immiscible displacement, after a certain capillary number known as critical capillary number, the residual oil saturation decreases as the capillary number increases.
2. During displacement, oil breaks into small blobs and is trapped due to insufficient viscous-pressure gradient acting across them. With increase in capillary number, the blob size decreases and the displacement becomes more and more piston type resulting in less trapping.
3. The methods by which capillary number is increased, either by decreasing IFT or increasing flow velocity, has big impact on displacement efficiency. Decrease in capillary forces provides more efficient displacement than increase in viscous forces. Viscous fingering, breaking of oil into small blobs and subsequent trapping, dominated by snap-off and *I2* mechanisms, result in poor efficiency in high velocity displacements.

Nomenclature

q	Flow rate of the displacing fluid	A	Flow area
Nc	Capillary number	σ	Interfacial tension between two fluids
Sor	Residual oil saturation	IFT	Interfacial tension
μ	Viscosity of the displacing fluid	CDC	Capillary Desaturation Curve

References

1. Chatzis, I. and Morrow, N.R.: "Correlation of Capillary Number Relationships for Sandstone," SPEJ (1984), 24, 555-562.
2. Zhou, D. and Stenby, E.H.: "Displacement of Trapped Oil from Water-Wet Reservoir Rock," Trans. Por. Med. (1993), 11, 1-16.
3. Lenormand, R. and Zarcone, C.: "Role of Roughness and Edges During Imbibition in Square Capillaries," paper SPE 13264 presented at the 59th Annual Technical Conference and Exhibition, Houston, Texas, 16-19 September 1984.

Paper X

URN:NBN:no-2347

Nordic Petroleum Technology V

Introducing Up-Scaling Techniques in Fractured Reservoir Simulation

M. S. Talukdar, H. A. Banu, O. Torsaeter and J. Kleppe
Norwegian University of Science and Technology
Trondheim
Norway

Nordic Petroleum Technology Series V (May 2001), 189-218.

Abstract

Much attention has been given to the simulation of naturally fractured reservoirs in the recent literature. Predicting the behavior of naturally fractured reservoirs has presented a challenge for petroleum engineers for many years. The use of reservoir simulation as a predictive tool has been complicated by the vast property discrepancies between the matrix rock and the interconnected fracture system. The most widely adopted approach to fractured reservoir simulation is dual porosity and/or dual permeability models where the matrix and fracture network are modelled as two overlapping continua.

The concept of up-scaling by pseudo functions is relatively new in fractured reservoir simulation. Up-scaling is normally applied to capture the details of small-scale fluid mechanics and reservoir heterogeneity in coarse-grid simulation models.

The early uses of the up-scaling techniques in conventional reservoir simulation were to: reduce three dimensional aspects into a two dimensional model, represent fine layering in a few layer model, and model the well effects such as coning, partial penetration etc. The up-scaling techniques in fractured reservoirs are rather limited in their ability to parameterise the conceptual Warren and Root model. The application of conventional up-scaling techniques to predict fractured reservoir performance through grid coarsening can dramatically reduce the time and cost involved in field-scale simulation.

URN:NBN:no-2347

Up-Scaling in Fractured Reservoir Simulation

In this study four widely used conventional up-scaling techniques (Kyte & Berry, Pore Volume Weighted, Weighted Relative Permeability, and Stone) are incorporated in the modelling and simulation of fractured reservoirs. The study methodology involves the calculation of pseudo properties from fractured fine-grid simulation using rock curves, and the application of these pseudo properties to the coarse-grid simulation, which give the correct flow behavior to the coarse-grid model.

Two models have been developed and simulated to verify the applicability and rate sensitivity of these techniques. Their acceptability in the dual porosity model is also investigated.

From the results, it can be concluded that these techniques can be used in fractured reservoir simulation. They may or may not be rate sensitive depending on the model type.

Introduction

Naturally fractured reservoirs consist of blocks of reservoir rock (matrix) surrounded by continuous network of various degrees of fractures distributed throughout the reservoir. They are sometimes termed as double-porosity or even double-porosity/double-permeability systems. One porosity (and permeability) is associated with the matrix blocks and the other with the fractures. The matrix blocks (low permeability but high porosity) usually act as fluid supply sources, which feed fluids into the fractures. The fractures (low porosity but high permeability) provide the main path for the fluids to flow from the reservoir to the wellbore.

Fractured reservoirs contain a substantial share of the world's petroleum reserves. Reservoir simulation is a widely accepted numerical method to predict the behavior of conventional and naturally fractured reservoirs. However, modelling of naturally fractured reservoirs remains a difficult task for reservoir engineers because of vast property discrepancies between the matrix rock and the interconnected fracture network.

URN:NBN:no-2347

Warren and Root (1963) first introduced an idealized model for fractured reservoirs for the purpose of studying the characteristic behavior. Their model consists of an array of parallelepipedic matrix blocks surrounded by

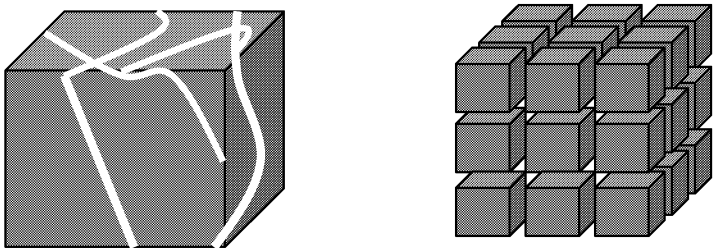

(a) Real Fractured Block (b) Idealized Fractured Block

Figure 1. The conventional Warren and Roots model.

a fracture network (Fig. 1). Following this model, several papers were published, dealing with modeling, and simulating flow dynamics, in fractured reservoirs (Kleppe and Morse 1974; Kazemi *et al.* 1976; Rossen 1977). One model differs from another in terms of: the number of phases, the number of flow directions, and the modeling technique of the matrix-fracture fluid exchange mechanism. Two early studies were published which predicted oil recovery from the matrix block by water displacement (Mattax and Kyte 1962; Kyte 1970).

Despite the simplicity of Warren and Root model, the difficulties arise when using it. The conceptual model needs to be parameterised, and equivalent fracture permeabilities and parallelepipedic blocks need to be found to enable the simulation of the reservoir flow dynamics. Moreover, recent field characterization studies show that fracture systems are very irregular. Both the orientation and intensity of the fracture affect the effective permeability of the fractures significantly. In addition, the rock-type, and size and shape of the matrix blocks strongly influence the matrix-fracture fluid exchange process.

The rock properties measured in the laboratory on small size core plugs are assumed to be applicable to the fine-scale reservoir simulation. To capture the highly detailed geological features and structural heterogeneity in field-

scale simulation, the rock properties need to be 'scaled-up' in order to match the flows obtained in a simulation using quantities defined on a coarser grid.

Lough, Lee and Kamath (1996) developed an up-scaling technique to calculate the effective permeability of grid blocks, which permits the inclusion of realistic fracture features into continuum models. The technique also accounts for flow through both the fracture and the matrix systems. Bourbiaux *et al.* (1997) presented another method to compute equivalent fracture permeability and equivalent matrix block dimensions from 3D geological images of the fracture network.

Simulation of large, complex reservoirs often requires an unacceptably large number of computational grid blocks. The use of pseudo-relative permeabilities and pseudo-capillary pressures is one way of decreasing the number of grids to a more tractable level with minimal loss of simulation accuracy. A proper up-scaling algorithm can bridge the gap between the reservoir description grid and the simulation grid.

Jacks *et al.* (1973) presented procedures for calculating dynamic pseudo-relative permeabilities from vertical cross-section model runs, which can be used to simulate three-dimensional flow accurately in a two-dimensional areal model. Kyte and Berry (1975) improved Jacks' model and included pseudo-capillary pressure. Thomas *et al.* (1983) introduced pseudo-capillary pressure for matrix blocks, calculated from vertical equilibrium calculations. Rossen and Shen (1989) calculated pseudo-capillary-pressure curves for both the matrix and fracture, which are similar to those derived by Dean and Lo (1988). Unlike Dean and Lo, however, they developed a more efficient procedure based on single fine-grid simulation without history matching. Stone (1991) proposed a new method of calculating black oil pseudo-functions from fine-grid simulation. This method reproduces fine-grid accuracy when applied to a coarse-grid model.

Guzman *et al.* (1996) investigated the reliability of several dynamic pseudo functions used to up-scale flow properties in reservoir simulation. They concluded that these functions, as commonly used in industry, might not be an adequate approach to up-scaling. This is due to the possibility of large errors and the difficulty predicting when they may occur. Barker and Thibeau (1996) critically reviewed the use of pseudo-relative permeabilities

for up-scaling. They concluded that pseudo-relative permeabilities cannot be used reliably to scale up from a “fine-grid” geological model to a “coarse-grid” fluid-flow model. The exception is where capillary or gravity equilibrium can be assumed at the coarse-gridblock scale.

As described above, the early uses of the pseudo functions for the rock properties (porosity and absolute permeability) and for the flow properties (relative permeability and capillary pressure) in conventional reservoir simulation were concerned with: a) representing three dimensional aspects in a two dimensional model, b) representing fine layering in a few layer model, c) controlling numerical dispersion, and d) modelling of the well effects such as coning, partial penetration, position of a well within a grid block, etc. The up-scaling techniques in fractured reservoirs were limited in their ability to parameterise the conceptual model of Warren and Root, i.e. to obtain equivalent fracture permeability, and equivalent matrix block dimensions and effective permeability.

The application of the conventional up-scaling techniques to predict fractured reservoir performance through grid coarsening can dramatically reduce the time and cost for field-scale simulation. In this study, four widely used techniques (Kyte & Berry, Pore Volume Weighted, Weighted Relative Permeability, and Stone) have been investigated to verify their applicability and rate sensitivity in fractured reservoir simulation.

Study Methodology

The following procedure is applied in the study:

- Develop fine-grid and equivalent coarse-grid simulation models.
- Simulate fine-grid model with rock curves to predict the actual behavior of the model. Eclipse 100 black oil reservoir simulator is used.
- Use fine-grid simulation results to generate pseudos for the equivalent coarse-grid model. The Eclipse Pseudo (Schlumberger GeoQuest 1998) program is used.
- Simulate coarse-grid model with pseudos.
  Compare the coarse-grid results with that of fine-grid.

URN:NBN:no-2347

Review of Theories

The formulations of the up-scaling techniques under consideration are reviewed briefly. Upper case variables refer to the coarse grid, lower case to the fine grid.

Kyte and Berry Pseudos
Coarse grid quantities are defined in terms of the fine grid quantities as follows.

Pore volumes: Defined as a simple sum over the fine grid cell in each coarse grid cell.

$$V_N = \sum_{n \in N} v_n \tag{1}$$

Porosities: Defined as the total pore volume of the coarse grid block divided by the total gross volume.

$$\Phi_N = \left(\sum_{n \in N} v_n \right) / \left(\sum_{n \in N} v_n / \Phi_n \right) \tag{2}$$

Cell Depths: Defined as a pore volume weighted average of the fine cell depths.

$$D_N = \left(\sum_{n \in N} v_n d_n \right) / V_N \tag{3}$$

Transmissibilities: The coarse grid transmissibilities are formed as a sum over the fine grid transmissibilities. For example, between coarse grid ‘I’ and coarse grid ‘J’, it can be expressed as below:

$$TX_N = 1 / \left\{ \sum_i \left[1 / \left(\sum_{jk} tx_{ijk} \right) \right] \right\} \tag{4}$$

Phase Saturations: Obtained as a pore volume weighted average of the fine grid saturations.

$$S_{pN} = \left(\sum_{n \in N} v_n s_{pn} \right) / V_N \tag{5}$$

Phase Flows: Obtained as a simple sum over the fine grid flows over fine grid cells on the appropriate face of the course grid.

$$F_{pI} = \sum_{ijk} f_{pijk} \tag{6}$$

Phase Pressures: These are obtained in a number of steps:

- Calculate the fine grid water pressures by adding the capillary pressure term to the oil pressures.
- Calculate the fine grid phase densities, and use these to normalize the fine grid phase pressures to the coarse grid cell center depths.

$$p_n^{center} = p_n + g\rho_n \left(D_N - d_n \right) \tag{7}$$

- Form the coarse grid phase pressure by averaging over the normalized fine grid phase pressures with suitable weighting factors.

$$P_{pN} = \frac{\sum_{n \in N} w_n p_n^{center}}{\sum_{n \in N} w_n} \tag{8}$$

Two types of pressures are formed:

- The block phase pressure. This is used to calculate the pseudo capillary pressure for a coarse grid cell. Here, the pore volume weighting factors are appropriate.
- The flowing phase pressures. In evaluating pseudo relative permeability values from flows in a given direction, Kyte and Berry pseudos use a weighting factor, which reflects the relative contribution made by each cell in that direction.

URN:NBN:no-2347

Phase Densities, Fluid Formation Volume Factors and Viscosities: Obtained as a pore volume weighted average of the fine grid quantities.

$$\rho_{pN} = \left(\sum_{n \in N} v_n \rho_{pn} \right) / V_N \tag{9}$$

$$\mu_{pN} = \left(\sum_{n \in N} v_n \mu_{pn} \right) / V_N \tag{10}$$

$$B_{pN} = \left(\sum_{n \in N} v_n b_{pn} \right) / V_N \tag{11}$$

Pseudo Relative Permeabilities: Once the above coarse grid quantities are in place, the pseudo relative permeabilities are obtained by applying Darcy's law on the coarse grid in each direction, using the flowing phase pressures:

$$K^d_{pN} = \frac{F^d_{pN} . \mu_{pN} . B_{pN}}{T^d_{pN}} \left[P_{pN} - P_{pM} + g \frac{1}{2} \left(\rho_{pN} + \rho_{pM} \right) \left(D_N - D_M \right) \right] \tag{12}$$

This expression is applied for all flows between neighboring cells in the coarse grid, but the resulting pseudo relative permeability value is associated with the upstream cell only.

Pseudo Capillary Pressures: The pseudo capillary pressures are obtained as the difference between the coarse-block phase pressures:

$$P_{cow} = P_o - P_w \tag{13}$$

Pore Volume Weighted Pseudos

For pore volume weighted pseudos almost all the expressions from the Kyte and Berry case carry over. The only exception is in the definition of the phase pressures. In this case only the block phase pressures are calculated, and these are used both to obtain pseudo capillary pressures and pseudo relative permeabilities. These replace the flowing phase pressures of the Kyte and Berry approach.

Weighted Relative Permeability Pseudos

Weighted relative permeability pseudos are very different from the Kyte and Berry and pore volume weighted cases. The aim is to concentrate on saturation effects. The dominant effect in determining the flow of a phase between two coarse grid cells is the phase relative permeability values over the upstream phase of the cell. Accordingly, the pseudo is defined as a weighted sum of these values. The weighting factor should reflect the relative importance of each fine grid cell, and so is taken as the transmissibility value across the interface to the upstream cell. The pseudo value is thus:

$$Kr_{pN} = \frac{\sum_{n \in N} kr_{pn} t_n}{\sum_{n \in N} t_n} \tag{14}$$

These pseudos are rather coarser than the Kyte and Berry type, as they ignore differences in pressure across various parts of the upstream face. However, they must yield physical values, and are much more robust. In good conditions for pseudo generation (large pressure differences dominating gravity effects, small pressure variations over the coarse grid cells) these give similar results to the Kyte and Berry approach. However, in adverse conditions, these pseudos often yield much better results. The pseudo capillary pressures are obtained in the same manner as Kyte and Berry and pore volume weighted pseudos.

Stone Pseudos

The Stone model looks at coarse grid boundaries, and equates the phase reservoir volume flows across the interface. In the case of the i-direction:

$$Q_p = \sum_j \sum_k q_{pjk} \tag{15}$$

The reservoir volume flux is the same as the usual flow term, but without the surface volume density, and summed over all phases. The coarse grid value is simply obtained by summation of the fine grid values over the interface:

$$Q_t = \sum_j \sum_k q_{tjk} \tag{16}$$

URN:NBN:no-2347

The total reservoir volume flow is the sum of the three phase contributions:

$$q_t = q_o + q_w + q_g \tag{17}$$

The fractional flow may be defined as $f = q_p / q_t$. The coarse grid fractional flow is then obtained as:

$$F_p = \frac{\sum_j \sum_k q_{pjk}}{\sum_j \sum_k q_{tjk}} \tag{18}$$

The coarse grid total mobility is obtained as transmissibility weighted average.

$$\lambda_t = \frac{\sum_j \sum_k T_x \lambda_t}{\sum_j \sum_k T_x} \tag{19}$$

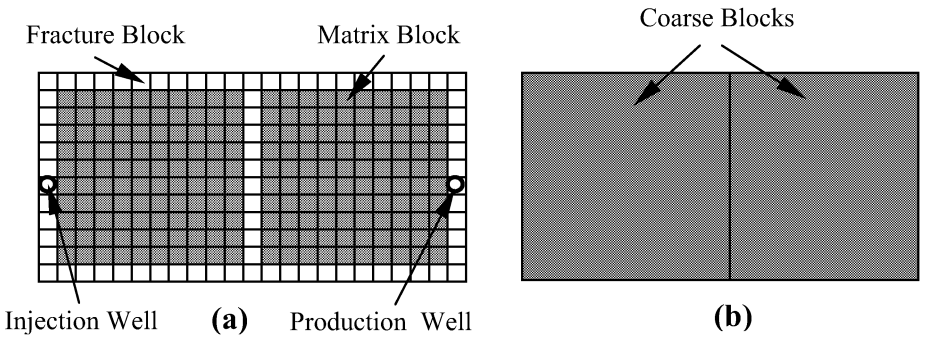

Figure 2. Model Type-1 (a) 23x12 fine-grid model (b) 2x1 equivalent coarse-grid model.

Model Studies

Two fine-grid, and their equivalent coarse-grid models (model type-1 and 2) have been developed and simulated at four different injection rates. Model type-2 has been converted to an equivalent dual-porosity form. They are described below.

URN:NBN:no-2347

Model Description

Fig. 2 illustrates model type-1. This model consists of a two dimensional 23x12 fine-grid and 2x1 equivalent coarse-grid. The fine-grid model has fractures around and in the middle of the matrix but the coarse-grid model has only matrix. The matrix blocks (shaded gray) of the fine-grid model have dimensions of 10cmX10cm each, whereas the fractures around and inside the matrix (no shading) have a width of 0.1cm, making the total model size 200.3cmX100.2cm. The width of the fractures is exaggerated in the figure.

The first 12x12 fine-grid (consisting of both matrix and fracture) form the first coarse grid and the other 11x12 fine-grid form the other coarse grid. Therefore, first coarse grid has a dimension of 100.2cmX100.2cm and the other has 100.1cmX100.2cm. The objective for developing this model is to convert a fractured fine-grid system into an equivalent coarse-grid system containing no fracture, which, in turn, may be simulated as a conventional reservoir.

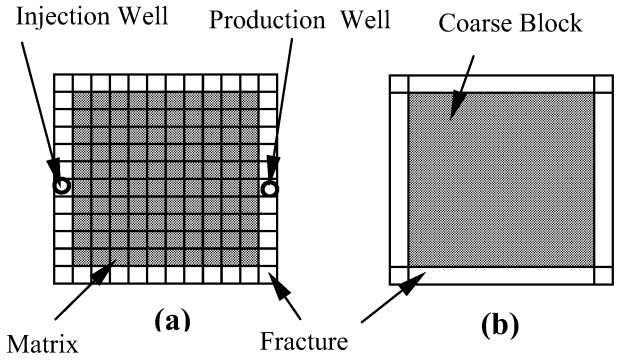

Figure 3. Model Type-2 (a) 12x12 fine-grid model (b) 3x3 equivalent coarse-grid model.

Fig. 3 illustrates model type-2, which is also a two dimensional case with 12x12 fine-grid and 3x3 equivalent coarse-grid. In both fine- and coarse-grid models, the matrix is surrounded by fractures. In this case, 10x10 fine-grid matrix blocks form the coarse-grid matrix block (no fracture is associated). The matrix and fracture blocks of the fine-grid model have dimensions similar to that of model type-1. Therefore, total model size is 100.2cmX100.2cm. The width of the fractures is not shown to scale relative

URN:NBN:no-2347

to the matrix. The objective for this model is to convert fractured fine-grid system into equivalent coarse-grid dual-porosity system.

To investigate the validity of the conventional pseudoization methods in dual-porosity models, model type-2 was converted to an equivalent dual-porosity model in order to be able to simulate it using dual-porosity option in Eclipse. The requirement for dual porosity models in Eclipse is that the number of layers must be even and at least two. This is because the matrix layer has to be underlain by a fracture layer.

Fig. 4 illustrates the equivalent dual-porosity model consisting of a 3x1x2 coarse-grid. The model size is now 100.2cmX100cmX10.1cm. The matrix and fracture blocks are again not shown to the relative scale.

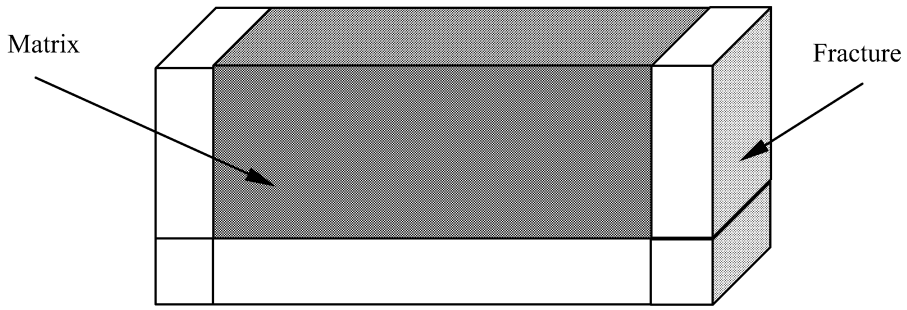

Figure 4. Equivalent dual-porosity model of 3x1x2 coarse-grid (model type-2 is converted).

Simulation Aspects

The system involves water displacing oil. The basic reservoir properties (rock and fluid) used in the simulation are listed in Table 1. The rock relative permeability and capillary pressure curves for the matrix can be seen in Fig. 5 and 6 respectively. For simplicity, linear relative permeability and zero capillary pressure have been assumed for the fracture.

The models were initialised with a pressure of 300-atma referenced at the top of the reservoir. Diameter of the wells was taken to be 0.01 cm. Injection and production wells were set to be ‘rate control’ and ‘bottom hole

Table 1. ***Basic reservoir properties.***	
Property	Value
Matrix permeability, k_{ma}	1.0 md
Fracture permeability, k_f	10,000.0 md
Matrix porosity, ϕ_{ma}	0.19
Fracture porosity, ϕ_f	1.0
Reservoir pressure, P	300.0 atma
Oil viscosity, μ_o	2.0 cp
Water viscosity, μ_w	0.5 cp
Oil formation volume factor, B_o	1.0 rml/sml
Water formation volume factor, B_w	1.0 rml/sml
Connate water saturation, S_{wi}	0.25
Residual oil saturation, S_{or}	0.3
Oil density, ρ_o	0.833 g/ml
Water density, ρ_w	1.025 g/ml

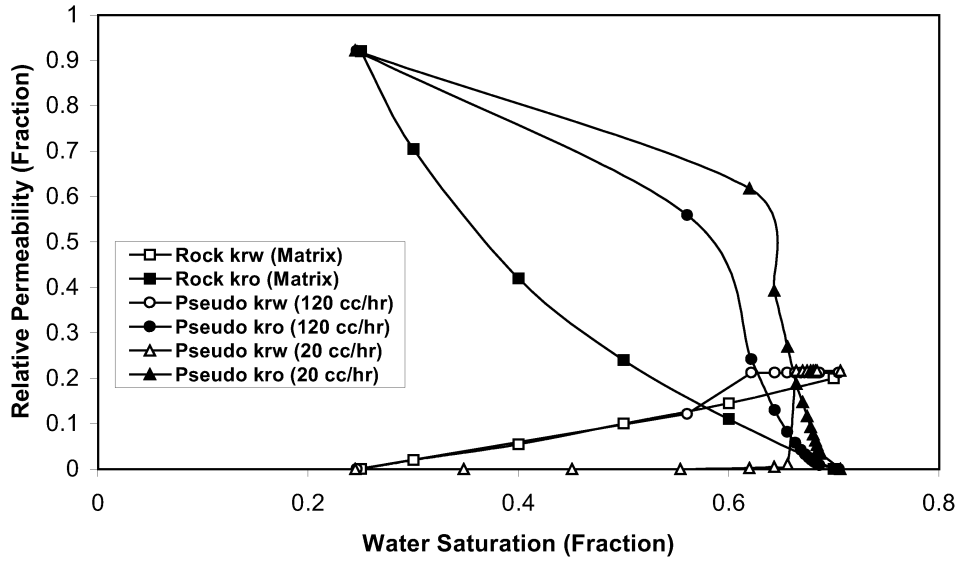

Figure 5. Rock and pseudo relative permeability curves (Kyte and Berry pseudos for model type-1 at 20 and 120 cc/hr injection rates).

URN:NBN:no-2347

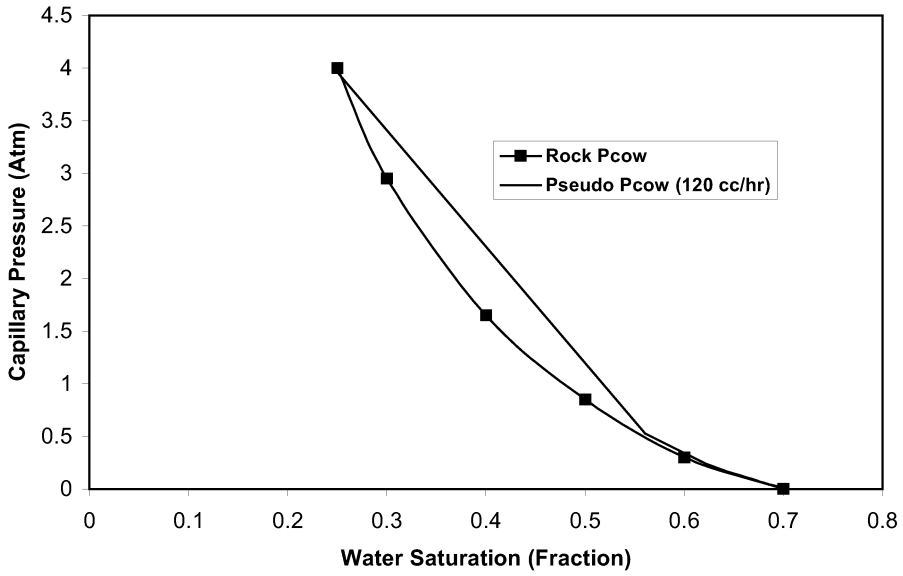

Figure 6: Rock and pseudo capillary pressure curves (Kyte and Berry pseudos for model type-1 at 120 cc/hr injection rate).

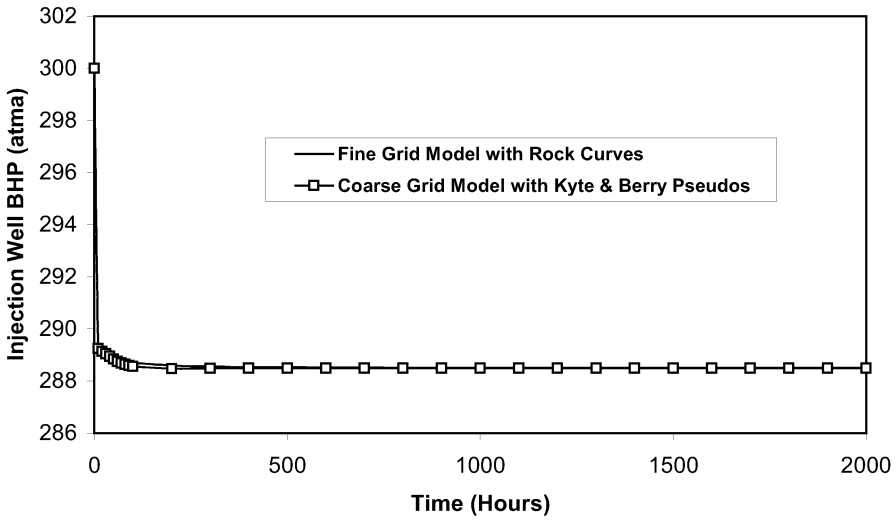

Figure 7. Change of injection well bottom hole pressure with time (model type-2, injection rate 20 cc/hr).

URN:NBN:no-2347

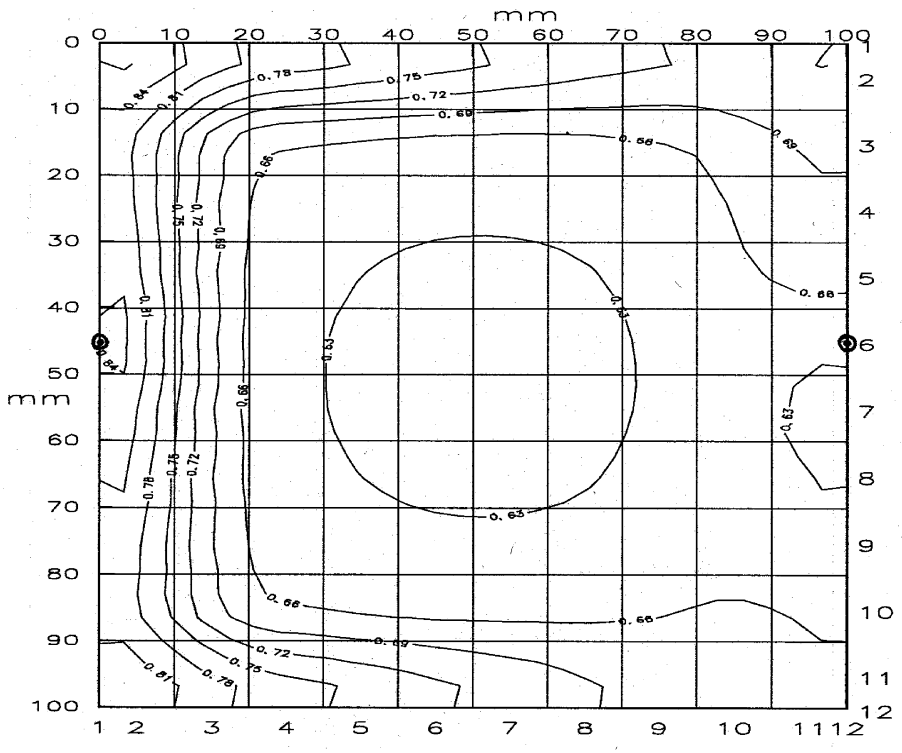

Figure 8. Water saturation contour map for the fine-grid model of type-2 at 200 hours (prior to water break-through), injection rate 20 cc/hr.

pressure control respectively. The minimum bottom hole pressure was set at 288.0 atma. As an example, the bottom hole pressure change with time for injection well in fine- and coarse-grid models of type-2 is plotted in Fig. 7. In order to see how the water-front behaves, a water saturation contour map has been presented in Fig. 8 for the fine-grid model of type-2 at 200 hours (prior to water break-through).

The two fine-grid models were simulated at four different injection rates (20, 40, 80 and 120 cc/hr) to observe the rate sensitivity of the models. Pseudo curves were generated for the respective coarse-grid models using: Kyte & Berry, Pore Volume Weighted, Weighted Relative Permeability and Stone

URN:NBN:no-2347

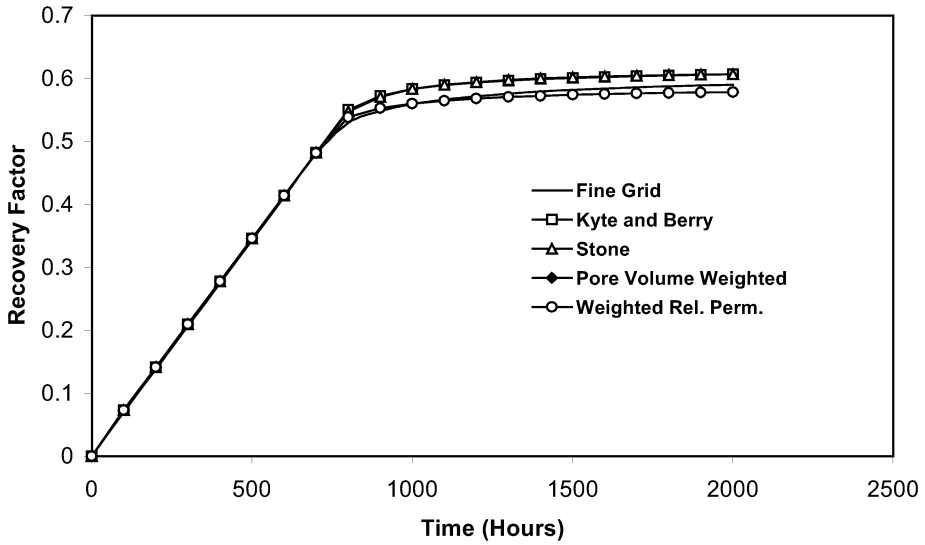

Figure 9. Field oil recovery factor (model type- 1,injection rate 20 cc/hr).

methods. The coarse-grid models were simulated at these rates using the generated pseudos. For dual-porosity model, the rock curves and four different pseudo curves were tested at a single injection rate (40 cc/hr). For comparison purpose, the Kyte and Berry pseudo relative permeability curves generated for model type-1 at 20- and 120-cc/hr injection rates are included in Fig. 5. The pseudo capillary pressure curve for the same model at 120 cc/hr injection rate is included in Fig. 6.

Results and Discussion

Model Type-1

The field oil recovery factor and field water cut obtained from fine-grid simulation are compared with those obtained from coarse-grid simulation using four different pseudos and at four different rates. Fig. 9 through 12 present the comparison plots for field oil recovery factor and Fig. 13 through 16 for field water cut respectively.

Some particular trends can be observed in the field oil recovery comparison plots. During early stages of the displacement process, where most of the

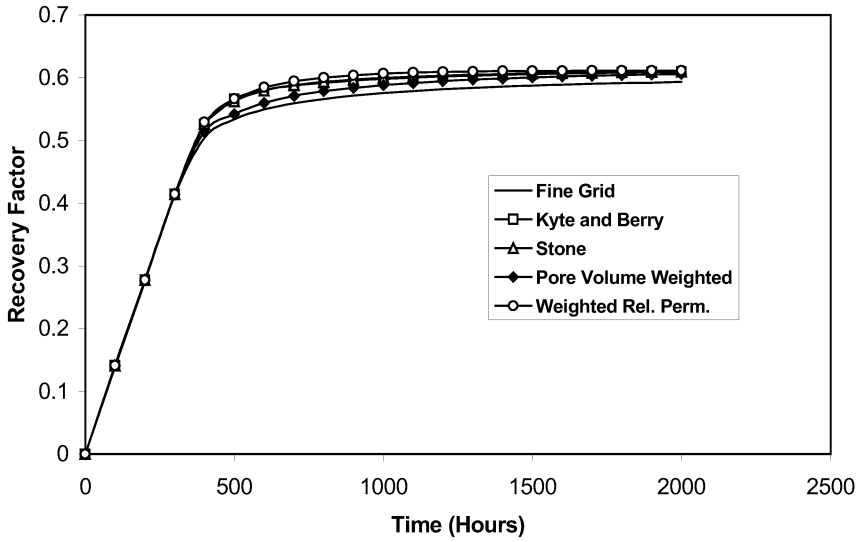

Figure 10. Field oil recovery factor (model type-1,injection rate 40 cc/hr).

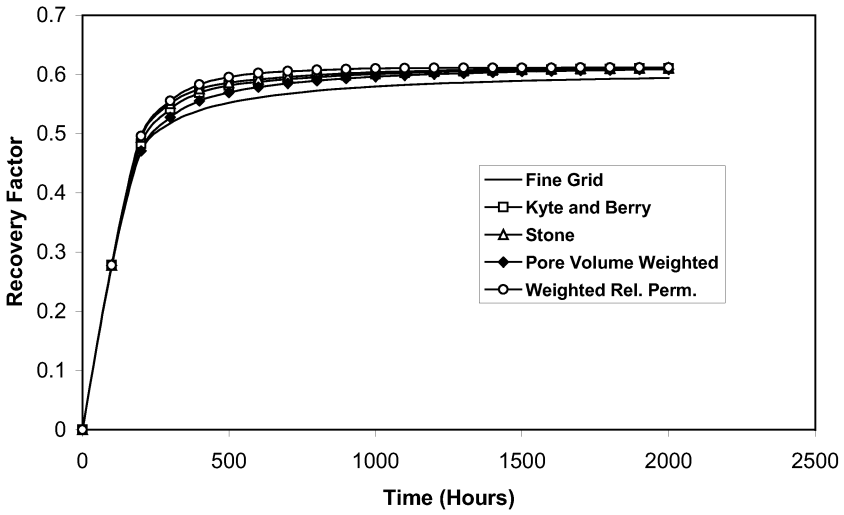

Figure 11. Field oil recovery factor (model type-1, injection rate 80 cc/hr).

URN:NBN:no-2347

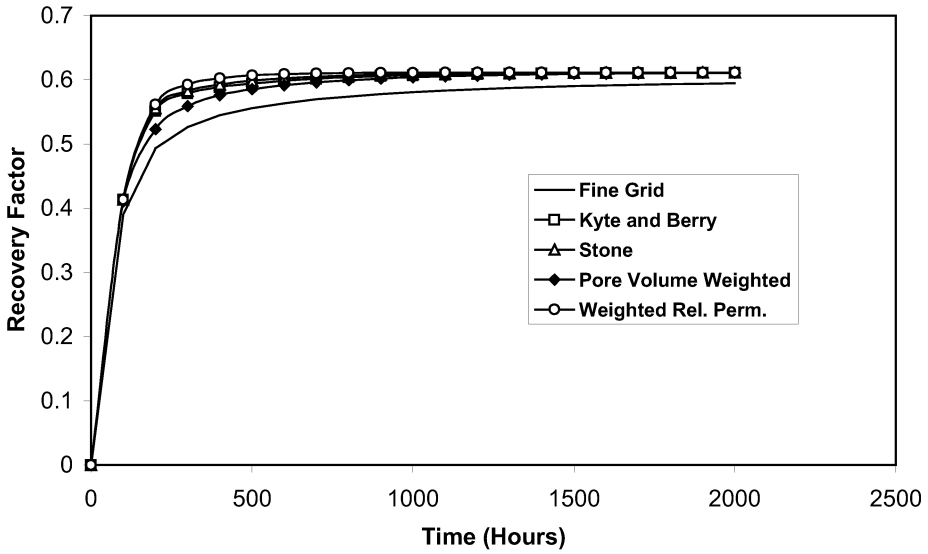

Figure 12. Field oil recovery factor (model type-1, injection rate 120 cc/hr).

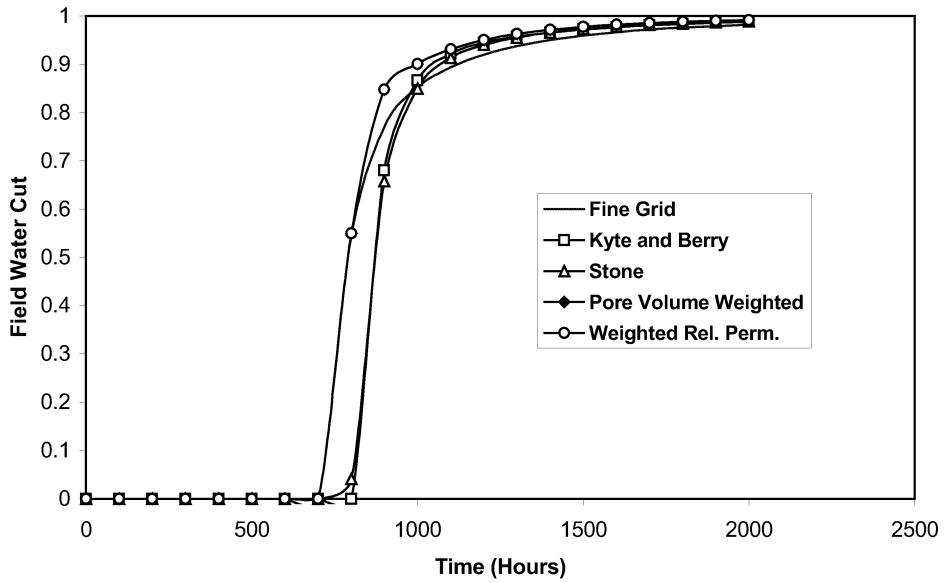

Figure 13. Field water cut (model type-1, injection rate 20 cc/hr).

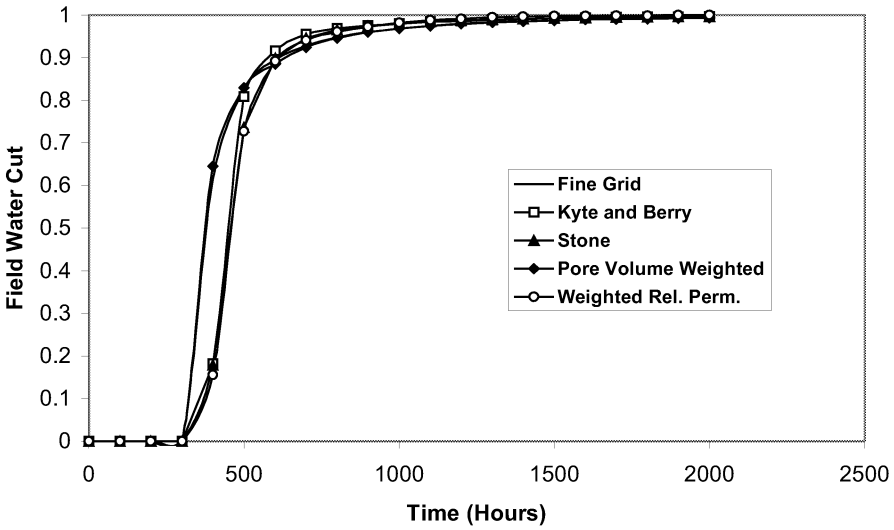

Figure 14. Field water cut (model type-1, injection rate 40 cc/hr).

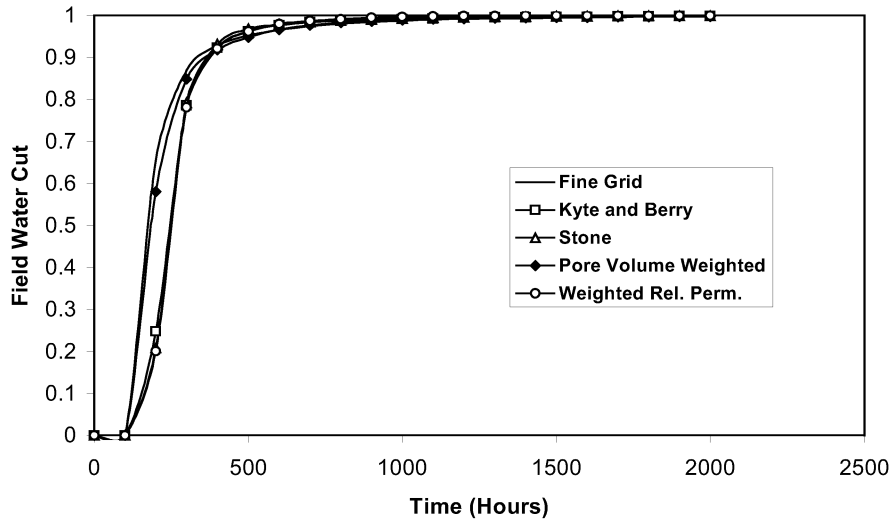

Figure 15. Field water cut (model type-1, injection rate 80 cc/hr).

URN:NBN:no-2347

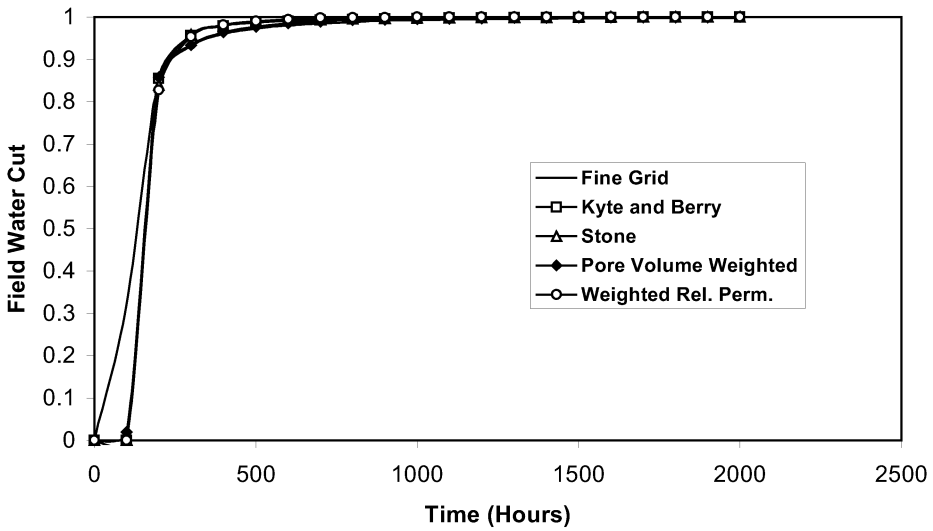

Figure 16. Field water cut (model type-1, injection rate 120 cc/hr).

recovery is taking place, the recovery obtained from coarse-grid simulations (with all four pseudos and at four rates) duplicate the recovery obtained from fine-grid simulation. At later time, coarse-grid recoveries are slightly higher than fine-grid recovery, but they appear to be rate sensitive. The difference is minimum at lower rates but increases as rate increases. At all rates, Kyte & Berry type pseudos give almost identical results as that of Stone but at higher rates, Weighted Relative Permeability pseudos provide similar results as that of Kyte & Berry and Stone. Recoveries obtained from Pore Volume Weighted pseudos are the closest to the fine-grid results at all rates.

Similar trends can be observed in the field water cut comparison plots. Time of water breakthrough appears to be similar for fine- and coarse-grid simulations at lower rates. At very high rate (120 cc/hr) the coarse-grid simulation delays water breakthrough. The probable reason for early breakthrough in fine-grid model is that the water moves very fast through the fractures and arrives at the production well quite early. The fractures are absent in the coarse-grid model and therefore, channelling is not possible.

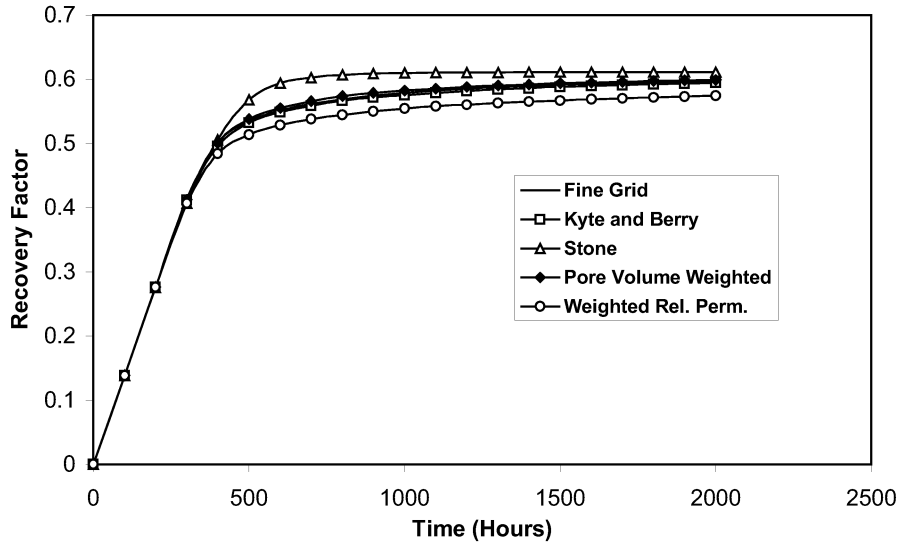

Figure 17. Field oil recovery factor (model type-2, injection rate 20 cc/hr).

Model Type-2

Fig. 17 through 20 present the comparison plots for field oil recovery factor and Fig. 21 through 24 for field water cut respectively for model type-2.

Considering model type-1, a similar conclusion can be made for this model, in terms of oil recovery, during the early stage of displacement. Fine-grid recovery and coarse-grid recoveries with different pseudos are very similar. Over time, a very good recovery match is obtained at all rates between fine-grid simulation and coarse-grid simulations, using only Kyte & Berry and Pore Volume Weighted type pseudos. Stone and Weighted Relative Permeability type pseudos appear to be slightly rate sensitive. Stone pseudos give a higher recovery, whereas Weighted Relative Permeability pseudos give lower recovery at all rates.

No particular water cut trend can be established among the different pseudo techniques. However, the time of water breakthrough for fine- and coarse-grid simulations is very similar.

URN:NBN:no-2347

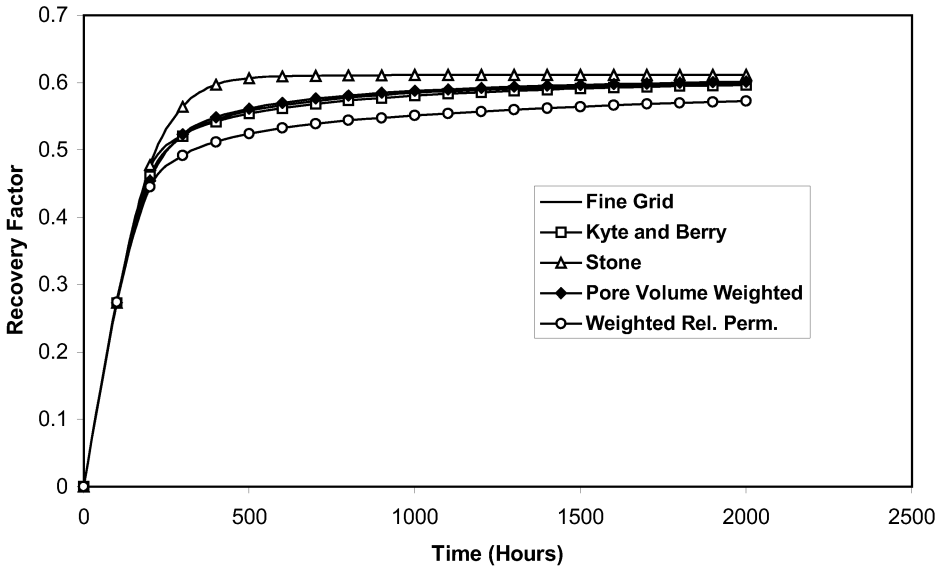

Figure 18. Field oil recovery factor (model type-2, injection rate 40 cc/hr).

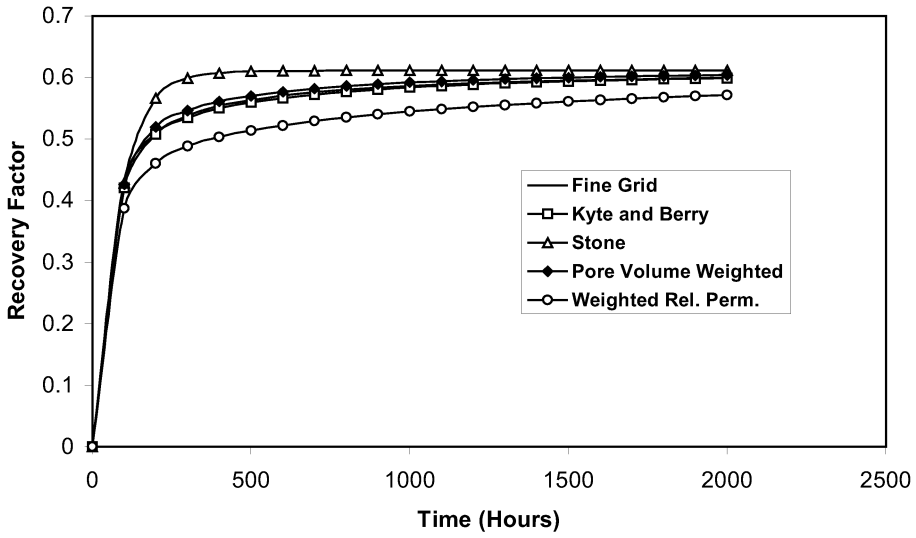

Figure 19. Field oil recovery factor (model type-2, injection rate 80 cc/hr).

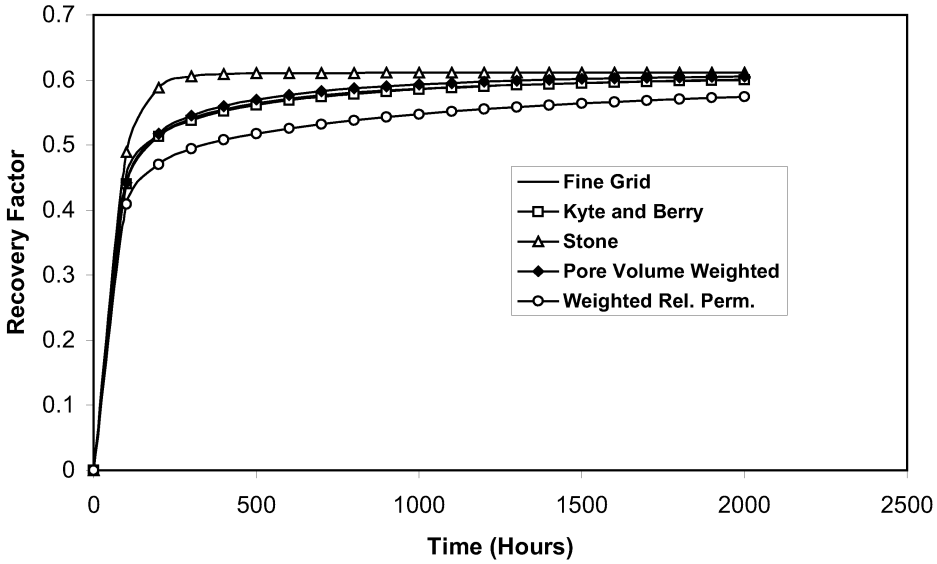

Figure 20. Field oil recovery factor (model type-2, injection rate 120 cc/hr).

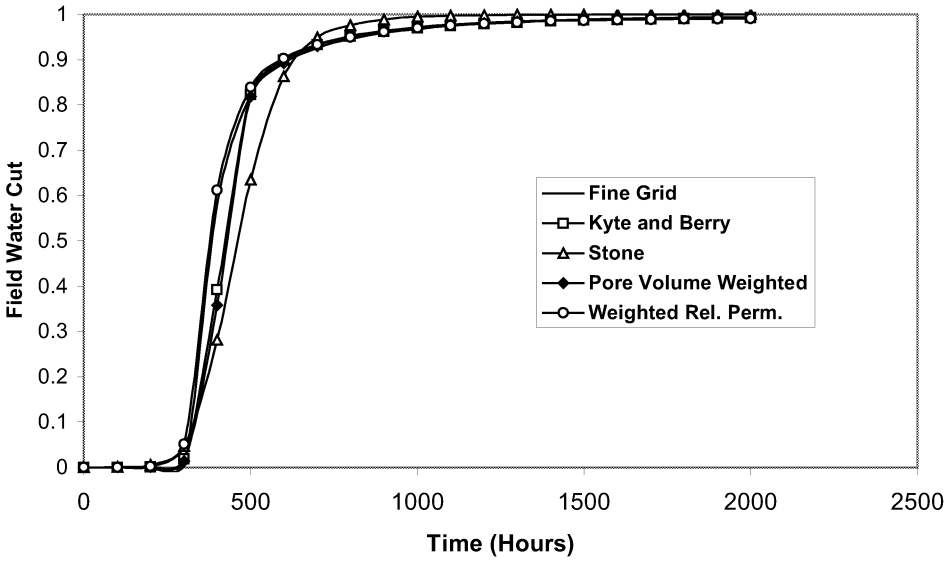

Figure 21. Field water cut (model type-2, injection rate 20 cc/hr).

URN:NBN:no-2347

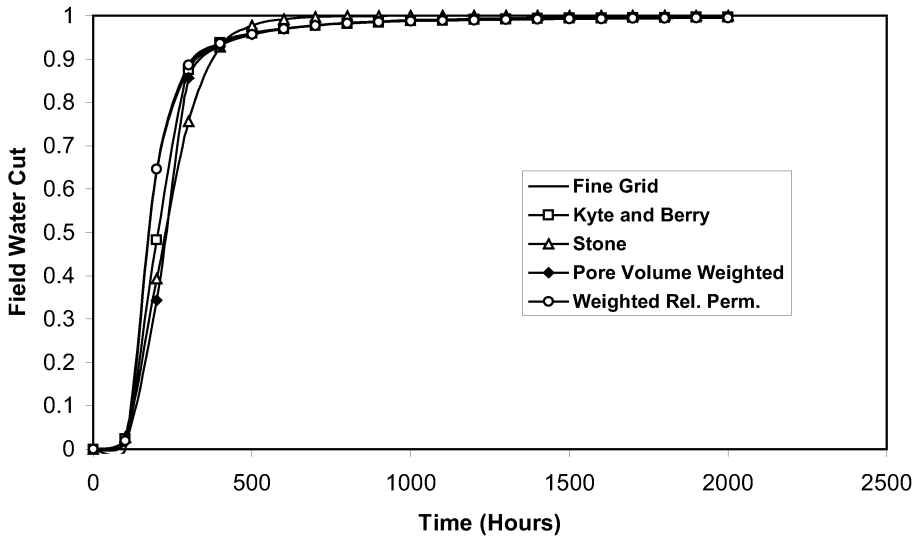

Figure 22. Field water cut (model type-2, injection rate 40 cc/hr).

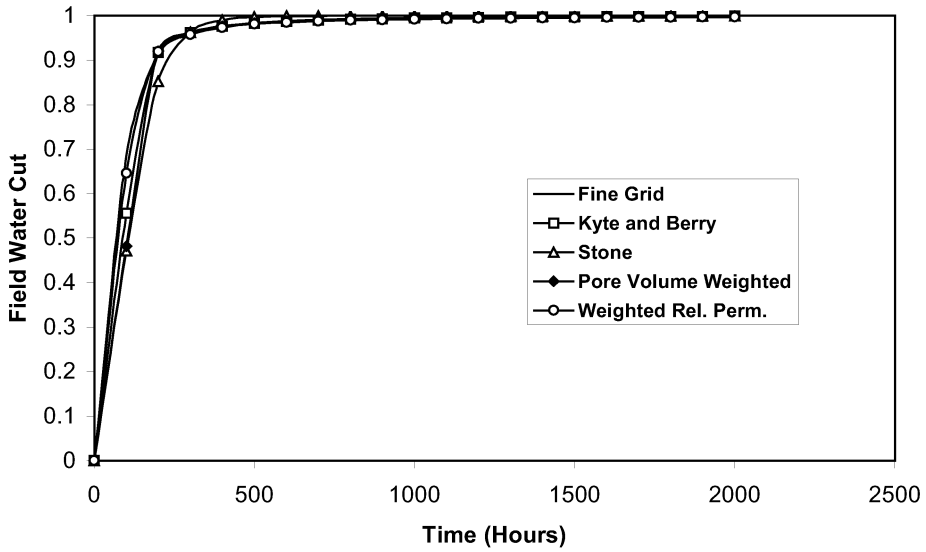

Figure 23. Field water cut (model type-2, injection rate 80 cc/hr).

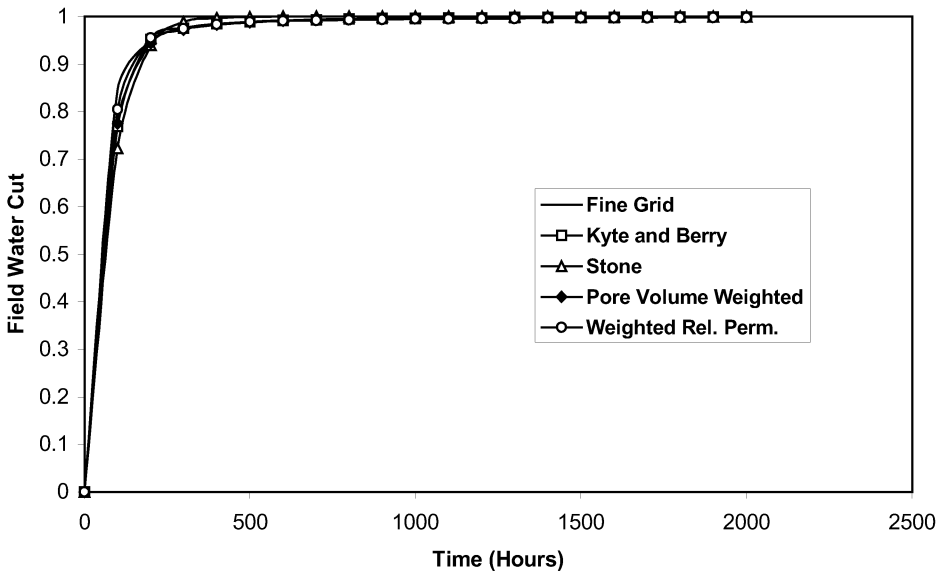

Figure 24. Field water cut (model type-2, injection rate 120 cc/hr).

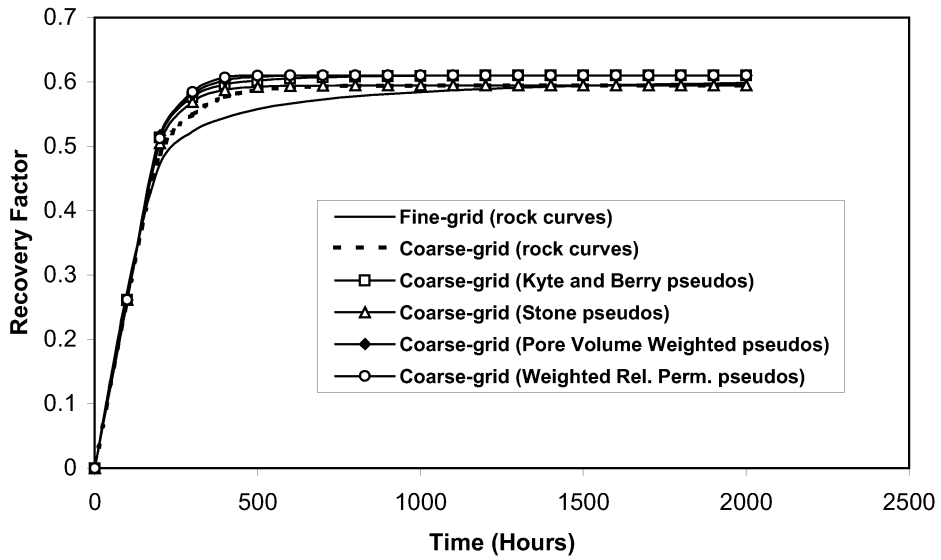

Figure 25. Field oil recovery factor (dual- porosity model, injection rate 40 cc/hr).

URN:NBN:no-2347

Dual-Porosity Model

The fine-grid model (not shown in Fig. 4) has been simulated with rock curves and the coarse-grid model has been simulated with both rock- and four different pseudo-curves. The pseudo curves are generated from a dual-porosity fine-grid run. The fine-grid results are compared with the coarse-grid results. The oil recovery and water cut comparison plots are presented in Fig. 25 and 26 respectively. In simulating dual-porosity models, the shape factor (σ), which controls the flow between the matrix and the fracture was assigned on a cell by cell basis and was calculated as outlined by Kazemi *et al.* (1976).

While the coarse-grid results are not very different from fine-grid results in model type-2, in this model the results obtained from coarse-grid simulation using either rock or pseudo curves are different from fine-grid results. The exception is oil recovery in the early stages. The coarse-grid model with rock curves gives identical results to those with pseudo curves. This means that the four pseudo generation techniques under consideration are not adequate to duplicate fine-grid results in a dual-porosity model. Possibly a special type of pseudo generation technique is needed to describe the flow behaviour of the coarse-matrix grid.

Further Work

In this study, the rock and fluid properties have been taken to reflect a typical water-wet chalk reservoir. The fine-grid block dimensions have been selected in such a way so that the coarse-grid block becomes 1mx1m, a typical matrix block size of the North Sea Ekofisk field. Sensitivity studies are needed to see the effect of oil-to-water viscosity ratio. In addition, the model can be extended to three dimensional cases. These studies are not within the scope of this paper and have already been presented elsewhere (Talukdar *et al.* 2000).

Conclusions

In order to explore the applicability of conventional up-scaling techniques in fractured reservoir simulation, two two-dimensional fine-grid and equivalent coarse-grid simulation models have been developed and simulated with rock- and pseudo-curves respectively. Four different pseudo techniques have been investigated at four recovery rates and with only one

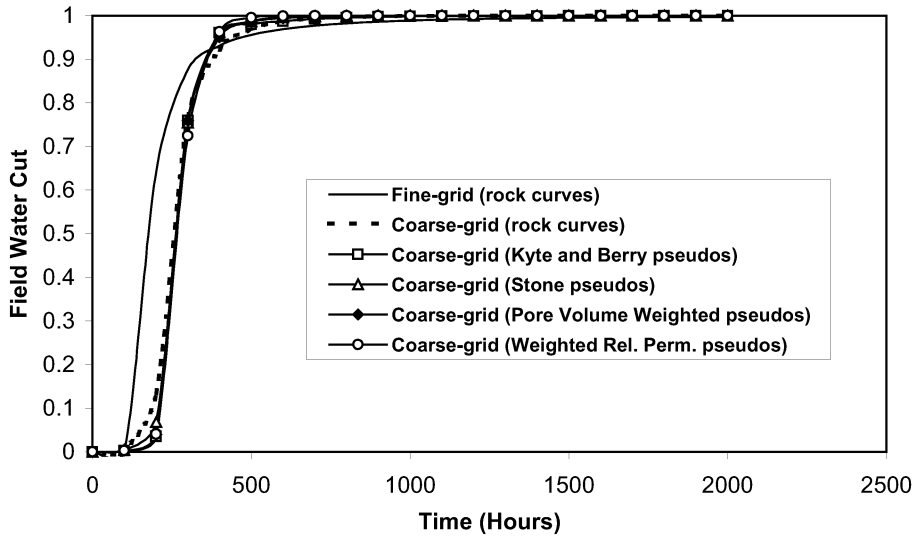

Figure 26. Field water cut (dual- porosity model, injection rate 40 cc/hr).

oil-to-water viscosity ratio. The pseudo techniques have also been applied to a dual-porosity case. From the results the following conclusions may be drawn:

- Kyte & Berry, Pore Volume Weighted, Weighted Relative Permeability, and Stone pseudo generation techniques may be used for fractured reservoir simulation.
- In model type-1, where the coarse-grid model does not contain separate fracture, but all the grids bear the generated pseudo properties, all of the four pseudo generation techniques appear to be rate sensitive. This model gives good result at low rates.

URN:NBN:no-2347

- In model type-1, Kyte & Berry and Stone pseudos give almost identical results at all rates. At higher rates, Weighted Relative Permeability pseudos provide similar results as that of Kyte & Berry and Stone. Results obtained from Pore Volume Weighted pseudos are the closest to the fine-grid results at all rates.
- In model type-2, where both the fine- and course-grid models contain separate fracture, the Stone and Weighted Relative Permeability pseudos are slightly rate sensitive but the other two are independent of rate.
- In model type-2, Kyte & Berry and Pore Volume Weighted pseudos provide almost exactly the same recovery as the fine-grid model at all rates. Stone pseudos give higher recovery and Weighted Relative Permeability pseudos give lower recovery at all rates.
- Results from coarse-grid in dual-porosity model using either rock or pseudo curves are different from fine-grid results. The coarse-grid model with rock curves gives results identical to those with pseudo curves. The implication of these results is that pseudoization by these four conventional methods in dual-porosity model is not adequate. Therefore, a special type of pseudo generation method may be needed for this model.

Nomenclature

b_{pn}, B_{pN}	Fine- and coarse-grid formation volume factors
d_n, D_N	Fine- and coarse-grid cell center depths
f^d_{pn}, F^d_{pN}	Fine- and coarse-grid phase flows in the positive d direction
g	Newton's constant
kr^d_{pn}, Kr^d_{pN}	Phase relative permeability values for fine- and coarse-grids Functions of s_p and S_p respectively
p_{pn}, P_{pN}	Fine- and coarse-grid pressures for phase p
P_{cow}, P_o, P_w	Oil-water capillary pressure, oil- and water-phase pressures, all for coarse-grids
s_{pn}, S_{pN}	Fine- and coarse-grid saturations for phase p
t_d, T_d	Fine- and coarse-grid transmissibilities in d direction
v_n, V_N	Fine- and coarse-grid volumes
w_{ijk}	Weighing factors for fine-grid n
ϕ_n, Φ_N	Fine- and coarse-grid porosities

μ_{pn}, μ_{pN}	Fine- and coarse-grid phase viscosities
ρ_{pn}, ρ_{pN}	Fine- and coarse-grid phase densities
q_p, Q_p	Fine- and coarse-grid phase reservoir volume flows
q_t, Q_t	Fine- and coarse-grid total reservoir volume flows (sum of all phases)
λ_t	Coarse-grid total mobility

Subscripts and Superscripts

d	Direction of flow (x, y or z)
p	Phase index (o for oil, w for water, etc.)
n, N	Cell numbers in normal order fine- and coarse grids
i, j, k	Fine-grid cell indices in x, y and z directions. The position of a cell may be specified by its indices (i, j, k) or cell number, n.
I, J, K	Coarse-grid cell indices in x, y and z directions

References

Barker, J.W. and Thibeau, S., 1996: A Critical Review of the Use of Pseudorelative Permeabilities for Upscaling, *paper SPE 35491 presented at the 1996 European 3D Reservoir Modeling Conference, Stavanger, Norway, April 16-19*.

Bourbiaux, B.J., Cacas, M.C., Sarda, S. and Sabathier, J.C., 1997: A Fast and Efficient Methodology to Convert Fractured Reservoir Images into a Dual-Porosity Model, *paper SPE 38907 presented at the 1997 Annual Technical Conference and Exhibition, Texas, USA, October 5-8*.

Dean, R.H. and Lo, L.L., 1988: Simulations of Naturally Fractured Reservoirs, *SPERE*, *May 1988*, 638-648.

Guzman, R.E., Giordano, D., Fayers, F.J., Godi, A. and Aziz, K., 1996: Evaluation of Dynamic Pseudo Functions for Reservoir Simulation, *paper SPE 35157 presented at the 1996 SPE Annual Technical Conference and Exhibition, Colorado, USA, October 6-9*.

Jacks, H.H., Smith, O.J.E., and Mattax, C.C., 1973: The modeling of a Three-Dimensional Reservoir with a Two-Dimensional Reservoir Simulator-The Use of Dynamic Pseudo Functions, *SPEJ*, *June 1973*, 175.

URN:NBN:no-2347

Kazemi, H., Merrill Jr., L.S., Porterfield, K.L. and Zeman, P.R., 1976: Numerical Simulation of Water-Oil Flow in Naturally Fractured Reservoirs, *SPEJ*, *Dec. 1976*, 317-326.

Kleppe, J. and Morse, R.A., 1974: Oil Production from Fractured Reservoirs by Water Displacement, *paper SPE 5084 presented at the 49th Annual Fall Meeting, Texas, Oct. 6-9, 1974*.

Kyte, J.R., 1970: A Centrifuge Method to Predict Matrix-Block Recovery in Fractured Reservoirs, *SPEJ*, *June 1970*, 164.

Kyte, J.R. and Berry, D.W., 1975: New Pseudo Functions to Control Numerical Dispersion," *SPEJ*, *Aug. 1975*, 269-276.

Lough, M.F., Lee, S.H. and Kamath, J., 1996: A New Method to Calculate the Effective Permeability of Grid Blocks Used in the Simulation of Natually Fractured Reservoirs, *paper SPE 36730 presented at the 1996 Annual Technical Conference and Exhibition, Colorado, USA, Oct. 6-9*.

Mattax, C.C. and Kyte, J.R., 1962: Imbibition Oil Recovery from Fractured Water Drive Reservoir, *SPEJ*, *June 1962*, 177.

Rossen, R.H., 1977: Simulation of Naturally Fractured Reservoirs with Semi-Implicit Source Terms, *SPEJ*, *June 1977*, 201.

Rossen, R.H. and Shen, E.I.C., 1989: Simulation of Gas/Oil Drainage and Water/Oil Imbibition in Naturally Fractured Reservoirs, *SPERE*, *Nov. 1989*, 464.

Schlumberger GeoQuest, 1998: *Pseudo Reference Manual, Version 1998A*.

Stone, H.L., 1991: Rigorous Black Oil Pseudofunctions, *paper SPE 21207 presented at the 11th SPE Symposium on Reservoir Simulation, Anaheim, California, Feb. 17-20, 1991*.

Talukdar, M.S., Banu, H.A., Torsæter, O. and Kleppe, J., 2000: Applicability and Rate Sensitivity of Several Up Scaling Techniques in Fractured Reservoir Simulation, *paper SPE 59048 presented at the 2000 SPE International Petroleum Conference and Exhibition in Mexico, Villahermosa, Mexico, 1-3 February*.

Thomas, L.K., Dixon, T.N. and Pierson, R.G., 1983: Fractured Reservoir Simulation, *SPEJ*, *Feb. 1983*, 42-54.

Warren, J.E. and Root, P.J., 1963: The Behavior of Naturally Fractured Reservoir, *SPEJ*, *September 1963*, 245.

Paper XI

URN:NBN:no-2347

SPE 59048

Applicability and Rate Sensitivity of Several Up Scaling Techniques in Fractured Reservoir Simulation

M.S. Talukdar, SPE, H.A. Banu*, O. Torsæter, SPE and J. Kleppe, SPE; Norwegian University of Science and Technology; *Now with Bangladesh Oil, Gas and Mineral Corporation (Petrobangla)

This paper was prepared for presentation at the 2000 SPE International Petroleum Conference and Exhibition in Mexico held in Villahermosa, Mexico, 1–3 February 2000.

Abstract

This paper presents the applicability/validity and rate sensitivity of several conventional up-scaling techniques in fractured reservoir simulation. Three different models have been developed and simulated using Kyte and Berry, Pore Volume Weighted, Weighted Relative Permeability, and Stone type pseudos at different rates and with different oil-to-water viscosity ratio.

From the results it can be concluded that these techniques may be used in fractured reservoir simulation in order to reduce number of simulation grids as well as to synthesize details of small-scale fluid mechanics and reservoir heterogeneity. They may or may not be rate sensitive depending on the model type.

Introduction

Up-scaling (pseudo) techniques are widely used in conventional reservoir simulation to synthesize details of small-scale fluid mechanics and reservoir heterogeneity in coarse-grid models. The frequent uses are to reduce the number of dimensions and layers, to control numerical dispersion, and to take into account the well effects, such as partial penetration, coning, etc. In fractured reservoirs, up-scaling techniques are mainly concerned with parameterization of the conceptual model of Warren and Root[1]. The essential parameters for this model are the equivalent fracture permeability, equivalent matrix block dimensions and block effective permeability.

Lough, Lee and Kamath[2] developed an up-scaling technique to calculate the effective permeability of grid blocks. Bourbiaux *et al.*[3] presented another method to compute equivalent fracture permeability and equivalent matrix block dimensions from 3D geological images of the fracture network.

Jacks *et al.*[4] presented procedures for calculating dynamic pseudo-relative permeabilities from vertical cross-section model runs which can be used to simulate three-dimensional flow accurately in a two-dimensional areal model. Kyte and Berry[5] improved Jacks' model and included pseudo-capillary pressure. Thomas *et al.*[6] introduced pseudo-capillary pressure for matrix blocks calculated from vertical equilibrium calculations. Rossen and Shen[7] calculated pseudo-capillary-pressure curves for both the matrix and fracture that are similar to those derived by Dean and Lo[8]. Unlike Dean and Lo, however, they developed a more efficient procedure based on single fine-grid simulation without history matching. Stone[9] proposed a new method of calculating black oil pseudo-functions from fine-grid simulation. This method reproduces fine-grid accuracy when applied in coarse-grid model.

Simulation of large, complex reservoirs often requires an unacceptably large number of computational grid blocks. The use of pseudo-functions is one way of decreasing the number of grids to a more tractable level with minimal loss of simulation accuracy. A proper up-scaling algorithm can bridge the gap between the reservoir description grid and the simulation grid.

The application of the conventional up-scaling techniques to predict fractured reservoir performance through grid coarsening can dramatically reduce the time and cost needed for field-scale simulation. Talukdar *et al.*[10] introduced conventional up-scaling techniques in fractured reservoir simulation. They developed two 2-dimensional models and simulated using Kyte and Berry, Pore Volume Weighted, Weighted Relative Permeability, and Stone type pseudos. The pseudo techniques were tested at four different rates with a single oil-to-water viscosity ratio of 4. This paper presents similar studies using viscosity ratio of 1 and 8. Moreover, the study has been extended to 3-dimensional model.

The theory of the convensional up-scaling techniques investigated in the study (Kyte and Berry, Pore Volume Weighted, Weighted Relative Permeability, and Stone) is

reviewed elsewhere[10]. The study procedure is straightforward. Fine-grid and equivalent coarse-grid simulation models were developed. Fine-grid models were simulated using rock curves to predict actual behavior of the models. Fine-grid simulation results were used to generate pseudos for all of the respective coarse blocks in the equivalent coarse-grid models. Coarse-grid models were then simulated using the generated pseudos. The fine-grid and equivalent coarse-grid simulation results were compared.

The results reveal that these up-scaling techniques may be applied in 2- and 3-dimensional fractured reservoir simulation. They may be used to coarsen simulation grids and to capture details of small-scale reservoir heterogeneity for a wide range of recovery rate and viscosity ratio.

Simulation Models

Two 2-dimensional and one 3-dimensional models have been developed. Each of the models consists of a fine-grid and an equivalent coarse-grid system. The 2-dimensional models will be termed as Model-1 and Model-2 and the 3-dimensional model as 3D-model.

Model-1. Fig. 1 illustrates the fine-grid and the equivalent coarse-grid systems. Fine-grid system consists of 12x12x1 grids. The hundred matrix blocks (shaded gray) are surrounded by fracture blocks. Matrix blocks have dimensions 10cmx10cmx10cm each, whereas the fracture blocks have 0.1cmx0.1cmx10cm each making the total model size of 100.2cmx100.2cmx10cm.

The equivalent coarse-grid system consists of three matrix blocks and no fracture. The main matrix block (middle) has dimension 100cmx100.2cmx10cm. The two narrow matrix blocks at the two opposite sides having dimensions 0.1cmx100.2cmx10cm each are just to put the wells at the respective locations.

The objective for developing this model is to convert fractured fine-grid system into equivalent coarse-grid system containing no fracture, which, in turn, may be simulated as conventional reservoir.

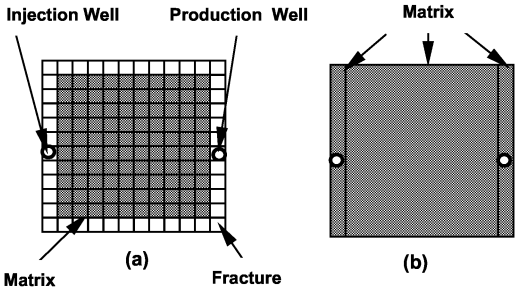

Fig. 1— Model-1 (a) 12x12x1 fine-grid system (b) 3x1x1 equivalent coarse-grid system

Model-2. The fine- and equivalent coarse-grid systems of Model-2 are illustrated in Fig. 2. The fine-grid system is exactly the same as Model-1, but unlike Model-1, the only one matrix block in coarse-grid system is surrounded by fractures. The equivalent coarse-grid system has 3x3x1 grid blocks.

The objective for this model is to convert fractured fine-grid system into equivalent coarse-grid dual-porosity system.

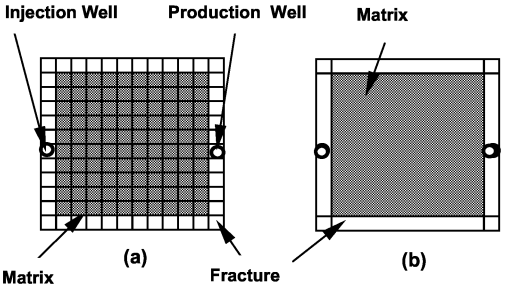

Fig. 2— Model-2 (a) 12x12 fine-grid system (b) 3x3 equivalent coarse-grid system

3D-Model. Fig. 3 illustrates the model. The fine-grid system of this model has been developed through adding 10 similar layers as the one of Model-1 or 2. The fine-grid system now consists of 12x12X10 grids and the equivalent coarse-grid system consists of 3x3x1 grids. The dimensions of the fine-grids are seleted in such a way to make the size of the coarse matrix block of 100cmx100cmx100cm. In both fine- and coarse-grid systems, the matrix blocks are surrounded by fracture blocks.

The model converts fractured fine-grid 3D system into equivalent 2D coarse-grid dual-porosity system.

Controls for the Simulator. The simulation models consist of one injection and one production well. The injection well is controlled by surface injection rate whereas the production well is set at bottom hole pressure control. The minimum bottom hole pressure is 288 atma. The models were initialized with a pressure of 300 atma referenced at the top of the reservoir. The wells are connected to the whole depth of the models. The well connection transmissibility was calculated manually and given as an input to the simulator.

Rock and Fluid Properties. The basic rock and fluid properties are listed in Table 1. The rock relative permeability and capillary pressure curves for matrix can be seen in Fig. 4 and Fig. 5 respectively. The fracture blocks are defined as separate region in the reservoir in order to assign different relative permeability and capillary pressure. For simplicity linear relative permeability and zero capillary pressure have been assumed for the fracture.

Run Options. The objective of the study is to investigate the applicability and rate sensitivity of widely used conventional up-scaling techniques in fractured reservoir simulation. Numerous simulation runs have been made to investigate the applicability of four up-scaling techniques in three different

fractured reservoir models. The sensitivity of these techniques is investigated at different recovery rates and at different oil-to-water viscosity ratios.

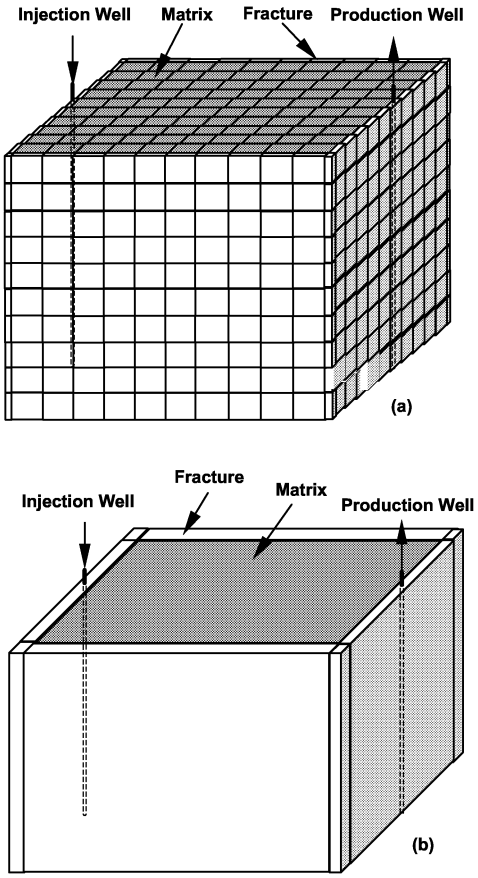

Fig. 3— 3D-model (a) 12x12x10 fine-grid system (b) 3x3x1 equivalent coarse-grid system

Water was injected at very high rates to flood the fracture almost instantly so that water imbibition mechanism takes place. The injection rates used for Model-1 and Model-2 are 20 cc/hr, 40cc/hr, 80cc/hr and 120 cc/hr. 3D-model has volume 10 times higher than the 2D-models. Three injection rates are considered for this model. These are 200 cc/hr, 600 cc/hr and 1200 cc/hr.

The oil-to-water viscosity ratio is 4. To investigate the effect of viscosity ratio, oil viscosity of 0.5 cp and 4.0 cp are also considered to make the ratio of 1 and 8 respectively.

The fine-grid systems of the three models are simulated with rock curves at the above rates and viscosity ratios. The coarse-grid systems are also simulated at these rates and viscosity ratios using both rock curve and four different pseudo curves. Field oil recovery efficiency and field water cut are reported for comparison. Therefore, an enormous volume of data has been generated. The significant results are discussed in the following section.

Table 1—Basic rock and fluid properties

Property	Value
Matrix permeability, k_{ma}	1.0 md
Fracture permeability, k_f	10,000.0 md
Matrix porosity, ϕ_{ma}	0.19
Fracture porosity, ϕ_f	1.0
Reservoir pressure, P	300.0 atma
Oil viscosity, μ_o	2.0 cp
Water viscosity, μ_w	0.5 cp
Oil formation volume factor, B_o	1.0 rml/sml
Water formation volume factor, B_w	1.0 rml/sml
Connate water saturation, S_{wi}	0.25
Residual oil saturation, S_{or}	0.3
Oil density, ρ_o	0.833 g/ml
Water density, ρ_w	1.025 g/ml

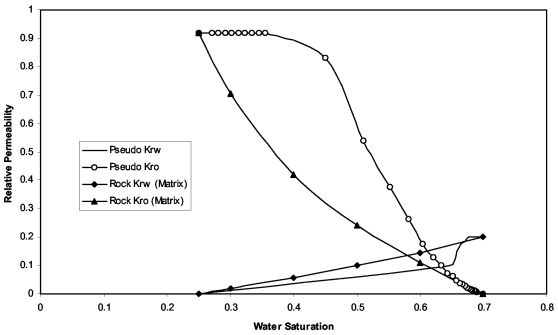

Fig. 4—Rock and pseudo relative permeability curves (Kyte and Berry pseudo curves are generated for 3D-model at 200 cc/hr injection rate and viscosity ratio of 8.0)

Results and Discussion

Pseudo Curves. The generated pseudo curves are different from rock curves. For comparison purpose, the Kyte and Berry pseudo- relative permeability and capillary pressure curves for 3D-model at 200 cc/hr injection rate and viscosity ratio of 8.0 are included in Fig. 4 and 5 respectively. The pseudo curves exhibit typical double slope behavior of fractured reservoir. Similar behavior is observed for other cases.

Oil Recovery and Water Cut. The field oil recovery factor and field water cut obtained from fine-grid simulation are compared with those obtained from coarse-grid simulation using both rock curve and different pseudo curves. The results for each of the models are discussed separately.

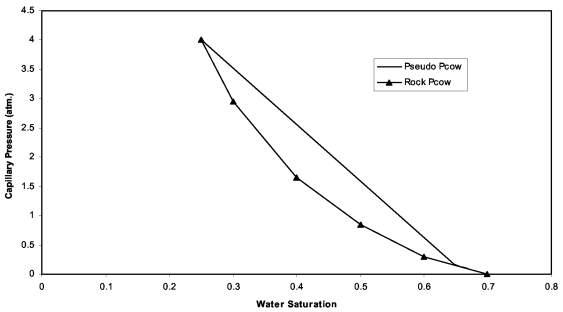

Fig. 5—Rock and pseudo capillary pressure curves (Kyte and Berry pseudo curves are generated for 3D-model at 200 cc/hr injection rate and viscosity ratio of 8.0)

Model-1. The field oil recovery factor and field water cut at the lowest injection rate (20 cc/hr) and at the highest injection rate (120 cc/hr) for viscosity ratio of 1 are presented in Fig. 6 through 9. Similar plots for viscosity ratio of 8 are shown in Fig. 10 through 12. The results at 40 cc/hr and 80 cc/hr injection rates for these viscosity ratios are not included in this paper as the overall trend is consistent with these extreme cases. For similar model, the oil recovery and water cut at 20 cc/hr, 40 cc/hr, 80 cc/hr and 120 cc/hr for viscosity ratio of 4 are presented elsewhere[10].

Each of the figures contains six graphs. The solid line is the prediction of the actual behavior obtained from fine-grid simulation using rock curves. The broken line represents coarse-grid behavior obtained from rock curves. The other four graphs represent coarse-grid prediction from four different pseudo curves.

For oil-to-water viscosity ratio of 1, the field oil recovery prediction from coarse-grid simulation using different pseudo curves is very close to that obtained from fine-grid simulation using rock curves. These results are different from coarse-grid prediction using rock curve (Fig. 6 and 7). Almost similar trend is obtained for field water cut (Fig. 8 and 9). The pseudo techniques have limited rate sensitivity as they predict almost silimar behavior in oil recovery and water cut at low and high rates.

In Model-1, the pseudo techniques appear to be sensitive to viscosity ratio. At both low and high rates, field oil recovery factors predicted from pseudos have bigger deviation from fine-grid prediction for high viscosity ratio compared to those for low viscosity ratio. This is evident when Fig. 6 is compared with Fig. 10 or Fig. 7 with Fig. 11. Deviation in field water cut is also observed when Fig. 8 is compared with Fig. 12.

At high viscosity ratio, pseodo techniques are rate sensitive to some extent as they produce different trend at different rates (Fig. 10 and 11). Also at high rate (Fig. 11), the field oil recovery predictions from these techniques differ considerably from fine-grid prediction.

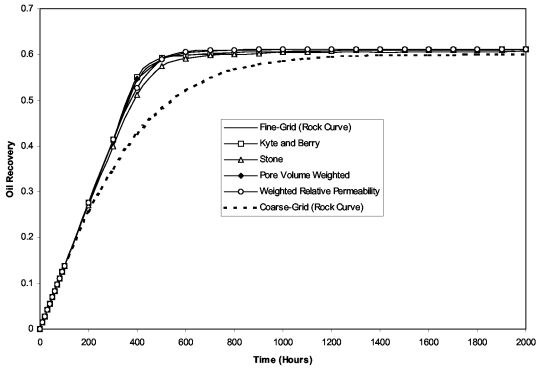

Fig. 6—Field oil recovery (Model-1, viscosity ratio 1, injection rate 20 cc/hr)

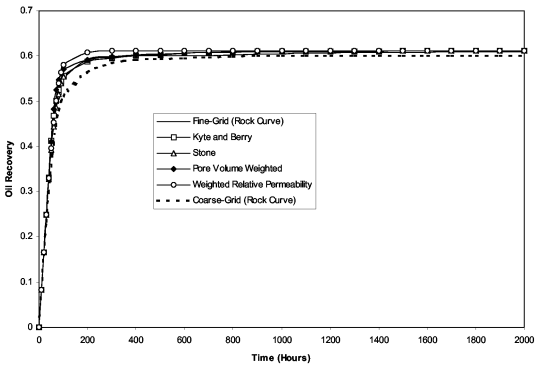

Fig. 7—Field oil recovery (Model-1, viscosity ratio 1, injection rate 120 cc/hr)

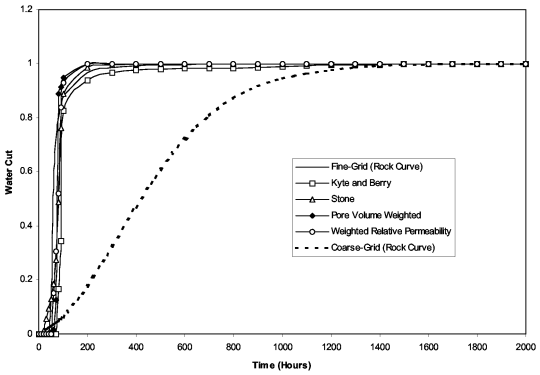

Fig. 8—Field water cut (Model-1, viscosity ratio 1, injection rate 20 cc/hr)

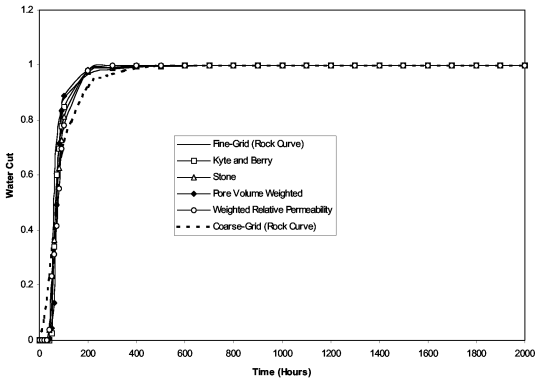

Fig. 9—Field water cut (Model-1, viscosity ratio 1, injection rate 120 cc/hr)

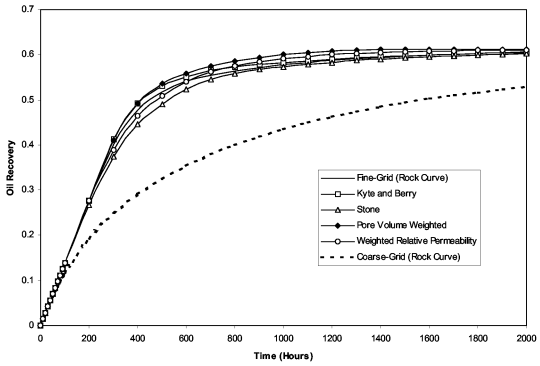

Fig. 10—Field oil recovery (Model-1, viscosity ratio 8, injection rate 20 cc/hr)

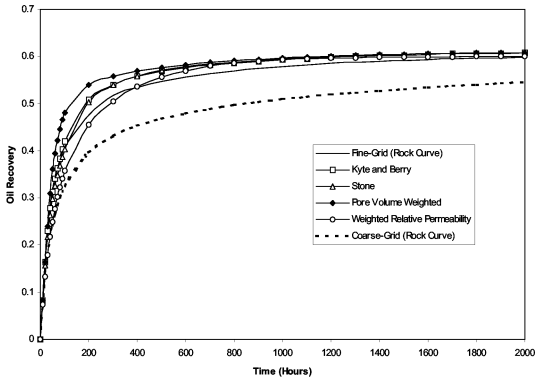

Fig. 11—Field oil recovery (Model-1, viscosity ratio 8, injection rate 120 cc/hr)

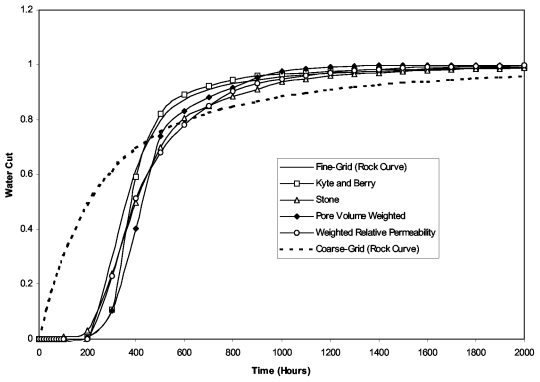

Fig. 12—Field water cut (Model-1, viscosity ratio 8, injection rate 20 cc/hr)

Model-2. This model is one of the models presented by Talukdar *et al.*[10]. They reported oil recovery and water cut at 20 cc/hr, 40 cc/hr, 80 cc/hr and 120 cc/hr for viscosity ratio of 4. The oil recovery and water cut at 20 cc/hr and 120 cc/hr injection rates for viscosity ratio of 1 and 8 are presented in Fig. 13 through 17. Other results are ommitted as the overall trend is consistent with the lowest and highest rates.

At low viscosity ratio, very good agreement between oil recovery by coarse-grid simulations using pseudos and that by fine-grid simulation with rock curve is observed at low rate. The Kyte and Berry and the Pore Volume Weighted pseudo techniques exactly reproduce the result, whereas the Stone technique predicts slightly higher and the Weighted Relative Permeability technique predicts slightly lower recovery (Fig. 13). Similar trend is observed at high rate though the Stone and the Weighted Relative Permeability techniques deviate considerably from fine-grid prediction (Fig. 14).

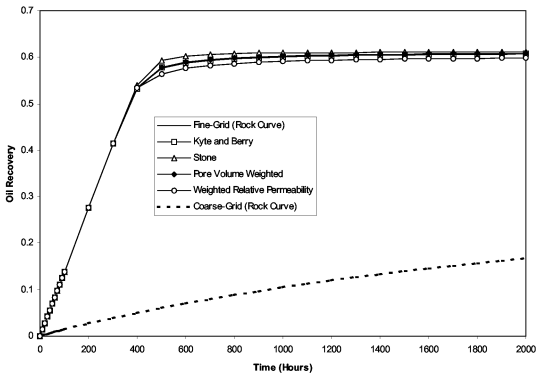

Fig. 13—Field oil recovery (Model-2, viscosity ratio 1, injection rate 20 cc/hr)

At high viscosity ratio, considerable deviations are observed for Stone and Weighted Relative Permeability techniques at both low and high rates though the trend is similar at low viscosity ratio (Fig. 15 and 16). The deviation is higher at high rates. Other two techniques are insensitive to viscosity ratio or injection rate.

No consistent trends are observed for field water cut results at low and high rates and with low and high viscosity ratios. But it appears that, at low rate, the Kyte and Berry and the Pore Volume Weighted pseudo techniques provide very good agreement with fine-grid behavior; the Stone technique predicts slightly lower whereas, the Weighted Relative Permeability technique predicts slightly higher water cut (Fig. 17). At high rate, all pseudo techniques duplicate fine-grid behavior. The time of water breakthrough and the maximum water cut are same for all techniques, which are consistent with the fine-grid prediction.

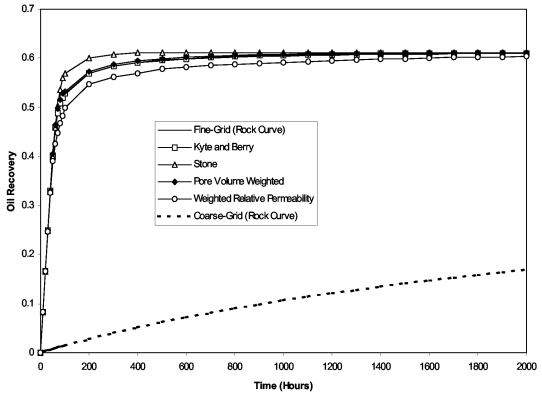

Fig. 14—Field oil recovery (Model-2, viscosity ratio 1, injection rate 120 cc/hr)

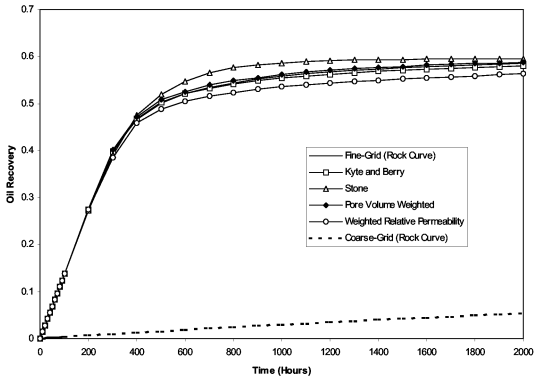

Fig. 15—Field oil recovery (Model-2, viscosity ratio 8, injection rate 20 cc/hr)

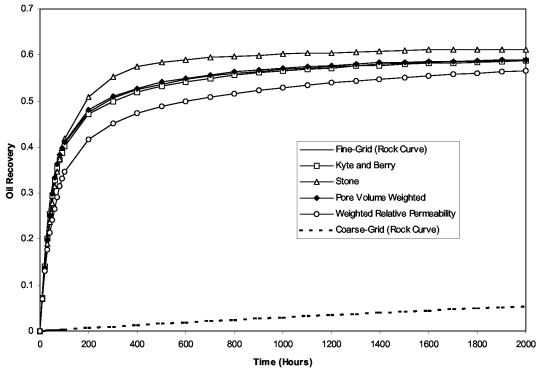

Fig. 16—Field oil recovery (Model-2, viscosity ratio 8, injection rate 120 cc/hr)

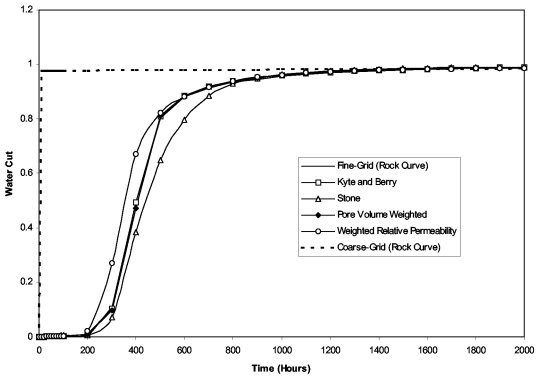

Fig. 17—Field water cut (Model-2, viscosity ratio 8, injection rate 20 cc/hr)

3D-Model. The fine-grid and coarse-grid systems of this model have been simulated at 200 cc/hr, 600 cc/hr and 1200 cc/hr injection rates and with viscosity ratio of 1, 4 and 8.

Very similar trends are observed for field oil recovery at all injection rates and with all viscosity ratios. The results for the extreme cases are presented in this paper since the trends are consistent.

At low injection rate and with low viscosity ratio, the oil recovery from coarse-grid simulations using pseudos produce very close results as that by fine-grid simulation with rock curves (Fig. 18). These results are quite different from that by coarse-grid simulation with rock curves. The Stone and the Pore Volume Weighted pseudo techniques give slightly higher recovery, whereas Kyte and Berry and the Weighted Relative Permeability techniques give slightly lower recovery.

As the injection rate increases with low viscosity ratio, the difference between fine-grid recovery and coarse-grid

recovery increases though the difference is not big. Trends are yet to be same (Fig. 19).

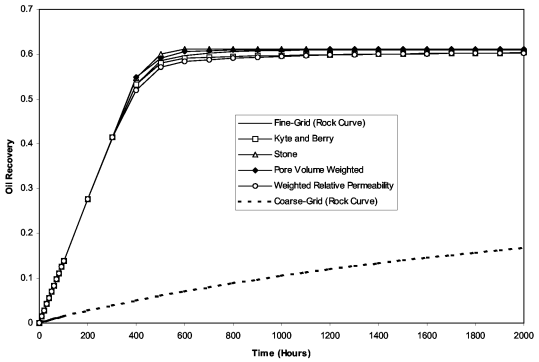

Fig. 18—Field oil recovery (3D-model, viscosity ratio 1, injection rate 200 cc/hr)

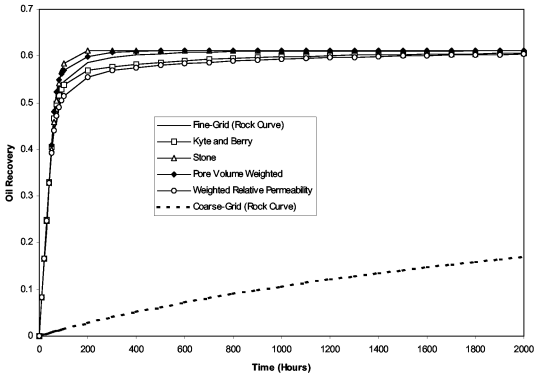

Fig. 19—Field oil recovery (3D-model, viscosity ratio 1, injection rate 1200 cc/hr)

At low injection rate, as the viscosity increases, the difference between fine-grid recovery and coarse-grid recovery increases. The differences are even higher than the increase in injection rate (Fig. 20). It is apparent that viscosity ratio has a more dominant effect on pseudo techniques than recovery rate.

A combined effect of increase in rate and increase in viscosity ratio can be observed in Fig. 21. The results obtained from pseudo techniques are deviating even more from the fine-grid result. The trends for these techniques are yet to be same with respect to fine-grid prediction.

No definite water cut trends can be observed for the pseudo techniques, but the trends are consistent with those for Model-2 with an exception that the fine-grid simulation predicts little earlier water breakthrough than the pseudo techiques. The time of water breakthrough for all pseudo techniques is the same. The reason for this early water breakthrough in fine-grid simulation is probably due to the segregation of water and early breakthrough in the bottom layers.

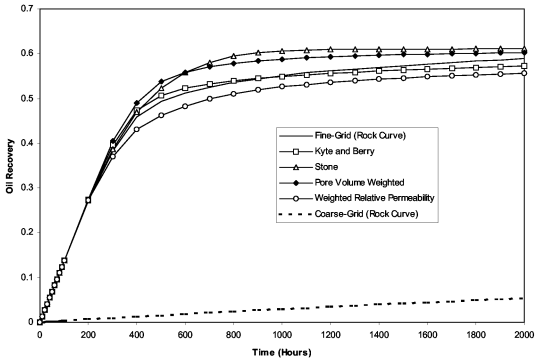

Fig. 20—Field oil recovery (3D-model, viscosity ratio 8, injection rate 200 cc/hr)

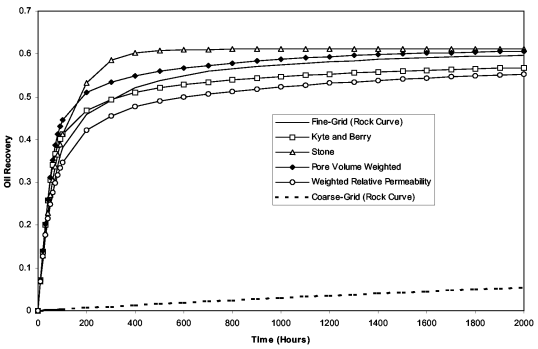

Fig. 21—Field oil recovery (3D-model, viscosity ratio 8, injection rate 1200 cc/hr)

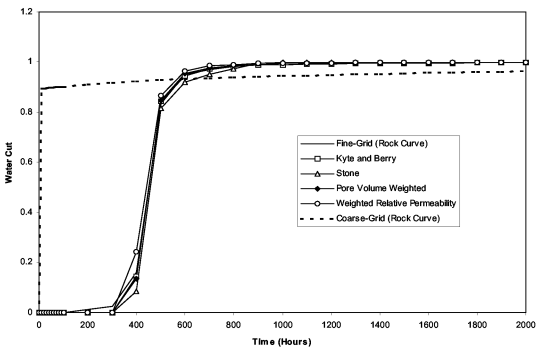

Fig. 22—Field water cut (3D-model, viscosity ratio 1, injection rate 200 cc/hr)

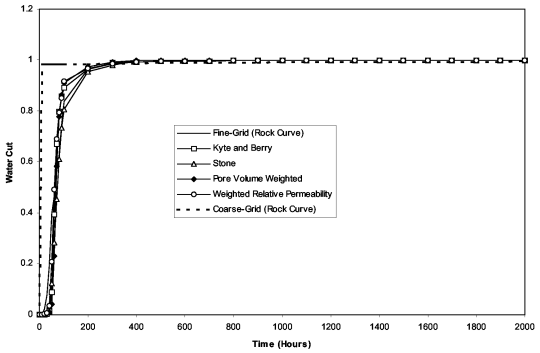

Fig. 23—Field water cut (3D-model, viscosity ratio 1, injection rate 1200 cc/hr)

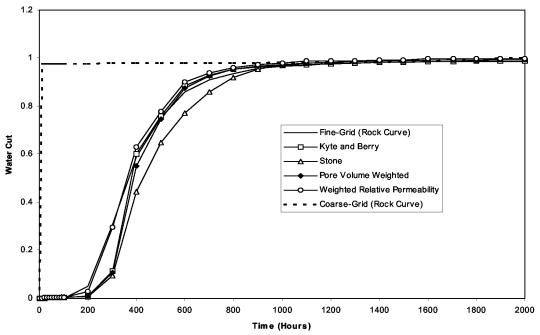

Fig. 24—Field water cut (3D-model, viscosity ratio 8, injection rate 200 cc/hr)

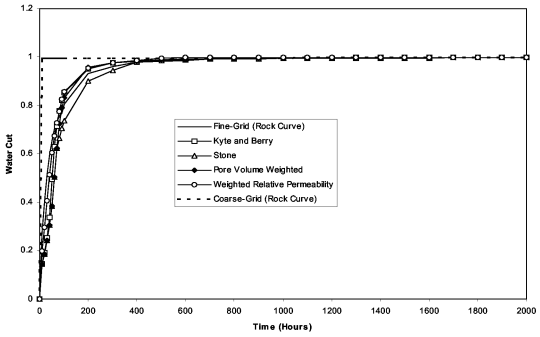

Fig. 25—Field water cut (3D-model, viscosity ratio 8, injection rate 1200 cc/hr)

Fig. 22 and 23 show water cut results for viscosity ratio of 1 at 200 cc/hr and 1200 cc/hr injection rates respectively. Water cut results at these rates but for viscosity ratio of 8 are shown in Fig. 24 and 25. The effect of injection rate and viscosity ratio on water cut behavior is apparent in the figures. In all cases, the maximum water cut predictions by pseudo techniques are consistent with that by fine-grid prediction. But in the early recovery stages at low injection rate, water cut behavior from pseudo techniques deviates considerably from fine-grid behavior as the viscosity ratio is increased. At high rate, the difference is not big.

Based on the results obtained from the models and the sensitivity studies, a rough guideline may be established to select the most effective pseudo technique for a particular situation. The recommended technique/techniques are listed in Table 2 with respect to the model type and the sensitivity cases.

Table 2—The most effective pseudo technique/techniques for the cases investigated

Model Type	Low Viscosity Ratio		High Viscosity Ratio	
	Low Rate	High Rate	Low Rate	High Rate
Model-1	WRP	K&B	K&B	K&B
Model-2	PVW K&B	PVW K&B	PVW K&B	PVW K&B
3D-model	PVW	PVW	K&B	K&B

For Model-1 at low rate with low viscosity ratio, though the Weighted Relative Permeability (WRP) technique is the most effective one, the Kyte and Berry (K&B) technique is very close to it. For 3D-model with low viscosity ratio, Kyte and Berry technique is also very close to Pore Volume Weighted (PVW) technique.

Conclusions

With an aim to verify the applicability and rate sensitivity of several conventional up-scaling techniques in fractured reservoir simulation, two 2D and one 3D fine-grid and equivalent coarse-grid simulation models have been developed. The fine-grid systems are simulated with rock curves to predict the actual behavior of the models. The coarse-grid systems are simulated with both rock- and generated pseudo curves. Four different pseudo techniques have been investigated at four recovery rates and with three oil-to-water viscosity ratios. The results obtained for a system in which water is displacing oil are analysed and the following conclusions are made:

1. The Kyte and Berry, Pore Volume Weighted, Weighted Relative Permeability and Stone pseudo generation techniques can be used in fractured reservoir simulation to coarsen simulation grids and to capture details of small-scale reservoir heterogeneity for a wide range of recovery rate and viscosity ratio.
2. In 2D model-1, where fractured fine-grid system has been converted into equivalent coarse-grid system without fracture and simulated as conventional reservoir, the pseudo techniques have negligible rate sensitivity at low oil-to-water ratio. They are sensitive to the viscosity ratio. At high viscosity ratio, they are slightly rate sensitive.

3. In 2D model-2, where fractured fine-grid system has been converted into equivalent coarse-grid dual-porosity system, the Kyte and Berry and the Pore Volume Weighted pseudo techniques are insensitive to viscosity ratio or injection rate. The Stone and the Weighted Relative Permeability techniques are sensitive to injection rate as well as to viscosity ratio. The Stone technique predicts slightly higher and the Weighted Relative Permeability technique predicts slightly lower recovery.
4. In 3D-model, where fractured fine-grid 3D system has been converted into equivalent 2D coarse-grid dual-porosity system, the pseudo techniques are sensitive to injection rate and viscosity ratio. The viscosity ratio has more dominant effect on pseudo techniques than recovery rate.
5. In 3D-model, the Stone and the Pore Volume Weighted pseudo techniques give higher recovery, whereas Kyte and Berry and the Weighted Relative Permeability techniques give lower recovery than the fine-grid prediction.
6. Based on the results obtained from the models and the sensitivity studies, it may be concluded that the Kyte and Berry type pseudo technique is the most effective technique irrespective of model type, injection rate and oil-to-water viscosity ratio.

Nomenclature

WRP	*Weighted Relative Permeability*
K&B	*Kyte and Berry*
PVW	*Pore Volume Weighted*
2D	*Two dimensional*
3D	*Three dimensional*

References

1. Warren, J.E. and Root, P.J.: "The Behavior of Naturally Fractured Reservoir," *SPEJ* (September 1963).
2. Lough, M.F., Lee, S.H. and Kamath, J.: "A New Method to Calculate the Effective Permeability of Grid Blocks Used in the Simulation of Natually Fractured Reservoirs," paper SPE 36730 presented at the 1996 Annual Technical Conference and Exhibition, Colorado, USA, October 6-9.
3. Bourbiaux, B.J., Cacas, M.C., Sarda, S. and Sabathier, J.C.: "A Fast and Efficient Methodology to Convert Fractured Reservoir Images into a Dual-Porosity Model," paper SPE 38907 presented at the 1997 Annual Technical Conference and Exhibition, Texas, USA, October 5-8.
4. Jacks, H.H., Smith, O.J.E., and Mattax, C.C.: "The modeling of a Three-Dimensional Reservoir with a Two-Dimensional Reservoir Simulator-The Use of Dynamic Pseudo Functions," paper *SPEJ* (June 1973) 175-185.
5. Kyte, J.R. and Berry, D.W.: "New Pseodo Functions to Control Numerical Dispersion," *SPEJ* (August 1975) 269-276.
6. Thomas, L.K., Dixon, T.N. and Pierson, R.G.: "Fractured Reservoir Simulation," *SPEJ* (February 1983) 42-54.
7. Rossen, R.H. and Shen, E.I.C.: "Simulation of Gas/Oil Drainage and Water/Oil Imbibition in Naturally Fractured Reservoirs," *SPERE* (November 1989) 464-470.
8. Dean, R.H. and Lo, L.L.: "Simulations of Naturally Fractured Reservoirs," SPERE (May 1988) 638-48; *Trans.*, AIME, 285.
9. Stone, H.L.: "Rigorous Black Oil Pseudofunctions," paper SPE 21207 presented at the 11th SPE Symposium on Reservoir Simulation, Anaheim, California, Feb. 17-20, 1991.
10. Talukdar, M.S., Banu, H.A., Torsæter, O. and Kleppe, J.: "Introducing Up-Scaling Techniques in Fractured Reservoir Simulation," paper presented at the 5th NORDIC Symposium on Petrophysics, Copenhagen, Denmark, August 19-20, 1999.